TENSILE AND FATIGUE BEHAVIOUR OF SHORT GLASS FIBRE REINFORCED PLASTIC COMPOSITES AT ELEVATED TEMPERATURE

Vicente Alejandro Perez Cervantes

A Thesis Presented for the Degree

of Doctor of Philosophy

The University Of Sheffield.

Department of Mechanical Engineering

Faculty of Engineering

December 2022

ABSTRACT

The present thesis proposes a chronology for the tensile and fatigue damage mechanisms leading to the failure of a 50wt% short glass-fibre reinforced polyamide 66 (PA66GF50) at elevated temperatures.

The aim of this investigation was to understand the deformation and damage mechanisms that lead to crack initiation and propagation under tensile and cyclic loading at high temperatures. To achieve this extensive experimental work was carried out at both room and elevated temperatures to characterise the material tensile and fatigue behaviour. In addition, state-of-the-art techniques such as X-ray micro-computed tomography with in situ mechanical testing and digital volume correlation at high temperatures were used to bring new knowledge about damage initiation and propagation mechanisms. Furthermore, new a multi-stage modelling methodology simulating the injection moulding manufacturing process and the heterogeneous stress and strain distributions in the composite specimens was developed to help understand the damage initiation and propagation mechanisms as well as to predict the fatigue life of the short glass fibre-reinforced polymers at both room and elevated temperatures.

An important temperature effect on the mechanical properties was observed, with a reduction of the Young's modulus, ultimate tensile strength and fatigue strength of the composite at elevated temperatures. Analysis of the specimen's fracture surfaces via scanning electron microscopy (SEM) and X-ray micro-computed tomography revealed the following damage mechanisms: Fibre failure, debonding at fibre ends, matrix cracking and debonding at the fibre-matrix interface. These damage mechanisms were found for both loading types and all temperatures.

Finally, chronologies were proposed for crack initiation and propagation mechanisms for tensile and fatigue loads. For tensile loads, the crack initiation occurs near the surface of the specimen, starting from debonding of the fibre ends and fibre-matrix interface, while for fatigue loads, crack initiation takes place in regions where fibres are less favourably orientated with respect to the load direction, commencing from debonding of fibre ends similar to the tensile failure. These crack initiation mechanisms occur at both room and elevated temperatures. Crack growth takes place through the propagation of the debonding of the fibre-matrix interfaces and fibre ends from one fibre to another at all temperatures and for both load types. However, under fatigue loads at elevated temperatures, voids and matrix micro-cracks accelerate crack propagation.

ACKNOWLEDGEMENTS

First, I would like to thank my research supervisor Dr. Christophe Pinna for his guidance and support through my PhD journey.

I would also like to acknowledge the Mexican government, through CONACYT, for providing financial support for this project.

Many thanks to Jaguar Land Rover for providing the material for this thesis and to Autodesk for letting me use their software to conduct this study.

I would also like to express my gratitude to all the friends I knew in Sheffield: Leo, Abraham, Hector, Kenneth, Rob and Daniel.

Finally, I must express my very profound gratitude to my family and fiancée for the continuous support and encouragement throughout all these years. This accomplishment would not have been possible without you. Thank you very much.

Table of Contents

1 INTRODUCTION 1
1.1 Motivation 1
1.2 Aim and key objectives 2
1.2.1 Key objectives 2
1.3 Novelty 3
1.1 Outline of the thesis 3
2 LITERATURE REVIEW 4
2.1 Polymer matrices 4
2.1.1 Glass transition temperature 5
2.2 Reinforcement fibres 5
2.2.1 Fibre length and critical fibre length 6
2.3 Manufacturing processes 8
2.4 Fibre orientation distribution 9
2.5 Fibre orientation tensor 11
2.6 Prediction of fibre orientation tensor 12
2.7 Mechanical behaviour of SFRP 14
2.7.1 Tensile behaviour 14
2.7.2 Fatigue of SFRP 28
2.8 Modelling of the fatigue behaviour 34
2.9 Discussion of the literature review 36
3 EXPERIMENTAL METHODOLOGY 38
3.1 Introduction 38
3.2 Material description 38
3.3 Specimens and conditioning 39
3.4 Tensile tests at room temperature 41

3.5 Tensile tests at 50 and 100° C 43
3.6 Fatigue tests at room temperature 47
3.7 Fatigue tests at 50 and 100 ° C 48
3.8 Damage mechanisms 50
3.8.1 In-situ tensile tests 50
3.8.2 In-situ tensile tests at 50 and 100° C 56
3.8.3 X-ray scanning of fatigued specimens after failure 60
3.9 Scanning Electron Microscopy (SEM) 61
3.10 Conclusion 62
4 MODELLING PROCEDURE 63
4.1 Introduction 63
4.2 Injection moulding process simulation 63
4.3 Simulation of the tensile tests 65
4.3.1 Boundary conditions 66
4.3.2 Mapping the orientation tensor 67
4.3.3 Material properties 68
4.3.4 Material characterisation for the simulation of tensile tests at room temperature, 50 and 100 Celsius degrees 70
4.4 Fatigue life prediction 72
4.5 Conclusion 76
5 MECHANICAL TESTING RESULTS 77
5.1 Tensile tests 77
5.1.1 Full-field strain measurements 80
5.2 Fatigue tests 89
5.2.1 Stiffness evolution of specimens tested at 50 and 100° C 90
5.2.2 Temperature measurements of specimens tested at 50 and 100° C 91
5.2.3 Hysteresis loops 96

6 DAMAGE MECHANISM 100
6.1 Fibre length, fibre diameter and volume fraction 100
6.2 Fibre orientation distribution 101
6.3 Orientation tensor 101
6.4 Digital volume correlation 105
6.4.1 0° specimen at room temperature 105
6.4.2 45° specimen at room temperature 112
6.4.3 90° specimen at room temperature 120
6.4.4 0° specimen at 50° C 128
6.4.5 0° specimen at 100° C 136
6.5 X-ray scanning of fatigued specimens after failure 142
6.6 Fracture surfaces 146
6.6.1 Tensile 0° specimens 146
6.6.2 Tensile 45° specimens 150
6.6.3 Tensile 90° specimens 153
6.6.4 Fatigue 0° specimens 156
6.6.5 Fatigue 45° specimens 159
6.6.6 Fatigue 90° specimens 162
6.7 Conclusion 166
7 MODELLING RESULTS 168
7.1 Injection moulding simulation 168
7.2 Stress analysis results 171
7.2.1 Room temperature specimens 172
7.2.2 50° C specimens 178
7.2.3 100° C specimens 183
7.3 Fatigue life predictions 189
7.4 Conclusion 191

8 DISCUSSION 193
8.1 Fibre orientation distribution 193
8.1 Tensile behaviour and failure mechanisms 194
8.1.1 Strain field distributions 196
8.1.2 Micro-tensile tests 198
8.1.3 Crack initiation and propagation under tensile load 201
8.1 Fatigue behaviour and damage mechanisms 208
8.1.1 Crack initiation and propagation under fatigue loads 209
9 CONCLUSION 212
9.1 Future work 214

LIST OF FIGURES

Figure 1-1 Automobile components made of SFRP. a) thermal dowel, b) oil filter module, c) thermostat housing, d) oil sensor [3].....1

Figure 2-1 Schematic of a) thermoplastics and b) thermosets [5] 4

Figure 2-2 Variation of tensile modulus with temperature for three different types of polymers: a) amorphous thermoplastic, b) semicrystalline thermoplastic, and c) thermoset [5]. 5

Figure 2-3 Stress variation with fibre length [7].....7

Figure 2-4 Schematic of the injection moulding process [19].....9

Figure 2-5 Diagram of the cross-section of an injected moulded SFRP.....10

Figure 2-6 Definition of the orientation vector $\boldsymbol{p}$ and angles θ and ∅ [24] 10

Figure 2-7 orientation tensor.....12

Figure 2-8 Comparison of predictions of fibre orientation tensor eigenvalues A11 and A22 using the Folgar and Tucker model (F-T) and the RSC model [33].....13

Figure 2-9 Comparison of different fibre orientation models. Adapted from [39].....14

Figure 2-10 Stress-strain curve and DIC images of the tensile test [40] 15

Figure 2-11 DIC strain distribution of PA66GF50 at room temperature. a) 0° specimen, b) 30° specimen, c) 45° specimen, c) 90° specimen. Adapted from [41] 16

Figure 2-12 Acoustic emission events during tensile tests [42] 16

Figure 2-13 Tensile stress-strain curves of SFRP at different orientations [44].....17

Figure 2-14 Tensile stress-strain curves for PA66GF50 at different orientations and locations [22].....18

Figure 2-15 Relation between fibre length and tensile strength: (a) carbon fibre epoxy resin composite; (b) glass fibre epoxy resin composite [45] 19

Figure 2-16 Stress-strain curves for short fibre epoxy composites with 1 mm, 5 mm and 15 mm length fibres [46].....19
Figure 2-17 Tensile properties variation for different orientations and temperatures of PBT and PA6 coupons. (a) tensile strength, (b) elastic modulus, and (c) strain at tensile strength [47].....21
Figure 2-18 Stress-strain curves at different strain rates for a) neat PP and b) PP with 40 wt% glass fibres [48].....22
Figure 2-19 Influence of moisture content on SFRP at different orientations [49].....23
Figure 2-20 a) fibre failure, b) damage at fibre ends, c) debonding at the fibre matrix interface, d) damage growth in the matrix, e) fibrillation. Adapted from [49].....23
Figure 2-21 Evolution of volumetric fraction of damage mechanism during tensile tests for different specimen orientations and relative humidity [49].....24
Figure 2-22 SEM images of a) damage at the fibre ends, b) fibre matrix debonding, c) matrix micro cracks. Adapted from [51].....25
Figure 2-23 Fracture surface of a tensile sample. The top right image is an image of a region of ductile failure. The bottom right image is a region of brittle failure [52].....26
Figure 2-24 Model of the failure process [52].....26
Figure 2-25 Evolution of damage during the tensile test for two different zones of the fracture surface [53].....27
Figure 2-26 Terminology used in fatigue [54].....28
Figure 2-27 S-N curve for PA66GF30 specimens of two different orientations [58].....28
Figure 2-28 Influence of the temperature on fatigue life [59].....29
Figure 2-29 Hysteresis loops at RT for a) R=0, b) R=-1, and at 130°C for c) R=0 and d) R=-1 [62].....30
Figure 2-30 Influence of moisture on fatigue life [64].....31

Figure 2-31 X-ray micro-computed tomography showing damage mechanisms in fatigue....32
Figure 2-32 Evolution at different fatigue cycles of a) fibre failure, b) debonding, c) crazing, d) micro-cracks 33
Figure 2-33 Schematic of fatigue damage process a) below Tg and b) above Tg [60] 34
Figure 2-34 S-N curve for PA66 GF50 at R=0 [68] 35
Figure 2-35 Comparison of fatigue modelling and experimental results using an energy-based criterion [70] 36
Figure 3-1 Dimensions of the specimens used for the fatigue and tensile tests. All dimensions are in mm. 39
Figure 3-2 Orientation and location of the manufacturing of the specimens in the plaque. Dimensions are in mm. The arrows indicate the injection flow. 40
Figure 3-3 Normal distribution of the moisture in the specimens after 72 hours of water immersion at 40°C 41
Figure 3-4 Example of DIC subsets and their deformation 42
Figure 3-5 DIC setup 42
Figure 3-6 Specimen with speckle pattern....43
Figure 3-7 Microstrains a) before alignment, b) zoom in to the strain of strain gauges 1-6, c) after alignment 44
Figure 3-8 a) Grips before the alignment, b) grips after the alignment 45
Figure 3-9 Strain distribution for a) specimen with the chamber door opened, b) with the door closed, and c) with the heat on....46
Figure 3-10 Setup for the tensile tests at high temperature 47
Figure 3-11 Set up of the fatigue machine for the test at high temperature....49
Figure 3-12 Instrumentation of the specimen 49
Figure 3-13 Dimensions of the µCT specimens 50

Figure 3-14 a) Standard deviation of principal strains for 0° specimen, b) Standard deviation of displacement for 0° specimen, c) Standard deviation of principal strains for 45° specimen, d) Standard deviation of displacement for 45° specimen, e) Standard deviation of principal strains for 90° specimen, f) Standard deviation of displacement for 90° specimen.....53
Figure 3-15 Region of interest in the 0° specimen where the orientation tensor was computed 54
Figure 3-16 a) In-situ tensile test rig, b) thermocouple at the centre of the gauge length 56
Figure 3-17 a) Standard deviation of principal strains for 0° specimen at 50° C, b) Standard deviation of displacement for 0° specimen at 50° C, c) Standard deviation of principal strains for 0° specimen at 100° C, d) Standard deviation of displacement for 0° specimen at 100° C58
Figure 3-18 a) Tabletop SEM, b) example of SEM specimen.....62
Figure 4-1 Modelling workflow.....63
Figure 4-2 Model and mesh of the plaque for the injection moulding simulation 64
Figure 4-3 Comparison of the a11 component at the centre of the specimen's gauge length for different mesh densities 64
Figure 4-4 Mesh independence study conducted on the specimen model.....66
Figure 4-5 Mesh and boundary conditions for the stress analysis 66
Figure 4-6 Superposition of the specimen at the manufacturing location in the plaque.....67
Figure 4-7 Visualisation of the superimposed meshes 68
Figure 4-8 Schematic of the process to obtain the material properties [84] 71
Figure 4-9 Diagram of the workflow and software used for the fatigue life estimation 72
Figure 4-10 Comparison of interpolated orientation tensor eigenvalues and Helius PFA eigenvalues.....74
Figure 4-11 Interpolation/extrapolation of S-N curves [97] 76
Figure 5-1 Stress-Strain curves at different temperatures.....77

Figure 5-2 Interval plots for specimens at different orientations and temperatures using a 95% confidence interval. a) Young's modulus, b) Ultimate tensile strength (UTS), c) Strain at break.....79
Figure 5-3 Strain distribution before failure on the front surface for a 0° specimen loaded in tension.....81
Figure 5-4 Strain distribution before failure on the front surface for a 45° specimen loaded in tension.....82
Figure 5-5 Strain distribution before failure on the front surface for a 90° specimen loaded in tension.....82
Figure 5-6 Strain in the loading direction before final failure for a 0° specimen at 50° C. a) front view, b) lateral view.....83
Figure 5-7 Strain in the loading direction before final failure for a 45° specimen at 50° C. a) front view, b) lateral view, c) fractured specimen showed in a).....84
Figure 5-8 Strain in the loading direction before final failure for a 90° specimen at 50° C. a) front view, b) lateral view, c) fractured specimen showed in a).....85
Figure 5-9 Strain in the loading direction before final failure for a 0° specimen at 100° C. a) front view, b) lateral view.....86
Figure 5-10 Strain in the loading direction before final failure for a 45° specimen at 100° C. a) front view, b) lateral view, c) fractured specimen showed in a).....87
Figure 5-11 Strain in the loading direction before final failure for a 90° specimen at 100° C. a) front view, b) lateral view.....88
Figure 5-12 Constant amplitude S-N curves for PA66GF50 at different temperatures 89
Figure 5-13 Stiffness evolution at 50° C of a) 0° specimens, b) 45° specimens, c) 90° specimens.....92

Figure 5-14 Stiffness evolution at 100° C of a) 0° specimens, b) 45° specimens, c) 90° specimens.....93
Figure 5-15 Chamber temperature and temperature evolution for a) 0° specimens, b) 45° specimens, c) 90° specimens tested at 50° C 94
Figure 5-16 Chamber temperature and temperature evolution for a) 0° specimens, b) 45° specimens, c) 90° specimens tested at 100° C.....95
Figure 5-17 Hysteresis loops of a) 0° specimen at 67.5 MPa, b) 45° specimen at 40 MPa, c) 90° specimen at 40 MPa. All specimens were tested at 50° C.....97
Figure 5-18 Hysteresis loops of a) 0° specimen at 50 MPa, b) 45° specimen at 40 MPa, c) 90° specimen at 25 MPa. All specimens were tested at 100° C.....99
Figure 5-19 Hysteresis area evolution of specimens tested at 50° C. a) 0° specimens, b) 45° specimens, c) 90° specimens.....99
Figure 5-20 Hysteresis area evolution of specimens tested at 100° C. a) 0° specimens, b) 45° specimens, c) 90° specimens.....99
Figure 6-1 Fibre distribution through the thickness of a) 0° specimen at room temperature, 45° specimen at room temperature, c) 90° specimen at room temperature, d) 0° specimen at 50° C, e) 0° specimen at 100° C.....103
Figure 6-2 Measured orientation tensor a) a11 component, b) a22 component, c) a33 component.....104
Figure 6-3 Schematic of the µCT sample views. a) front view, b) lateral view (thickness)..105
Figure 6-4 Tensile strain in the loading direction of a 0° specimen at room temperature at different stresses, a) 25% of UTS, b) 50% of UTS, c) 75% of UTS, d) 95% of UTS. Front view.....106

Figure 6-5 Tensile strain in the loading direction of a 0° specimen at room temperature at different stresses, a) 25% of UTS, b) 50% of UTS, c) 75% of UTS, d) 95% of UTS. Lateral view 107
Figure 6-6 Tensile strain in the loading direction of a 0° specimen at room temperature at different stresses, a) 25% of UTS, b) 50% of UTS, c) 75% of UTS, d) 95% of UTS. Front view at mid thickness 108
Figure 6-7 Tensile strain in the loading direction of a 0° specimen at room temperature at different stresses, a) 25% of UTS, b) 50% of UTS, c) 75% of UTS, d) 95% of UTS. Lateral view at mid thickness 109
Figure 6-8 Superimposed deformed mesh on the microstructure of a 0° specimen. Front view. a) full gauge length of the specimen, b) zoom in to the region of strain localisation 110
Figure 6-9 Superimposed deformed mesh on the microstructure of a 0° specimen. Front view at mid-thickness. a) full gauge length of the specimen, b) zoom in to the region of strain localisation 110
Figure 6-10 Superimposed deformed mesh on the microstructure of a 0° specimen. Lateral view. a) full gauge length of the specimen, b) zoom in to the region of strain localisation, c) Lateral view at mid-width, d) zoom in to the region of strain localisation at mid-width 111
Figure 6-11 Deformed DVC mesh superimposed on the fractured 0° specimen. a) Front view, b) lateral view 112
Figure 6-12 Tensile strain in the loading direction of a 45° specimen at room temperature at different stresses, a) 25% of UTS, b) 50% of UTS, c) 75% of UTS. Front view 113
Figure 6-13 Tensile strain in the loading direction of a 45° specimen at room temperature at different stresses, a) 25% of UTS, b) 50% of UTS, c) 75% of UTS. Lateral view 114

Figure 6-14 Tensile strain in the loading direction of a 45° specimen at room temperature at different stresses, a) 25% of UTS, b) 50% of UTS, c) 75% of UTS. Front view at mid thickness.....115
Figure 6-15 Tensile strain in the loading direction of a 45° specimen at room temperature at different stresses, a) 25% of UTS, b) 50% of UTS, c) 75% of UTS. Lateral view at mid width 116
Figure 6-16 Superimposed deformed mesh on the microstructure of a 45° specimen. Front view. a) full gauge length of the specimen, b) zoom in to the region of strain localisation ..117
Figure 6-17 Superimposed deformed mesh on the microstructure of a 45° specimen. Lateral view. a) full gauge length of the specimen, b) zoom in to the region of strain localisation ..117
Figure 6-18 Deformed DVC mesh superimposed on the fractured 45° specimen. a) Front view, b) lateral view.....118
Figure 6-19 μCT image of the broken 45° specimen.....119
Figure 6-20 μCT image of the 45° specimen. a) before loading, b) after failure.....119
Figure 6-21 Tensile strain in the loading direction of a 90° specimen at room temperature at different stresses, a) 25% of UTS, b) 50% of UTS, c) 75% of UTS. Front view.....122
Figure 6-22 Tensile strain in the loading direction of a 90° specimen at room temperature at different stresses, a) 25% of UTS, b) 50% of UTS, c) 75% of UTS. Lateral view 123
Figure 6-23 Tensile strain in the loading direction of a 90° specimen at room temperature at different stresses, a) 25% of UTS, b) 50% of UTS, c) 75% of UTS. Front view at mid-thickness.....124
Figure 6-24 Tensile strain in the loading direction of a 90° specimen at room temperature at different stresses, a) 25% of UTS, b) 50% of UTS, c) 75% of UTS. Lateral view at mid-width 125

Figure 6-25 Superimposed deformed mesh on the microstructure of a 90° specimen. Front view. a) full gauge length of the specimen, b) zoom in to the region of strain localisation ..126
Figure 6-26 Superimposed deformed mesh on the microstructure of a 90° specimen. Front view at mid-thickness. a) full gauge length of the specimen, b) zoom in to the region of strain localisation 126
Figure 6-27 Superimposed deformed mesh on the microstructure of a 90° specimen. Lateral view. a) full gauge length of the specimen, b) zoom in to the region of strain localisation, c) Lateral view at mid-width, d) zoom in to the region of strain localisation at mid thickness .127
Figure 6-28 Deformed DVC mesh at 75% of the UTS superimposed on the fractured 90° specimen. a) Front view, b) lateral view 128
Figure 6-29 Tensile strain in the loading direction of a 0° specimen at 50°C at a) 25% of UTS, b) 50% of UTS, c) 75% of UTS, d) 95% of UTS. Front view 129
Figure 6-30 Tensile strain in the loading direction of a 0° specimen at 50°C at a) 25% of UTS, b) 50% of UTS, c) 75% of UTS, d) 95% of UTS. Lateral view 130
Figure 6-31 Tensile strain in the loading direction of a 0° specimen at 50°C at a) 25% of UTS, b) 50% of UTS, c) 75% of UTS, d) 95% of the UTS. Front view at mid-thickness 131
Figure 6-32 Tensile strain in the loading direction of a 0° specimen at 50°C at a) 25% of UTS, b) 50% of UTS, c) 75% of UTS, d) 95% of UTS. Lateral view at mid-width 132
Figure 6-33 Superimposed deformed mesh on the microstructure of a 0° specimen at 50° C. Front view. a) front surface, b) cut at mid-thickness 134
Figure 6-34 Superimposed deformed mesh on the microstructure of a 0° specimen at 50° C. Lateral view. a) surface, b) cut at mid-width 135
Figure 6-35 µCT image of 0° specimen at 50° C showing damage in the sample 136
Figure 6-36 Tensile strain in the loading direction of a 0° specimen at 100° C at a) 25% of UTS, b) 50% of UTS, c) 75% of UTS, d) 95% of UTS. Front view 137

Figure 6-37 Tensile strain in the loading direction of a 0° specimen at 100° C at a) 25% of UTS, b) 50% of UTS, c) 75% of UTS, d) 95% of UTS. Lateral view 138
Figure 6-38 Tensile strain in the loading direction of a 0° specimen at 100° C at a) 25% of UTS, b) 50% of UTS, c) 75% of UTS, d) 95% of the UTS. Front view at mid-thickness....139
Figure 6-39 Tensile strain in the loading direction of a 0° specimen at 100° C at a) 25% of UTS, b) 50% of UTS, c) 75% of UTS, d) 95% of UTS. Lateral view at mid-width.....140
Figure 6-40 Superimposed deformed mesh on the microstructure of a 0° specimen at 100° C. Front view. a) front surface, b) cut at mid-thickness 141
Figure 6-41 Superimposed deformed mesh on the microstructure of a 0° specimen at 100° C. Lateral view. a) surface, b) cut at mid-width 142
Figure 6-42 Scanned fracture surface of a fatigue 0° specimen tested at 50° C. a) front view, b) lateral view 143
Figure 6-43 Scanned fracture surface of a fatigue 90° specimen tested at 50° C. a) front view, b) lateral view 144
Figure 6-44 Scanned fracture surface of a fatigue 90° specimen tested at 100° C. a) surface, b) 114.6µm below the surface, c) 229.2µm below the surface.....145
Figure 6-45 Fracture surface of a tensile 0° specimen at room temperature 147
Figure 6-46 Fracture surface of a tensile 0° specimen at 50° C 148
Figure 6-47 Fracture surface of a tensile 0° specimen at 100° C 149
Figure 6-48 Fracture surface of a tensile 45° specimen at room temperature 150
Figure 6-49 Fracture surface of a tensile 45° specimen at 50° C 151
Figure 6-50 Fracture surface of a tensile 45° specimen at 100° C 152
Figure 6-51 Fracture surface of a tensile 90° specimen at room temperature 153
Figure 6-52 Fracture surface of a tensile 90° specimen at 50° C 154
Figure 6-53 Fracture surface of a tensile 90° specimen at 100° C 155

Figure 6-54 Fracture surface of a fatigue 0° specimen at room temperature.....156
Figure 6-55 Fracture surface of a fatigue 0° specimen at 50° C.....157
Figure 6-56 Fracture surface of a fatigue 0° specimen at 100° C.....158
Figure 6-57 Secondary crack in a fatigue 0° specimen at 100° C 159
Figure 6-58 Fracture surface of a fatigue 45° specimen at room temperature.....160
Figure 6-59 Fracture surface of a fatigue 45° specimen at 50° C.....161
Figure 6-60 Fracture surface of a fatigue 45° specimen at 100° C.....162
Figure 6-61 Fracture surface of a fatigue 90° specimen at room temperature.....163
Figure 6-62 Fracture surface of a fatigue 90° specimen at 50° C.....164
Figure 6-63 Secondary crack in a fatigue 90° specimen at 50° C 165
Figure 6-64 Fracture surface of a fatigue 90° specimen at 100° C.....166
Figure 7-1 Moldflow a11 orientation component results. Surface and thickness views 168
Figure 7-2 Measured orientation tensor compared to simulation results. a) a11 component, b) a22 component, c) a33 component 170
Figure 7-3 Schematic of the specimen's view. a) front view, b) lateral view (thickness), c) cross-section cut.....171
Figure 7-4 Comparison of experimental Stress-Strain and predicted curves before and after reverse engineering (RE) for specimens tested at room temperature 172
Figure 7-5 Evolution of the maximum principal stress and maximum principal strain distributions of a simulated tensile 0° specimen at room temperature.....174
Figure 7-6 Cross section cuts at the middle and end of the gauge length of the 0° specimen at room temperature. a) stress distribution, b) strain distribution.....175
Figure 7-7 Evolution of the stress and strain distribution of a simulated tensile 45° specimen at room temperature 176

Figure 7-8 Cross section cuts at the middle and end of the gauge length of the 45° specimen at room temperature. a) stress distribution, b) strain distribution 176
Figure 7-9 Evolution of the stress and strain distribution of a simulated tensile 90° specimen at room temperature 177
Figure 7-10 Cross-section cuts at the middle and end of the gauge length of the 90° specimen. a) stress distribution, b) strain distribution 178
Figure 7-11 Comparison of experimental Stress-Strain and predicted curves before and after reverse engineering (RE) for specimens tested at 50° C..... 178
Figure 7-12 Evolution of the stress and strain distribution of a simulated tensile 0° specimen at 50° C 180
Figure 7-13 Cross-section cuts at the middle and end of the gauge length of the 0° specimen at 50° C. a) stress distribution, b) strain distribution 180
Figure 7-14 Evolution of the stress and strain distribution of a simulated tensile 45° specimen at 50° C 181
Figure 7-15 Cross section cuts at the middle and end of the gauge length of the 45° specimen at 50° C. a) stress distribution, b) strain distribution 182
Figure 7-16 Evolution of the stress and strain distribution of a simulated tensile 90° specimen at 50° C 183
Figure 7-17 Cross-section cuts at the middle and end of the gauge length of the 90° specimen at 50° C. a) stress distribution, b) strain distribution 183
Figure 7-18 Comparison of experimental Stress-Strain and predicted curves before and after reverse engineering (RE) for specimens tested at 100° C..... 184
Figure 7-19 Evolution of the stress and strain distribution of a simulated tensile 0° specimen at 100° C 186

Figure 7-20 Cross-section cuts at the middle and end of the gauge length of the 0° specimen at 100° C. a) stress distribution, b) strain distribution 186
Figure 7-21 Evolution of the stress and strain distribution of a simulated tensile 45° specimen at 100° C 187
Figure 7-22 Cross section cuts at the middle and end of the gauge length of the 45° specimen at 100° C. a) stress distribution, b) strain distribution 188
Figure 7-23 Evolution of the stress and strain distribution of a simulated tensile 90° specimen at 100° C 189
Figure 7-24 Cross section cuts at the middle and end of the gauge length of the 90° specimen at 100° C. a) stress distribution, b) strain distribution 189
Figure 7-25 Results of S-N fatigue modelling.....190
Figure 8-1 Effect of the Ramberg-Osgood parameters on the simulated stress-strain curve of a 90° specimen at room temperature.....195
Figure 8-2 Comparison of DIC results at room temperature of the current study (left images) against results in the literature *[105]* (right images). a) 0° specimen, b) 45° specimen, c) 90° specimen 196
Figure 8-3 Thickness comparison between FEA and DIC for validation. a) 0° specimen, b) 45° specimen, c) 90° specimen. All samples were loaded in tension at 50° C.....197
Figure 8-4 Comparison between FEA and DIC for validation. a) 0° specimen, b) 45° specimen, c) 90° specimen. All samples were loaded in tension at 100° C. Front view.....198
Figure 8-5 Comparison of DVC results at the end of the tensile test. a) 45° specimen, b) 90° specimen, c) 0° specimen at 50° C, d) 0° specimen at 100° C 199
Figure 8-6 DVC results at the end of the tensile test for 0° specimen. a) lateral view at the surface, b) lateral view at mid-width 200

Figure 8-7 Comparison of damage during in situ tensile tests. a) damage found in this study, b) damage reported in the literature [53] 201
Figure 8-8 Lateral view of the DVC results for 0° specimens at a) room temperature, b) 50° C, c) 100° C 202
Figure 8-9 Stress in the thickness of 0° specimens at a) room temperature, b) 50° C, c) 100° C 202
Figure 8-10 SEM images of the shell layer of 0° specimens at a) room temperature, b) 50° C, c) 100° C 203
Figure 8-11 Cross-section view of the gauge length of 0° specimens at a) room temperature, b) 50° C, c) 100° C.....203
Figure 8-12 Transition area between ductile and brittle failures in 0° specimens under tension at a) room temperature, b) 50° C, c) 100° C 204
Figure 8-13 Chronology of tensile failure 0° specimen. a) debonding at fibre ends, b) propagation of debonding to the fibre-matrix interface, c) propagation of debonding, d) initial crack, e) rapid propagation 205
Figure 8-14 SEM images of the shell layer of 90° specimens at a) room temperature, b) 50° C, c) 100° C 206
Figure 8-15 SEM images of the core layer of 90° specimens at a) room temperature, b) 50° C, c) 100° C 206
Figure 8-16 Chronology of tensile failure 90° specimen. a) debonding at fibre- matrix interface b) propagation of debonding to the adjacent fibre-matrix interface and initial crack, e) rapid propagation through pulled-out fibres 207
Figure 8-17 SEM images of the core layer of fatigue 0° specimens at a) room temperature, b) 50° C, c) 100° C.....210
Figure 8-18 Propagation of damage. Ductile and brittle fracture regions 210

Figure A-1 Schematic of the Python workflow for the mappig of the rientation tensors.....216

Figure A-2 Workflow of the Python script for fatigue life estimation 217

LIST OF TABLES

Table 2-1 Typical properties of some reinforcing fibres[7].....6

Table 2-2 Comparison of fibre reinforced polymer composites manufacturing processes [17]8

Table 3-1 Material properties for dry as moulded and conditioned state [71].....38

Table 3-2 Forces and stresses for the fatigue tests at room temperature 47

Table 3-3 Stress levels for the fatigue tests at 50 and 100°C.....48

Table 3-4 Loads for the in-situ tensile tests 51

Table 3-5 Scanning parameters.....51

Table 3-6 Selected subcell size and precision of strain and displacement 53

Table 3-7 Cylinder correlation parameters 55

Table 3-8 Parameters for the centre-line tracing.....55

Table 3-9 Loads for the in-situ tensile tests at 50 and 100° C 57

Table 3-10 Scanning parameters for the in-situ tensile tests at 50° and 100°C.....57

Table 3-11 Selected subcell size and precision of strain and displacement for each specimen 59

Table 3-12 Cylinder correlation parameters for the 50 and 100° C specimens 59

Table 3-13 Centre-line parameters for the 50 and 100 C specimens.....59

Table 3-14 Scanning parameters for fracture surfaces of fatigue specimens 61

Table 3-15 Scanning parameters for the second scan of the fracture surfaces of fatigue specimens.....61

Table 4-1 Values of the coefficients of the MRD model.....65

Table 5-1 Parameters of Basquin's equation 90

Table 6-1 Fibre length, fibre diameter and volume fraction of all the scanned samples.....100

Table 7-1 Material parameters at room temperature before and after reverse engineering (RE) 173

Table 7-2 Material parameters at 50° C before and after reverse engineering (RE).....179

Table 7-3 Material parameters at 100° C before and after reverse engineering (RE) 185

Table 7-4 Basquin's equations for experimental data and model prediction at different temperatures.....191

ACRONYMS

µCT	Micro-computed tomography
DIC	Digital image correlation
DVC	Digital volume correlation
FEA	Finite element analysis
MRD	Moldflow Rotational Diffusion model
NI	National Instruments
SEM	Scanning electron microscope
SFRP	Short fibre reinforced polymer
S-N	Stress-Life curve
UTS	Ultimate tensile stress

NOMENCLATURE

Symbol	Unit	Description
K_d	kN/mm	Dynamic stiffness
T_g	°C	Glass transition temperature
l_c	µm	Critical fibre length
β_0	m	Displacement resolution
β_1	Pixel	Image displacement accuracy
Ci	-	Interaction coefficient
E	MPa	Young's modulus
F	kN	Force
L	m^2	Field of view
N	Cycles	Fatigue life
R	-	Stress ratio
α	-	Orientation tensor
δ	mm	Displacement
λ	-	Fibre share
l	-	Absolute maximum principal stress direction
$\vec{p}$	-	Orientation vector
θ	°	Angle
∅	°	Angle

1 INTRODUCTION

1.1 Motivation

Current regulations against global warming are leading industries to consider the replacement of traditional metallic components with lightweight composites suitable for mass production.

Interest in short fibre reinforced polymers (SFRP) is increasing in the automotive industry as the European Parliament introduced strict rules for car manufacturers on CO_2 emissions from cars. These new rules force car manufacturers to reduce these emissions from 158.7 g/km to 95 g/km [1]. Typically, SFRP were used in components bearing low loads, but nowadays, more applications to these materials in components carrying high static and cyclic loads are of interest. In addition to this, around 25% of the total SFRP are located under the hood [2], where high temperatures are predominant. Figure 1-1a-d shows some automobile components made of SFRP.

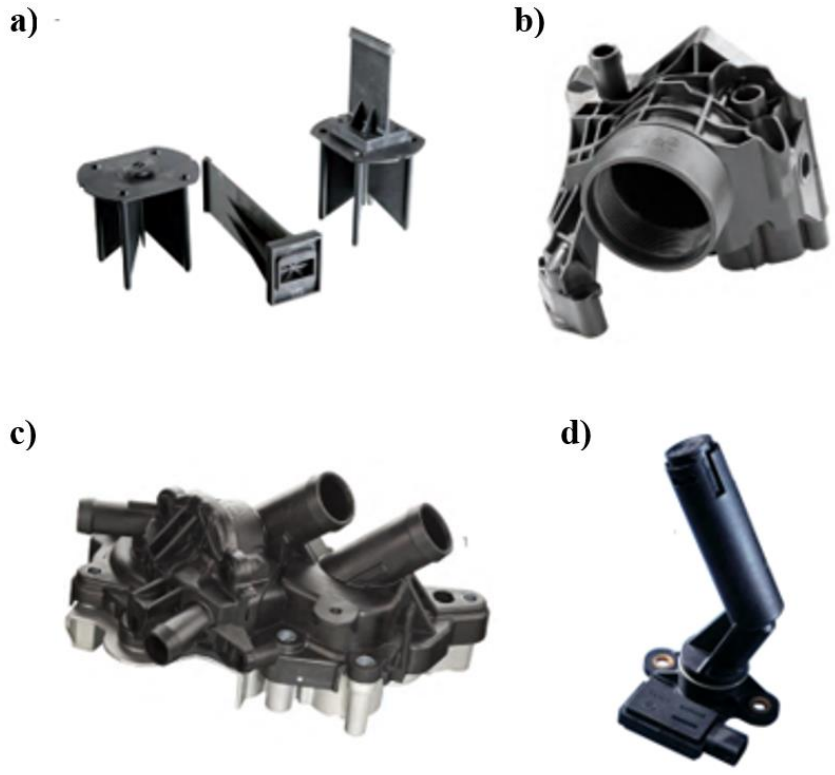

Figure 1-1 Automobile components made of SFRP. a) thermal dowel, b) oil filter module, c) thermostat housing, d) oil sensor [3]

Engineers and designers are constrained by economic, technical and environmental limitations. The SFRP are well-positioned to provide solutions and cannot be ignored. These polymer composites are a combination of a polymer matrix with a reinforcing phase of

discontinuous fibres to enhance the mechanical properties. They offer a good ratio between weight and performance, allowing a weight reduction of the components. Besides this, they give design freedom to manufacture complex shapes that would be very expensive or difficult to fabricate with metals thanks to production processes such as injection moulding.

There are several production methods but the main techniques used are injection moulding and compression moulding. These conventional manufacturing processes make SFRP good candidates for components that need to be manufactured on a large scale compared to continuous fibre reinforced composites which have a more time-consuming fabrication process and are more expensive to produce.

However, these production methods make the design of SFRP components a challenging task. This is due to the complex mechanical behaviour resulting from the continuous variation of fibre orientations through the thickness of the moulded parts caused by these production techniques.

Although several research studies have been reported over the past decade for the characterisation and the modelling of the static and cyclic behaviour of SFRP, there is still a general lack of understanding of the deformation and damage mechanisms operating in the complex microstructure of this material. Furthermore, studies carried out at elevated temperatures are ever scarcer in the literature.

1.2 Aim and key objectives

The aim of this project is to generate new knowledge of the deformation and damage mechanisms of short glass fibre-reinforced polymers under tensile and fatigue loads at elevated temperatures with the purpose of predicting the fatigue life of this materials.

1.2.1 Key objectives

- To review the existing published literature on SFRP and identify knowledge gaps
- To characterise the material response under tensile and fatigue loads at elevated temperatures
- To characterise the complex fibre distribution along the material thickness
- To understand the crack initiation and propagation damage mechanisms that lead to the final failure of SFRP at elevated temperatures
- To propose a damage chronology for the failure of SFRP
- To predict the fatigue life of SFRP at elevated temperatures

1.3 Novelty

The present work aims to address the gaps in knowledge regarding the deformation and damage mechanisms of short glass-fibre reinforced polymer composites under tensile and fatigue loads at elevated temperatures.

It proposes damage chronologies to describe the failure of SFRP under tensile and fatigue loads at both room and elevated temperatures. These chronologies are based on extensive experimental work carried out at both room and high temperatures and state-of-the-art analysis techniques such as in situ tensile tests at both room and elevated temperatures inside a X-ray micro-computed tomography microscope, digital volume correlation and a new method to conduct digital image correlation at high temperatures. In combination with the experimental testing, a new multi-scale modelling approach that includes the prediction of fibre orientation distribution caused by the manufacturing process and validated at every step of the modelling stages to assess the accuracy of the results was used to understand the stress and strain distributions in the specimens and to predict the fatigue life of SFRP.

1.1 Outline of the thesis

This thesis is organised as follows:

In chapter 2, an in-depth review of the most relevant currently publish literature regarding short fibre reinforced polymers is presented. In chapter 3 the material used in this investigation, the injection moulded polyamide 66 reinforced with 50 wt% glass fibres (PA66GF50) is introduced. It describes the geometries of the specimens, the experimental methodology and the equipment utilised. Chapter 4, presents in detail the multi-scale modelling procedure followed. The results of this study were divided into three chapters: the results of the mechanical testing are shown in chapter 5. In chapter 6, the results of the damage mechanisms are analysed, and the modelling results are presented in chapter 7. Afterwards, in chapter 8 the results are discussed and damage chronologies are proposed. Finally, chapter 9 presents an overall conclusion of this investigation and suggestions for further work.

2 LITERATURE REVIEW

Short Fibre Reinforced Plastics (SFRP) are a combination of a matrix phase and a reinforcing phase. These two constituents and the manufacturing method play a major role in the resulting mechanical properties of the component.

This is explained in the following sections.

2.1 Polymer matrices

The matrix material transfers the load to the fibres, binds them together and holds them in place.

The matrix constituent of SFRP is a polymeric resin. Polymers are giant chainlike molecules coupled by intermolecular interactions such as hydrogen bridges, dipole and Van der Waals forces, whilst the atoms in each molecule are bound by covalent forces [3, 4].

There are two major types of polymers: thermoset and thermoplastic polymers.

Molecules in thermosets are joined together by cross-links forming a three-dimensional network structure, which is formed when the thermosets undergo a curing process. These cross-links cause the sliding of molecules difficult, making the thermoset strong and rigid [3, 5].

On the other hand, thermoplastic chain molecules are not cross-linked. Figure 2-1 illustrates this difference. Thermoplastics soften with the application of heat. This is because the bonds between molecules break, allowing them to move. On cooling, the molecules freeze, and the bonds restore. Thus, thermoplastics can be melted and reshaped as many times as desired, while thermosets decompose when heated [3-5].

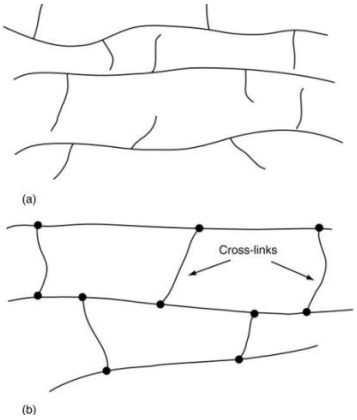

Figure 2-1 Schematic of a) thermoplastics and b) thermosets [5]

Some examples of thermoplastics are: Polyamide (PA), Polyethylene (PE), Polypropylene (PP), Polystyrene (PS) and Polycarbonate (PC) [6]

This work investigates a SFRP made of a thermoplastic polyamide matrix named Nylon 66 (PA66).

2.1.1 Glass transition temperature

The mechanical properties of thermoplastics are strongly dependent on loading conditions, humidity and temperature. Many properties (e.g., viscosity, heat capacity, elastic modulus, and expansion coefficient) change rapidly around the glass transition temperature (T_g). Above T_g, the thermoplastics change into rubber-like solids with the ability to undergo large deformations under external loads [3, 5]. The reason for this is that in a temperature surrounding the T_g the material morphology changes from crystalline to amorphous, allowing a greater mobility of the molecules [4]. Figure 2-2 shows the general trend of tensile modulus variation of several polymers with temperature.

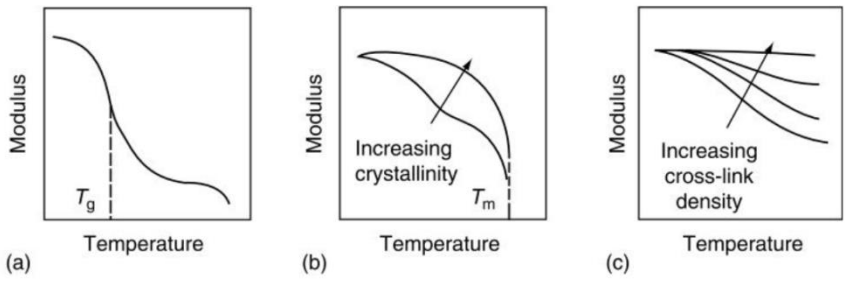

Figure 2-2 Variation of tensile modulus with temperature for three different types of polymers: a) amorphous thermoplastic, b) semicrystalline thermoplastic, and c) thermoset [5].

2.2 Reinforcement fibres

The purpose of reinforcement fibres is to improve the mechanical properties of matrices, and their main function is to carry the load.

Reinforcements can be of different shapes such as particles, flakes, whiskers, sheets, long fibres or short fibres.

Most reinforcements have a fibrous shape because materials are stronger and stiffer in that form than in any other [3]. They usually have diameters of around 10 μm [7, 8].

Three types of fibres dominate the SFRP scene. These are glass fibres, carbon fibres and aramid fibres. The most common reinforcement fibres are glass fibres due to their low cost

and superior properties relative to the matrix [3, 4, 7, 8]. Glass fibres are composed of silica (SiO_2), which is then mixed with chemicals to produce different types of glass. A few examples of glass fibres are [3, 4, 7, 8]:

- A-glass; good resistance to chemicals but low electrical properties
- C-glass; excellent chemical resistance
- E-glass; good strength all-around and electrical insulation
- S-glass; high strength

Table 2-1 summarises some physical and mechanical properties of a few selected reinforcing fibres.

Table 2-1 Typical properties of some reinforcing fibres[7]

Fibre material	Specific density (g/cm^3)	Young's modulus (GPa)	Tensile strength (GPa)
Carbon (PAN HM)	1.8	400	2-2.8
Carbon (PAN A)	1.9	220	3.2
Kevlar-29	1.44	60	2.8
Kevlar-49	1.45	130	2.8-3.6
E-glass	2.5-2.54	70-72.4	1.5-3.5
S-glass	2.48-2.6	85.5-90	4.6

2.2.1 Fibre length and critical fibre length

Most SFRP are produced by injection moulding, which causes the fibres to break, leading to a distribution of fibre length that can be modelled by a Weibull probability density function [9-11].

Fibre length is governed by several factors, such as the original length, fibre content and processing conditions [9-11]. It has been observed that the mean fibre length is inversely proportional to fibre content. The higher the fibre content, the lower the final mean fibre length, hence a lower fibre reinforcing efficiency for the composite strength and modulus [7, 9].

The mechanical properties of SFRP are unquestionably related to the fibre length distribution. In composites, the loads are not applied directly to the fibres but to the matrix and transferred to the fibres through shear stress. The stress starts at the corners of the fibres and continues to

grow as it moves towards the middle of the fibre, where the stress is maximum. The fibre length needs to be greater than the critical length (l_c) to obtain the best reinforcement from the fibres. The parameter l_c is the minimum fibre length necessary to build up the axial fibre stress to the ultimate tensile stress of the fibre (σ_F^u) [12-14]. Figure 2-3 shows the stress variation throughout the fibre for different lengths.

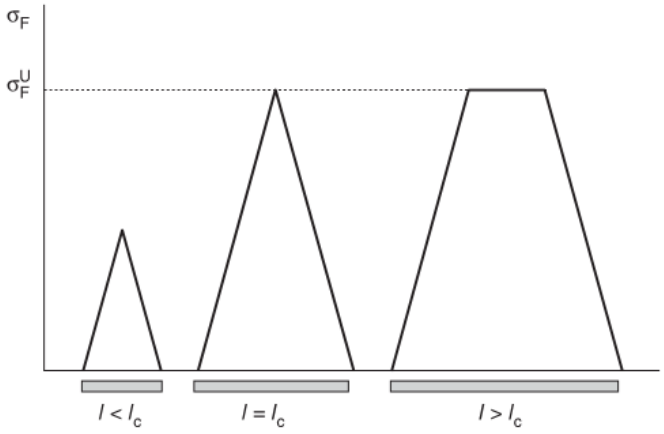

Figure 2-3 Stress variation with fibre length [7]

From Figure 2-3, it is easy to observe that if the final fibre length (l) is less than l_c, the fibre stress may never reach the ultimate tensile stress of the fibre. In this case, either the fibre-matrix interfacial bond or the matrix itself might fail before the fibres achieve their maximum strength. Thus, to have an effective fibre reinforcement the following condition l > l_c needs to be met.

The parameter l_c can be estimated by [5, 15]:

$$l_c = \frac{\sigma_F^u}{2\tau_i} d_f \quad \textbf{(2-1)}$$

Where:

σ_F^u= ultimate tensile stress of the fibre

d_f= fibre diameter

τ_i= shear strength of the fibre-matrix interface

Since l_c is inversely proportional to the shear strength of the fibre-matrix interface, increasing the adhesion strength reduces l_c. Thus the strength of a SFRP can be improved through proper fibre surface treatments. This was verified experimentally by Ozkoc et al. [16]. They studied

the effect of incorporating acidic groups by blending acrylonitrile-butadiene-styrene (ABS) with various amounts of PA6 to obtain improved interfacial adhesion between the glass fibres and polymer on a 30 wt% short glass fibre reinforced composite with ABS/PA6 matrix.

2.3 Manufacturing processes

There are several production techniques for components made of fibre reinforced polymer composites. Table 2-2 shows an overview of the essential characteristics of some of the manufacturing processes.

Table 2-2 Comparison of fibre reinforced polymer composites manufacturing processes [17]

Manufacturing process	Equipment costs	Rate of production	Part strength	Operator skill required	Part complexity	Reproducibility	Possible fibre forms (R-Random/ C-Continuous)
Hand lay-up	L	L	L	H	H	L	R,C
Spray-up	M	M	L	H	H	L	R
Tape lay-up (manual)	L	L	-	H	N	L	C
Tape lay-up (automated)	H	H	-	L	M	H	C
Vacuum bag moulding (wet lay-up)	L	M	M	H	H	L	R, C
Autoclave Moulding (tape lay-up)	H	M	H	M	M	H	C
Filament winding	M	M	H	L	L	H	C
Pultrusion	H	H	H	L	L	H	C
Compression moulding	H	H	-	M	H	H	R, C
Resin transfer moulding	M	M	-	M	H	H	R, C
Reaction injection moulding	M	H	-	M	H	H	R, C
Injection moulding	H	H	L	H	H	H	R
Stitched/Thermoform preforms	M	H	M	M	M	H	R,C
Random fibre preforms	M	L	L	H	H	L	R
3-D Woven/Braided preforms	H	M	H	L	H	H	C
Legend: H-high, M-medium, L-low							

The most common manufacturing process for SFRP components is injection moulding. This process can be simplified into three steps:

1. Melt (plasticize) the polymer
2. Inject it into the mould cavity or cavities
3. Apply pressure until it cools down and can be extracted in a solid-state

Figure 2-4 presents a schematic of the machine used to carry out the previously mentioned steps. The SFRP are most frequently provided in the form of granules roughly cylindrical of 3-5 mm long and 3 mm diameter [18]. These granules are fed into the hopper to the barrel. Inside the barrel, the screw spin and drives the granules to the front and against the wall of the barrel. The granules are melted due to the friction and conduction from the heating units surrounding the barrel. The melted material is transferred to the front of the screw. Once the desired amount of melted material at the tip is obtained, the rotation of the screw stops. Then the filling process starts, and the screw advance and push the melted material into the mould cavity. After that, the screw stays in that position to maintain the pressure. The material starts to cool down and solidify. When the material is stiff enough, it is ejected from the mould.

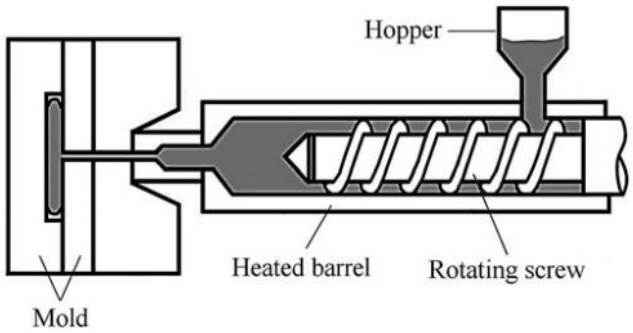

Figure 2-4 Schematic of the injection moulding process [19]

The manufacturing process has a massive impact on the mechanical properties of the SFRP due to its influence on fibre orientation distribution.

2.4 Fibre orientation distribution

Knowing the fibre orientation distribution (FOD) is of significant importance as this is responsible for the anisotropic behaviour of the material. The variation of the FOD throughout the material leads to the anisotropic response regardless of the scale at which the material is

observed. Studies [20-22] have demonstrated that the orientation of the fibres is not the same through the thickness. This is the result of the injection moulding process.

A structure consisting of three main layers can be identified: skin-shell-core. The skin is a thin layer of randomly oriented fibres that are immediately frozen in their position due to thermal shock between the mould walls and the melted material. The shell layer is a region where the fibres adjacent to mould walls tend to be aligned in the injection flow direction. This is due to the shear effect caused by the velocity profile of the fluid. This velocity profile is caused by the temperature gradient between the mould walls and the temperature of the core of the fluid. The fibres in the core tend to align perpendicular to the flow direction due to an extensional flow [23].

Figure 2-5 presents the skin-shell-core structure previously described.

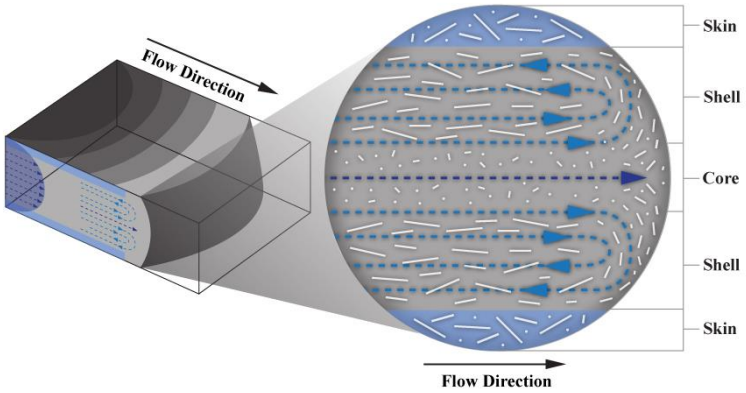

Figure 2-5 Diagram of the cross-section of an injected moulded SFRP

As shown in Figure 2-6, the orientation of a fibre can be described from two angles, θ and ∅. The angle ∅ describes the spatial orientation, while θ accounts for the planar orientation.

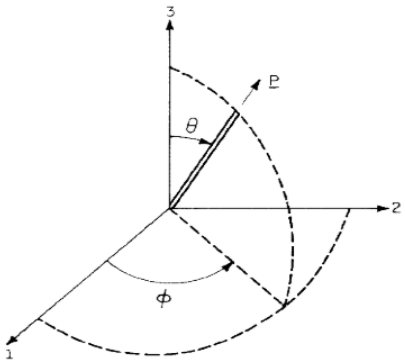

Figure 2-6 Definition of the orientation vector $\vec{p}$ and angles θ and ∅ [24]

Thus, the orientation of a single fibre can be resolved by its orientation vector $\vec{p}$,

$$\vec{p} = \begin{pmatrix} \cos\emptyset \sin\theta \\ \sin\emptyset \cos\theta \\ \cos\theta \end{pmatrix} \tag{2-2}$$

Due to the extremely high number of fibres within the composite, describing the orientation of every single fibre is a formidable task. Therefore a probability distribution function $\psi(\vec{p})$ is used instead. This function is given by:

$$\psi(\theta, \emptyset) \sin\theta d\theta d\emptyset \tag{2-3}$$

Which gives the probability of finding a fibre between the angles θ and $\theta + d\theta$, and between $\emptyset$ and $\emptyset + d\emptyset$ [23].

The probability distribution function must satisfy certain conditions. First, a fibre oriented at an angle $(\theta, \emptyset)$ is indistinguishable from a fibre oriented at any angle $(\pi - \theta, \emptyset + \pi)$, and thus:

$$\psi(\vec{p}) = \psi(-\vec{p}) \tag{2-4}$$

Second, since every fibre has some orientation, ψ must be normalised:

$$\oint \psi(\vec{p}) dp = 1 \tag{2-5}$$

2.5 Fibre orientation tensor

Even though the probability distribution function is a complete description of the fibre orientation, in numerical applications, using it is very impractical and inefficient. In 1987 Advani and Tucker [24] introduced the idea of using tensors to describe the fibre orientation. These orientation tensors are defined as dyadic products of $\vec{p}$ and then integrating the result of these tensors with the probability distribution function over all directions. Due to the symmetry condition (2-4) the integrals of odd-order are zero. Thus, only the even-order tensors are important. The second and fourth-order tensors are given by:

$$a_{ij} = \oint p_i p_j \psi(\vec{p}) dp \tag{2-6}$$

$$a_{ij} = \oint p_i p_j p_k p_l \psi(\vec{p}) dp \tag{2-7}$$

Advani and Tucker [24] demonstrated that these tensors are enough to have an accurate representation of $\psi(\vec{p})$. These tensors are symmetric (i.e. $a_{ij} = a_{ji}$), normalized (i.e. $a_{ij} = 1$) and the diagonal terms cannot be negative.

The second-order orientation tensor is used in injection moulding simulations due to its simple structure. The eigenvectors (e_i) of this tensor are the principal directions of fibre alignment and the eigenvalues (λ_i) indicate the statistical proportions (0 to 1) of fibres aligned to those directions [25]. A value close to 1 means a high degree of probability of fibre alignment in that direction, whereas a value close to 0 indicates a low probability. Figure 2-7 shows a representation of the orientation tensor.

$$a_{ij} = \begin{bmatrix} a_{11} & a_{12} & a_{13} \\ a_{21} & a_{22} & a_{23} \\ a_{31} & a_{32} & a_{33} \end{bmatrix} \rightarrow \begin{bmatrix} \lambda_1 & 0 & 0 \\ 0 & \lambda_2 & 0 \\ 0 & 0 & \lambda_3 \end{bmatrix}; [e_1 \quad e_2 \quad e_3]$$

Figure 2-7 orientation tensor

The fourth-order orientation tensor is used to predict the mechanical properties. To approximate the fourth-order orientation tensor in terms of the second-order tensor, a closure function is employed. There are several closure functions, such as the linear, quadratic and hybrid formulations proposed by Advani and Tucker [24], the orthotropic [26] and the more recently developed fast exact closure [27].

2.6 Prediction of fibre orientation tensor

Knowing the fibre orientation state is useful but not enough, it is necessary to predict the fibre orientation from processing conditions.

The Folgar and Tucker model [28] is the most widely used to compute fibre orientation. This model is based on the work done by Jeffery [29] and predicts the orientation distribution function of fibres in concentrated suspensions. However, as mentioned in section 2.5, using the orientation distribution function is impractical. Thus, Advani and Tucker [24] recast the Folgar and Tucker model [28] in terms of the second-order orientation tensor. The prediction of the second-order orientation tensor is given by:

$$\frac{Da_2}{Dt} = \frac{Da_{ij}}{Dt} = -\frac{1}{2}\left(\omega_{ik}a_{kj} - a_{ik}\omega_{kj}\right) + \frac{1}{2}\lambda\left(\dot{\gamma}_{ik}a_{kj} + a_{ik}\dot{\gamma}_{kj} - 2\dot{\gamma}_{kl}a_{ijkl}\right) + 2D_r\left(\delta_{ij} - 3a_{ij}\right) \quad \textbf{(2-8)}$$

a_{ij} is the second-order orientation tensor, ω_{ij} being the vorticity tensor, λ represents a constant related to the geometry of the fibre, $\dot{\gamma}_{ij}$ is the strain rate tensor and D_r is the rotary diffusivity, which can be replaced by $C_{i\dot{\gamma}}$ where $\dot{\gamma}$ is the scalar magnitude of the strain rate tensor and C_i is the fibre interaction coefficient. This C_i appears in most of the models, a high value results in an isotropic fibre orientation prediction, while a low value leads to a prediction of fibres more aligned to the flow [30]

Experimental data [31] has shown that the Folgar and Tucker model over-predicts the fibre alignment, this is attributed to a slower orientation change than predicted by the model. In 2008 Wan et al. [32] introduced the Reduced-Strain Closure (RSC) Model, which uses a "reduction factor" to decrease the growth rates of the eigenvalues of the fibre orientation tensor providing good agreement with experimental data, as can be seen in Figure 2-8.

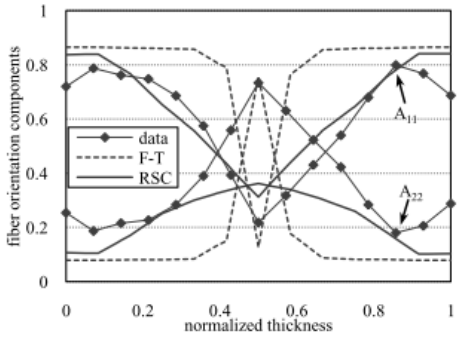

Figure 2-8 Comparison of predictions of fibre orientation tensor eigenvalues A11 and A22 using the Folgar and Tucker model (F-T) and the RSC model [33]

Many more models have been developed to improve the prediction of fibre orientation, such as the anisotropic rotary diffusion approach (ARD) [34], the improved anisotropic rotatory diffusion (iARD) model [35], and the latest ones: the principal anisotropic rotary diffusion (pARD) [36] and the Moldflow Rotational Diffusion (MRD) model, proposed by Bakharev et al. [37] and implemented in the commercial software Autodesk Moldflow®. Four parameters characterise this MRD model: a fibre interaction coefficient (Ci) and the coefficients of asymmetry D1, D2 and D3 that show how the rotational diffusion is biased towards the principal vectors of the fibre orientation tensor [38]. This MRD model is given by [37]:

$$\frac{Da_{ij}}{Dt} = -\frac{1}{2}\left(\omega_{ik}a_{kj} - a_{ik}\omega_{kj}\right) + \frac{1}{2}\lambda\left(\dot{\gamma}_{ik}a_{kj} + a_{ik}\dot{\gamma}_{kj} - 2\dot{\gamma}_{kl}a_{ijkl}\right) + 2C_{i\dot{\gamma}}\left(\mathcal{D} - tr(\mathcal{D})a_{ij}\right) \quad \textbf{(2-9)}$$

Where $\mathcal{D}$ is an anisotropy factor tensor accounting for anisotropy of fiber-fiber interactions.

For injection moulding simulations this anisotropy factor tensor has the same principal directions as the fibre orientation tensor and fixed eigenvalues D1, D2 and D3. That is in the coordinate system of the principal directions of the fibre orientation tensor:

$$\mathfrak{D} = \begin{pmatrix} D1 & 0 & 0 \\ 0 & D2 & 0 \\ 0 & 0 & D3 \end{pmatrix} \quad \textbf{(2-10)}$$

Favaloro and Tucker [39] compared several fibre orientation models. They calibrated the parameters of the models to match a given orientation tensor at a steady state. The results obtained are shown in Figure 2-9. From the results, it can be seen that the iARD, pARD and MRD models are the most accurate. They are all able to fit representative shell-layer orientation states, but according to the authors, the MRD model offers the most flexibility.

Model	C_I	ARD Parameters	A_{11}	A_{33}	A_{13}
Target			0.650	0.0100	0.0300
FT	0.0311		0.650	0.1312	0.1141
Dz	0.0258	$D_z = 0.0051$	0.650	0.0100	0.0465
iARD	0.0562	$C_M = 0.9977$	0.650	0.0100	0.0301
pARD	0.0169	$\Omega = 0.9868$	0.650	0.0100	0.0301
WPT	0.0504	$w = 0.9950$	0.650	0.0102	0.0303
MRD	0.0198	$D_2 = 0.4796$, $D_3 = 0.0120$	0.650	0.0100	0.0300
PT		Eq. (25)	0.650	0.0100	0.0300

Figure 2-9 Comparison of different fibre orientation models. Adapted from [39]

2.7 Mechanical behaviour of SFRP

2.7.1 Tensile behaviour

The tensile response of SFRP is one of the most important mechanical properties, and understanding and predicting it is crucial in designing composite parts. Several techniques have been used to study the tensile behaviour and damage mechanisms of SFRP. In work done by Crupi et al. [40], tensile tests were performed on a SFRP using DIC to obtain the stress-strain curves and identify the fracture location at the early stages of the tests. Figure 2-10 presents the stress-strain curve obtained and DIC images from where a strain localization at the fracture zone was detected even at low strain levels. During the test, the progression of strain was constant, giving a reasonable estimation of the failure zone. Even though these results are insightful, they were only obtained at room temperature.

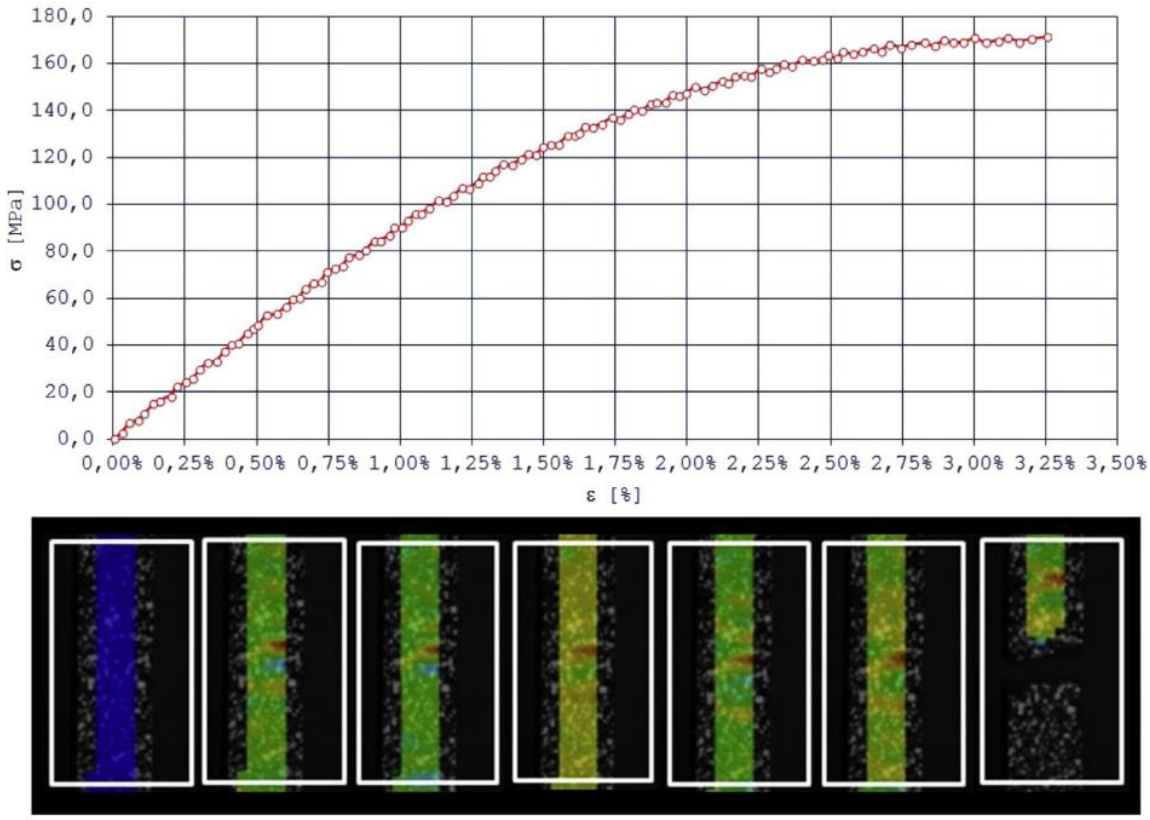

Figure 2-10 Stress-strain curve and DIC images of the tensile test [40]

Lizama-Camara [41] also used DIC to investigate the strain distribution on a PA66 with 50wt% reinforcement of short glass fibres. They analysed coupons cut from plaques at 0°, 30°, 45° and 90° with respect to the injection flow direction. The tests were conducted at room temperature, and the strain distribution on the front and thickness views were studied. From the results shown in Figure 2-11a-d, the author reported that the crack propagated along the path of the highest strain. This agrees with what Crupi et al. [40] have described before. Lizama-Camara [41] also mention that this high strain path seems to depend on the fibre orientation, with 0° and 90° coupons showing strain concentrations and cracks perpendicular to the load direction. In contrast, the 30° and 45° samples presented strain localisations and cracks at an angle.

Finally, the author reported that the strain concentrations in all specimen orientations appear to be localised primarily in the centre of the specimen and close to the end of the gauge length.

These results, albeit very insightful, are limited to room temperature and strain distributions on the surface of the specimens.

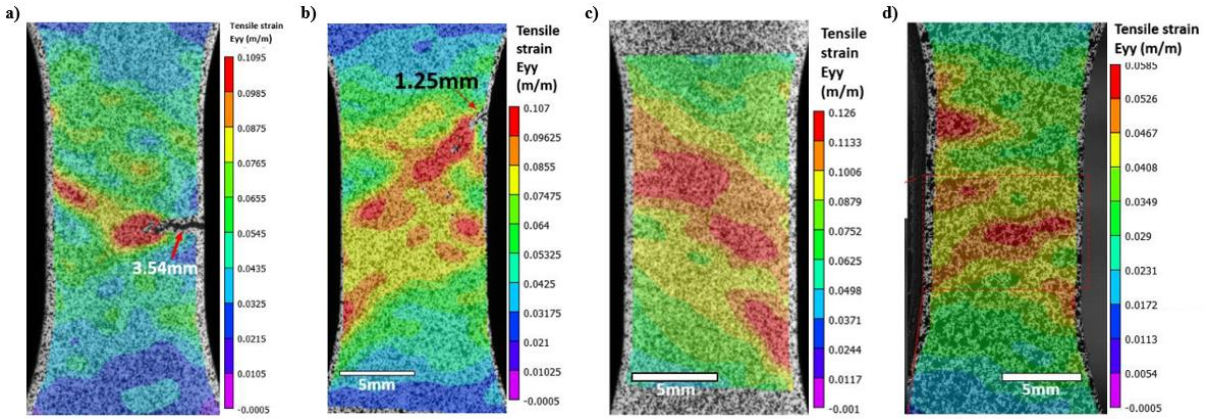

Figure 2-11 DIC strain distribution of PA66GF50 at room temperature. a) 0° specimen, b) 30° specimen, c) 45° specimen, c) 90° specimen. Adapted from [41]

Mouhmid et al. [42] studied the mechanical behaviour of an unfilled PA66 and PA66 with different fibre contents: 15, 30 and 50 wt%. They carried out uniaxial tensile tests and used the acoustic emission (AE) technique combined with SEM observations of the fracture surface to identify the damage mechanisms. Figure 2-12 illustrates the counts of AE events during the tensile test of the PA66 with 15 wt% of glass fibre. From these results, they reported three stages of the damage process: an elastic zone where the acoustic activity is insignificant, a second zone controlled by matrix plasticity and micro-cracks with an AE amplitude range between 40 and 60 dB, and the third zone of severe damage represented by consequent AE activity prior to failure.

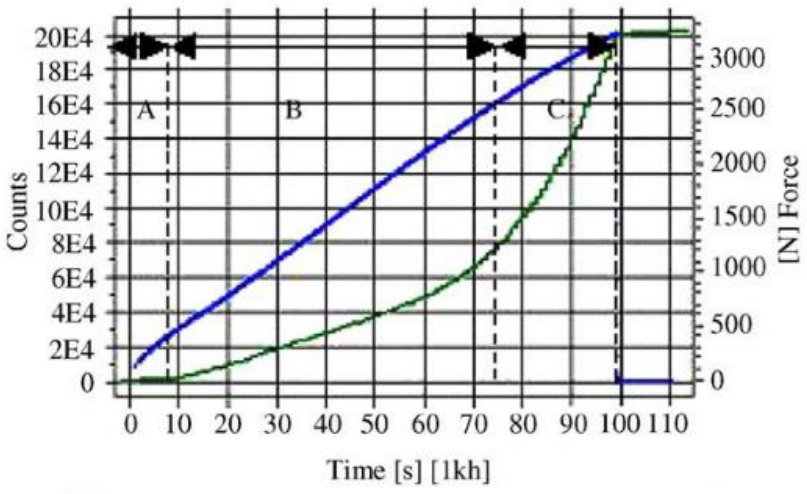

Figure 2-12 Acoustic emission events during tensile tests [42]

Another study involving AE was carried out by Barre and Benzeggagh [43] on a SFRP reinforced with 40 wt% of glass fibres of lengths ranging from 0.5 to 15 mm. They found that AE events begin between 0.125% and 0.5% of the strain, indicating that the damage in the

material starts at an early stage, mainly due to matrix cracking. They established four ranges of AE amplitudes which they correlated to damage mechanisms. Matrix cracking was correlated to AE amplitudes between 40 to 55 dB, interface fracture to AE amplitudes around 60 to 65 dB, the range from 65 to 86 dB was attributed to fibre pull-out and the fibre fracture was associated with AE amplitudes within the limits of 85 to 95 dB.

This mechanical behaviour is influenced by several factors, such as the fibre orientation relative to the loading direction, fibre length, temperature, moisture and strain rate. These factors are discussed in the following sections.

2.7.1.1 Effect of fibre orientation and fibre length

Since each fibre contributes to the stiffness and strength along the direction of its axis, the orientation of the fibres is critical for the mechanical properties of the SFRP. Bernasconi et al. [44] conducted tensile tests on coupons of polyamide-6 reinforced with 30 wt% of glass fibre (PA6 GF30) machined from 3.2 mm thick plaques. The specimens were extracted at 0°, 30°, 60°and 90° with respect to the injection flow direction. Figure 2-13 presents the stress-strain curves obtained from the tensile tests of the coupons at different orientations. As expected, the specimens aligned at 0° had the highest ultimate tensile strength (UTS) and Young's modulus (E) values, whereas the 90° coupons showed around half of the UTS and E compared to the 0° specimens.

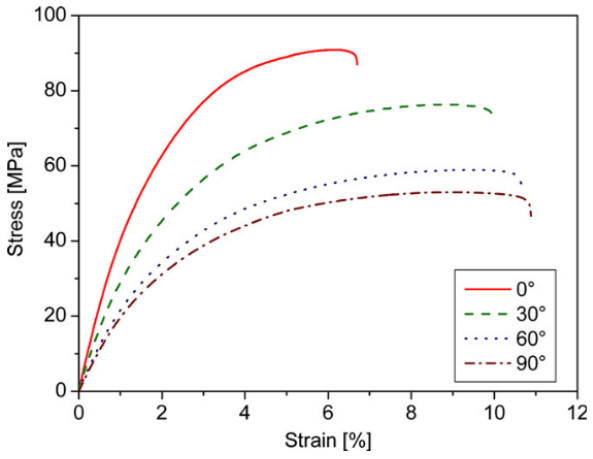

Figure 2-13 Tensile stress-strain curves of SFRP at different orientations [44]

Similar results were obtained by Lizama-Camara et al. [22]. They investigated the effect of fibre orientation on nylon 6,6 reinforced with 50 wt% short glass fibres (PA66GF50). Dog bone coupons were extracted from 4 mm thick plaques at 0°, 45° and 90° with respect to the

injection flow direction. Two more coupons were machined, one close to the injection gate perpendicular to the flow and one in the direction of the flow located close to one side edge of the mould. The coupons were conditioned up to 1-1.4% of moisture prior to testing. The tensile stress-strain curves are shown in Figure 2-14.

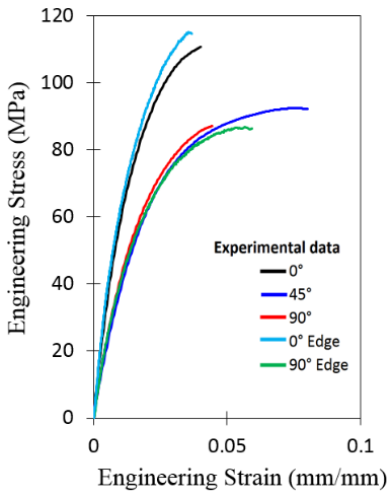

Figure 2-14 Tensile stress-strain curves for PA66GF50 at different orientations and locations [22]

A clear effect of the fibre orientation on the tensile response is observed. The 0° coupons show a higher stiffness and strength but lower strain at break compared to the other orientations due to a higher number of fibres aligned to the loading direction.

Miwa and Horiba [45] investigated the effect of fibre length on the tensile strength of a carbon fibre epoxy resin composite and a glass fibre epoxy resin composite. They used five different fibre lengths between 0.15 mm and 4 mm. The tensile tests were carried out at five temperatures in the range of 20-100° C. Results of the effect of fibre length on tensile strength are shown in Figure 2-15a and b. It can be seen that the tensile strength increases with the increment of the fibre length until it reaches a plateau around 1 mm, where the tensile strength is not enhanced anymore. In Figure 2-15a and b, the detrimental effect of temperature on the tensile strength is evident, with the strength at 100° C around ¼ of the strength at 20° C.

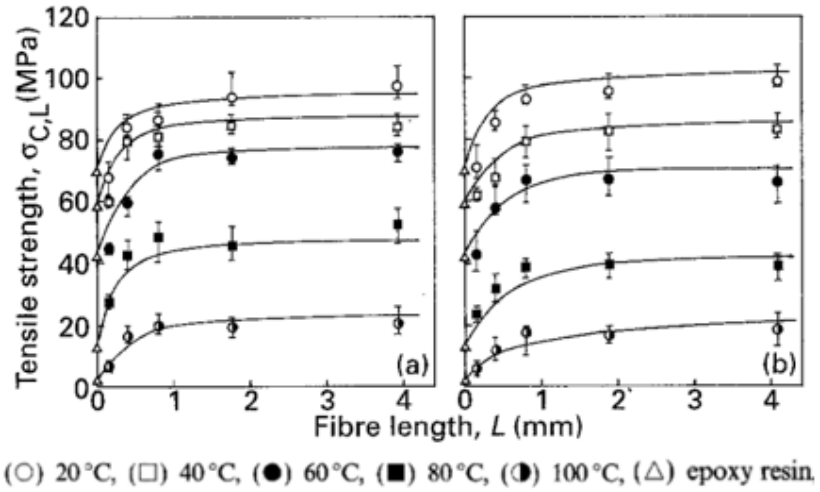

Figure 2-15 Relation between fibre length and tensile strength: (a) carbon fibre epoxy resin composite; (b) glass fibre epoxy resin composite [45]

In a study by Hitchen et al [46], an analogous effect of fibre length was observed on the stress-strain curves. In order to study this, coupons made of epoxy reinforced with short fibres with lengths of 1 mm, 5 mm and 15 mm were subjected to tensile tests at a crosshead speed of 1 mm/min. The results illustrated in Figure 2-16 show an increase in stiffness with an increase in fibre length. It can also be seen a lower strain at break for longer fibre length composites. Besides this, for composites with fibre lengths of 5 and 15 mm a linear stress-strain curve was obtained, whereas for the composite containing 1 mm fibres, the curve is slightly non-linear.

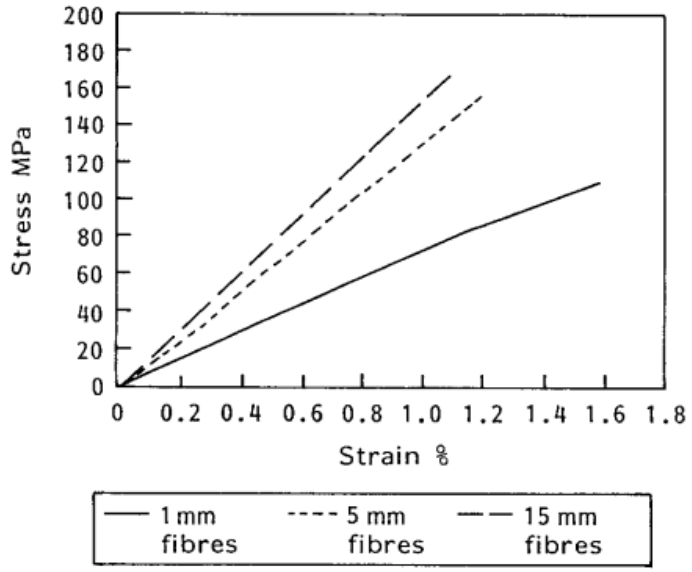

Figure 2-16 Stress-strain curves for short fibre epoxy composites with 1 mm, 5 mm and 15 mm length fibres [46]

2.7.1.2 Influence of temperature, strain rate and humidity

Some applications of SFRP are in harsh environmental conditions, such as in the automotive industry, where components made of SFRP are used under the hood. These extreme conditions affect the mechanical properties, and understanding them is of great importance.

Mortazavian and Fatemi [47] studied the effect of fibre orientation and temperature on the tensile properties of two SFRP: polybutylene terephthalate (PBT) reinforced with 30 wt% glass fibres and polyamide-6 (PA6) with 35 wt% glass fibres and 10 wt% rubber impact modifier. They conducted tensile tests at different strain rates and temperatures on coupons machined from plaques of 3 and 3.8 mm thickness at 0°, 18°, 45° and 90° with respect to the injection flow direction. Several coupons were extracted from the same plaque. Results of tensile strength, Young's modulus and strain at tensile strength for different orientations and temperatures are shown in Figure 2-17a-c. It can be seen that the 45° coupons of both materials have a similar Young's modulus value to that of the 90° coupons. The tensile strength of 45° specimens was closer to the 90° coupons, especially for the PA6 samples.

Observing the strain results at tensile strength, it is evident that the 45° coupons elongate more than the 0° and 90° specimens for PA6 between 60% and 160% depending on the temperature. This higher ductility is due to the fibres, for 0° coupons, more fibres are aligned to the loading direction, and the low strain capacity of the fibres results in low ductility of the composite. As the angle between the fibres and the load direction increases, the matrix straining becomes more dominant. According to them, in the 45° coupons, the matrix has more space to elongate between fibres than the other orientations. This could explain why the 45° coupons have a higher strain at tensile strength.

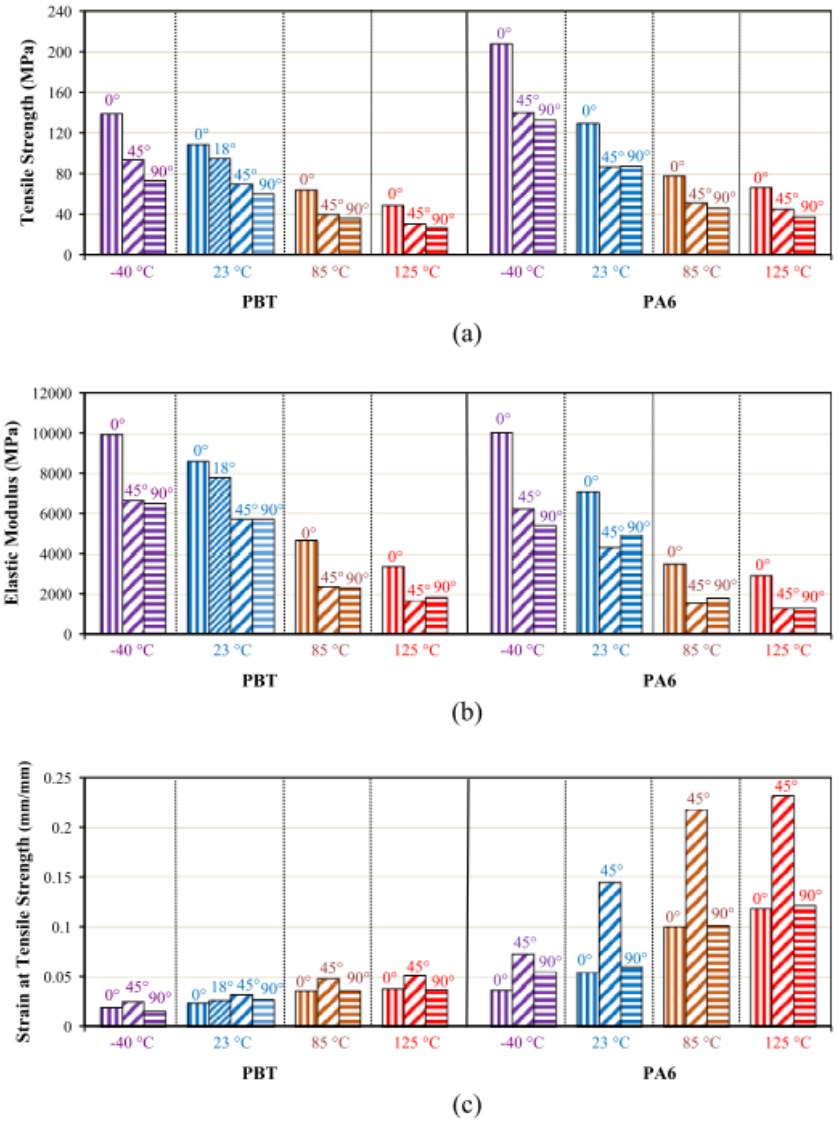

Figure 2-17 Tensile properties variation for different orientations and temperatures of PBT and PA6 coupons. (a) tensile strength, (b) elastic modulus, and (c) strain at tensile strength [47]

As the use of SFRP materials is more common in applications where high strain rates can be realised, the characterisation of the behaviour under different strain rates is important. Schossig et al [48] investigated the impact of strain rate on neat and short glass fibre-reinforced polypropylene (PP) and polybutene-1 (PB-1). They carried out tensile tests at strain rates varying between 0.007 and 174 s^{-1}. Their results shown in Figure 2-18 indicate a different behaviour for different strain rates. The strength increases at higher strain rates, while a reduction of strain to failure occurs.

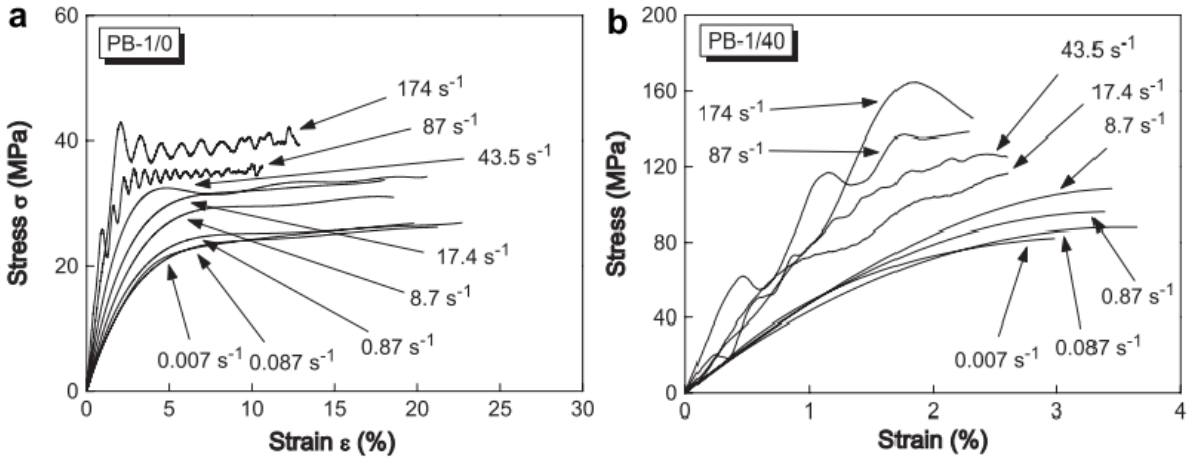

Figure 2-18 Stress-strain curves at different strain rates for a) neat PP and b) PP with 40 wt% glass fibres [48]

Rolland et al. [49] studied the effect of humidity and fibre orientation on a polyamide 6,6 reinforced with 30wt% of short glass fibre by carrying out in situ tensile tests in a synchrotron. The specimens were obtained from plaques of 3.24 mm thickness and extracted at 0°, 45° and 90° with respect to the injection direction. They were conditioned to three relative humidity levels, RH=0%, 50% and 80%. The stress strain curves for each coupon and moisture level are presented in Figure 2-19. The observed effect is a reduction of tensile strength and an increase in ductility as the humidity increases. This effect can be seen regardless of the orientation of the coupons. From the images obtained from the synchrotron, they identified 5 damage mechanisms, fibre failure, damage at fibre ends, debonding, damage growth in the matrix and fibrillation, see Figure 2-20a-e. The evolution of these damage mechanisms at different stress levels, orientations and humidity levels is shown in Figure 2-21. Following this evolution presented in Figure 2-21, a four steps damage progression is proposed:

1. First, the damage initiated at fibre ends or due to fibre failure.
2. Then the density of damage at fibre ends or fibre failure increases.
3. Fibre failure and damage at fibre ends keep developing, and fibrillation appears with densities depending on relative humidity and coupon orientation.
4. Finally, the macroscopic failure happens due to a density increase of all mechanisms. For 45° and 90° specimens with RH=50% and 80%, the damage mechanisms are not only denser but also larger. Debonding grows along all the fibre interfaces joining both fibre ends.

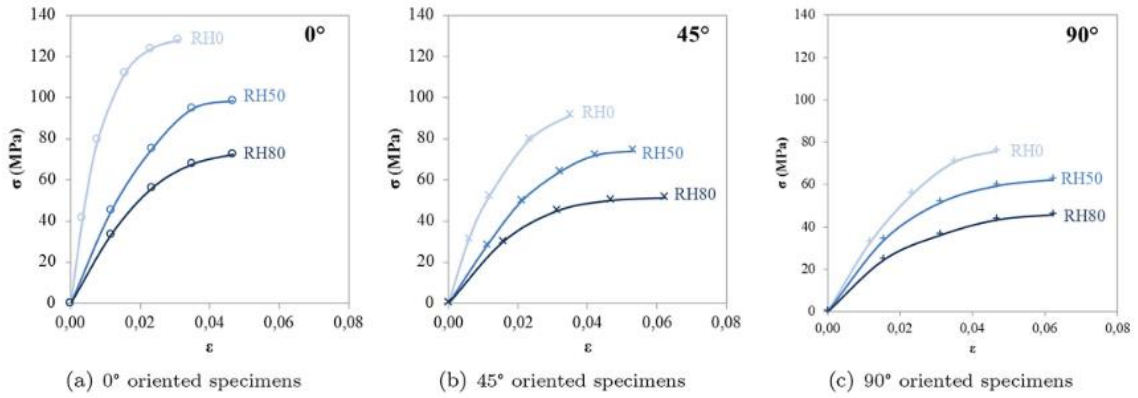

Figure 2-19 Influence of moisture content on SFRP at different orientations [49]

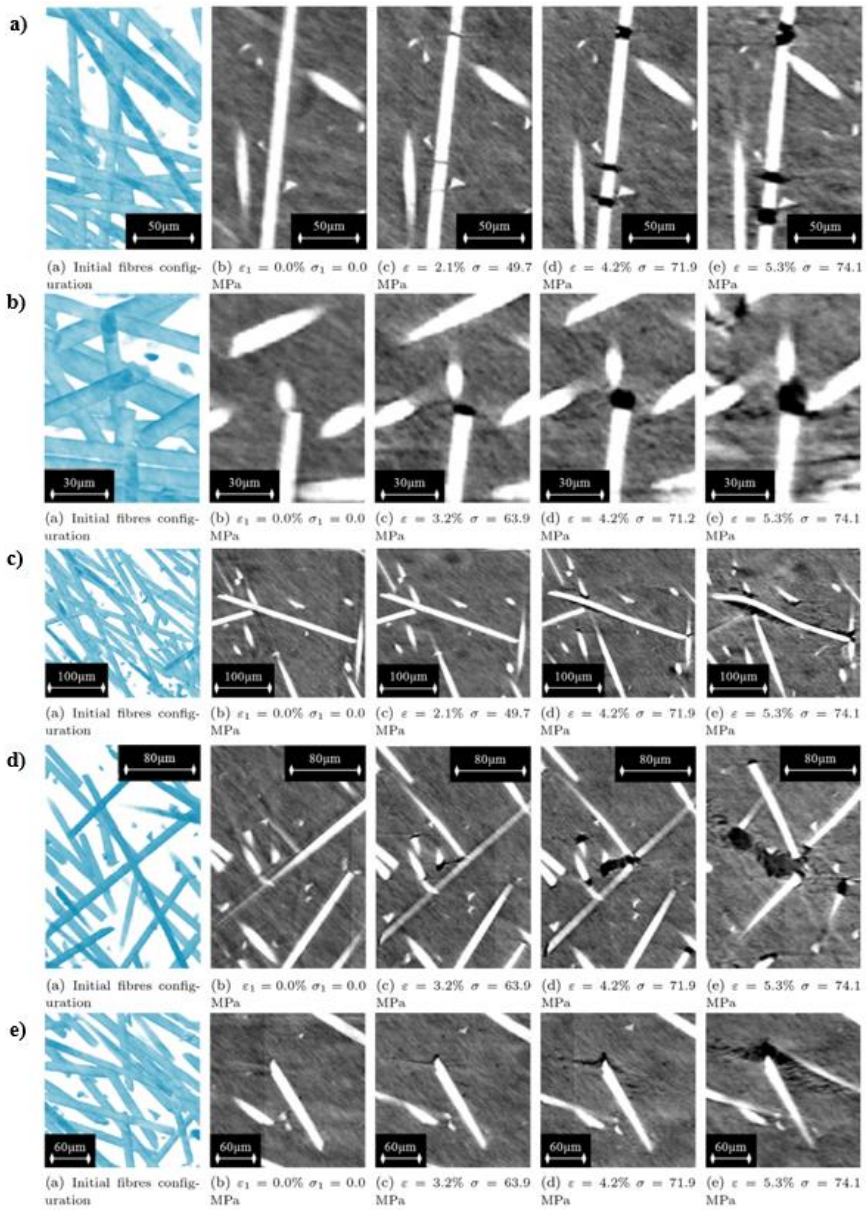

Figure 2-20 a) fibre failure, b) damage at fibre ends, c) debonding at the fibre matrix interface, d) damage growth in the matrix, e) fibrillation. Adapted from [49]

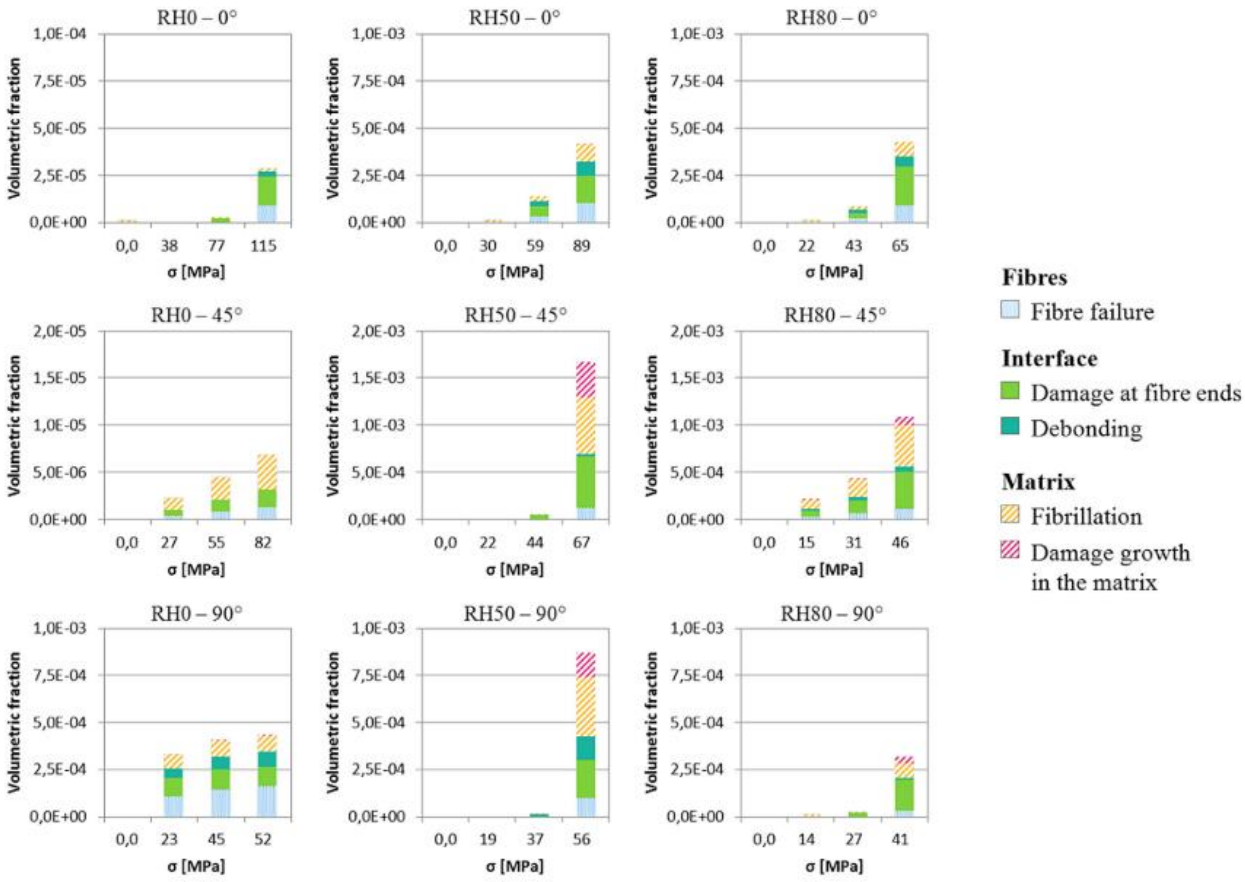

Figure 2-21 Evolution of volumetric fraction of damage mechanism during tensile tests for different specimen orientations and relative humidity [49]

2.7.1.3 Damage mechanism under tensile load

Damage in composites is caused by changes in the microstructure due to a combination of failure mechanisms such as matrix cracking, fibre breakage, fibre pull-out, debonding, fibre bridging, etc. [50].

Several experimental techniques, such as optical microscopy, scanning electron microscopy (SEM) and X-ray micro-computed tomography (µCT), have been used to study the failure mechanisms of SFRP

Arif et al. [51] studied the damage mechanisms of a polyamide 66 reinforced with 30wt% of fibre glass using in situ SEM tensile test on specimens conditioned at three humidity levels. They proposed a damage chronology where the damage initiation occurs at the fibre ends due to fibre matrix debonding and at locations where fibres are relatively close to each other because of the generation of local stress concentration, see Figure 2-22a. Then these debonded

zones propagate along the fibre matrix interface (Figure 2-22b). After that, matrix micro-cracks appear and grow, as seen in Figure 2-22c, leading to the final failure.

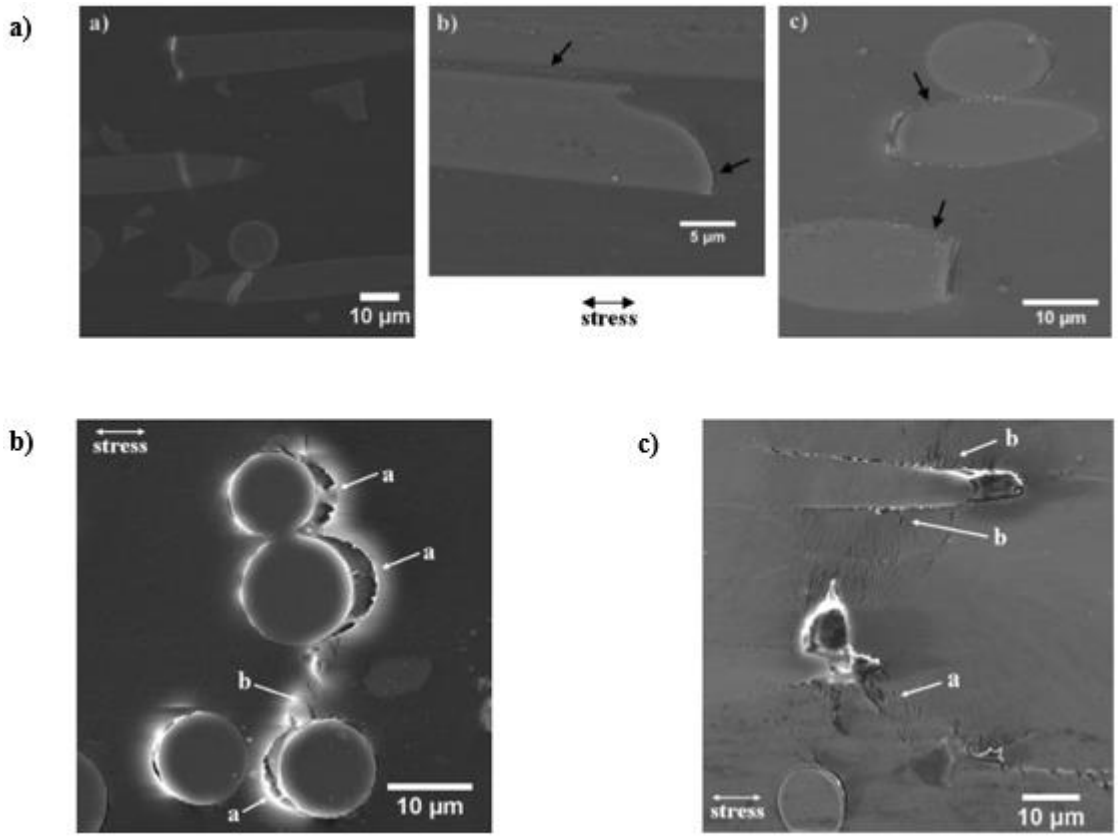

Figure 2-22 SEM images of a) damage at the fibre ends, b) fibre matrix debonding, c) matrix micro cracks. Adapted from [51]

Sato et al. [52] also analysed the failure behaviour of a polyamide 66 with 30 wt% glass fibre reinforcement. The authors conducted a bending test inside a SEM and compared the failure mechanisms to the mechanisms found by SEM observation on a tensile tested specimen. The failure mechanisms of the tensile sample were analogous to the sample subjected to bending loads. Figure 2-23 shows an SEM image of the fracture surface of the sample, where ductile and brittle failures were observed. Most of the fracture surface was covered by fibre pull-outs, and only in small region ductile failure was observed. This ductile area was considered the region for the crack initiation and the crack propagated in a brittle manner through the sample leading to final failure. A model of the failure process, shown in Figure 2-24, is also proposed. Even though this work brings some understanding about the failure mechanism, it is only limited to room temperature and fibres oriented to the loading direction.

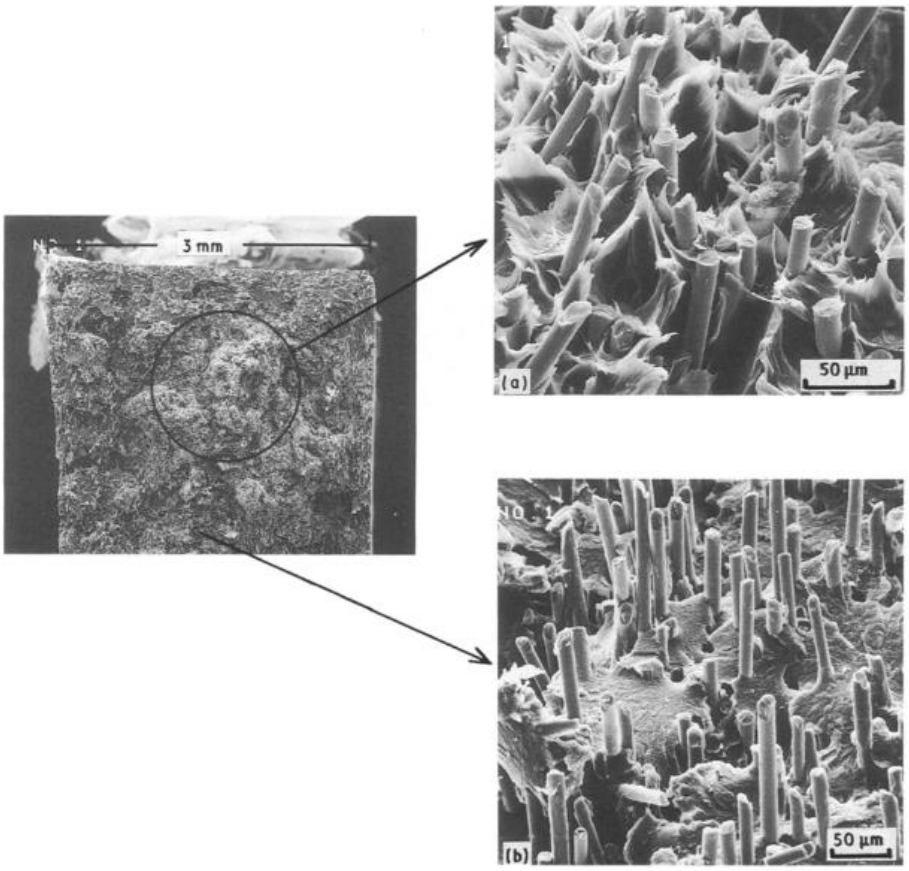

Figure 2-23 Fracture surface of a tensile sample. The top right image is an image of a region of ductile failure. The bottom right image is a region of brittle failure [52]

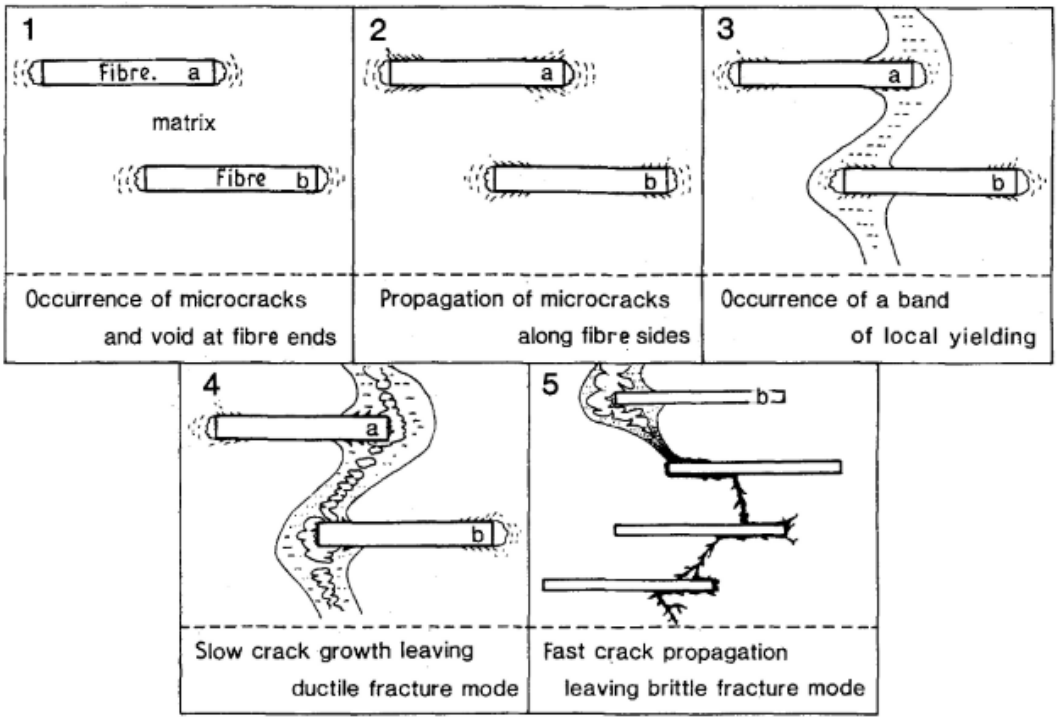

Figure 2-24 Model of the failure process [52]

Another technique used to study the damage mechanisms is X-ray micro-computed tomography. Rolland et al. [53] conducted tensile tests inside a synchrotron using a polyamide 66 with 30 wt% of short glass fibre reinforcement. The sample was obtained by water-cut from an injected plaque of 3.24 mm thick and was extracted at 45° with respect to the injection flow direction. The average fibre orientation in the shell layers was 45° and in the core 63° with respect to the load. However, due to the configuration used to acquire the images and achieve a small voxel size (0.7 µm), the observed zone was a cylinder of 1.4 mm diameter and 1.4 mm height located at the centre of the specimen. Therefore, the damage mechanisms near the sample surface were excluded from this study. The authors identify four damage mechanisms: fibre failure, matrix damage, debonding at the fibre ends and debonding at the fibre matrix interface. These last two damage mechanisms were influenced by the local fibre orientation. Less fibre ends debonding was observed in the core layer than in the shell due to the less favourable fibre orientation. Debonding, on the other hand, occurred more in the core than in the shell layers due to more favourable fibre orientation. Figure 2-25 presents the damage evolution for two different zones of the fracture surface. At both locations, one can see that there is more damage in the shell layers than the core up to the final load stages.

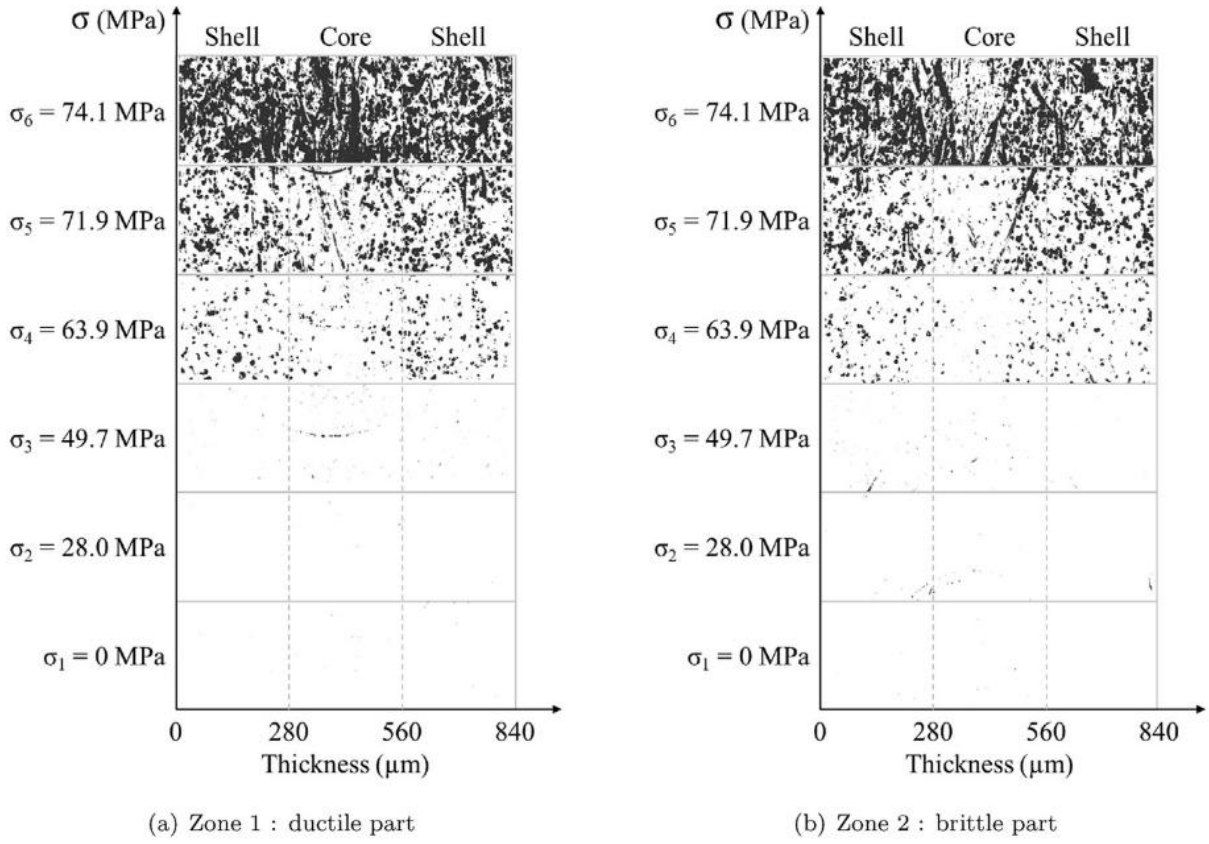

Figure 2-25 Evolution of damage during the tensile test for two different zones of the fracture surface [53]

2.7.2 Fatigue of SFRP

The phenomenon of fatigue is the failure caused by alternating loads. Figure 2-26 depicts the terminology of the alternating stresses.

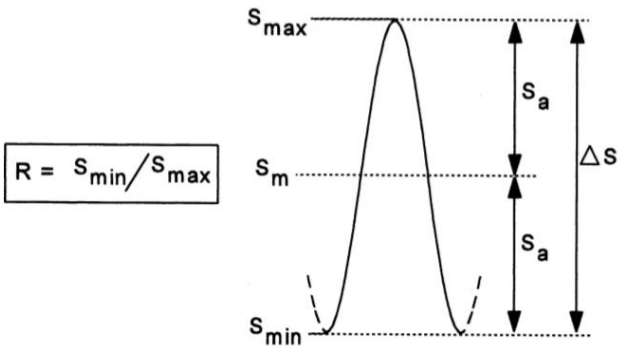

Figure 2-26 Terminology used in fatigue [54]

Frequently the stress and number of cycles at failure are plotted in a log-log plot named Stress-Life Curve (S-N Curve). Basquin stated in 1910 that when stress is reduced, the fatigue life increases as a power law [55]. This relationship can be described as:

$$\sigma = \sigma_0 N^k \tag{2-11}$$

Where σ is any cyclic stress, N represents the number of cycles at failure for that stress, σ_0 is the fatigue coefficient defined as the intercept and k denotes the slope of the resultant curve.

Diverse studies have confirmed that the orientation of the fibres has a strong influence on the fatigue strength [56-58]. Similar to the tensile behaviour, increasing the degree of fibre alignment with the load direction improves the fatigue strength. In Figure 2-27 a typical S-N curve and the influence of the fibre orientation can be seen.

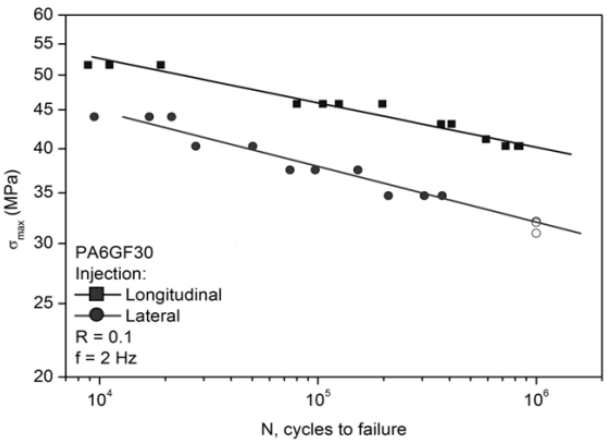

Figure 2-27 S-N curve for PA66GF30 specimens of two different orientations [58]

2.7.2.1 Influence of the temperature and moisture on the fatigue behaviour of SFRP

Components made of SFRP are commonly subjected to different environmental conditions combined with cyclic loading. Thus, it is necessary to investigate the impact of temperature and moisture on the fatigue response of SFRP.

Mortazavian and Fatemi [59] evaluated the fatigue behaviour of two SFRP at -40, 23 and 125°C using specimens manufactured transversely and longitudinally with respect to the injected flow direction and reported that the influence of temperature in both directions was similar. Figure 2-28 shows their results with the fatigue strength being lower at higher temperatures [59].

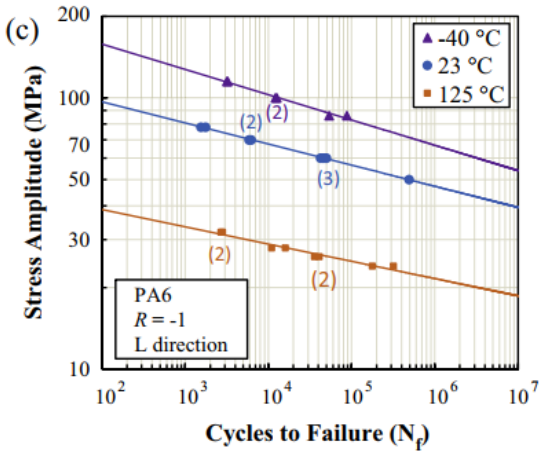

Figure 2-28 Influence of the temperature on fatigue life [59]

Similar results were obtained by Jia and Kagan [60]. They carried out fatigue tests on SFRPC at R=0.1 at three different temperatures -40, 23 and 121°C and showed that the highest fatigue strength was achieved at -40°C and that at 121°C the fatigue strength decreased considerably.

In another study performed by Handa et al [61], they conducted fatigue tests at a frequency of 20 Hz at eight different temperatures between 0 and 120° C on a polyamide 66 with 33% glass fibre reinforcement. The results showed that the slope of the S-N curve decreases as the temperature increases until the glass transition temperature is reached, and from there the slope remained constant.

De Monte et al [62] investigated the effect of temperature on a PA66 GF35 under tension-tension and tension-compression cyclic loading at room temperature (RT) and 130° C. According to the authors, the temperature affects only the matrix and therefore the influence of temperature on the fatigue behaviour has to be the same for different fibre orientations.

Thus they only carried out the fatigue tests on coupons oriented in the direction of the flow. At RT the material behaved in a linear elastic manner showing a very small area within the hysteresis loops, (see Figure 2-29a) and b)), while coupons tested at 130° C presented a non-linear response with a bigger area within the hysteresis loops, (Figure 2-29c) and d)). In Figure 2-29a) and c) a shift of the hysteresis loops can be seen due to creep caused by the mean load. The creep strain is more pronounced at higher temperatures as the material behaviour becomes more matrix controlled. This phenomenon did not occur in coupons tested at R=-1.

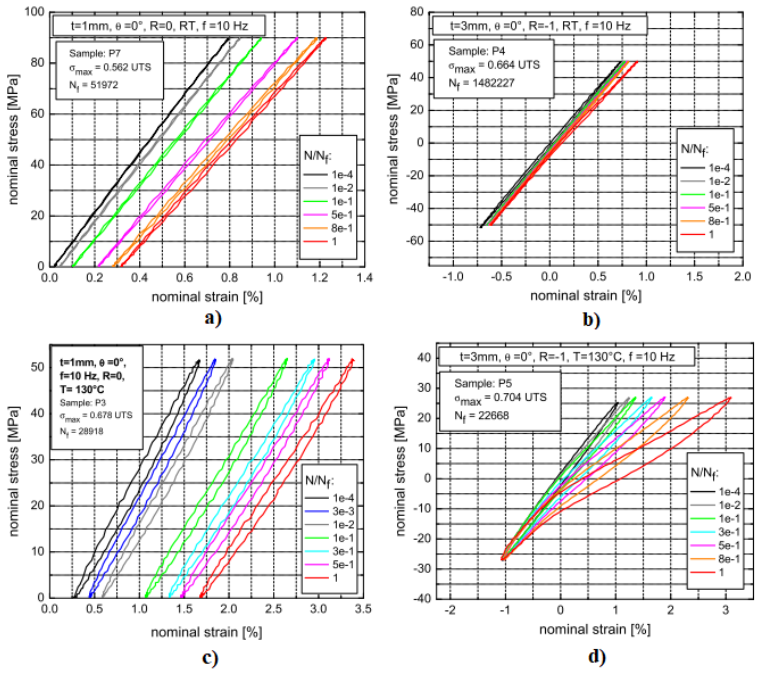

Figure 2-29 Hysteresis loops at RT for a) R=0, b) R=-1, and at 130°C for c) R=0 and d) R=-1 [62]

On the other hand, the effect of the moisture in the SFRP may be two-fold. First, the molecules of water cause a loosening of the molecular bonding and act as a plasticizer allowing the polymer chains to move more easily. Second, the moisture absorption causes swelling that modifies the residual stresses of the curing process and increases the shear stresses at the interfaces [63].

Barbouchi et al. [64] tested specimens of PA66 with 30% fibre glass for two different levels of moisture, 0.2% and 3.5%. They observed a decrease in the fatigue strength as the moisture increased and that the slope of the S-N curve is dependent on the moisture content. Confirming the results obtained by Hoppel [65]. Figure 2-30 presents the influence of moisture on the fatigue life of a SFRPC.

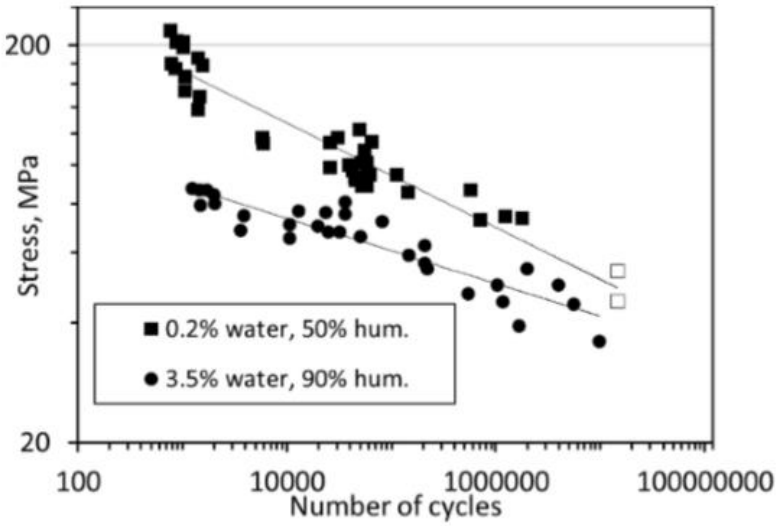

Figure 2-30 Influence of moisture on fatigue life [64]

2.7.2.2 Fatigue damage mechanisms

As the SFRP are becoming more used in structural components, it is necessary to understand damage mechanisms due to cyclic loads in order to improve their long-term reliability.

Rolland et al. [66] conducted fatigue tests at room temperature inside a synchrotron using samples of PA66 reinforced with 30 wt% of glass fibre. The coupons were cut from plaques of 3.24 mm thick and extracted at 0°, 45° and 90° with respect to the injection direction. The scanning parameters yield a voxel size of 0.65 µm, a diameter of 1.33 mm and a 1.33 mm height. This means that not all the thickness was included in the study.

The authors reported six damage mechanisms: fibre failure, damage at fibre ends, debonding, cavitation, crazing and micro-cracks. These damage mechanisms are illustrated in Figure 2-31.

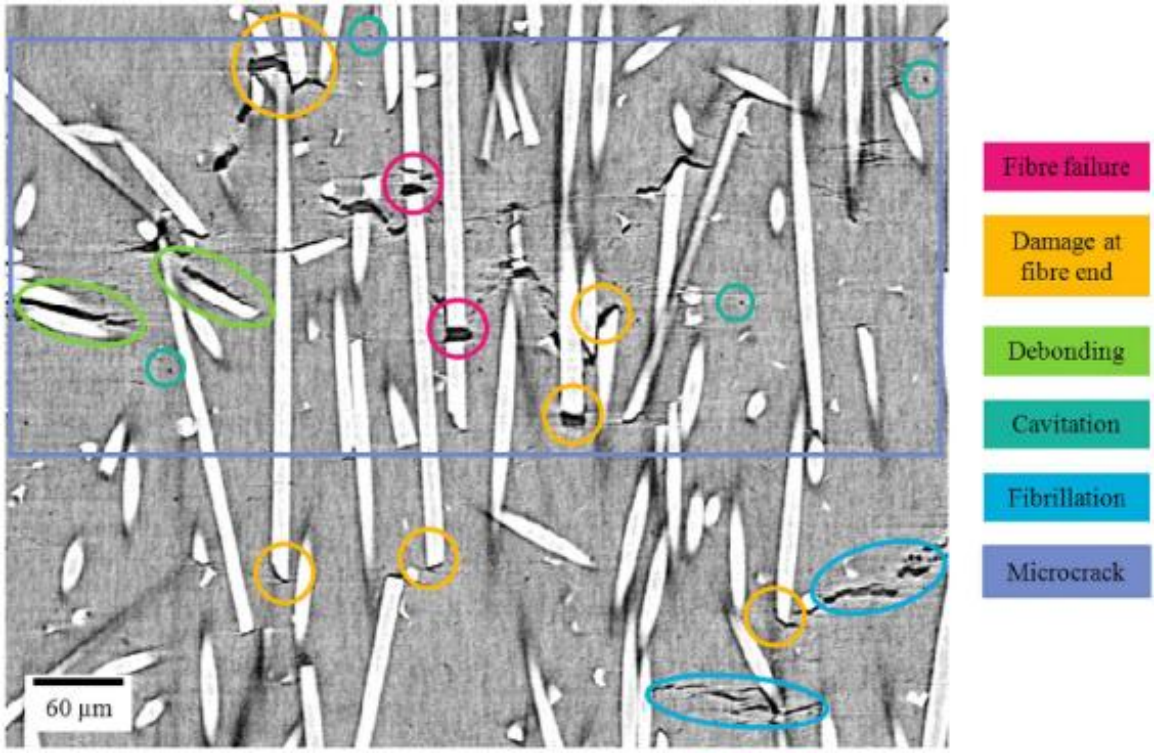

Figure 2-31 X-ray micro-computed tomography showing damage mechanisms in fatigue

The evolution of some of the fatigue damage mechanisms is also presented. Figure 2-32a shows the progression of the fibre failure which has been observed to occur all along the fatigue life of the samples and has been considered to take place due to fatigue and not by quasi-static failure. The development of the debonding process is illustrated in Figure 2-32b. According to the authors, this mechanism appears at a later stage of the fatigue life (approximately 90%) and is one of the major contributors of the crack propagation. It was observed that the debonding primarily initiated from the debonding of the fibre ends. Another failure mechanism reported is crazing, which is the damage in the matrix and it was found close to the fibre-matrix interface or between damaged matrix zones. The evolution of this damage mechanism is depicted in Figure 2-32c. Finally, Figure 2-32d, presents the development of micro-cracks in fatigue loading. The micro-cracks appeared at an advanced stage of the fatigue life of specimens. The micro-cracks were found to be initiated by the coalescence of matrix damage and seemed to propagate differently depending on the fibre orientation. For the 0° sample, the damage localization in the form of 45° bands between existing damage regions is what primarily drives the propagation process. In contrast, for the 90° coupons the favourable orientation of the fibre-matrix interface provides an easy crack propagation path.

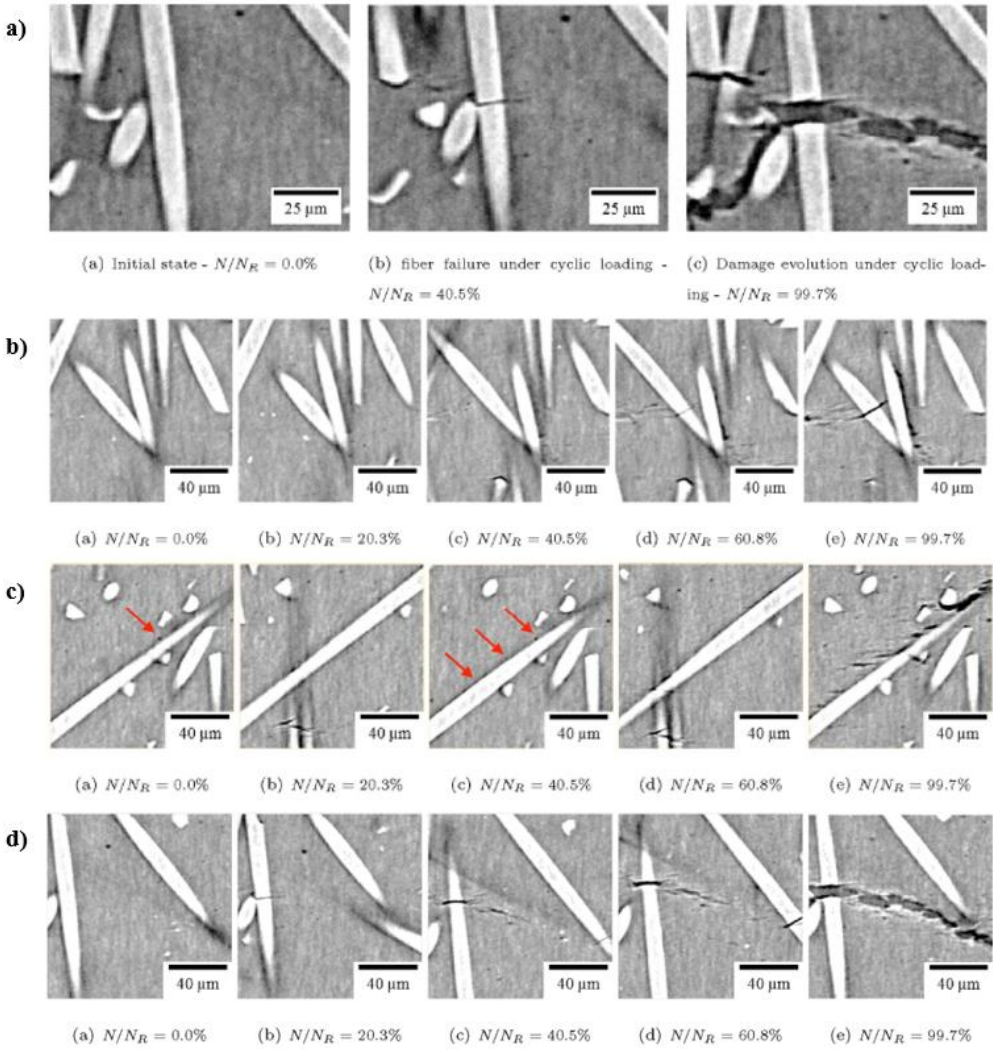

Figure 2-32 Evolution at different fatigue cycles of a) fibre failure, b) debonding, c) crazing, d) micro-cracks

Noda et al [67] conducted fatigue tests on coupons made of PA66 reinforced with 33 wt% glass fibre reinforcement and 0.2 wt% of moisture content. The tests were conducted at temperatures in the range of 0 and 150° C using frequencies of 10 and 20 Hz. After the specimens failed, they observed the fracture surfaces utilizing SEM. The authors described the failure mechanisms below and above the glass transition temperature, see Figure 2-33a) and b). Below this temperature, the failure began with void nucleation and initiation of micro-cracks at the end of the fibres, then damage propagated around the fibre ends, and finally a crack propagated rapidly in a brittle manner perpendicular to the loading direction. Above the glass transition temperature, the failure mechanisms described corresponded initially to the formation of micro voids, which then propagated along the interface of the matrix and the fibres causing debonding and the formation of crack walls. These were then connected by

bridging at different points and then fast crack propagation occurred in a ductile manner leading to the failure of the specimens.

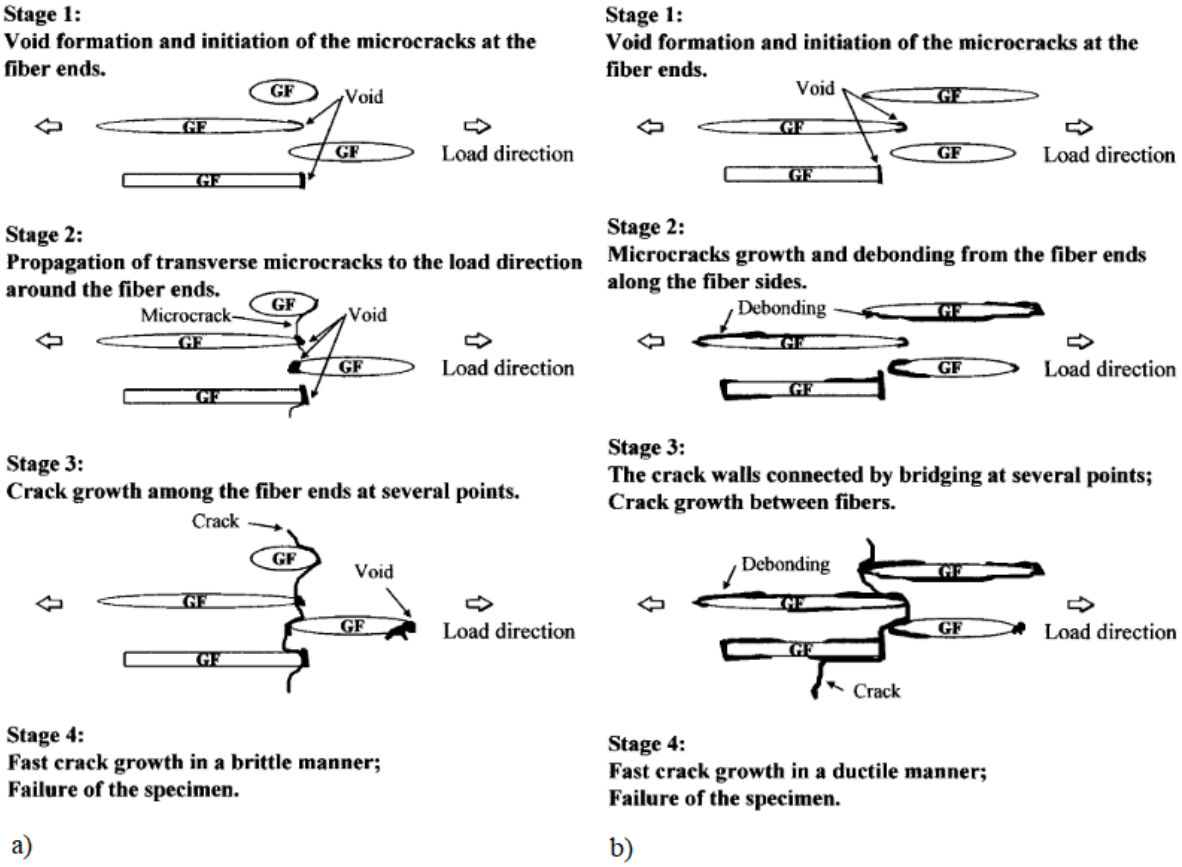

Figure 2-33 Schematic of fatigue damage process a) below Tg and b) above Tg [60]

2.8 Modelling of the fatigue behaviour

A recent paper published by Lizama et al. [68] presents the modelling of the fatigue behaviour of a PA 66 GF50 using a multi-stage approach. Specimens at 0°, 45° and 90° with respect to the injection flow were fatigue tested at R=0 at room temperature, and tensile tests at room temperature were also carried out. In Figure 2-34, the S-N curve obtained from the tests is presented. These tests were performed to obtain the material properties to implement them in a further stage of the modelling process. The results from this study show that the multi-stage modelling approach is needed to achieve reliable results, starting from the simulation of the manufacturing process to considering the anisotropy of the material.

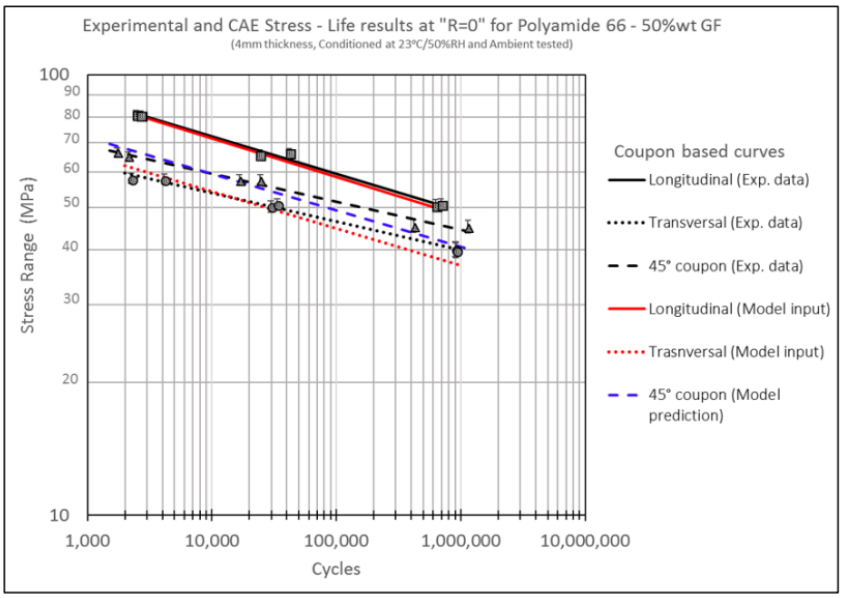

Figure 2-34 S-N curve for PA66 GF50 at R=0 [68]

Sonsino and Moosbrugger [69] studied an automotive component made of PA66 GF35 at room temperature and 130°C. In order to obtain the material properties, notched and unnotched specimens were fatigue tested at room temperature, 80°C and 130°C using stress ratios of R=-1, R=0 and also at variable amplitude. Even though the results at room temperature were in good agreement with the experimental results, the specimens used to obtain the material parameters were injected moulded; thus, the orientation of the fibres was only considered in the direction of the injection flow. Besides that, the tests were carried out at R=-1, and the stress ratio for the modelling was R=0.

Another paper by Wilson and Heyes [70] also uses a multi-stage modelling approach for the fatigue modelling of a PA66 GF50. They started the modelling process by simulating the injection moulding process of plaques and an engine component. They compared the results against CT measurements and observed a good agreement. Specimens of three orientations (0°,45° and 90°) and the actual component were fatigue tested at R=0.1. Finite element simulations were carried out in the commercial software Abaqus coupled with Digimat using the results from the simulation of the injection moulding process. From the simulations of the specimens, the stress and elastic strain tensors were obtained and used to compute a strain energy-based fatigue criterion. This criterion was used for calibrating the fatigue model to assess the fatigue life of the component showing conservative results. Figure 2-35 shows the comparison modelling and experimental results with conservative fatigue predictions.

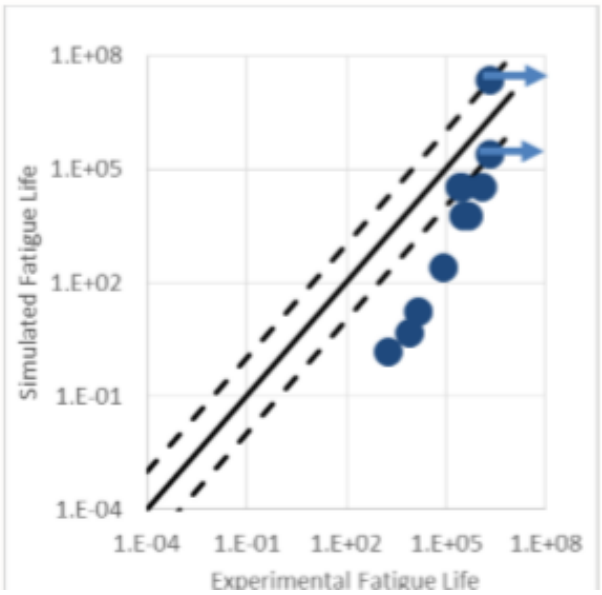

Figure 2-35 Comparison of fatigue modelling and experimental results using an energy-based criterion [70]

2.9 Discussion of the literature review

As seen in the literature review, several factors influence the behaviour of SFRP making it a complex and challenging task to develop accurate lifetime prediction models. One of the most important elements in the mechanical response of SFRP is the fibre orientation distribution resulting from the manufacturing process. Thus, it is important to characterise the complex fibre distribution in order to study its impact on the mechanical behaviour of SFRP. Advanced techniques such as X-ray Micro-Computed Tomography are going to be used for this purpose in this investigation. To study the anisotropy caused by the fibre orientation distribution, many researchers have extracted samples from plaques at different orientations, and some of them manufactured more than one specimen per plaque. Research has shown [22] that coupons cut at the same orientation from the same plaque but in different locations present differences in mechanical properties that can lead to deviations in the lifetime estimations. For this study, coupons will be extracted from the same location in an attempt to avoid such deviations.

In order to account for the effect of the fibre orientation distribution and obtain accurate and reliable lifetime assessments, it is necessary to use a multi-stage modelling approach starting from the manufacturing process, as suggested by the promising results of the works [68-70] discussed in the previous section. Even though these results are encouraging, there is a lack of studies including the effect of temperature. In this work, a robust multi-stage modelling

methodology including the effect of temperature will be carried out with validation at every stage.

Because the components made of SFRP are subjected to different environmental and loading conditions, efforts must be made to create models that integrate these factors to help the industry obtain precise and reliable results for the design of components.

Besides understanding the repercussion of the aforementioned factors, it is paramount to gain deep knowledge of the damage mechanisms of the SFRP under different loading and environmental conditions to develop more accurate prediction models. Even though damage mechanisms for SFRP have been reported in the literature [20, 40, 42, 43, 47, 49, 61] most studies have been carried out at room temperature with observations relying on two-dimensional imaging techniques. Investigations using three-dimensional techniques and in-situ mechanical testing are scarce. To address the lack of understanding of the actual damage process below the surface related to crack initiation and propagation, state-of-the-art experimental techniques combining mechanical testing inside an X-ray Micro-Computed Tomography microscope will be used. This new knowledge will help to develop more accurate and reliable models that can integrate different factors affecting the SFRP behaviour under various loading and environmental conditions to predict the lifetime of SFRP.

3 EXPERIMENTAL METHODOLOGY

3.1 Introduction

This chapter presents the experimental methodology followed during the project. A description of the material, specimens used and conditioning is outlined. The experimental equipment, the methodology and the techniques used for the analysis of the material are thoroughly detailed.

3.2 Material description

The constituent materials of the short glass fibre reinforced plastic composite material used for this project are Polyamide 66 (PA66 or Nylon 66) for the matrix, and the fibres are made of short glass fibre type E. The abbreviation of the composite material is PA66GF50, and it is made of 50wt% ($V_f = 0.3$) of fibres. The fibres have an approximate length of 200 µ and a diameter of 10 µ, giving an aspect ratio of 20. Actual measurements of the length and diameter of the fibres were done using information extracted from micro-computed tomography (µCT). The procedure followed is described in sections 3.8.1.2 and 3.8.2.2, and the results are shown in section 6.1.

The material is manufactured by BASF under the denomination of A3WG10 CR and was supplied in plaques of 150 x 150 x 4 mm in dry as moulded condition. The glass transition temperature is 65-70°C, and it has a density of 1.57 g/cm^3 [71].

The material properties specified by the supplier at room temperature in conditioned at 23°C/50% R.H and dry as moulded states are shown in Table 3-1:

Table 3-1 Material properties for dry as moulded and conditioned state [71]

Property	Dry	Conditioned (23°C/50% R.H)
Tensile modulus	16400 MPa	11500 MPa
Stress at break	230 MPa	160 MPa
Strain at break	2.5 %	4.1 %
Flexural modulus	15500 MPa	11300 MPa
Flexural strength	370 MPa	260 MPa

3.3 Specimens and conditioning

The geometry of the specimens used for the fatigue tests and the tensile test is shown in Figure 3-1. They were machined from injected moulded plaques provided by the supplier. To study the effect of fibre orientation, they were cut in three different directions (0°, 45° and 90°) with respect to the injection flow. Several authors [47, 68, 72-74] have used this method. The centre of the sample gauge length sample was located at the same position in the plaque regardless of the specimen orientation, see Figure 3-2.

There is no consensus about the dimensions of the specimens; in consequence of this, they were determined according to the dimensions of the grips considering similar geometries and dimensions found in the literature [59, 68].

The specimens were CNC milled from the plaques using a spindle speed of 3500 RPM, a feed rate of 350 mm/min and a depth cut of 8 mm.

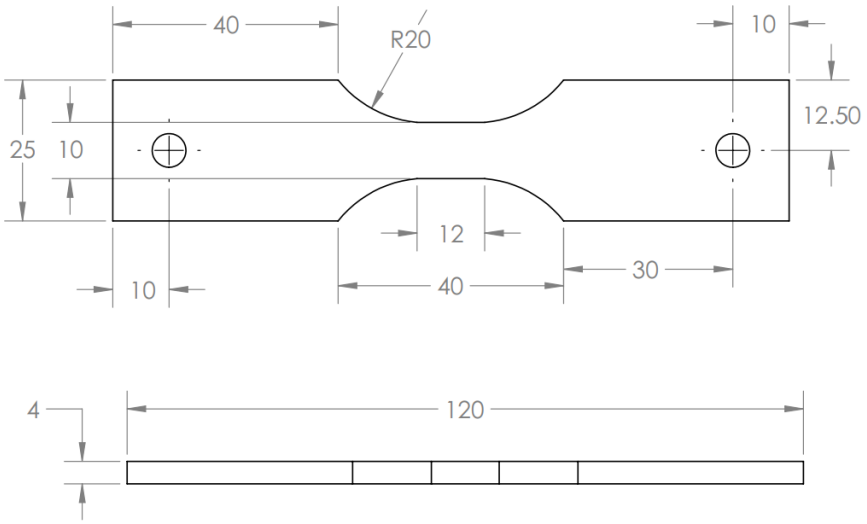

Figure 3-1 Dimensions of the specimens used for the fatigue and tensile tests. All dimensions are in mm.

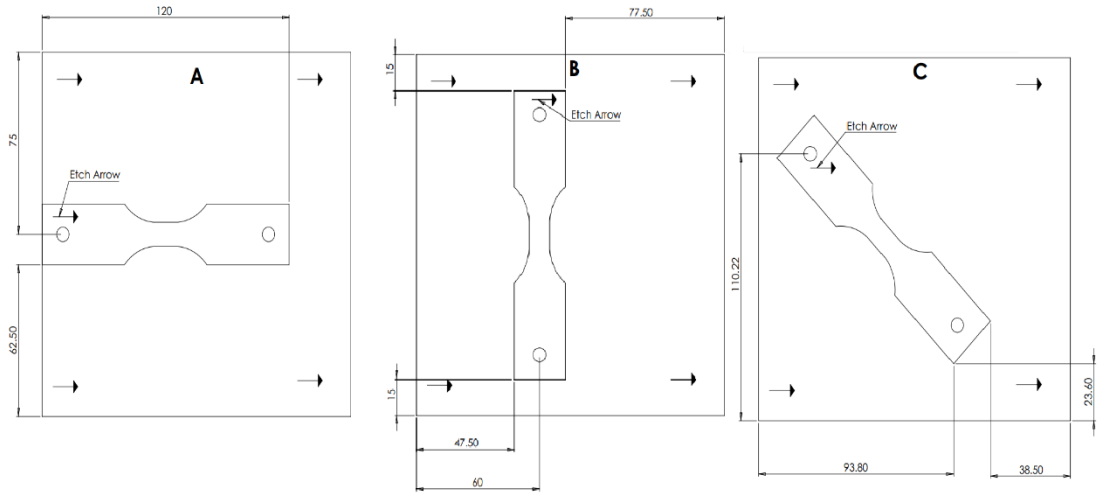

Figure 3-2 Orientation and location of the manufacturing of the specimens in the plaque. Dimensions are in mm. The arrows indicate the injection flow.

As stated in Chapter 0, moisture performs an important role in the mechanical behaviour of SFRP. Therefore, it is necessary to standardise the percentage of moisture in the specimens to obtain consistent, reliable and reproducible results. To do this, the specimens were conditioned. There is a considerable amount of methods to do the conditioning of the specimens [75, 76]. The method used for the conditioning is explained as follows:

First, the specimens were dried at 40° C for 24 hours in a furnace. Then the specimens were immersed in water and placed in the furnace at 40°C. This was realised to speed up the process of moisture absorption.

The moisture absorption was assessed by weight gain measurements over time taking into consideration the weight of the specimens after the drying phase as a baseline for the measurements. The specimens were weighted every 24 hours to evaluate the moisture absorption until they reached between 1 and 1.4% of moisture. According to [68], this percentage range corresponds to the moisture equilibrium at standard laboratory conditions of 23° C and 50% relative humidity. This percentage of moisture was reached after 72 hours of water immersion. The specimens were then stored in aluminium-sealed bags to reduce contact with the environment and to keep the desired amount of moisture in the specimens until tests were carried out.

Figure 3-3 shows the normal distribution of moisture in the specimens after 72 hours of conditioning in water at 40° C. A mean value of 1.088% for the moisture content and a standard deviation of 0.025 were calculated from these results

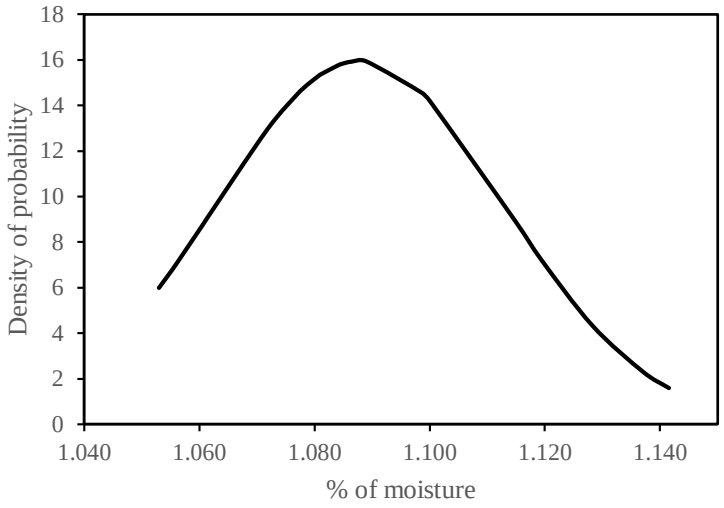

Figure 3-3 Normal distribution of the moisture in the specimens after 72 hours of water immersion at 40°C

3.4 Tensile tests at room temperature

To characterise the behaviour under static loading conditions quasi-static tensile tests were carried out. The tests were performed in an electromechanical machine Tinius Olsen H25KS with a capacity of 25kN. The speed of the tests was 2 mm/min as stated in the ASTM D3039/D3039M-17 Standard Test Method for Tensile Properties of Polymer Matrix Composite Materials [77]. Specimens of the three orientations were tested.

Full-field strain measurements were carried out using digital image correlation (DIC). This technique tracks a group of pixels, named subsets and shown in Figure 3-4 from a digital image of a specimen or component subjected to loads or displacements, through different stages of deformation and compares the images against a reference image [78]. After correlating the images, displacement fields are computed and then differentiated to produce strain values displayed as strain distribution maps.

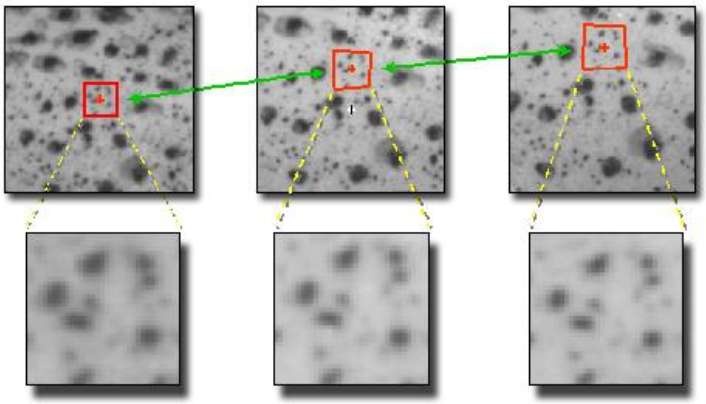

Figure 3-4 Example of DIC subsets and their deformation

The setup of the machine and the DIC equipment is shown in Figure 3-5.

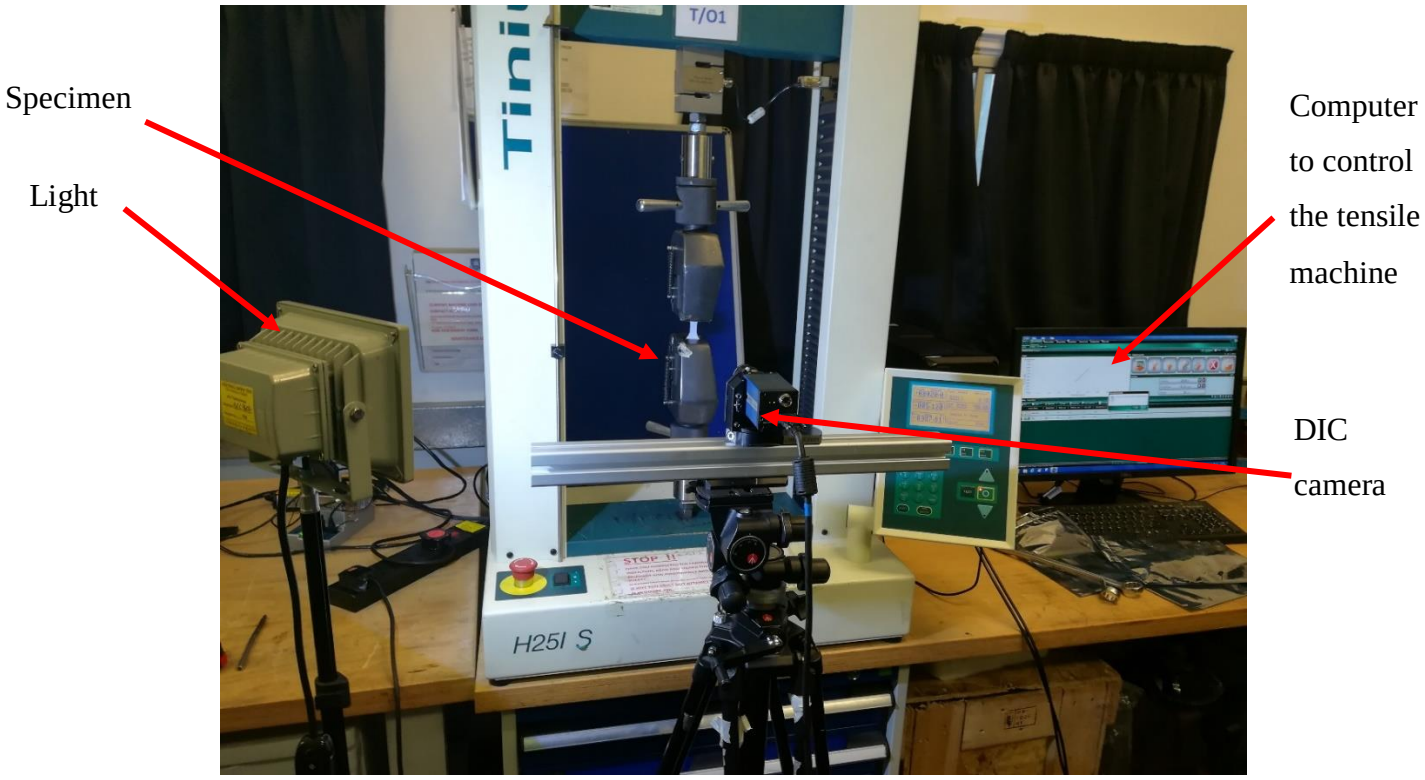

Figure 3-5 DIC setup

To use the DIC technique it is, first, necessary to produce a speckle pattern at the surface of the specimens. This is done by covering the surface with white paint to obtain a matte finish on which the speckle pattern is produced by spraying dots using black paint in order to create a good contrast, as shown in Figure 3-6.

Figure 3-6 Specimen with speckle pattern

The quality of the experimental images determines the smallest displacement values that can be measured with DIC as well as the spatial resolution. DIC algorithms can typically detect sub-pixel displacements of up to 0.01 pixels [79]. However, the smallest displacement measurements that may be expected from DIC in practice are on the order of 0.1 pixels since experimental variables add errors to the measurements [79].

The software VIC-2D 6 was used to conduct the correlations, and a virtual extensometer covering the length of the gauge length was placed on the images to measure the strain plotted on the stress-strain curves.

3.5 Tensile tests at 50 and 100° C

Tensile tests were performed in a Nene Testing System servo-hydraulic machine with an Interface 1020 load cell with a capacity of ± 12.5 kN with a static error of ±0.04% and fatigue rated up to 10^8 cycles. The machine had an LVDT (Linear Variable Differential Transformer) with an operating range of ± 55 mm. The equipment was controlled by a MOOG SmartTest One test controller.

The temperature was achieved using an EC2043A environmental chamber mounted onto the hydraulic machine, with a temperature range of -100°C to 500°C. The environmental chamber was controlled by a CU2043A control unit. The setup of the test rig is shown in Figure 3-11. The environmental chamber has a K-type thermocouple placed at the rear and a fan to ensure an even distribution of the hot air through the chamber and better temperature uniformity inside the chamber.

When the grips are perfectly aligned, the specimen experiences a uniform axial tensile strain. Thus, to measure the alignment of the grips, a rectangular specimen with eight strain gauges was constructed as per the standard ASTM E1012-19 Standard Practice for Verification of

Testing Frame and Specimen Alignment Under Tensile and Compressive Axial Force Application [80]. The strain gauges model FLA-2-17 had a 2 mm active grid and a 5% strain limit. The strain acquisition data was done via LabView using a Ni 9235 card. Figure 3-7 shows the strain measurements of the rectangular specimen before and after the alignment correction. Figure 3-8 depicts the position of the grips before and after the alignment correction.

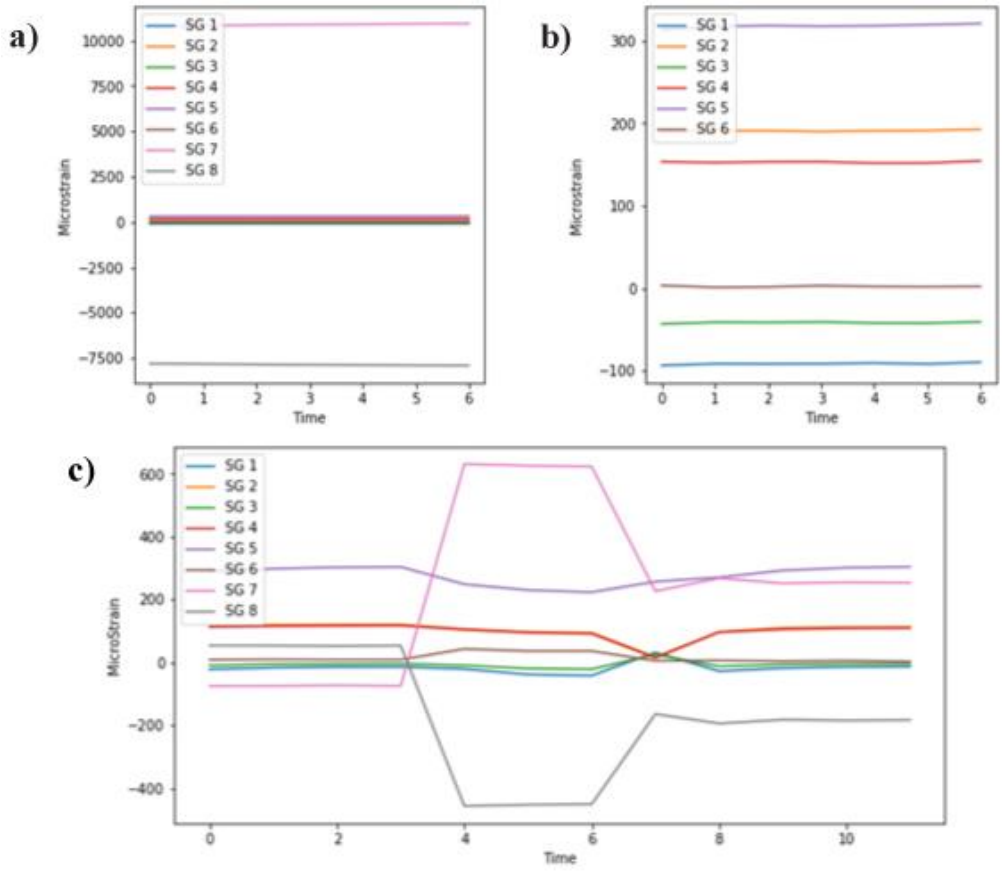

Figure 3-7 Microstrains a) before alignment, b) zoom in to the strain of strain gauges 1-6, c) after alignment

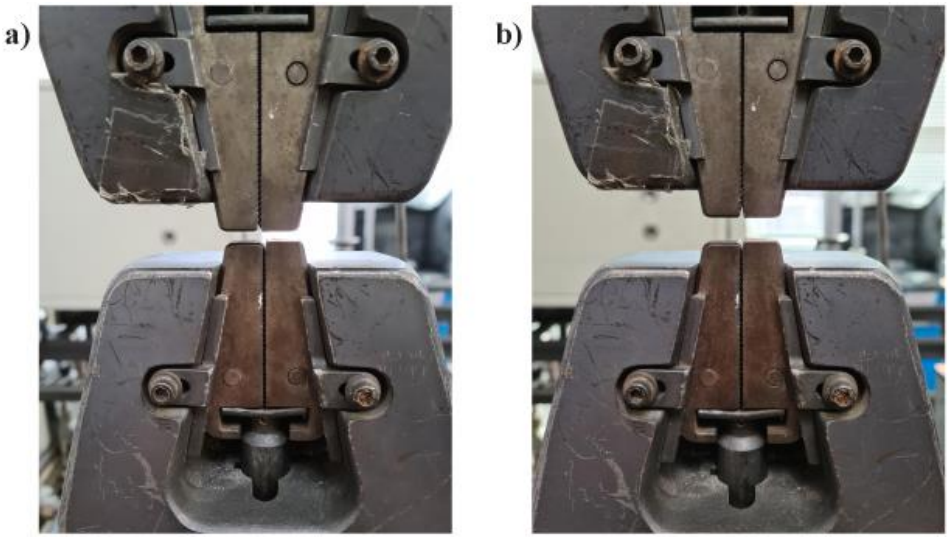

Figure 3-8 a) Grips before the alignment, b) grips after the alignment

Strain measurements were obtained using DIC taking special care to avoid the reflection of the light in the region of interest. The images were captured every 100 μs, and the synchronisation of the images to the applied force was done with a Limess DAQhw data acquisition box. To assess the influence of the glass window and the temperature, strain calculations were performed with the chamber door opened, closed, and with the heat on. The specimen was subjected to the same stress level for each condition. The strain results for the specimen tested at 100° C are shown in Figure 3-9. It can be seen that there is a difference of 1.35% between the strain measurement with the chamber door opened and the strain measurement with the door closed and the heat on.

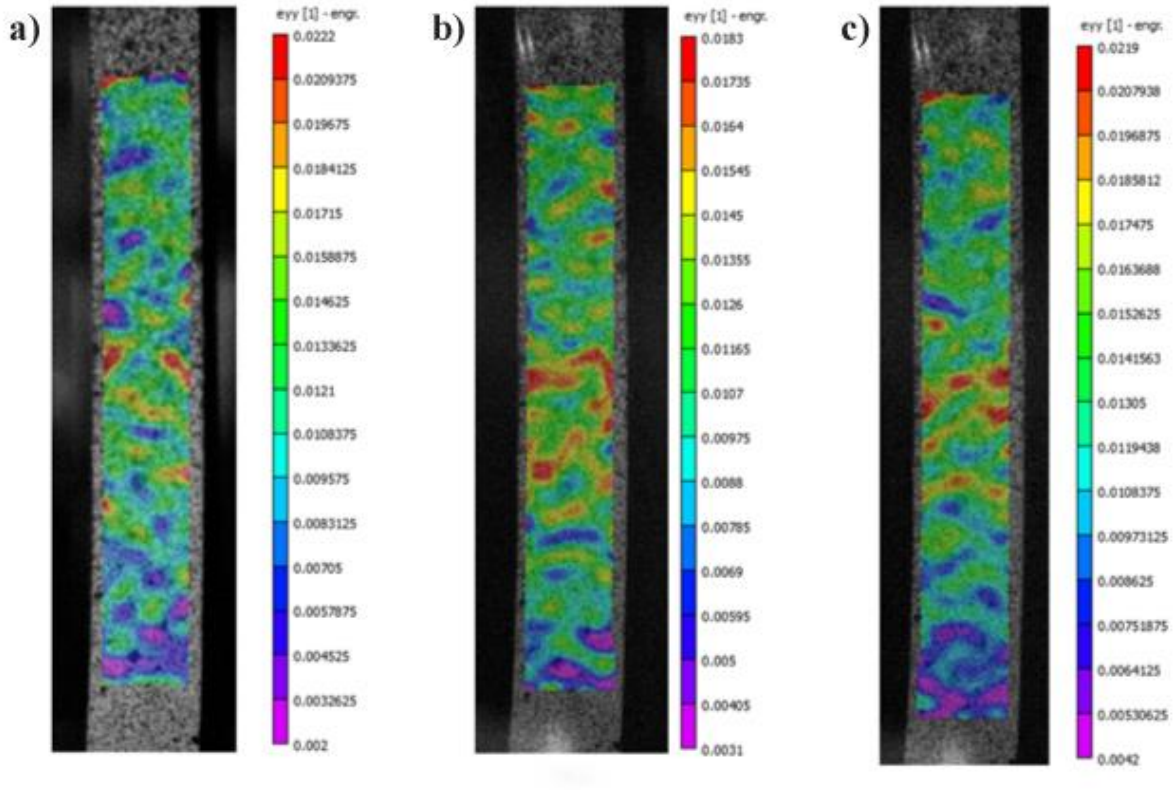

Figure 3-9 Strain distribution for a) specimen with the chamber door opened, b) with the door closed, and c) with the heat on

The tensile tests were started once the selected temperature was reached, and a cross-head speed of 2 mm/min was used in agreement with ASTM D3039/D3039M-17 [77]. Three specimens were tested for each orientation.

The setup for the tensile tests is illustrated in Figure 3-10.

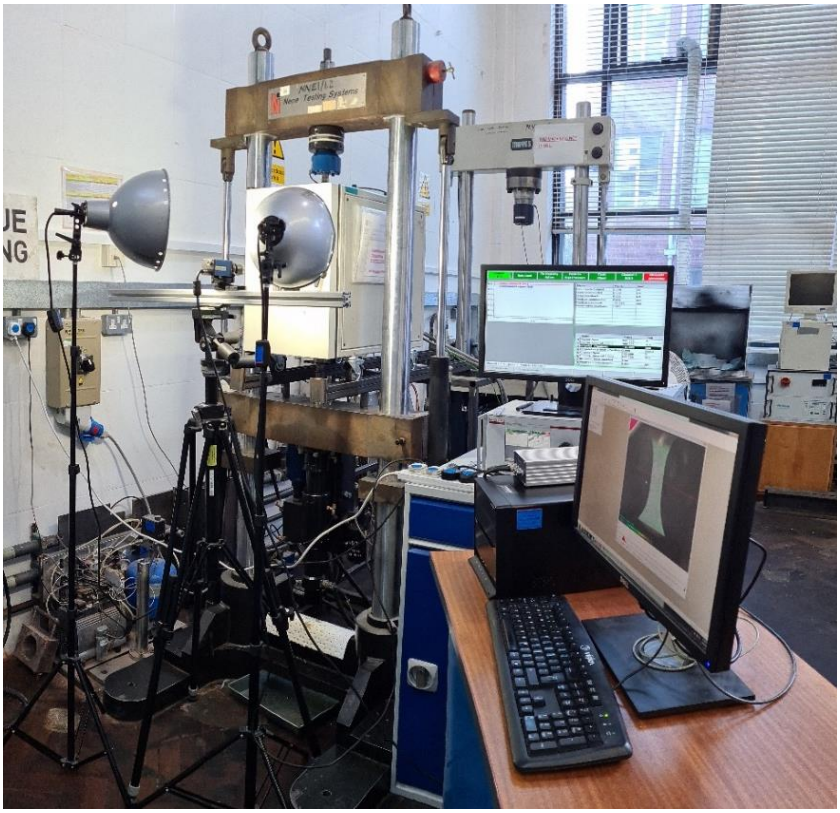

Figure 3-10 Setup for the tensile tests at high temperature

3.6 Fatigue tests at room temperature

Uniaxial fatigue tests were conducted in the Nene Testing System servo-hydraulic machine with the MTS 533 Alignment Fixture previously described in section 3.5.

The tests were carried out at constant amplitude using four different stress levels and a stress ratio of R=0, two tests were performed with each stress level. The frequency used was 5 Hz to avert self-heating. The stresses and forces applied to each specimen are shown in Table 3-2

Table 3-2 Forces and stresses for the fatigue tests at room temperature

Orientation	Max. stress / Min. stress (MPa)	
0°	80 / 0	67.5 / 0
90°	57.5 / 0	50 / 0
45°	65 / 0	57.5 / 0

An S-N curve was plotted using the nominal stresses and the resultant number of cycles.

3.7 Fatigue tests at 50 and 100 ° C

Fatigue tests under constant amplitude at 50 and 100°C were conducted. The same load ratio (R=0) and frequency (5 Hz) as for the room temperature tests were applied to be consistent and compare the results. The same servo-hydraulic machine, load cell, test controller and alignment fixture described in section 3.5 were used. To achieve the desired temperatures, the EC2043A environmental chamber controlled by the CU2043A control unit used for the tensile tests at 50 and 100° C (see section 3.5) was utilised. The setup of the test rig is shown in Figure 3-11.

Data such as force and displacement of the actuator, specimen strain, and the temperature of the gauge length and inside the chamber were recorded simultaneously via a Labview code. A Ni 9215 acquisition card logged the force and displacement of the actuator. The specimen strain was measured by an Instron 2620-602 Series fatigue-rated extensometer, with a linearity error of ±0.15%, a full-scale range of ±5 mm and a temperature range of -80°C to 200°C connected to a Ni 9237 card. The temperature at the centre of the gauge length and a reference temperature inside the chamber were measured with two separate thermocouples type T with a temperature range of -270°C to 370°C and accuracy of ±1°C plugged into two Ni 9211 acquisition cards. The instrumentation of the specimen is shown in Figure 3-12.

The number of cycles was recorded directly from the MOOG controller.

The maximum and minimum stresses used for each specimen orientation and temperature are shown in Table 3-3.

Table 3-3 Stress levels for the fatigue tests at 50 and 100°C

Specimen	50°C				100°C		
	Max. stress / Min. stress (MPa)				Max. stress / Min. stress (MPa)		
0°	80 / 0	67.5 / 0	50 / 0	40 / 0	50 / 0	40 / 0	35 / 0
45°	65 / 0	57.5 / 0	50 / 0	40 / 0	50 / 0	40 / 0	30 / 0
90°	57.5 / 0	50 / 0	40 / 0	-	40 / 0	30 / 0	25 / 0

The nominal stresses were plotted against the number of cycles to obtain the S-N curve for each temperature tested. A cut-off limit of 10^6 cycles, corresponding to the high cycle fatigue (HCF) regime was set.

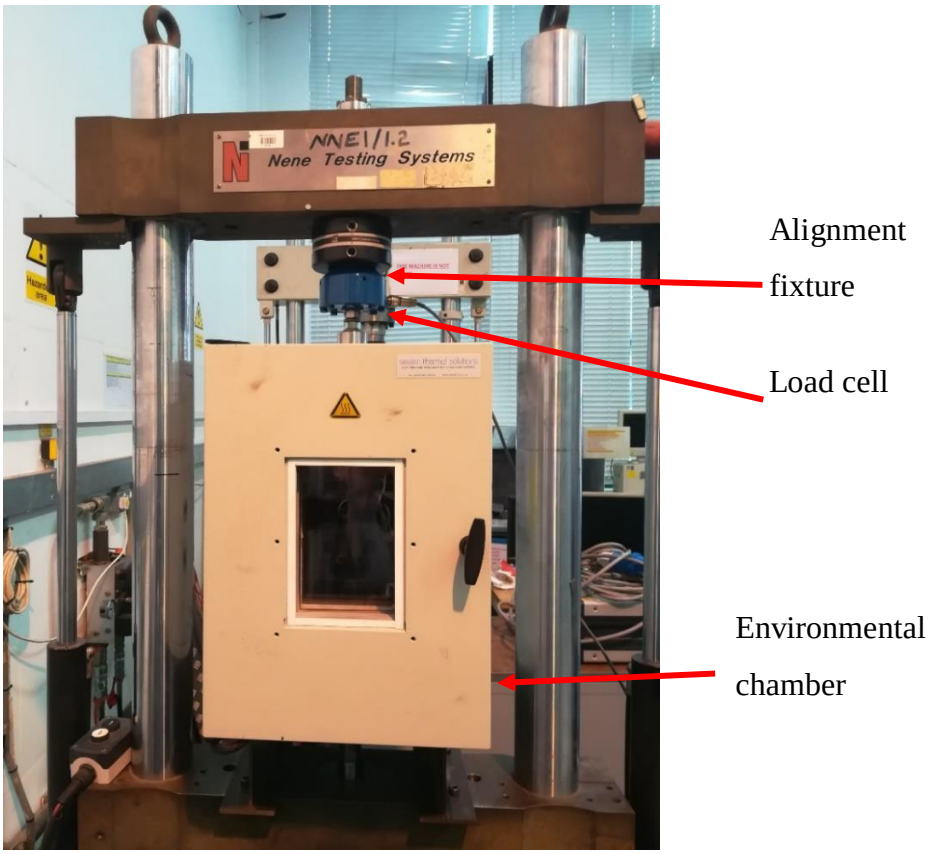

Figure 3-11 Set up of the fatigue machine for the test at high temperature

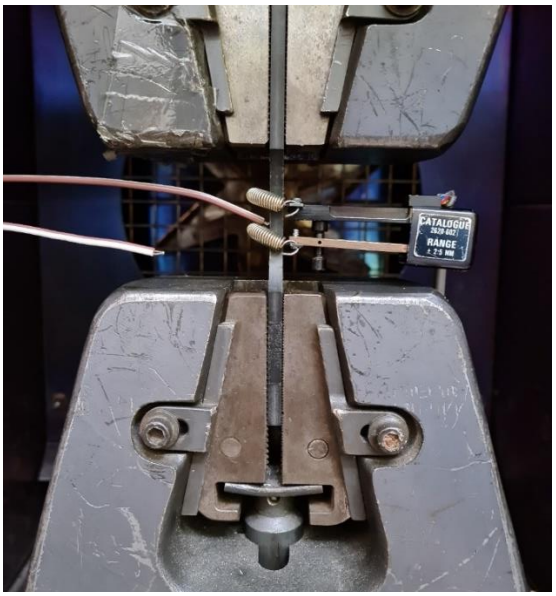

Figure 3-12 Instrumentation of the specimen

3.8 Damage mechanisms

3.8.1 In-situ tensile tests

In order to understand the damage mechanisms occurring during tensile loads, in-situ tensile tests were carried out inside a micro-computed tomography (μCT).

Smaller specimens were extracted from the supplied plaques preserving the centre of the gauge length in the same location as in the fatigue and tensile specimens. One sample of each orientation (0°, 45° and 90°) was milled using the same manufacturing parameters described in section 3.3. Figure 3-13 shows the dimensions of the smaller samples. The specimens were conditioned to a moisture level between 1 and 1.4%.

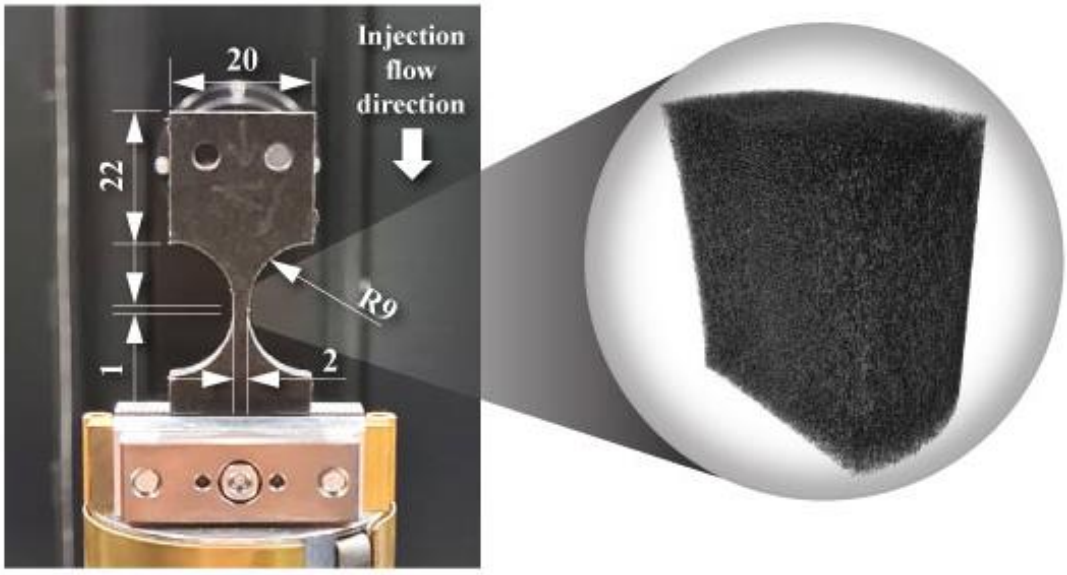

Figure 3-13 Dimensions of the μCT specimens

The in-situ tensile test was carried out in a Zeiss Xradia Versa 620 at Sheffield Tomography Centre (STC) at the University of Sheffield, UK. The μCT was equipped with a DEBEN rig with a capacity of 5000 N. The specimen was subjected to 5 loads corresponding to 25%, 50%, 75%, 95% and 99% of the ultimate tensile strength obtained from the tensile tests. The loads used for each specimen are shown in Table 3-4.

Table 3-4 Loads for the in-situ tensile tests

Orientation	Load for 0% of UTS	Load for 25% of UTS	Load for 50% of UTS	Load for 75% of UTS	Load for 95% of UTS	Load for 99% of UTS
0°	0 N	204 N	408 N	612 N	775.2 N	807.84 N
45°	0 N	190 N	380 N	570 N	722 N	752.4 N
90°	0 N	166 N	332 N	498 N	630.8 N	657.36 N

Two scans were taken before loading the specimen to determine the uncertainty of the subsequent DVC computations. After that, scans were taken at each loading phase.

The scanning parameters utilised are shown in Table 3-5

Table 3-5 Scanning parameters

Parameter	0° specimen	45° specimen	90° specimen
X-ray tube voltage	160 kV	160 kV	160 kV
Tube current	156 µA	156 µA	156 µA
Exposure time	2 seconds	2 seconds	2 seconds
Projections	1601	1601	1601
Optical magnification	4x	4x	4x
Voxel size	4 µm	4.4 µm	4.4 µm

The voxel size allowed a field of view large enough to observe the whole thickness of the specimens, as priority was given to studying the effect of the variation of the fibre orientation in the damage process. The 2D projections were reconstructed using the filtered back-projection algorithm of the Zeiss Microscopy commercial software (XMReconstructor) and a filtered back-projection algorithm.

The scanned regions comprised a volume of 993 x 1014 x 994 voxels and were located at the gauge length of the specimens, as depicted in Figure 3-13.

3.8.1.1 Digital Volume Correlation (DVC)

Digital Volume Correlation (DVC) was utilised for the 3D full-field characterisation of the deformation and damage process under tensile loads.

The DVC technique is an extension of the DIC. The image is divided into sub-volumes (subcells), and for each subcell, the displacement of a random pattern is calculated. This random pattern is caused by the variation of material density, for instance, due to the presence of different material types, air, voids, or cracks.

Mainly there are two DVC approaches: local and global. The local DVC divides the reference and deformed images into subsets which are then individually correlated. Normally, is only kept the displacement vector at the centre of each subset. Therefore, a post-processing step is needed to generate a smooth displacement field.

On the other hand, global DVC computes a continuous displacement field based on finite-element interpolation using all voxels of the entire region of interest at once.

The correlations were carried out using the DVC extension called XDigital Volume Correlation from the commercial software Avizo. The region of interest (ROI) was tailored to the specimen geometry, and a global DVC approach was utilised with an initial displacement obtained from a local DVC analysis of the complete ROI.

Prior to conducting the global DVC analysis on the loading steps, a suitable subcell size and uncertainty were estimated by correlating the two scans at the unloading condition. Figure 3-14a-f illustrates the variation of the standard deviation of principal strains and displacements for different subcell sizes.

The selected subcell size for each specimen and the precision achieved for strain and displacement are presented in Table 3-6.

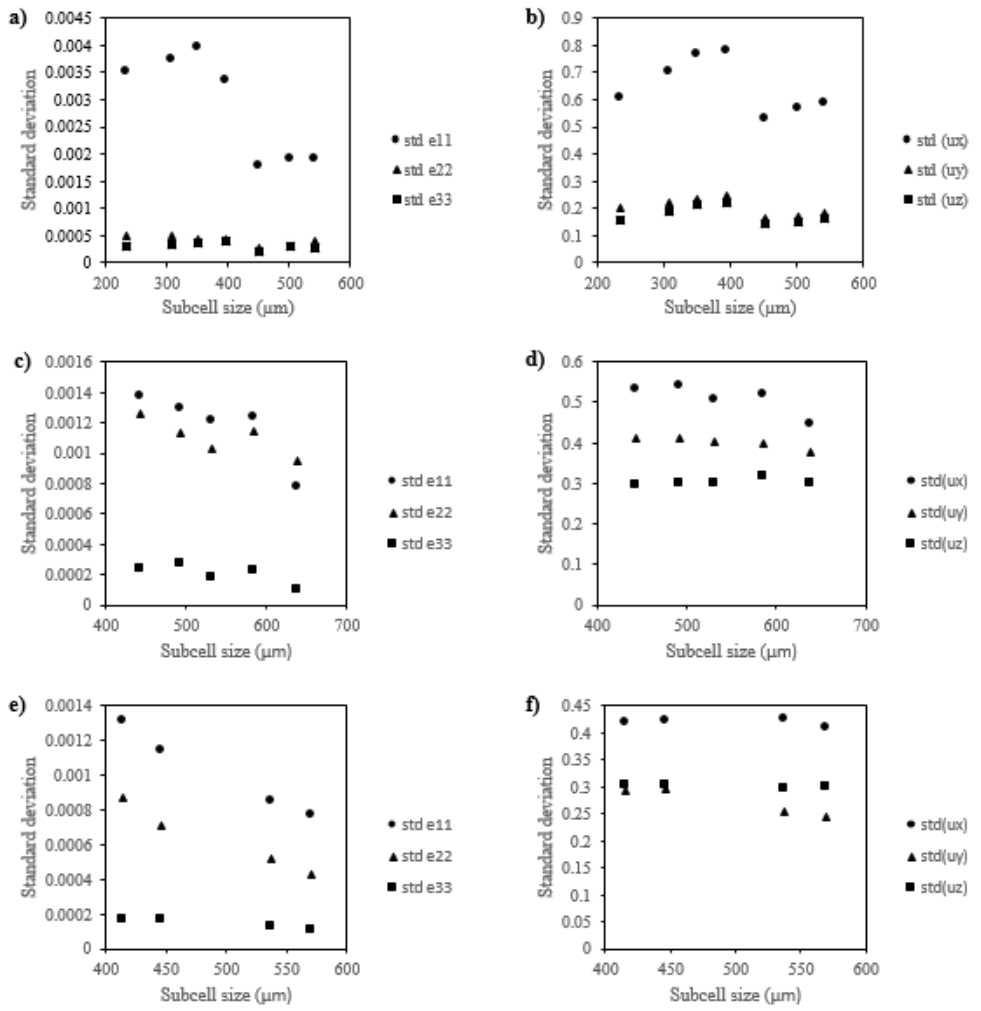

Figure 3-14 a) Standard deviation of principal strains for 0° specimen, b) Standard deviation of displacement for 0° specimen, c) Standard deviation of principal strains for 45° specimen, d) Standard deviation of displacement for 45° specimen, e) Standard deviation of principal strains for 90° specimen, f) Standard deviation of displacement for 90° specimen

Table 3-6 Selected subcell size and precision of strain and displacement

Specimen	Subcell size	Strain precision	Displacement precision
0°	450 μm	0.17%	0.52 voxels
45°	531 μm	0.12%	0.50 voxels
90°	571 μm	0.08%	0.40 voxels

3.8.1.2 Determination of the fibre orientation tensor and fibre length

The fibre orientation tensor was computed from a region of 500 x 500 μm at the centre of the gauge length of the scanned volume and considered all the specimen thickness. An example of the region of interest where the orientation tensor was extracted is depicted in Figure 3-15.

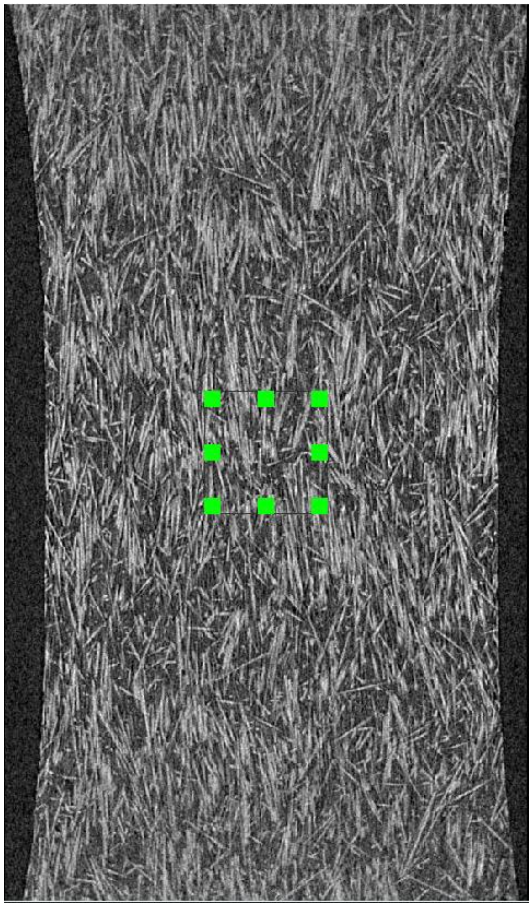

Figure 3-15 Region of interest in the 0° specimen where the orientation tensor was computed

This process was carried out in the commercial software Avizo using the XFiber extension, which allows for the tracking of fibre-like shapes and facilitates the segmentation for further analysis. The extension works by creating a cylindrical template and searches in the grey scale images from the μCT for a good agreement using a cross-correlation algorithm. This process is called cylinder correlation. Then the centre lines of those found fibres are tracked to allow for the estimation of the fibre length and determination of the fibre orientation tensor.

The parameters used for the cylinder correlation are shown in Table 3-7.

Table 3-7 Cylinder correlation parameters

Specimen	0°	45°	90°
Parameter		Value	
Cylinder length	200 µm	200 µm	200 µm
Angular sampling	5 µm	5 µm	5 µm
Mask cylinder radius	5.1 µm	5.1 µm	5.1 µm
Outer cylinder radius	5 µm	5 µm	5 µm
Inner cylinder radius	0 µm	0 µm	0 µm

In Table 3-8 the parameters used for the centre-line tracing are presented.

Table 3-8 Parameters for the centre-line tracing

Specimen	0°	45°	90°
Parameter		Value	
Minimum seed correlation	68 µm	68 µm	68 µm
Minimum continuation quality	45 µm	60 µm	60 µm
Direction coefficient	0.05	0.1	0.1
Minimum distance	10 µm	10 µm	10 µm
Minimum length	10 µm	40 µm	40 µm
		Search cone	
Length	200 µm	200 µm	200 µm
Angle	37°	37°	37°
Minimum step size	10%	10%	10%

3.8.2 In-situ tensile tests at 50 and 100° C

Tensile tests at 50 and 100° C were conducted inside the μCT Zeiss Xradia Versa 620 at Sheffield Tomography Centre (STC) at the University of Sheffield, UK.

Specimens of the dimension shown in Figure 3-13 were milled from the plaques in a 0° orientation. The specimens were conditioned to reach a moisture level between 1-1.4%.

The DEBEN rig used to conduct the in-situ tensile tests has the capability to perform tensile tests at high temperatures of up to 160° C. The temperature of the specimens was increased by heating the grips. Due to the low thermal conductivity of the material, a dummy specimen was tested to identify the correct temperature of the grips to reach the desired temperatures. The temperature at the centre of the gauge length of the dummy specimens was measured with a T-type thermocouple with a temperature range of -270°C to 370°C and an accuracy of ±1°C connected to a Ni 9211 acquisition card. The setup is shown in Figure 3-16a-b. To achieve 50°C at the centre of the specimen gauge length, a grip temperature of 76° C was needed. For the test at 100° C, the temperature of the grips was set to 160° C.

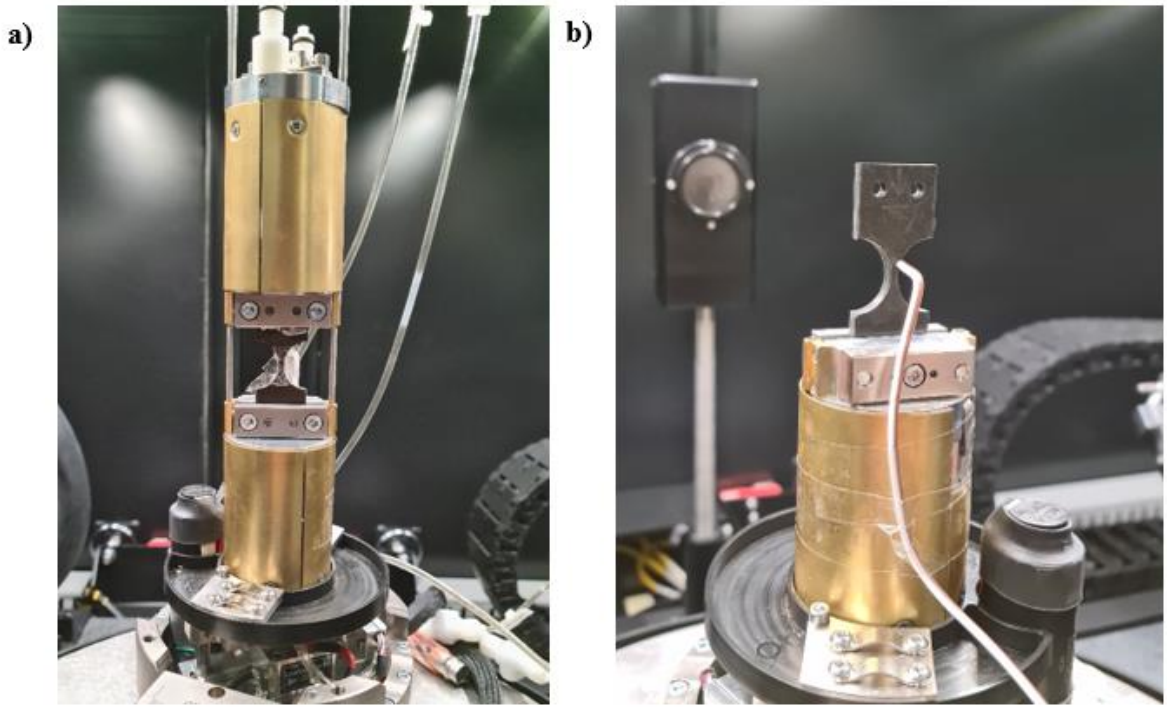

Figure 3-16 a) In-situ tensile test rig, b) thermocouple at the centre of the gauge length

Loads corresponding to 0%, 25%, 50%, 75% and 95% of the UTS were applied to the specimens. The loads applied are presented in Table 3-9

Table 3-9 Loads for the in-situ tensile tests at 50 and 100° C

50° C					
Orientation	Load for 0% of UTS	Load for 25% of UTS	Load for 50% of UTS	Load for 75% of UTS	Load for 95% of UTS
0°	0 N	195 N	390 N	585 N	741 N
45°	0 N	158 N	316 N	474 N	600.4 N
90°	0 N	152 N	304 N	456 N	577.6 N
100° C					
0°	0 N	148 N	296 N	444 N	562.4 N
45°	0 N	121 N	242 N	363 N	459.8 N
90°	0 N	118 N	236 N	354 N	448.4 N

The scanning parameters are shown in Table 3-10.

Table 3-10 Scanning parameters for the in-situ tensile tests at 50° and 100°C

Parameter	50° C	100° C
X-ray tube voltage	160 kV	160 kV
Tube current	156 µA	156 µA
Exposure time	2 seconds	2 seconds
Projections	1601	1601
Optical magnification	4x	4x
Voxel size	4.4 µm	4.4 µm

3.8.2.1 DVC

Similar to the in-situ tensile tests at room temperature, two scans were taken without load to assess the uncertainty of the DVC and select the correct subcell size. The XDigital Volume Correlation extension from the Avizo was used to perform the correlations.

Similar to the room temperature DVC analyses, an assessment of a suitable subcell size and uncertainty was performed. Figure 3-17a-d illustrates the variation of the standard deviation of principal strains and displacements for different subcell sizes.

Table 3-11 presents the selected subcell size with the corresponding strain and displacement precision.

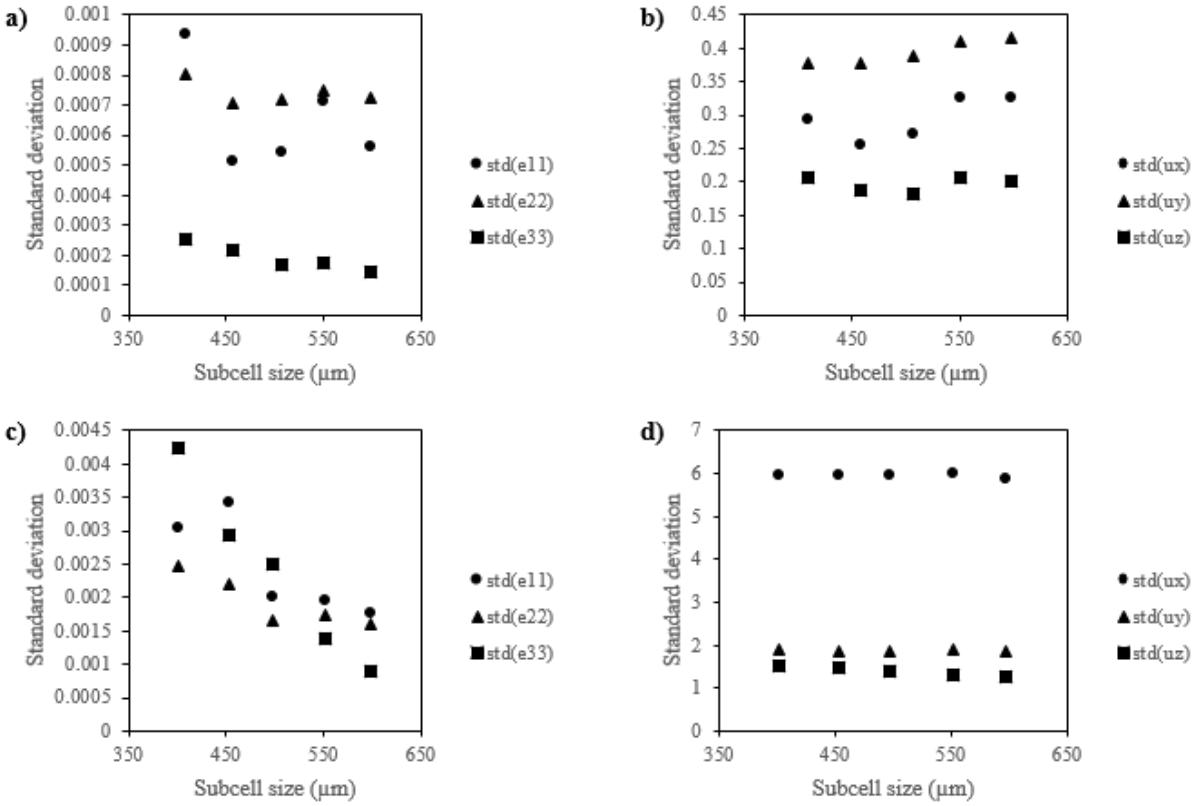

Figure 3-17 a) Standard deviation of principal strains for 0° specimen at 50° C, b) Standard deviation of displacement for 0° specimen at 50° C, c) Standard deviation of principal strains for 0° specimen at 100° C, d) Standard deviation of displacement for 0° specimen at 100° C

Table 3-11 Selected subcell size and precision of strain and displacement for each specimen

Specimen	Subcell size	Strain precision	Displacement precision
50° C	508 µm	0.072 %	0.38 voxels
100° C	552 µm	0.2 %	6 voxels

3.8.2.2 Fibre orientation tensor and fibre length

A region of 500 x 500 µm at the centre of the gauge length of the scanned volumes was selected to compute the orientation tensor of each specimen. The procedure followed is analogous to the room temperature one and was also carried out in the commercial software Avizo using the XFiber extension. The parameters used for the cylinder correlation and centre-line tracing are shown in Table 3-12 and Table 3-13, respectively.

Table 3-12 Cylinder correlation parameters for the 50 and 100° C specimens

Parameter	Value	
Specimen	50° C	100° C
Cylinder length	200 µm	200 µm
Angular sampling	5 µm	5 µm
Mask cylinder radius	5.1 µm	5.1 µm
Outer cylinder radius	5 µm	5 µm
Inner cylinder radius	0 µm	0 µm

Table 3-13 Centre-line parameters for the 50 and 100 C specimens

Parameter	Value	
Specimen	50° C	100° C
Minimum seed correlation	50 µm	68 µm
Minimum continuation quality	80 µm	60 µm
Direction coefficient	0.1	0.1

Minimum distance	10 μm	10 μm
Minimum length	40 μm	40 μm
Search cone		
Length	200 μm	200 μm
Angle	37°	37°
Minimum step size	10%	10%

3.8.3 X-ray scanning of fatigued specimens after failure

Regions close to the fracture surfaces of 0° and 90° specimens that were fatigue tested at 50 and 100° C were scanned in an attempt to understand the damage mechanisms for fatigue failure. All the samples were carefully examined prior to scanning and samples with evidence of secondary cracks were selected.

Two scans were taken to improve the resolution and have a relatively small voxel size, each covering half of the specimen width, and later stitched together to have a view of the full width. This process was performed in the μCT Zeiss Xradia Versa 620 software.

After scanning the entire width of the fractured samples, a second scan was performed at a location where secondary cracks were detected. This time, a better resolution was achieved due to a smaller field of view.

The 0° specimen tested at 100° C presented a secondary crack that covered the entire width of the specimen. Thus, no further zoom-in to the secondary crack was performed.

The scanning parameters are shown in Table 3-14 and Table 3-15

Table 3-14 Scanning parameters for fracture surfaces of fatigue specimens

Parameter	50° C		100° C	
	0°	90°	0°	90°
X-ray tube voltage	100 kV	100 kV	100 kV	100 kV
Tube current	140 µA	140 µA	140 µA	140 µA
Exposure time	2 seconds	2 seconds	2 seconds	2 seconds
Projections	1601	1601	1601	1601
Optical magnification	0.4x	0.4x	0.4x	0.4x
Voxel size	6.78 µm	6.24 µm	7.42 µm	6.24 µm

Table 3-15 Scanning parameters for the second scan of the fracture surfaces of fatigue specimens

Parameter	50° C		100° C
	0°	90°	90°
X-ray tube voltage	120 kV	120 kV	100 kV
Tube current	146 µA	146 µA	140 µA
Exposure time	2 seconds	2 seconds	2 seconds
Projections	1601	1601	1601
Optical magnification	4x	4x	4x
Voxel size	3 µm	3 µm	3.81 µm

3.9 Scanning Electron Microscopy (SEM)

The fracture surfaces of the samples tested under tensile load and cyclic load were observed using a scanning electron microscope (SEM).

The equipment used for the observation was a SEM Hitachi TM3030 Tabletop Microscope, shown in Figure 3-18a, with a magnification of 15 to 60, 000x (digital zoom of 2x and 4x)

Because the material is non-conductive, applying a layer of conductive coating was necessary before observing the samples in the SEM. Specimens cut at a small distance from the fracture surface were mounted on aluminium stubs utilising Acheson Silver DAG compound. Then the fracture surfaces were coated with a thin gold layer via sputtering. Figure 3-18b shows an example of a specimen gold coated and ready to be observed in the SEM.

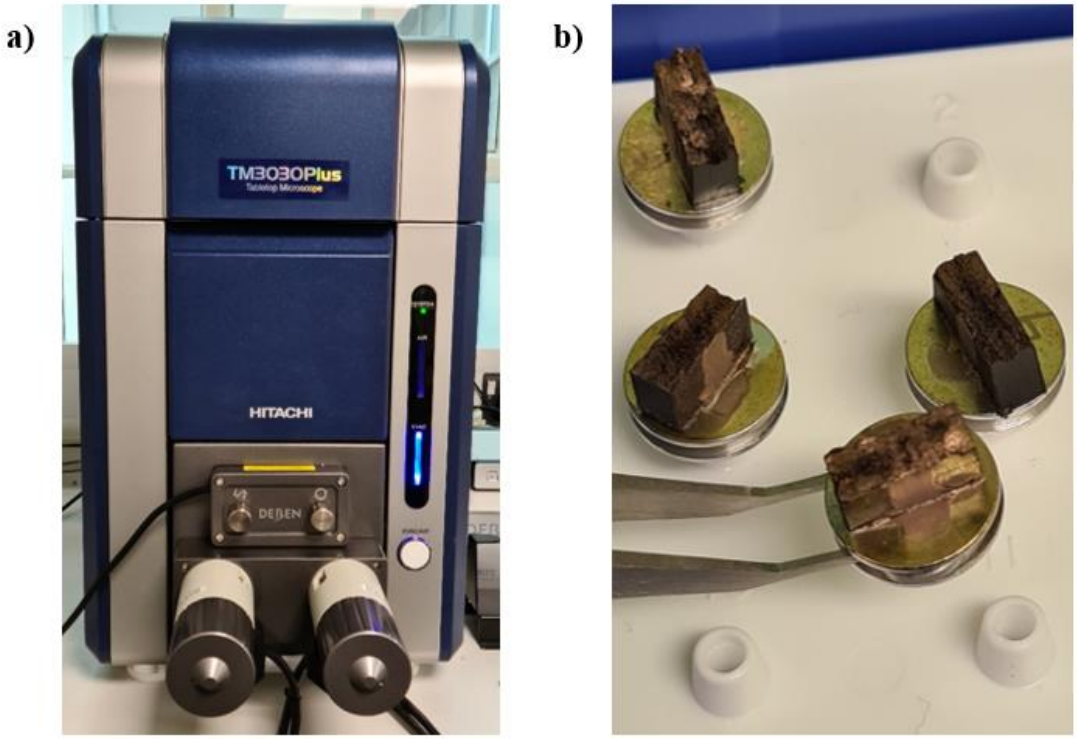

Figure 3-18 a) Tabletop SEM, b) example of SEM specimen

3.10 Conclusion

This chapter presented the experimental methodology followed to characterise the material properties of the PA66GF50 used for this study. To assess the influence of the fibre orientation distribution, specimens in three different orientations with respect to the injection flow were manufactured from plaques provided by the supplier. Tensile and fatigue tests at room temperature, 50 and 100° C, were conducted in an effort to understand the effect of temperature on the mechanical properties and damage mechanisms of the SFRP. A detailed description of the instrumentation equipment used to measure key data from the tests is given. It is also discussed the steps followed to apply state-of-the-art techniques such as Digital Image Correlation, Digital Volume Correlation and Scanning Electron Microscopy to analyse and investigate the damage process of the SFRP utilised in this research. Micro-computed tomography was employed to obtain the fibre orientation tensor and fibre length of the material, and a comprehensive description of the parameters used is provided. This technique was also utilised in specimens cyclically loaded to understand the failure mechanisms behind the fatigue failure.

4 MODELLING PROCEDURE

4.1 Introduction

This chapter describes the multi-stage methodology followed to carry out the tensile test simulations and fatigue life predictions. This methodology is summarised and depicted in Figure 4-1. It starts from the simulation of the injection moulding process to obtain the fibre orientation tensors in the specimen. Then those orientation tensors were transferred from the injection moulding mesh to the structural mesh. The material properties were computed using the constituent properties, an incremental Mori-Tanaka model and experimental tensile curves to calibrate and obtain the parameters of the model. Afterwards, the tensile test simulations were set up to replicate the experimental conditions. Finally, the fatigue life predictions were carried out using the results from stress analysis performed following the steps mentioned previously and the orientation tensors of each element.

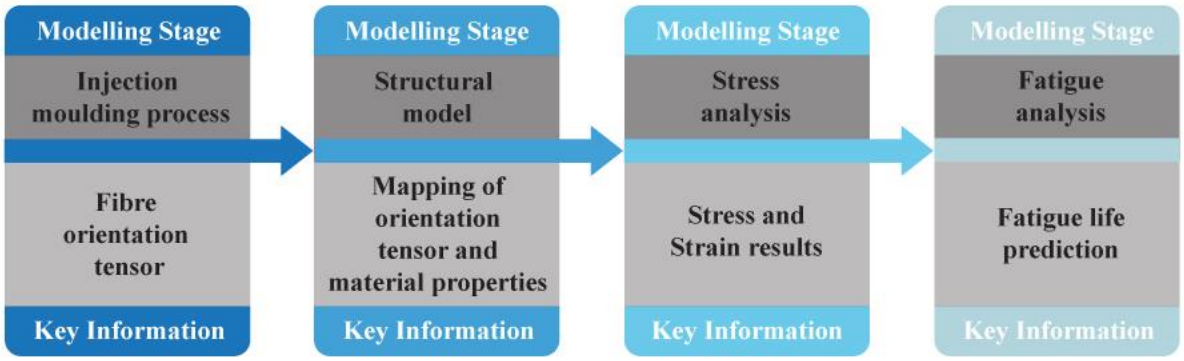

Figure 4-1 Modelling workflow

4.2 Injection moulding process simulation

As stated in Chapter 0, the manufacturing process has a substantial effect on the behaviour of the SFRPC. Because of this, it is necessary to start the modelling with the injection moulding process simulation. The major outcome of this simulation is the orientation tensor that will be used in the later stages of the modelling process.

A plaque of the same dimensions (150 x 150 x 4 mm), as the ones from where the specimens were manufactured, was modelled. A fan gate and runner were also modelled and the injection gate was located at the end of the runner. The model can be seen in Figure 4-2

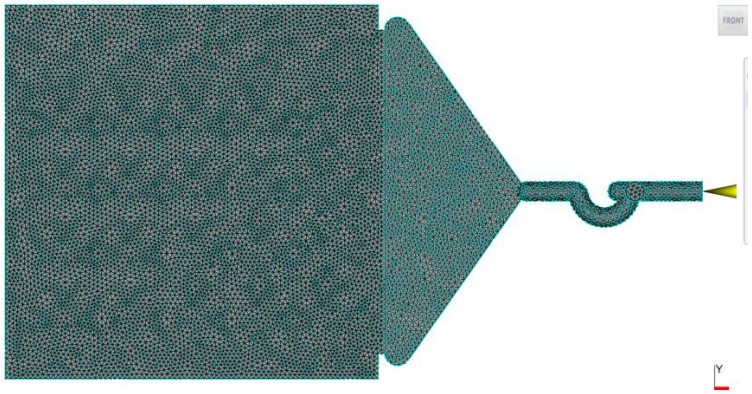

Figure 4-2 Model and mesh of the plaque for the injection moulding simulation

The software used for the simulation was Autodesk Moldflow Insight 2019 [81]. The parameters used in the analysis followed the manufacturing process. They were: melt temperature: 300°C, mould surface temperature: 85°C, injection time: 1.8 seconds, injection rate: 5,000 cm^3/s, maximum injection pressure: 180 MPa, packing pressure: 60% of the filling pressure and cooling time: 20 seconds.

The injection moulding simulation was done using a 3D mesh. A mesh independence study was carried out in terms of the orientation tensor component in the flow direction (a11). For simplicity for this mesh independence study, the Folgar-Tucker model [28] was chosen (see section 2.6), leaving the selection of the coefficient Ci automatic. Figure 4-3 shows the variation of the a11 component through the thickness at the location of the centre of the gauge length of the specimen.

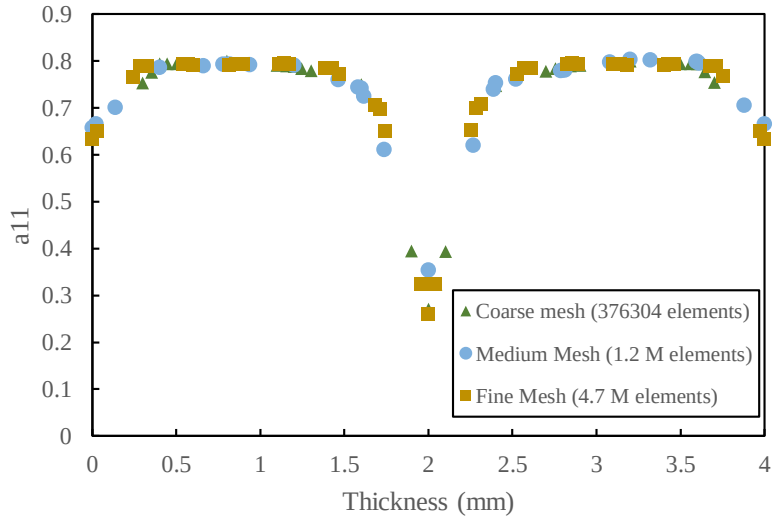

Figure 4-3 Comparison of the a11 component at the centre of the specimen's gauge length for different mesh densities

As can be seen, there is no significant difference between the results of the various mesh sizes. Similar results have been reported in the literature [30]. Thus for the sake of computational efficiency, the coarse mesh was chosen. This mesh comprised 376304 four-node solid tetrahedral elements, with 31 layers of elements across the thickness.

For the computing of the orientation tensor, the MRD model [38] was used. As seen in section 2.6, this model is currently the one that gives the most accurate estimations of the fibre orientation tensor. The coefficients Ci, D1, D2 and D3 were adjusted to best fit the orientation tensor obtained from the CT measurements shown in Figure 6-2.

The values of the coefficients Ci, D1, D2 and D3 are shown in Table 4-1

Table 4-1 Values of the coefficients of the MRD model

Coefficient	Value
Ci	0.004
D1	1
D2	0.05
D3	0.1

4.3 Simulation of the tensile tests

A model of the specimen with the dimensions shown in Figure 3-1 in Section 3.3 was created in Abaqus [82] to simulate the tensile tests.

The specimen model was meshed with an eight-node linear brick element with one integration point located in the centroid of the element (C3D8R). An hourglass control was set in Abaqus to mitigate the hourglass phenomenon that causes false element deformation.

To ensure accurate results a mesh independence study was conducted. The mesh was gradually refined towards the gauge length, and 31 elements through the thickness were used. This was done to have the same number of elements across the thickness of both models, the coupon model and the plaque model, and to prevent loss of information during the mapping of the orientation tensor. This procedure is described in section 4.3.2. The results of the mesh independence study can be seen in Figure 4-4.

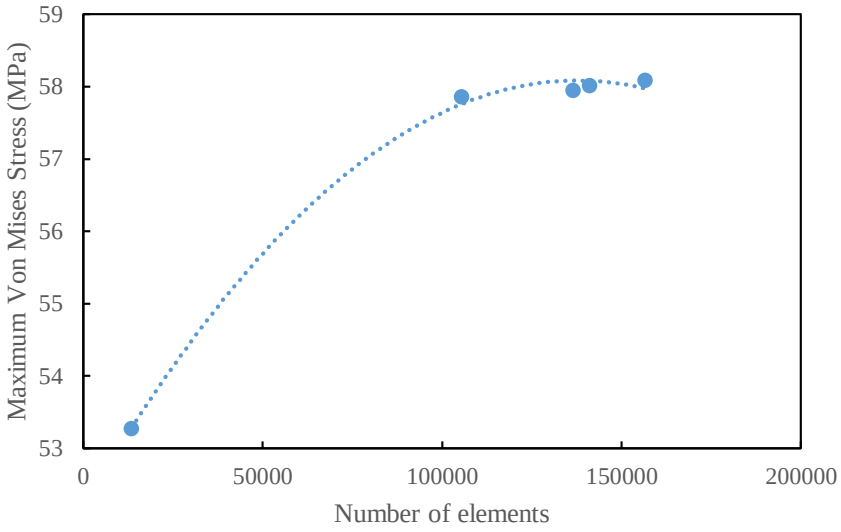

Figure 4-4 Mesh independence study conducted on the specimen model

The selected mesh had 136400 elements with a minimum size of 0.1 mm and a maximum size of 0.3 mm at the gauge length. The final mesh is shown in Figure 4-5.

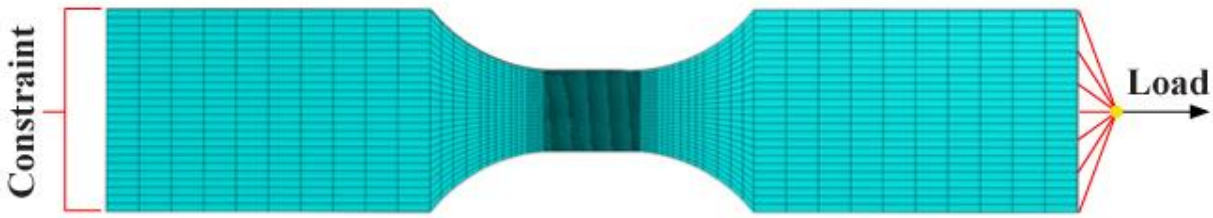

Figure 4-5 Mesh and boundary conditions for the stress analysis

4.3.1 Boundary conditions

After having the right mesh for the specimen model, the following step was to set the boundary conditions to simulate the tensile tests. These boundary conditions are illustrated in Figure 4-5. On one side of the specimen, all displacements were constrained, i.e. UX=UY=UZ=0. On the other side of the model, a reference point was created and connected to all the nodes on that end of the specimen through a kinematic coupling. The kinematic coupling constrains all the connected nodes to the rigid body motion of the reference point. On this reference point, a displacement was applied and transmitted uniformly to the specimen.

4.3.2 Mapping the orientation tensor

The key result from the injection moulding simulation was the orientation tensor at each node of the tetrahedral mesh. However, the orientation tensor does not remain constant along and across the plaque, nor through the thickness. Therefore, different fibre orientations will be observed in the specimens depending on where they were extracted from the plaque. Because of this, it is necessary to transfer the orientation tensors from the injection moulding simulation mesh to the structural mesh of the modelled specimen. This process was performed in the commercial software Helius PFA [83]. The procedure is as follows: First, the two meshes are superimposed. Then, the specimen's mesh is located where the specimens were cut from the plaque, as shown in Figure 4-6.

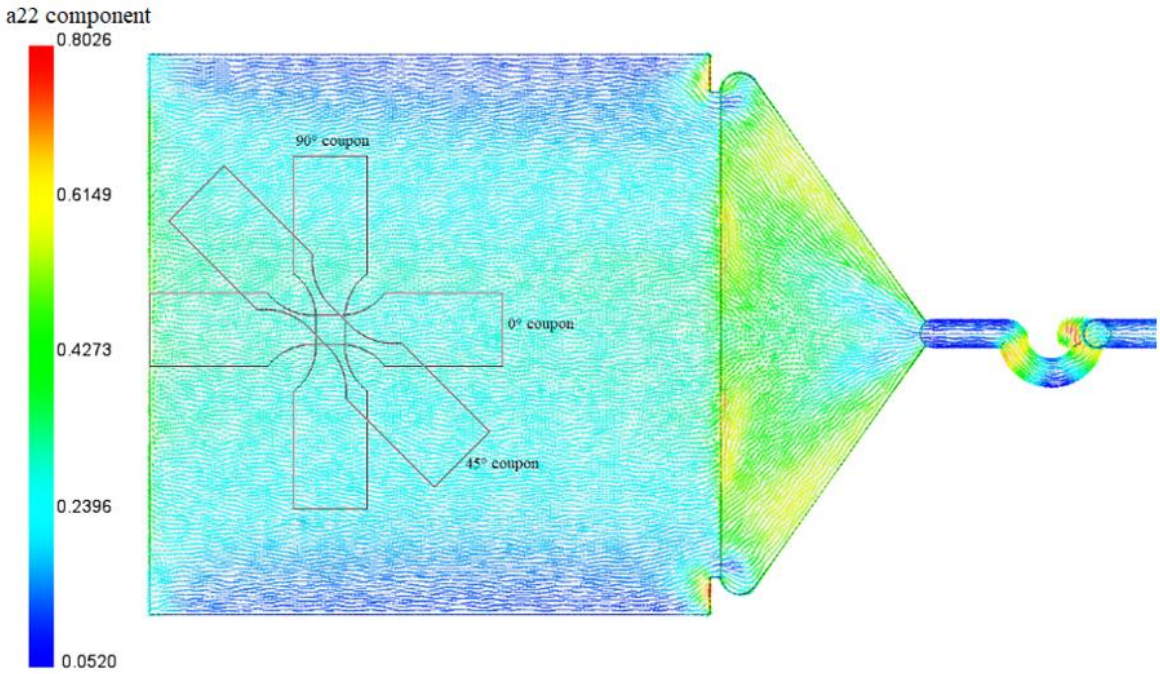

Figure 4-6 Superposition of the specimen at the manufacturing location in the plaque

The orientation tensors are then interpolated from the nodes of the plaque's mesh to the closest integration point of the specimen's mesh using the shape function of the tetrahedral elements [84]. Figure 4-7 is a schematic of the transfer of the fibre orientation tensor results from the mesh of the injection moulded plaque to the specimen's mesh.

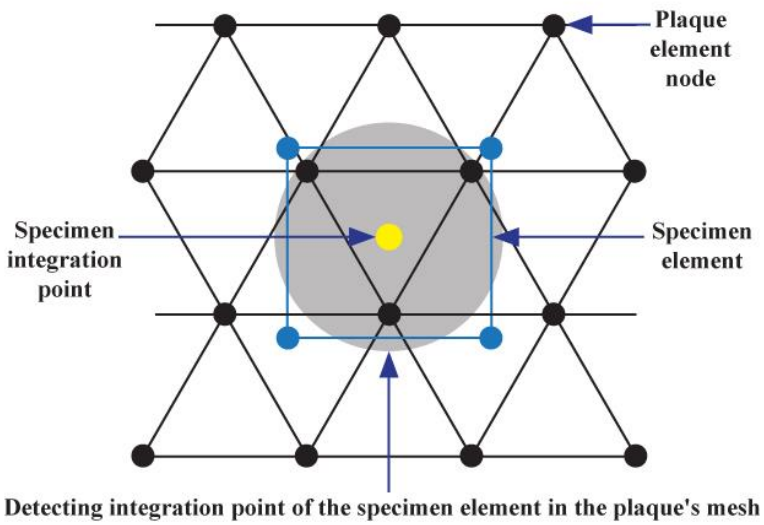

Figure 4-7 Visualisation of the superimposed meshes

4.3.3 Material properties

As seen in the literature review, there is a direct correlation between the material properties of the SFRP and the orientation of the fibres, and due to the injection moulding process, these fibre orientations are not constant across the model. Therefore, to achieve a better representation of the SFRP mechanical response is necessary to obtain the material properties at each element according to that local fibre orientation. This is done using homogenisation techniques which using the properties of the fibres and matrix, produce a material model of an equivalent homogeneous material that has an equal stiffness to the composite material under the same conditions.

In this study, the material properties were obtained with the aid of Helius PFA by means of an incremental Mori-Tanaka model [85-87] that can accommodate evolving matrix properties. A schematic of the entire process to obtain the material properties is shown in Figure 4-8. This incremental Mori-Tanaka model is based on the Mori-Tanaka (M-T) model [85] and the interpretation of this model given by Benveniste [86], which states that each inclusion behaves as an isolated particle in the matrix, simplifying the problem to the Eshelby's single inclusion model [87]. First, this model produces the material properties for an idealised material with the fibres perfectly aligned. Then the properties of the unidirectional material are averaged over all directions weighted by the orientation distribution function. This procedure is called fibre orientation averaging [24].

Once the homogenised material properties are obtained, the strain increment in the composite is calculated by FEA, and a process named decomposition takes place. The decomposition process is based on the work by Nguyen et al. [88, 89], and it consists of decomposing the strain of the composite into the fibre and matrix strains. The matrix strain is then applied to a Ramberg-Osgood model [90] to describe the nonlinear behaviour of the matrix. This approach considers the following assumptions and limitations:

- The fibres only present a linear elastic behaviour
- The matrix exhibits plasticity and rupture
- The idealised model's matrix plasticity is intended to account for any fibre/matrix debonding
- All nonlinear behaviour of the composite material is due to the matrix
- The plasticity of the matrix is driven by the stress in the matrix only, not in the homogenised composite material
- The plasticity of the matrix is strongly dependent on the alignment of the fibres

An in-depth mathematical description of the Ramberg-Osgood model implementation can be found in [88, 89, 91]. A summary is presented here:

The effective hardened yield strength of the matrix is calculated using the following:

$$\sigma_Y^h\left(\varepsilon_{p.eff}\right) = E_m^{1/n}(\sigma_0)^{(n-1)/n}\left(\varepsilon_{p.eff}\right)^{1/n} \quad \textbf{(4-1)}$$

Where σ_0 and n are the reference stress and power-law exponent of the Ramberg-Osgood model, E_m is the Young's modulus of the matrix, and $\varepsilon_{p.eff}$ represents the effective plastic strain in the matrix.

The yield function is satisfied when:

$$f\left(\varepsilon_{p.eff}\right) = \sigma_{eff}\left(\varepsilon_{p.eff}\right) - \sigma_Y^h\left(\varepsilon_{p.eff}\right) = 0 \quad \textbf{(4-2)}$$

Where σ_{eff} is the Von Mises stress, which is calculated as:

$$\sigma_{eff} = \sqrt{\frac{(\alpha\sigma_{11} - \beta\sigma_{22})^2 + (\beta\sigma_{22} - \beta\sigma_{33})^2 + (\beta\sigma_{33} - \alpha\sigma_{11})^2 + 6\left[(\sigma_{12})^2 + (\sigma_{23})^2 + (\sigma_{31})^2\right]}{2}} \quad \textbf{(4-3)}$$

Where the stress components are the average stress in the matrix, α and β are weighting coefficients that are linear functions of the degree of fibre alignment, quantified by the largest eigenvalue of the orientation tensor (λ_I). These coefficients are given by:

$$\alpha(\lambda_I) = \theta + \left(\frac{\alpha_m - \theta}{\lambda_{m,I} - 1/2}\right)(\lambda_I - 1/2) \quad \textbf{(4-4)}$$

$$\beta(\lambda_I) = \theta + \left(\frac{\beta_m - \theta}{\lambda_{m,I} - 1/2}\right)(\lambda_I - 1/2) \quad \textbf{(4-5)}$$

The values of α_m and β_m are the optimised values of α and β to fit the response of a highly aligned material that has the largest fibre orientation eigenvalue ($\lambda_{m,I}$)

Effective stress is also a function of the $\varepsilon_{p.eff}$ in that instantaneous tangent modulus ($E_{\tan}$) of the matrix:

$$E_{\tan} = \frac{E_m E_m^p}{E_m + E_m^p} \quad \textbf{(4-6)}$$

Where E_m^p is the plastic modulus and is determined as:

$$E_m^p = \frac{d\bar{\sigma}_m}{d\bar{\varepsilon}_m^p} = \frac{E_m^{1/n}(\sigma_0)^{(n-1)/n}\left(\varepsilon_{p.eff}\right)^{(1-n)/n}}{n} \quad \textbf{(4-7)}$$

Thus, the determination of $E_{\tan}$is reduced to solving equation (4-2) iteratively for $\varepsilon_{p.eff}$ using equations (4-6) and (4-7).

The computation of $E_{\tan}$ allows the estimation of the matrix tangent stiffness tensor and, therefore, the tangent stiffness tensor of the composite throughout the homogenisation process.

4.3.4 Material characterisation for the simulation of tensile tests at room temperature, 50 and 100 Celsius degrees

The simulations of the tensile tests were carried out following the procedure previously described starting from the injection moulding simulation. The material model detailed in section 4.3.3 is fitted to a collection of experimental data to determine the Young's and shear modulus of the matrix and fibre, and the four plastic coefficients σ_0, n, α and β needed to compute the material properties. According to [88, 92], a good fit can be achieved using three different experimental tensile test curves.

Experimental curves of 0°, 45° and 90° coupons were used for fitting the model. These curves are shown in Figure 5-1 and were obtained as explained in chapter 3.

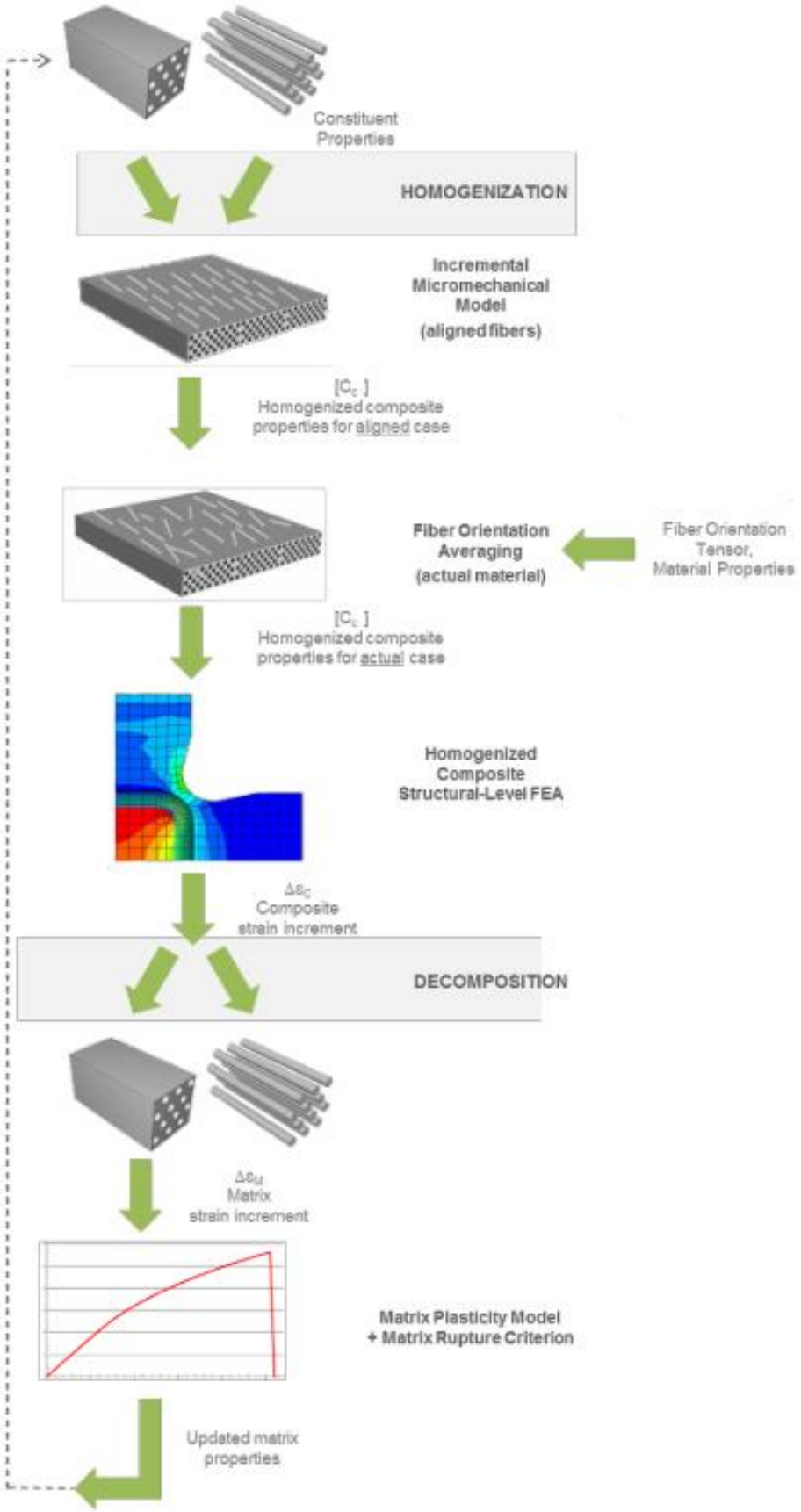

Figure 4-8 Schematic of the process to obtain the material properties [84]

4.4 Fatigue life prediction

The fatigue life prediction was carried out following the methodology presented in Figure 4-9 and implemented in Python. In the Appendix in Figure A-2 a more detail diagram of the workflow is presented.

A similar methodology for fatigue life prediction has been followed by several researchers [22, 93-96] and commercial software such as HBM nCode [97] and FEMFAT [97]

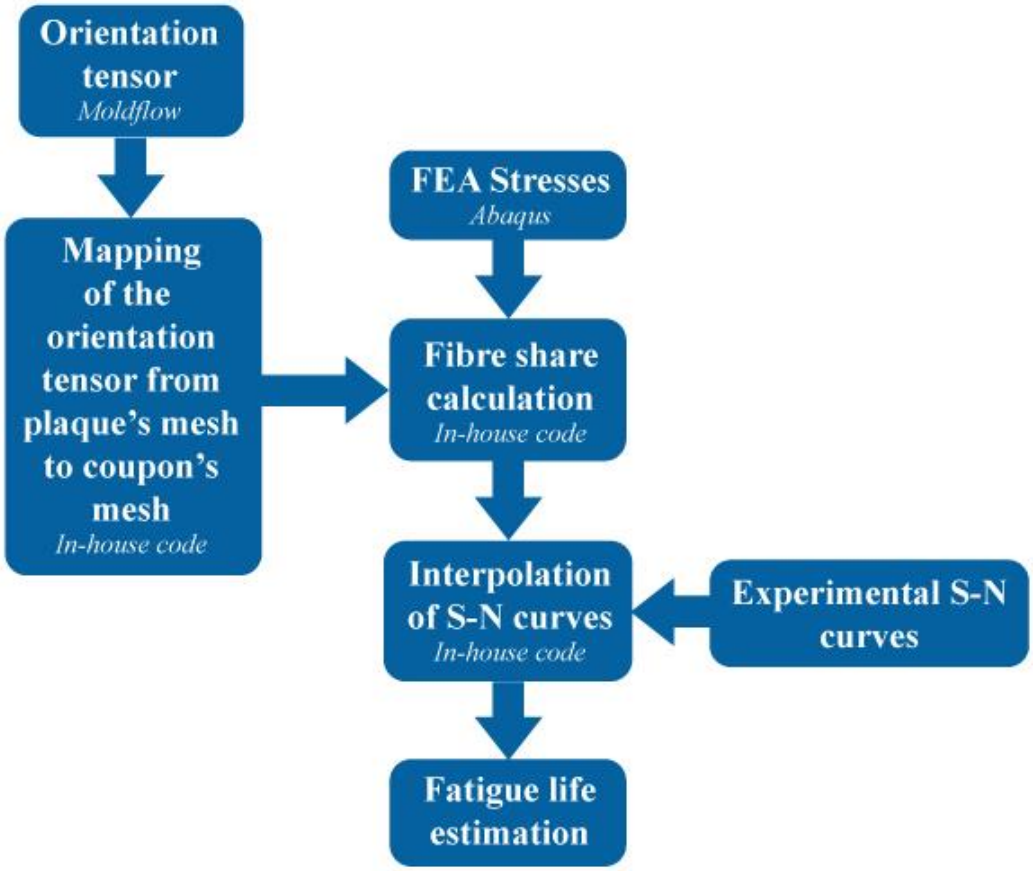

Figure 4-9 Diagram of the workflow and software used for the fatigue life estimation

First, stress analyses were conducted for coupons of the three orientations using the exact same modelled specimen shown in Figure 4-5 that was used for the simulation of the tensile tests. The boundary conditions were similar to the ones explained in section 4.3.1 with the only difference being that a force was applied instead of a displacement. The applied loads were the maximum force utilised in the experimental tests. For instance, for the 0° specimen at room temperature the force used was 3.2 KN. The material properties were obtained as described in sections 4.3.3 and 4.3.4 using the orientation tensors from the simulation of the injection moulding and the modified Ramber-Osgood model.

After conducting a stress analysis, the stress tensor at each element integration point is obtained. With the aid of the orientation tensor of each element, the fibre share is estimated (λ). This λ describes the portion of fibre aligned to the loading direction, and it is calculated as:

$$\lambda = l\alpha l^T \quad \textbf{(4-8)}$$

Where:

l: Absolute maximum principal stress direction

α: Orientation tensor

Due to the incapability to retrieve the orientation tensor of each element from Helius PFA, the transfer of the orientation tensor from the nodes of the injection moulding mesh to the structural mesh was also done separately in a python script. A diagram of the workflow followed for this process is presented in Figure A-1 in the Appedix. First, the node coordinates and element connectivity were extracted from Abaqus and Moldflow. Then the Abaqus node coordinates were translated and rotated to the position where the specimens were cut in the plaque. Afterwards, the element connectivity information helped to know which nodes compose each element and therefore compute the location of the integration points. Knowing the integration points coordinates of each mesh, the closest integration point between meshes was determined to identify from which element the orientation tensor has to be interpolated to the structural integration point.

Helius PFA can provide the eigenvalues of the orientation tensors, which were used to check the accuracy of the interpolated orientation tensors. Figure 4-10 shows the comparison of the first, second and third eigenvalues of the orientation tensors interpolated using Helius PFA and with the python script. For this comparison, only the elements in the gauge length were considered. As can be seen, there is a maximum discrepancy of 0.83% for the first eigenvalue. For the second eigenvalue, a maximum difference of 2.95%, and for the third eigenvalue, 3.86%.

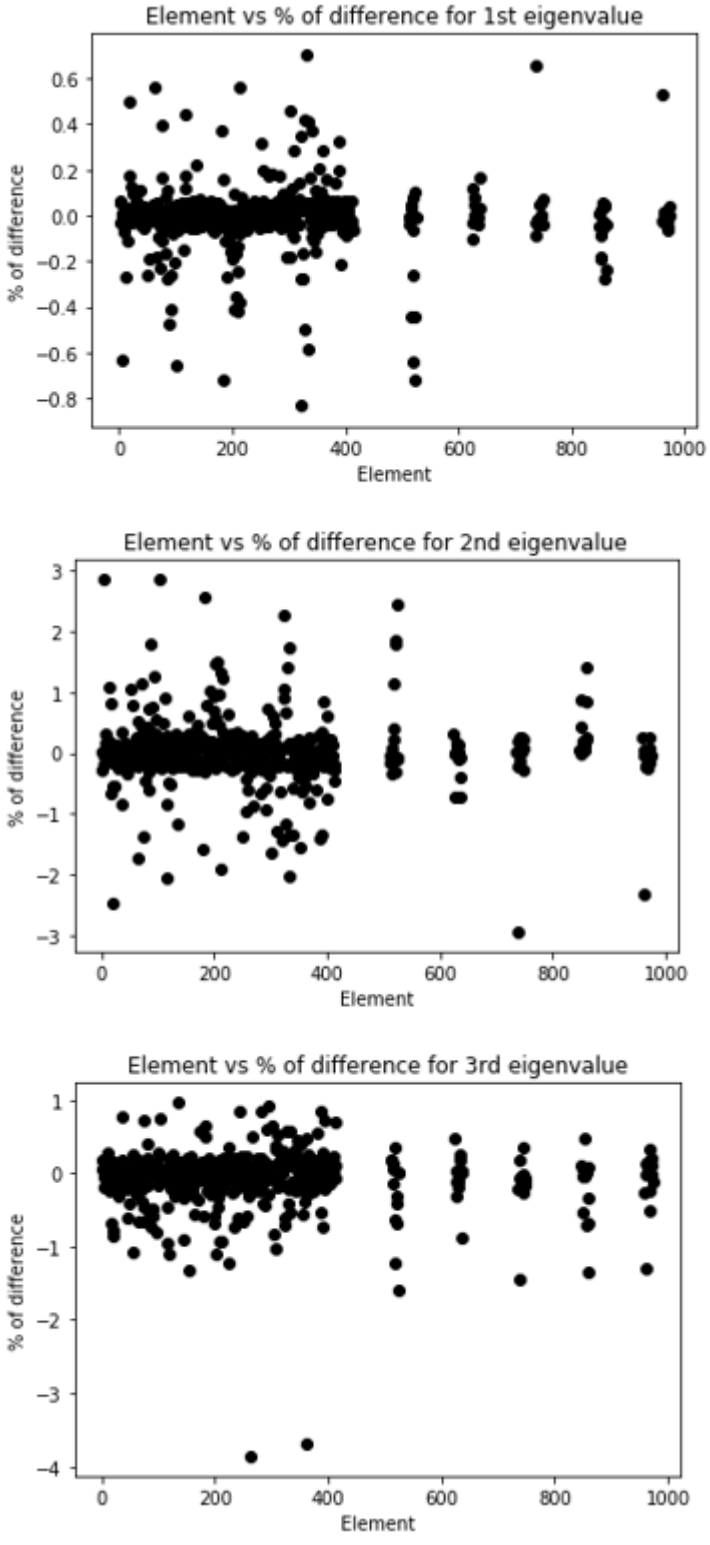

Figure 4-10 Comparison of interpolated orientation tensor eigenvalues and Helius PFA eigenvalues

These interpolated orientation tensors were introduced in equation (4-8) to obtain λ for the 0°, 45°, and 90° samples. Because each element has a different fibre orientation tensor, the stress distribution is not uniform through the gauge length, resulting in a different λ at each element.

However, the stress used to plot the experimental S-N curves was the engineering stress, i.e. force divided by the cross-section area, considering it homogeneous through the gauge length. Contrary to what has been seen in the FEA results, where at the same applied force, the stress variation is not uniform due to the effect of the fibres. Thus, in order to be consistent with this consideration, the fibre share of all elements in the gauge length of the specimens was averaged to obtain one λ for each specimen.

Then to predict the S-N curve for the 45° coupon, an interpolation factor was computed using the following equation:

$$I = \frac{\lambda - f1}{f2 - f1} \quad \textbf{(4-9)}$$

Where:

I: Interpolation factor

λ: Fibre share of the 45° specimen

$f1$: Fibre share of the 0° specimen

$f2$: Fibre share of the 90° specimen

The first point of the local S-N curves was computed using [99] :

$$SRI1_{calc} = UTS1_1 + (UTS1_2 - UTS1_1) \times I \quad \textbf{(4-10)}$$

Where:

$SRI1_{calc}$: Stress for cycle 1 of the predicted S-N curve

$UTS1_1$; Ultimate tensile stress of the 0° specimen

$UTS1_2$: Ultimate tensile stress of the 90° specimen

Then the next point of the S-N curve was computed through the following equations:

$$S1_{calc} = S1_1 + (S1_2 - S1_1) \times I \quad \textbf{(4-11)}$$

Where:

$S1_{calc}$: Stress at the second point of the predicted S-N curve

$S1_1$: Stress at an arbitrary point of the S-N curve for a 0° specimen

$S1_2$: Stress at an arbitrary point of the S-N curve for a 90° specimen

The interpolation/extrapolation process is shown in Figure 4-11

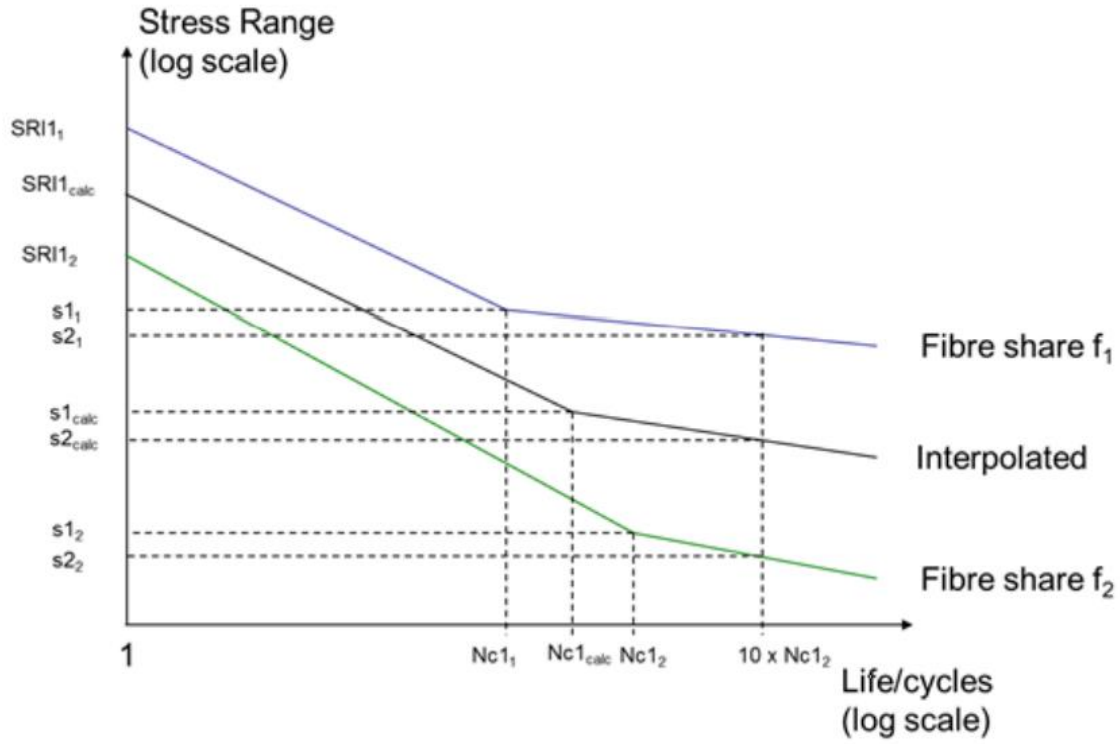

Figure 4-11 Interpolation/extrapolation of S-N curves [97]

Once the two points of the S-N were determined, they were plotted in a log-log plot, where the Basquin's equation that describes the predicted S-N curve was obtained using a linear regression.

4.5 Conclusion

This chapter presented the multi-stage methodology followed in this study. First, a mesh independence study was carried out to ensure the accuracy of the injection moulding simulation and structural analysis. The injection moulding simulation was validated by comparing the experimental CT measurements to the results obtained from the fitted MRD model. Third, the procedure to conduct the simulation of the tensile tests and to obtain the material properties was exhaustively documented. A detailed description of the steps to perform the fatigue life predictions is presented, showing the solution proposed to solve the inability to extract the orientation tensor from Helius PFA.

5 MECHANICAL TESTING RESULTS

5.1 Tensile tests

Tensile tests were carried out on specimens cut at different orientations from a plaque, as shown in Figure 3-2. These tensile tests were conducted at room temperature, 50 and 100° C. Specifics of the tensile tests are described in sections 3.4 and 3.5.

Figure 5-1 presents the Stress-Strain curves obtained at the three tested temperatures. The engineering strain was determined using DIC and a virtual extensometer inside the VIC 2D software used to process the DIC images.

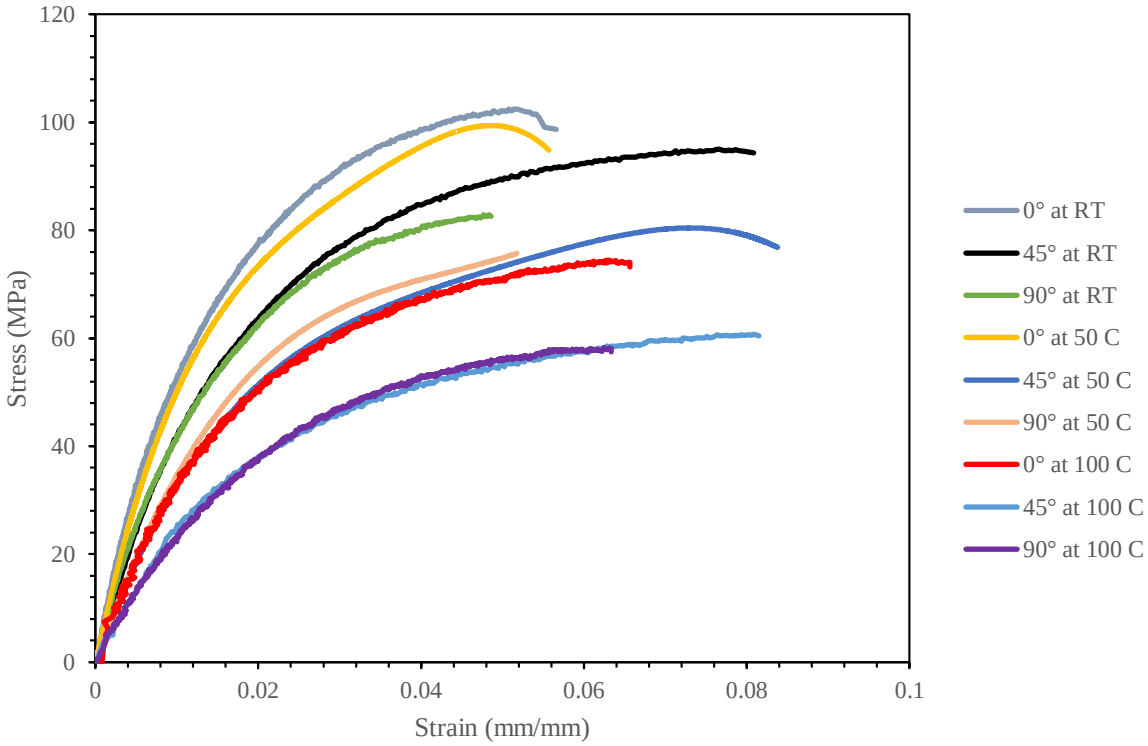

Figure 5-1 Stress-Strain curves at different temperatures

Figure 5-1 shows that, regardless of the testing temperature, all specimens exhibit non-linear behaviour. As expected, the samples tested at room temperature presented the highest strength. Results show that the highest recorded UTS value is for the 0° coupons, with an average of 102.47 MPa. The detrimental effect of temperature is also noticeable; as the temperature increases, the strength decreases. The 45° and 90° specimens tested at 100°C showed the lowest UTS, 60.734 MPa and 58.25 MPa, respectively. On the other hand, material ductility seemed to increase with the temperature, with 45° samples presenting the

highest strain at failure at any temperature. The specimens tested at 100° C experienced the highest deformation before failure.

Notably, the 45° and 90° specimens lay close to each other at the three temperatures, suggesting a significant influence of the matrix on the material's mechanical response at these orientations.

Figure 5-2a-c presents the interval plots at 95% of confidence of the mean value of Young's modulus, ultimate tensile strength (UTS) and the strain at break for different orientations and temperatures.

As mentioned before, Young's modulus was computed using the chord modulus method established in ASTM D3039/3039M–17 [97]. Analysing Figure 5-2a, the beneficial effect of fibre alignment is observed, as the 0° specimens showed the highest mean Young's modulus value. On the other hand, the 45° coupons exhibited the lowest average value. This was observed at all temperatures tested. At room temperature, the mean value of Young's modulus of the 90° specimens (E = 4958 MPa) was almost identical to the 45° specimens (E = 4923 MPa). However, at 50 and 100° C, the 90° specimens showed a higher average value, 342 MPa more at 50° C and 416 MPa at 100° C. The effect of temperature was also evident. As the temperature increased, the average value decreased. This temperature effect was true except for the 0° specimens tested at room temperature and 50° C, which presented a similar Young's modulus value.

Observing Figure 5-2b, the effect of fibre orientation and temperature on the UTS is also visible. Specimens tested at 50 and 100° C showed a lower average UTS, excluding the 0° coupons at 50° C, which exhibited a similar UTS to the 0° samples at room temperature. The specimens oriented at 0° presented a higher UTS than the other orientations but showed the lowest strain at break, as can be seen in Figure 5-2c, while the 45° and 90° coupons had a similar UTS. Figure 5-2c shows that the 45° specimens presented the highest deformation at failure. The temperature does not seem to have an enormous influence on the strain at break for the 0° and 90° samples. However, for the 45° specimens, the strain at break incremented as the temperature increased, especially at 100° C.

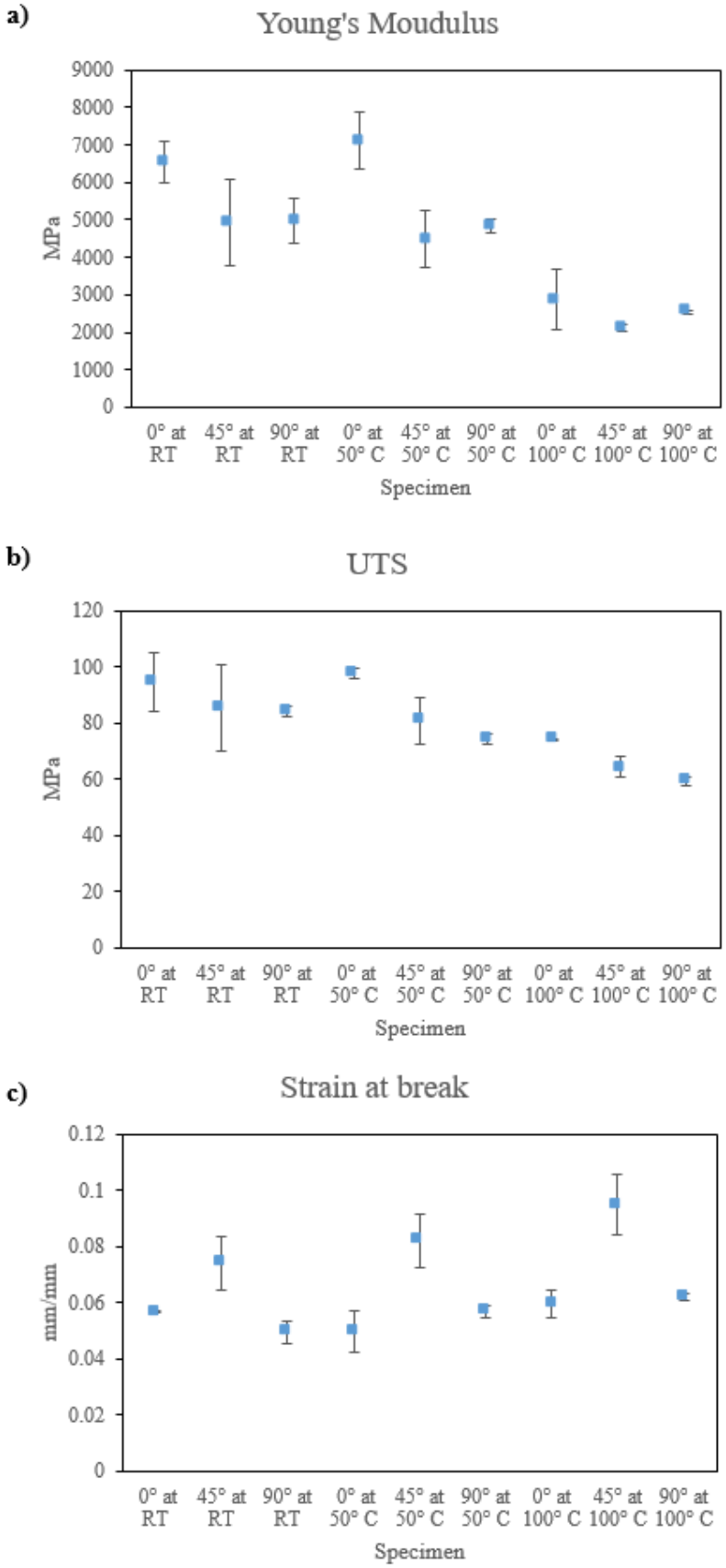

Figure 5-2 Interval plots for specimens at different orientations and temperatures using a 95% confidence interval. a) Young's modulus, b) Ultimate tensile strength (UTS), c) Strain at break

5.1.1 Full-field strain measurements

As explained before, DIC was employed during the tensile tests to analyse the strain distribution on the surface of the specimens. The technique was used on samples of the three orientations and at all temperatures investigated in this study. The resolution of the DIC measurements was between 0.1695 and 0.1792 μm and computed using the following formula given in [97]:

$$\beta_0 = \frac{L}{N}\beta_1 \quad \textbf{(5-1)}$$

Where:

β_0 is the displacement resolution

L stands for the field of view (m^2)

N represents the recording resolution of the camera (pixels)

β_1 is the image displacement accuracy required (pixels). In this case, it was 0.01 pixel

5.1.1.1 Specimens tested at room temperature

Figure 5-3 illustrates the strain distribution before failure on the surface of a 0° specimen tested at room temperature. The highest strain was located at the tip of a crack that started from the edge of the coupon and oriented perpendicular to the load direction. These cracks are difficult to capture due to the fast failure. The strain distribution on the gauge length of the specimen seems to be homogenous, with some strain concentration close to the top left shoulder and the bottom right one. The failure plane of this specimen was at the location of the crack and looked like it started from it.

The strain distribution on the surface of a 45° specimen is shown in Figure 5-4. The highest strain values were seen at this orientation, even higher than at the crack tip of the 0° specimen. For this specimen orientation, the strain distribution at the gauge length appears to be at an angle of 45°, with the highest strain located at the centre.

Finally, Figure 5-5 presents the strain field on the surface of a 90° specimen prior to failure. For the case of this orientation, the strain developed transversal to the loading direction at the middle of the specimen's gauge length. This strain localisation coincided with the location where the specimen failed.

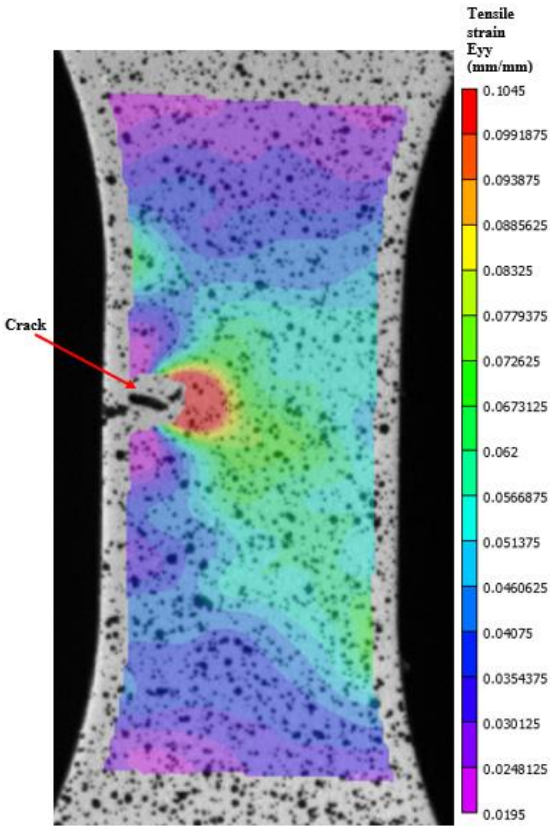

Figure 5-3 Strain distribution before failure on the front surface for a 0° specimen loaded in tension

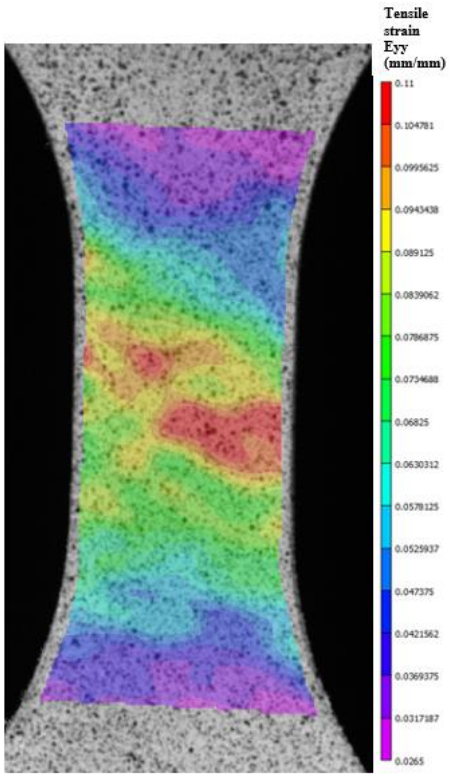

Figure 5-4 Strain distribution before failure on the front surface for a 45° specimen loaded in tension

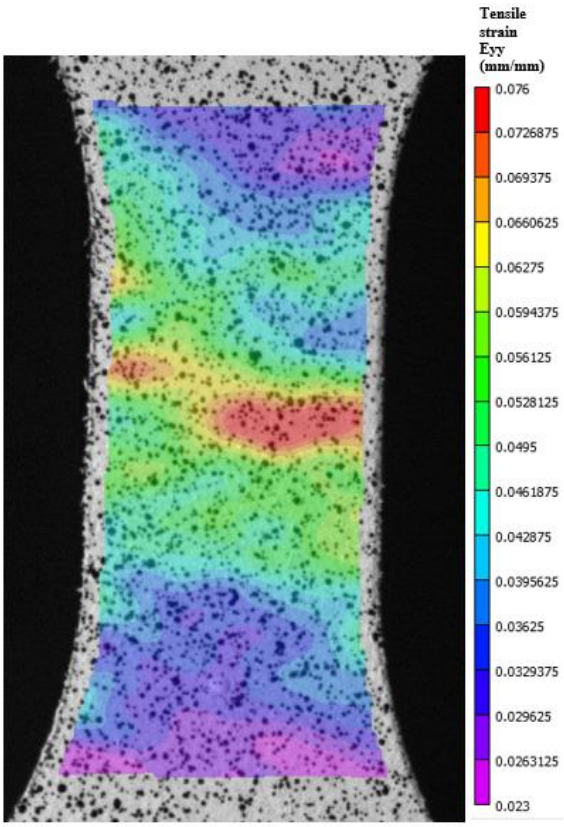

Figure 5-5 Strain distribution before failure on the front surface for a 90° specimen loaded in tension

5.1.1.2 Specimens tested at 50° C

The strain distribution on the front and thickness surface of 0° specimens tested at 50° C is depicted in Figure 5-6a-b. Inspecting Figure 5-6a shows that the strain presents a strain localisation near the end of the specimen's gauge length and a crack starting from the edge at an angle of ~45°. Figure 5-6b shows the lateral view of another 0° specimen tested at the same temperature. Here, strain concentrations are also observed nearby the end of the gauge length in the shell region, where, for this orientation, the fibres are aligned with the load direction. In addition, the maximum strain values are 10% higher along the thickness than on the front surface.

Figure 5-7a shows the strain distribution on the front face of a 45° specimen before failure. A strain concentration at an angle of ~45° is evident at the centre of the gauge length, and a crack following the strain concentration starting from the edge is also observable. This crack started from the edge and went across the whole width of the gauge length of the specimen. In Figure 5-7b, another crack starting again from the edge of the specimen can be noticed.

Again, the crack seems to follow the angled strain localisation. Similar to the 0° specimen, the maximum strain on the thickness surface is higher than the maximum strain on the front. But this time 44% higher. Even though the crack seen in Figure 5-7a went through the entire specimen width, the failure plane did not correspond to the full crack length, as noticed in Figure 5-7c. The fracture plane changed its direction perpendicular to the load. This change of direction coincides with the end of the high strain concentration observed in Figure 5-7a.

The strain distribution on the front surface of a 90° specimen is illustrated in Figure 5-8a. This specimen also exhibited a crack starting from the edge. In this case, the highest strain was not located at the crack tip but close to the shoulder of the specimen where the failure occurred with no evident crack, as illustrated in Figure 5-8c. Another 90° specimen was analysed at the thickness, see Figure 5-8b. Three strain concentrations are distinguishable, two at the centre of the end of the gauge length and one at the middle of it. For this orientation, the thickness strain was lower than the strain on the front surface.

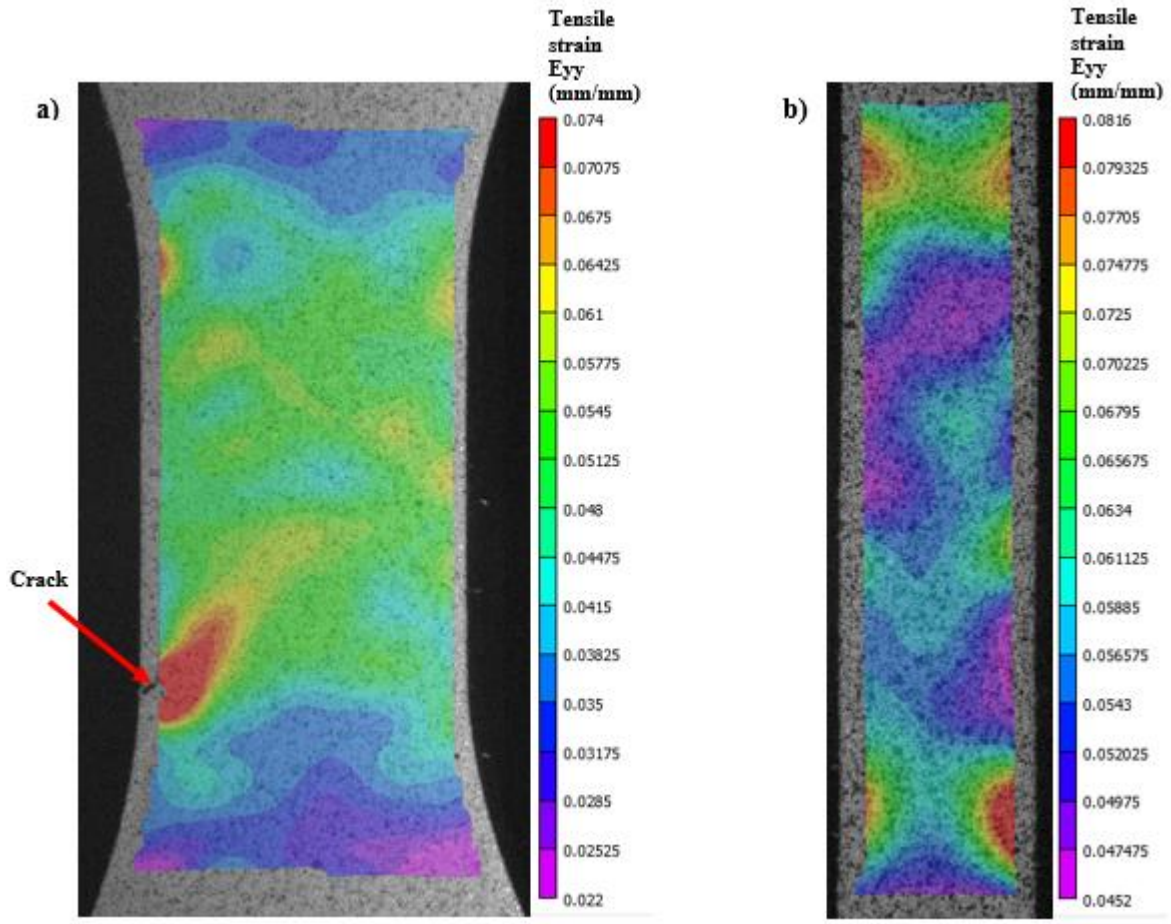

Figure 5-6 Strain in the loading direction before final failure for a 0° specimen at 50° C. a) front view, b) lateral view

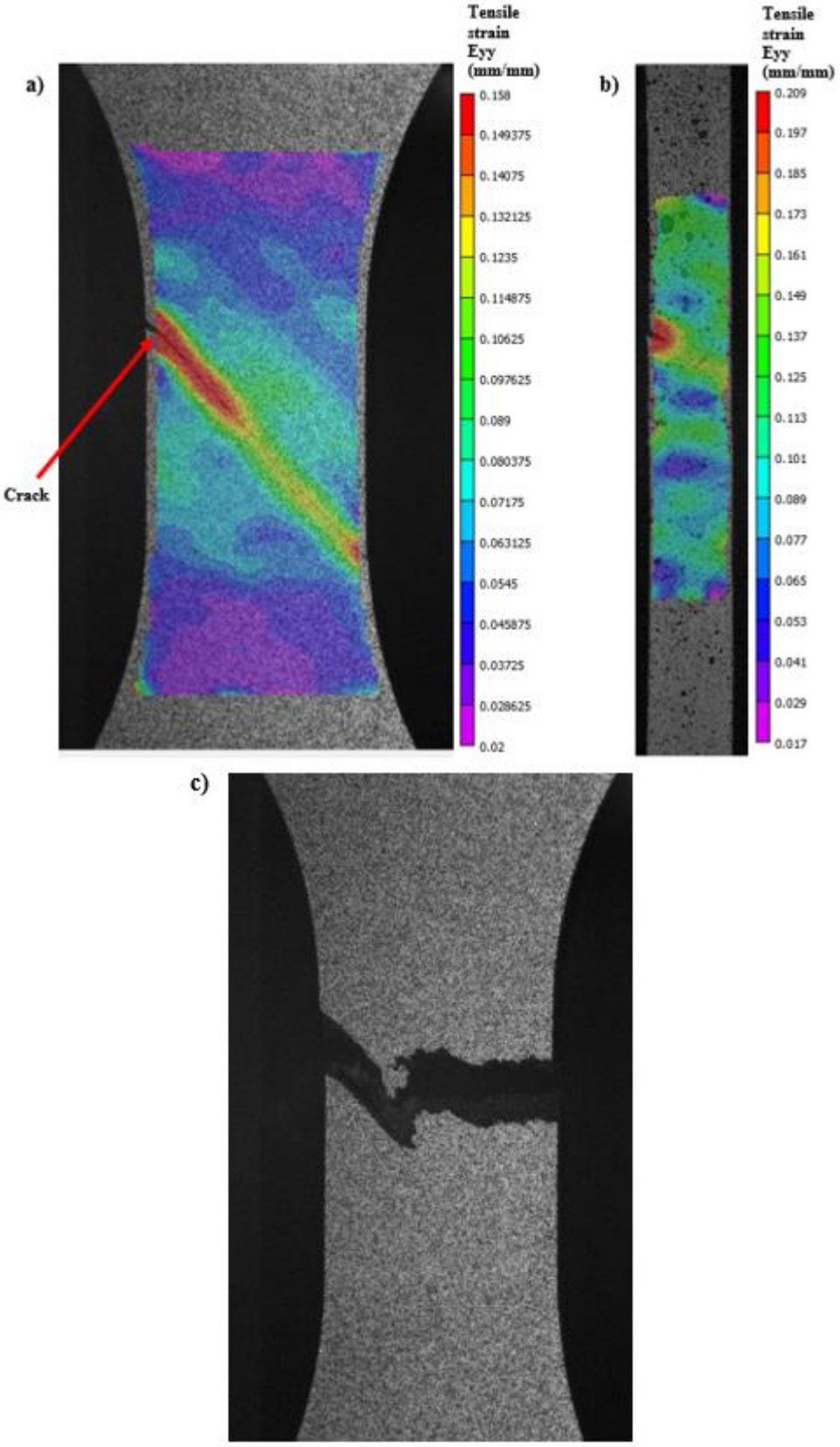

Figure 5-7 Strain in the loading direction before final failure for a 45° specimen at 50° C. a) front view, b) lateral view, c) fractured specimen showed in a)

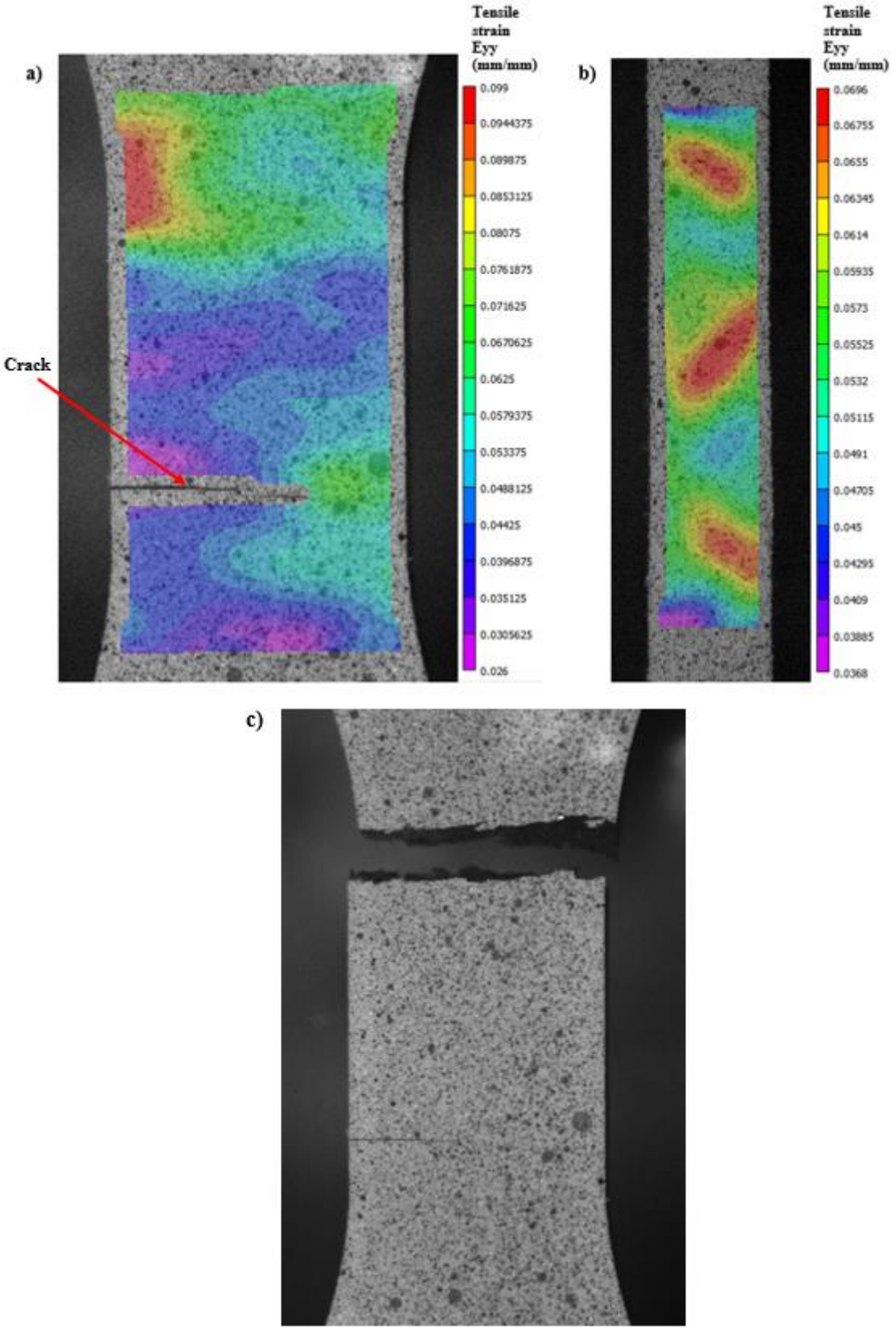

Figure 5-8 Strain in the loading direction before final failure for a 90° specimen at 50° C. a) front view, b) lateral view, c) fractured specimen showed in a)

5.1.1.3 Specimens tested at 100° C

Figure 5-9a presents the strain distribution before failure on the front surface of a 0° specimen. Three cracks can be observed at the bottom of the gauge length. Two of these cracks started from the edge, and the other is located close to the middle of the width. These cracks seem to be independent before merging to cause the failure of the specimen at that location. A different specimen was used to analyse the strain on the thickness, Figure 5-9b. In this specimen, two high strain concentrations can be seen at the bottom part of the gauge length and two slightly lower at the top. These four strain localisations were in the shell region, similar to the 0° specimen tested at 50° C, shown in Figure 5-8b. The maximum strain values along the thickness were higher than those at the front surface.

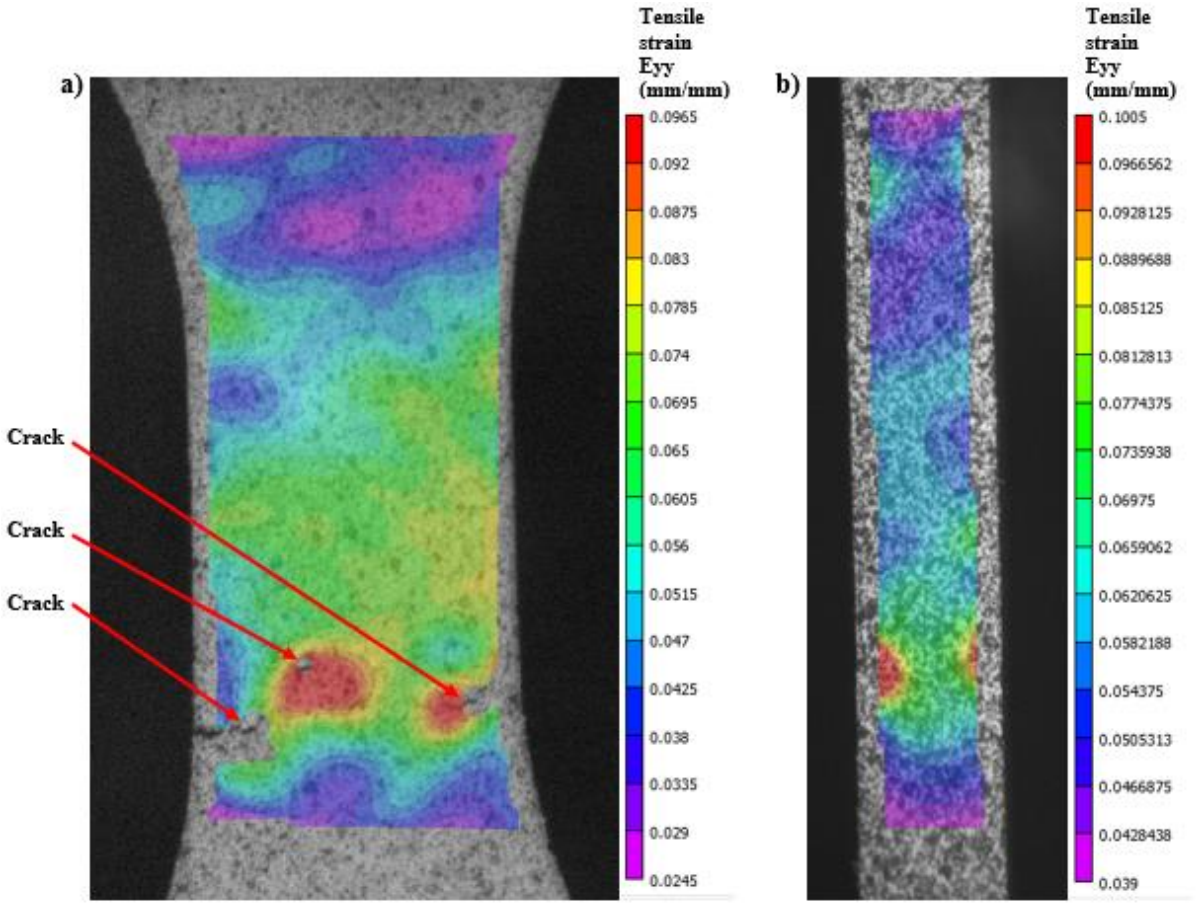

Figure 5-9 Strain in the loading direction before final failure for a 0° specimen at 100° C. a) front view, b) lateral view

Figure 5-10a shows the strain distribution on a 45° specimen's front face before failure. Similar to the other 45° specimens tested at room and 50° C temperatures, the strain concentration on the front surface was at an angle of ~45°. The strain field on the thickness

surface measured on a different 45° specimen, shown in Figure 5-10b, reveals a strain concentration at an angle of ~45° close to the centre of the gauge length. Even though the strain concentration in Figure 5-10a was at an angle of ~45°, the fracture plane of the same specimen, illustrated in Figure 5-10c, was perpendicular to the loading direction.

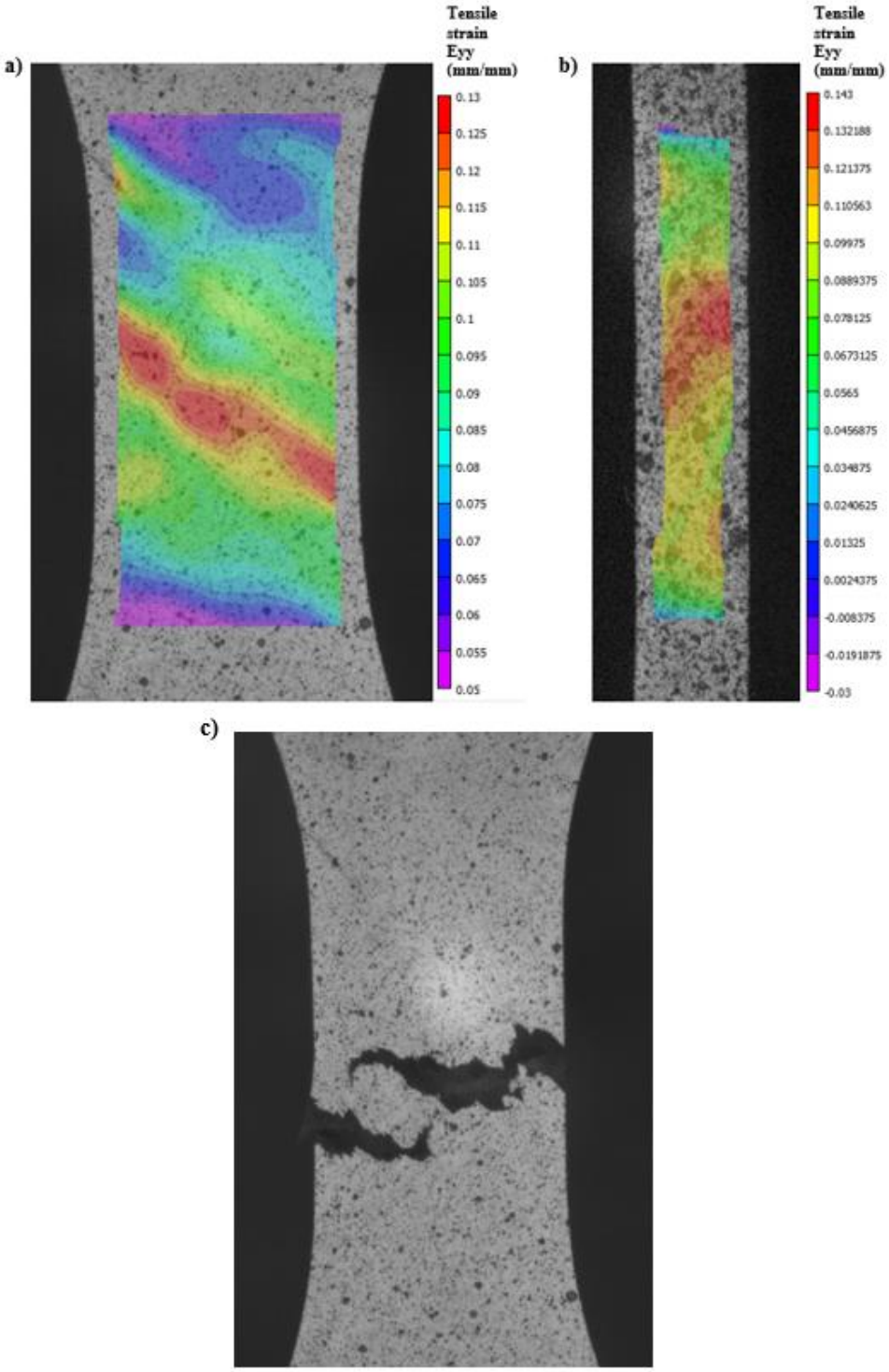

Figure 5-10 Strain in the loading direction before final failure for a 45° specimen at 100° C. a) front view, b) lateral view, c) fractured specimen showed in a)

The strain distribution on the front surface of a 90° specimen is depicted in Figure 5-11a. The highest strain on this specimen seems to be transversal to the load direction and located in the middle of the gauge length. Figure 5-11b presents the strain distribution before failure on the thickness surface of a separate 90° specimen. Two strain localisation occurred at the shoulders of the specimen at the core region where the fibres are aligned to the loading direction, resembling what was observed in the 90° specimen at 50° C (see Figure 5-8b). Inspecting the strain values of the front and thickness surfaces, one can observe that the highest strain values are very close to each other.

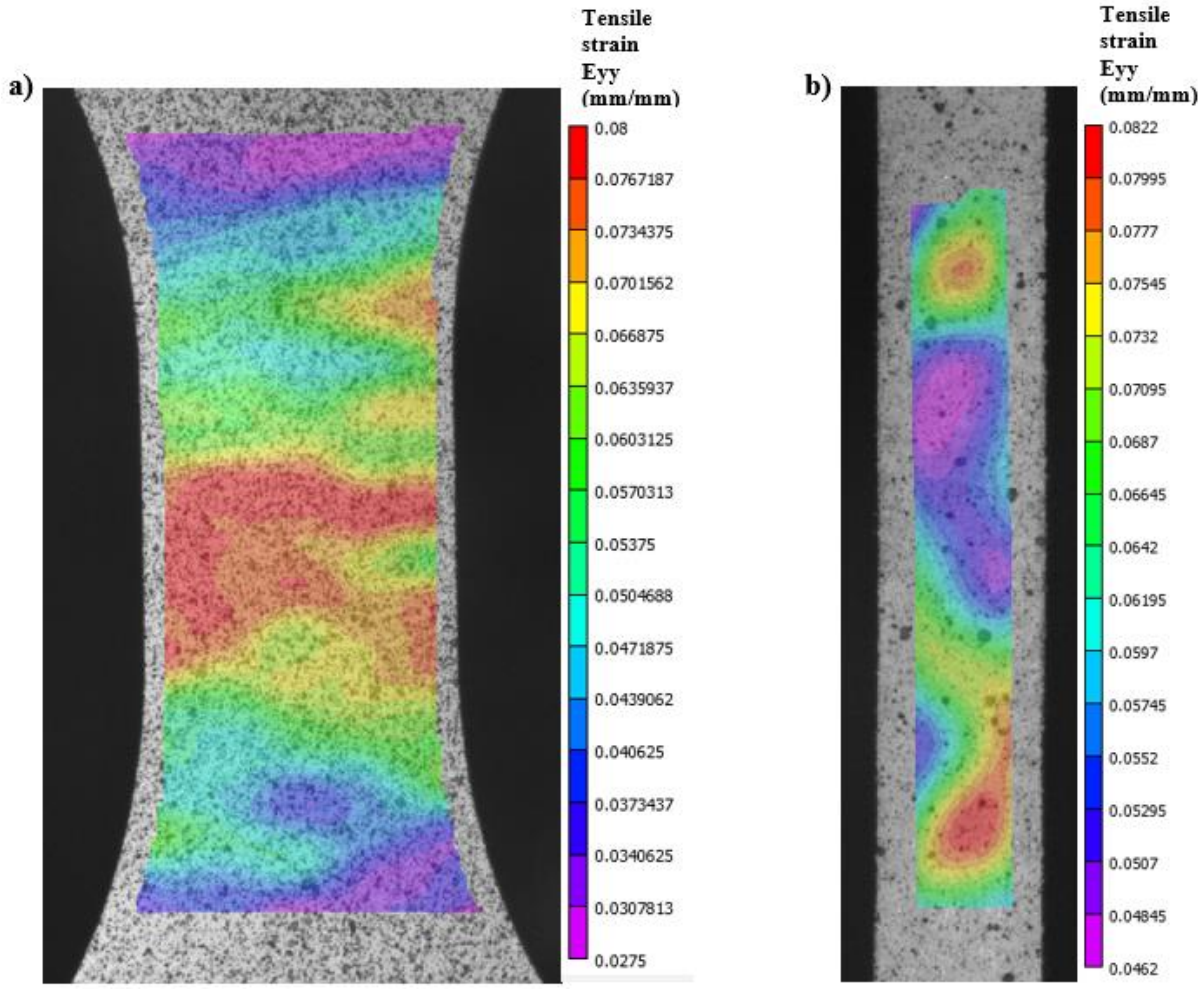

Figure 5-11 Strain in the loading direction before final failure for a 90° specimen at 100° C. a) front view, b) lateral view

5.2 Fatigue tests

Fatigue tests were performed to characterise the fatigue behaviour of the material. Specimens oriented at 0°, 45° and 90° were utilised, and all the specimens were cut at the same location from different plaques. Three temperatures were used: room temperature, 50 and 100° C. The tests were conducted under force control using a 5 Hz frequency and a load ratio R=0. A cut-off limit of 10^6 cycles was set as an endurance limit.

The results were plotted in a log-log chart using the nominal stress against the number of cycles. The resultant plot is shown in Figure 5-12.

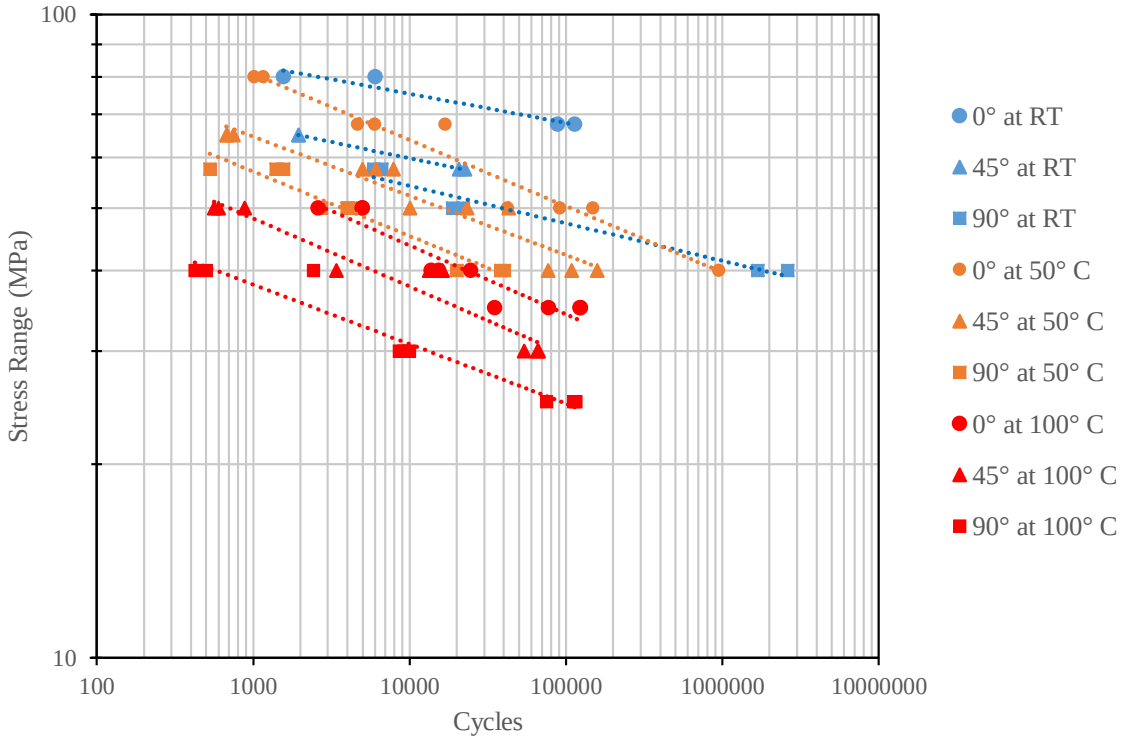

Figure 5-12 Constant amplitude S-N curves for PA66GF50 at different temperatures

Figure 5-12 shows that, in a log-log plot, the fatigue data follow a linear trend. Thus, it can be described using Basquin's equation:

$$\sigma_a = AN^B \quad \textbf{(5-2)}$$

Where A is the stress at cycle 1 and B is the slope of the curve.

Table 5-1 presents Basquin's equation parameters for each specimen orientation at the three tested temperatures.

Table 5-1 Parameters of Basquin's equation

Temperature	Orientation	A	B
Room temperature	0°	114.33	-0.45
	45°	95.542	-0.061
	90°	92.642	-0.058
50° C	0°	164.65	-0.103
	45°	122.22	-0.092
	90°	113.92	-0.1
100° C	0°	117.22	-0.107
	45°	100.15	-0.106
	90°	72.086	-0.092

From Figure 5-12, effect of specimen orientation and temperature on the fatigue performance of the material is clearly observed. The 0° specimens exhibited the longest fatigue lives, with the shortest lives recorded for the 90° specimens at each temperature. Additionally, the influence of the temperature on fatigue lives is clearly observed, with the fatigue life decreasing as the temperature increases. Finally, it is worth noting that specimens tested at the same temperature seem to have similar slopes.

5.2.1 Stiffness evolution of specimens tested at 50 and 100° C

An extensometer was attached to the gauge length of the specimens tested at 50 and 100° C, as mentioned in section 3.7. With the displacements measured during the cyclic loading, a dynamic stiffness was calculated by:

$$K_d = \frac{\Delta F}{\delta} \tag{5-3}$$

Where K_d is the dynamic stiffness, ΔF represents the dynamic force, and δ is the dynamic displacement.

This dynamic stiffness was estimated in an attempt to analyse the damage accumulation during the cyclic loading, looking for a stiffness decay caused by damage accumulation.

The stiffness evolution of specimens at different temperatures is shown in Figure 5-13a-c and Figure 5-14a-c. In order to compare the stiffness variation throughout the fatigue tests, the number of cycles to failure and the stiffness were normalised.

No clear stiffness drop was observed for the 0° specimens, see Figure 5-13a, except for one specimen at 80 MPa, where a steep decay is noticed above 80% of the fatigue life. Figure 5-14a shows the stiffness evolution of the 0°coupons tested at 100°C, where it can be seen that most of the samples showed similar behaviour. The minor variation in the stiffness suggests a sudden failure that could be related to the orientation of the fibres and the damage mechanisms.

The 45° specimens tested at 50° C presented a similar behaviour for the lower stress levels, as can be seen in Figure 5-13b. In contrast, the higher stress levels exhibited a stiffness drop at the beginning of the fatigue lives with a gentle decreasing slope until failure, with an average stiffness reduction of around 12%. On the other hand, as illustrated in Figure 5-14b, all the 45° specimens at 100° C showed a stiffness decrease. Furthermore, the specimens at lower stress levels had a minor stiffness decay at approximately 10% of their fatigue lives, where the slope was reduced.

The behaviour of the 90° specimens showed a stable stiffness with a very modest decreasing slope for the specimens tested at 50° C, illustrated in Figure 5-13c, and a steeper slope for the stress level of 57.5 MPa. The stiffness performance of the specimens at 100° C started with a stiffness decay of about 10% at the beginning of their fatigue lives, as seen in Figure 5-14c. However, their stiffness remained constant for approximately 80% of their lives, after which a consistent stiffness drop occurred. This indicates that some micro-damage happened at the beginning, perhaps some debonding of the fibre-matrix interface.

5.2.2 Temperature measurements of specimens tested at 50 and 100° C

The temperature at the centre of the specimens' gauge length and the chamber temperature was measured to identify the increment of the temperature of the specimens due to self-heating. In Figure 5-15a-c and Figure 5-16a-c, the measured temperatures are plotted against the normalised number of cycles. It is clear that the temperature of the specimens reached a temperature close to the chamber temperature and was stable for most of the duration of the tests. However, a few specimens had an increase in temperature until they achieved thermal equilibrium with the temperature of the environmental chamber. As shown in Figure 5-15c,

the highest increment of temperature was observed in the 90° specimens tested at 50° C under stress levels of 50 and 57.5 MPa, presenting a rise in temperature of 0.5 and 2.5° C respectively. This gives the confidence to say that no self-heating occurred during the tests.

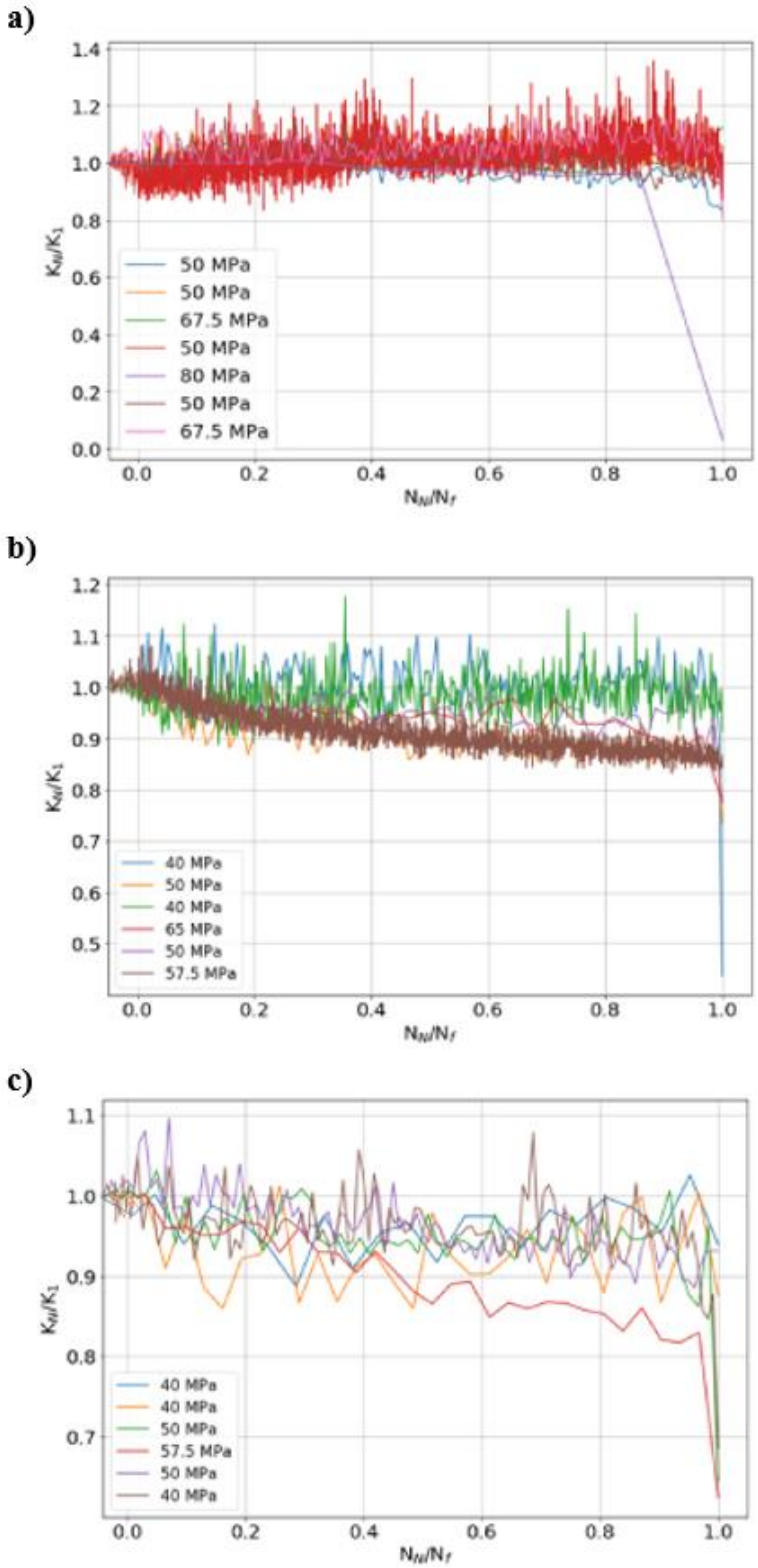

Figure 5-13 Stiffness evolution at 50° C of a) 0° specimens, b) 45° specimens, c) 90° specimens

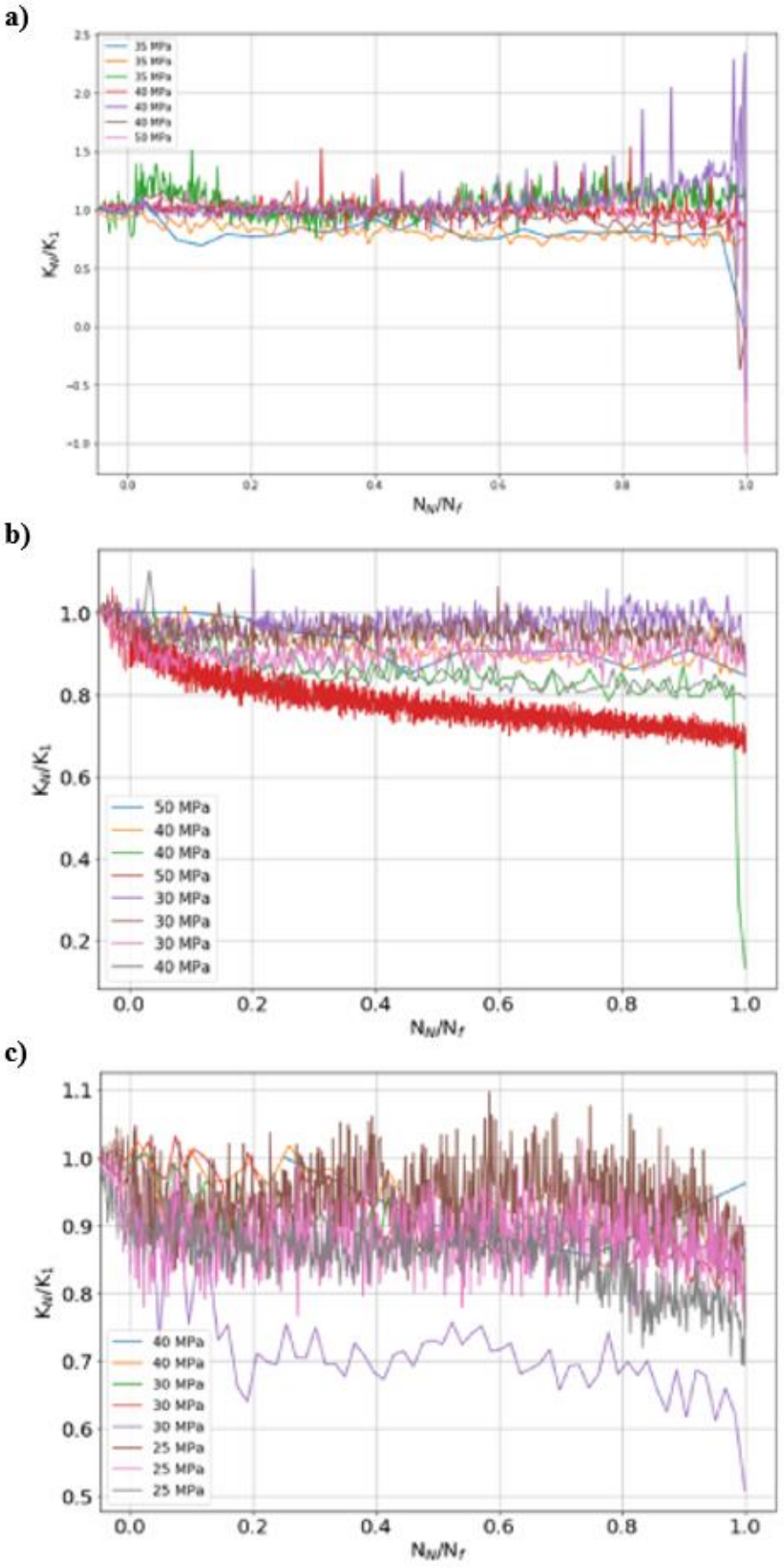

Figure 5-14 Stiffness evolution at 100° C of a) 0° specimens, b) 45° specimens, c) 90° specimens

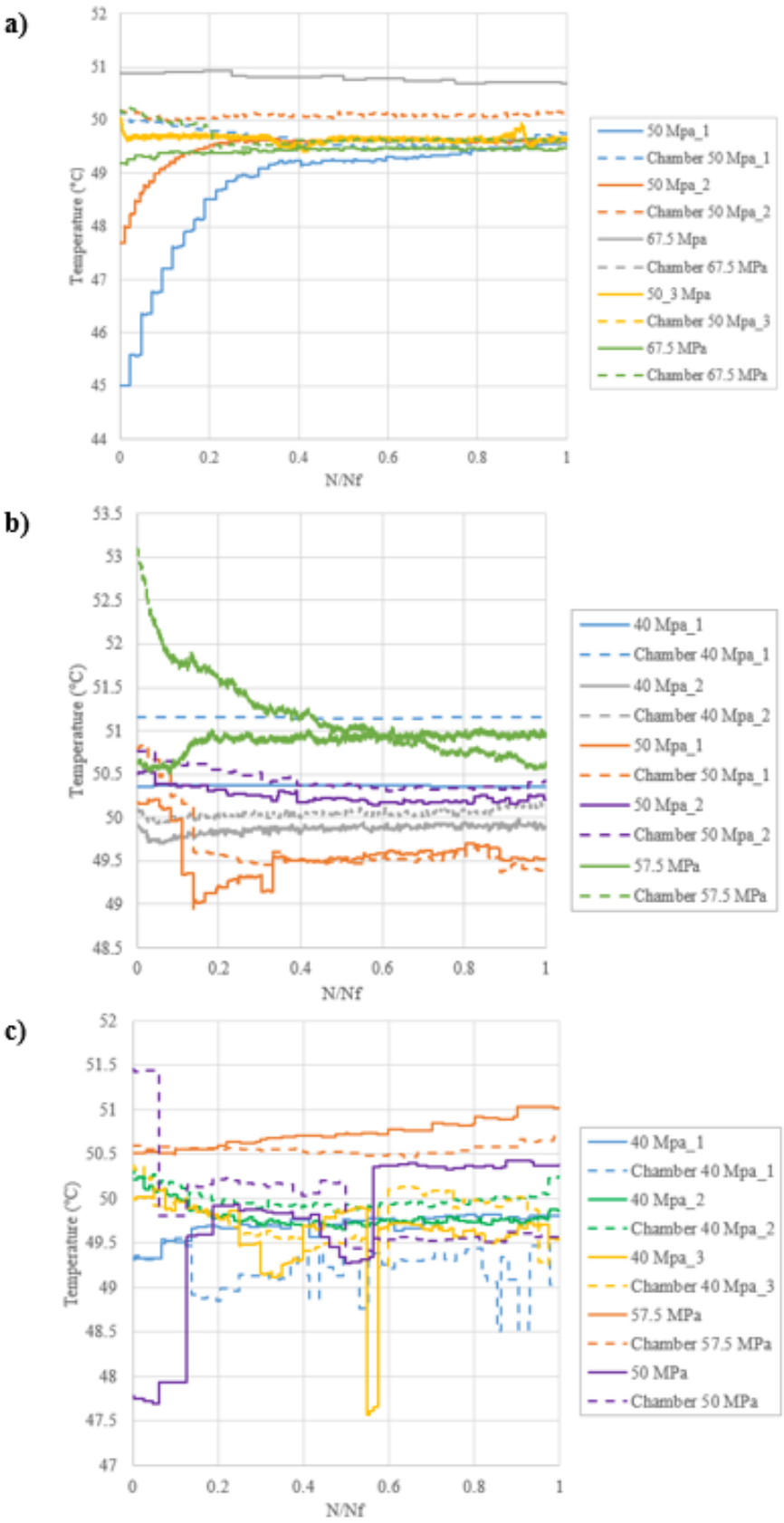

Figure 5-15 Chamber temperature and temperature evolution for a) 0° specimens, b) 45° specimens, c) 90° specimens tested at 50° C

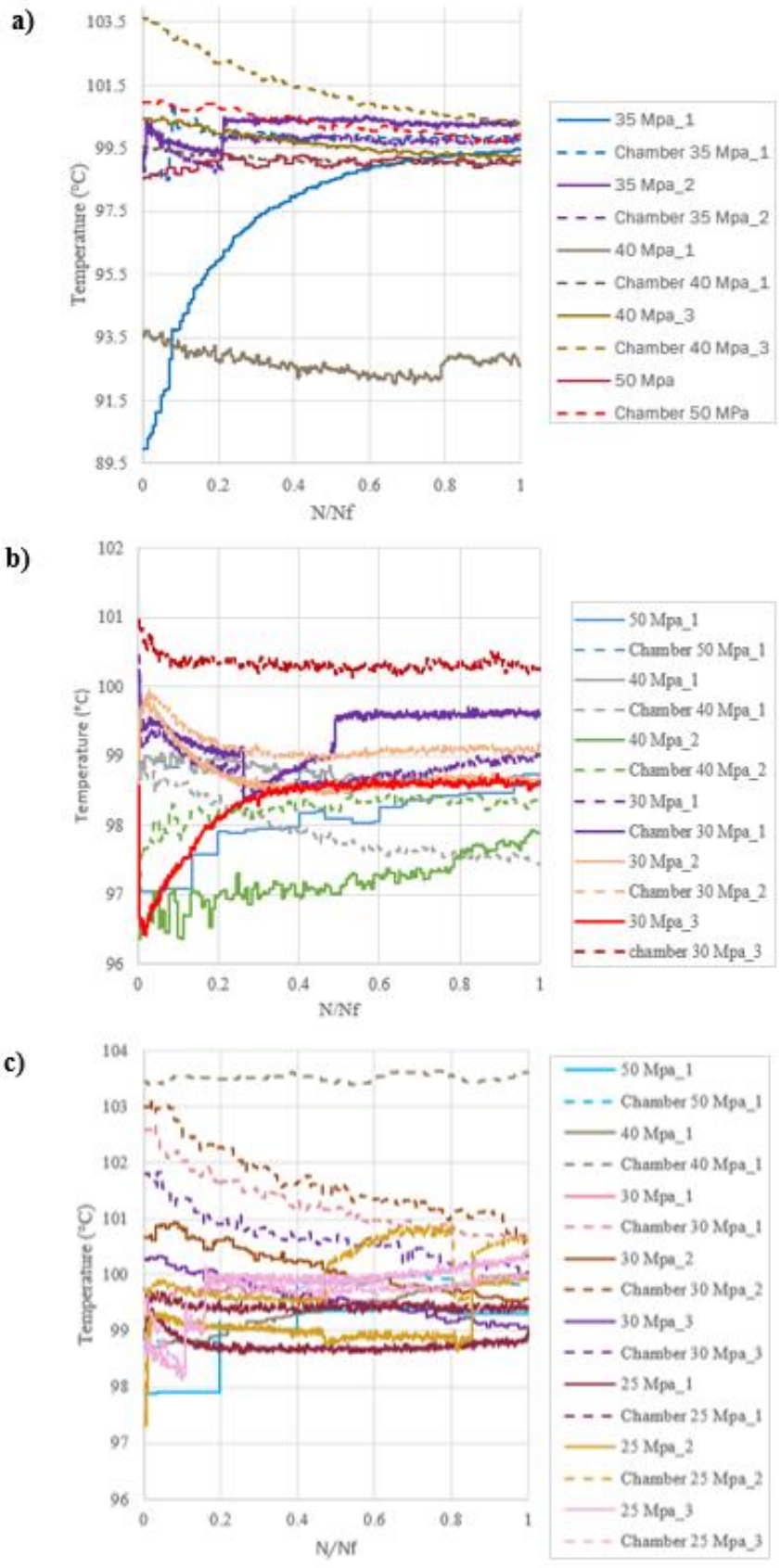

Figure 5-16 Chamber temperature and temperature evolution for a) 0° specimens, b) 45° specimens, c) 90° specimens tested at 100° C

5.2.3 Hysteresis loops

Figure 5-17a-c and Figure 5-18a-c show the hysteresis loops of specimens tested at 50 and 100° C.

Observing the figures, it is evident that the material presented a non-linear behaviour denoted by the hysteresis loops. Furthermore, these hysteresis loops exhibited a shift along the strain axis, which could be caused by the accumulation of plastic strain due to the mean stress. This was observed for all temperatures and specimen orientations.

Some specimens at low to intermediate stress levels showed a stabilisation stage before failure. This is illustrated in Figure 5-17b for a 45° specimen, and Figure 5-17c shows this for a 90° specimen. This behaviour was observed at both temperatures.

The area inside the hysteresis loop represents the dissipated energy. This area was computed at several cycles during the fatigue life of the specimens of the three orientations tested at 50 and 100° C. Figure 5-19a-c and Figure 5-20a-c illustrate the change of the dissipated energy for specimens tested at 50° C and 100° C respectively. To compare specimens at different stress levels the number of cycles was normalised.

The 0° specimens at both temperatures showed a steady energy dissipation throughout their entire fatigue lives despite the stress level, as seen in Figure 5-19a and Figure 5-20a.

Figure 5-20b illustrates the energy dissipation for 45° coupons at 100° C, where a stable dissipation was observed, with a steady increase for the higher stress level. On the other hand, the 45° specimens at 50° C displayed an increment close to the end of the tests, but for most of the duration of the experiment, the area remained constant, as shown in Figure 5-19b.

The 90° samples tested at 50° C, illustrated in Figure 5-19c, presented an increase close to the end of the experiment. In comparison, the 90° specimens at 100° C, depicted in Figure 5-20c, showed an exponential increment earlier in their fatigue lives. At both temperatures, the area of the hysteresis loops of the 90° specimens at high stress levels had a steeper rise before 50% of their lives. After that, the slope reduced and remained constant until the end of the test. The specimen at 50° C showed exponential growth after this stage at above 90% of the fatigue life.

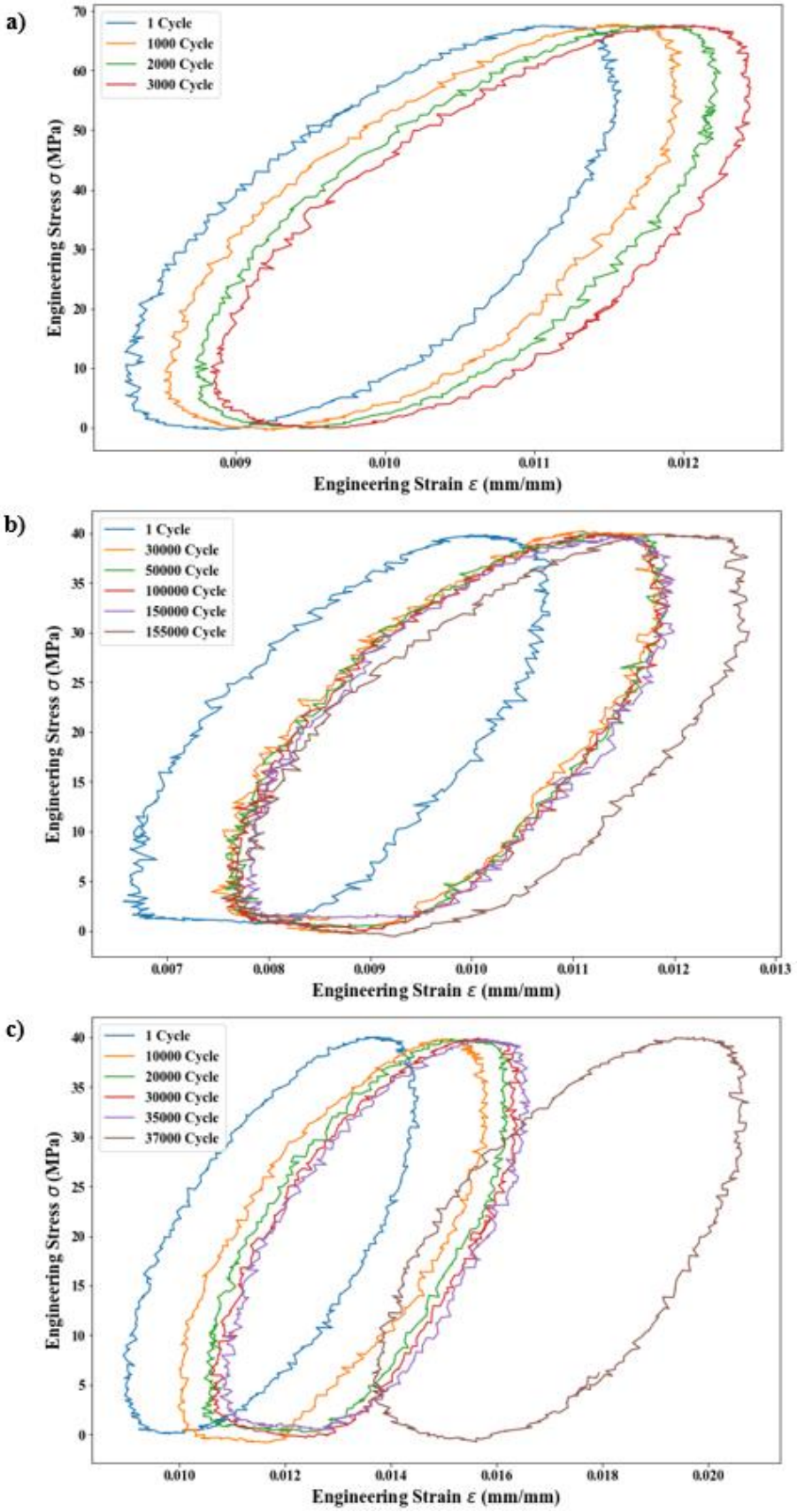

Figure 5-17 Hysteresis loops of a) 0° specimen at 67.5 MPa, b) 45° specimen at 40 MPa, c) 90° specimen at 40 MPa. All specimens were tested at 50° C

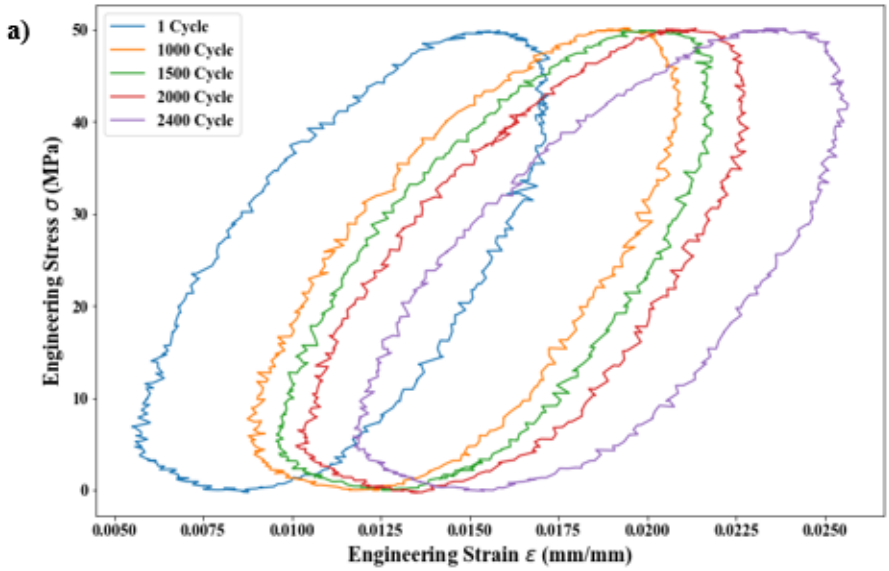
a)
1 Cycle
1000 Cycle
1500 Cycle
2000 Cycle
2400 Cycle
Engineering Stress σ (MPa)
Engineering Strain ε (mm/mm)

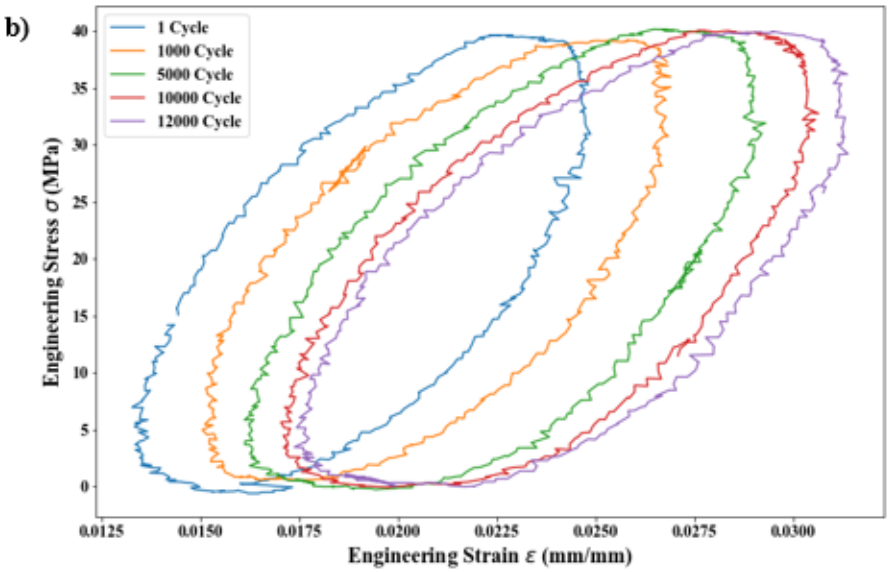
b)
1 Cycle
1000 Cycle
5000 Cycle
10000 Cycle
12000 Cycle
Engineering Stress σ (MPa)
Engineering Strain ε (mm/mm)

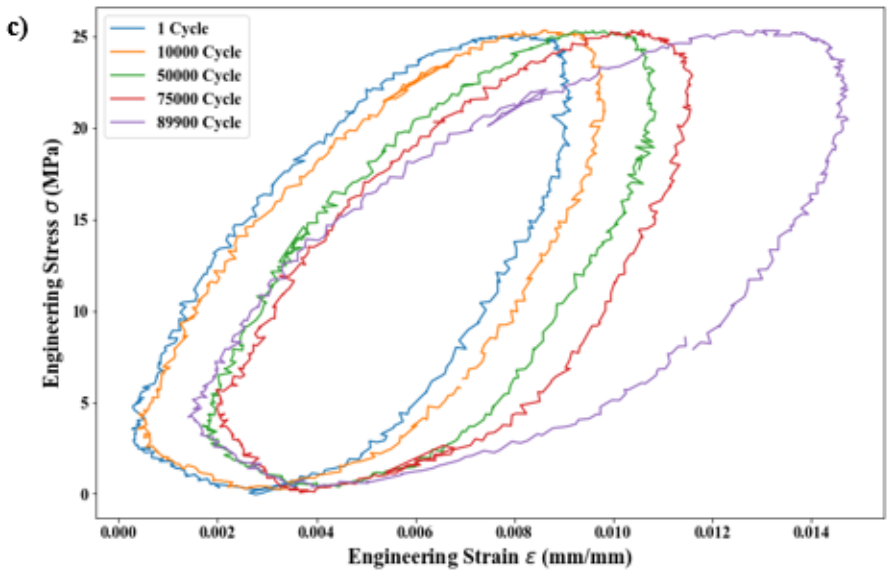
c)
1 Cycle
10000 Cycle
50000 Cycle
75000 Cycle
89900 Cycle
Engineering Stress σ (MPa)
Engineering Strain ε (mm/mm)

Figure 5-18 Hysteresis loops of a) 0° specimen at 50 MPa, b) 45° specimen at 40 MPa, c) 90° specimen at 25 MPa. All specimens were tested at 100° C

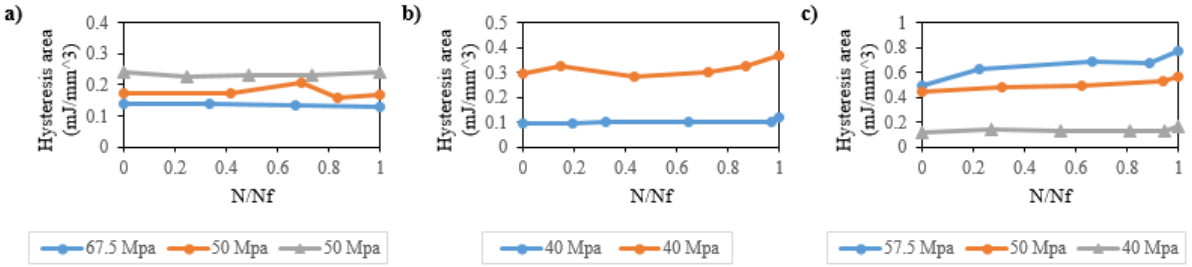

Figure 5-19 Hysteresis area evolution of specimens tested at 50° C. a) 0° specimens, b) 45° specimens, c) 90° specimens

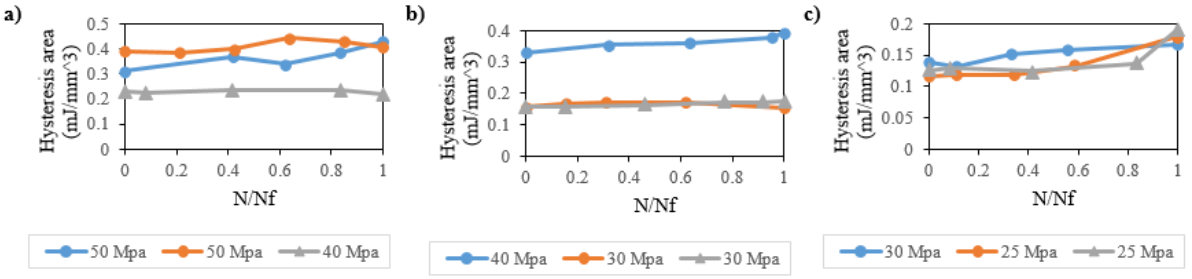

Figure 5-20 Hysteresis area evolution of specimens tested at 100° C. a) 0° specimens, b) 45° specimens, c) 90° specimens

6 DAMAGE MECHANISMS

6.1 Fibre length, fibre diameter and volume fraction

As described in the literature review, the fibre length, fibre diameter and volume fraction are key characteristics of the SFRP and have an important effect on the mechanical response of the material. Based on this, the μCT data was also used to study the microstructure of the material. Specifics of the experimental procedure and parameters used are detailed in section 3.8.1.2 and Determination of the fibre orientation tensor and fibre length3.8.2.2

Table 6-1 presents the values of fibre length, diameter, and volume fraction estimated for all specimens scanned.

The fibre critical length (l_c) was calculated using equation (2-1). The fibre strength was taken from textbook values for a typical E-glass fibre, $\sigma_F^u = 2500\ MPa$ [77], The interfacial shear strength can be calculated from the matrix strength (σ_m) if a strong fibre-matrix bonding is assumed using the equation (6-1) [100]:

$$\tau_i = \frac{\sigma_m}{\sqrt{3}} \quad \textbf{(6-1)}$$

Thus considering σ_m= 50 MPa [7] gives a value of $\tau_i = 28.867\ MPa$. The fibre diameter used was the average value obtained from the μCT measurements, $d_f = 12.126$ μm. With these values, the estimated critical fibre length is $l_c = 525.071$ μm.

Table 6-1 Fibre length, fibre diameter and volume fraction of all the scanned samples

Specimen	Fibre length (μm)	Fibre diameter (μm)	Volume fraction (%)
0°	228.808	11.645	27.958
45°	220.687	13.402	34.26
90°	252.997	12.484	39.574
0° at 50° C	221.089	9.73	24.559
0° at 100° C	208.286	13.369	27.866
Mean value	226.3734	12.126	30.8434
Std Deviation	14.84694	1.361879	5.377372

6.2 Fibre orientation distribution

From the images obtained from μCT, it is possible to observe a typical shell-core-shell structure inherent to SFRP produced by injection moulding. Figure 6-1a-e shows slices of the middle section of the scanned specimens. The 0° samples, shown in Figure 6-1a, exhibit a visible region in the centre, or core, where the fibres are aligned transversally to the injection flow, and two regions closer to the surface, the shell regions, where the fibres are mainly aligned in the direction of the injection flow. In the case of the 45° coupon, illustrated in Figure 6-1b, it is more difficult to identify the structure. However, because it was cut from an injection moulded plaque, it must have a similar shell-core-shell structure. The microstructure of the 90° specimen is depicted in Figure 6-1c. This orientation shows an inverse microstructure than the 0° samples, with fibres aligned to the injection flow in the core and transversal fibres in the shell regions, with no skin layer. The 0° specimens utilised for the in-situ tests at 50 and 100° C exhibited an asymmetric fibre distribution with a skin layer on one side only, as can be seen in Figure 6-1d and Figure 6-1e. Apart from that, they showed a similar microstructure to that of the 0° sample at room temperature.

Accurate measurements of the layers were not possible as there was no clear boundary between the regions. Despite this, approximate measurements were performed where the fibres were visually more aligned in a specific orientation. The length of the shell region varied from 935.26 μm to 1500.92 μm. This represented a range between 48 and 66% of the specimen thickness covered by the shell layer. The average shell region was 1139.331 μm long (58%). The core section occupied, on average, 39 % of the specimen thickness and varied between 33and 45%, having a length within the range of 1325.12 μm and 1788.48 μm with a mean length of 1517.068 μm. For the specimens where a skin layer was observed, this section had an average length of 240.115 which is 6% of the specimen thickness.

6.3 Orientation tensor

The orientation tensor was measured through the thickness at the centre of the specimen's gauge length. Figure 6-2a-c shows the principal components of the orientation tensor, which represent the strength of alignment in each coordinate direction. For this study, component a11 corresponds to the injection flow direction, a22 is the orthogonal direction to the flow, and a33 is the out-of-plane direction.

Figure 6-2a illustrates the a11 component tensor variation through the thickness where the shell-core-shell structure mentioned previously is evident. A steep drop in the tensor

component at the beginning of one side is observed. This sudden drop represents the skin layer, which is followed by the shell layer seen as an increase of the orientation tensor component. Towards the centre, a decrease in fibre alignment is observed, with the lowest alignment slightly shifted from the centre. This section of low a11 value represents the core layer. While the a11 component decreased, the a22 component increased and reached its highest point, where the a11 component value is the lowest, as can be seen in Figure 6-2b. Figure 6-2c shows the degree of out-of-plane alignment expressed by the a33 component. This component is the lowest of the three and is constant throughout the thickness.

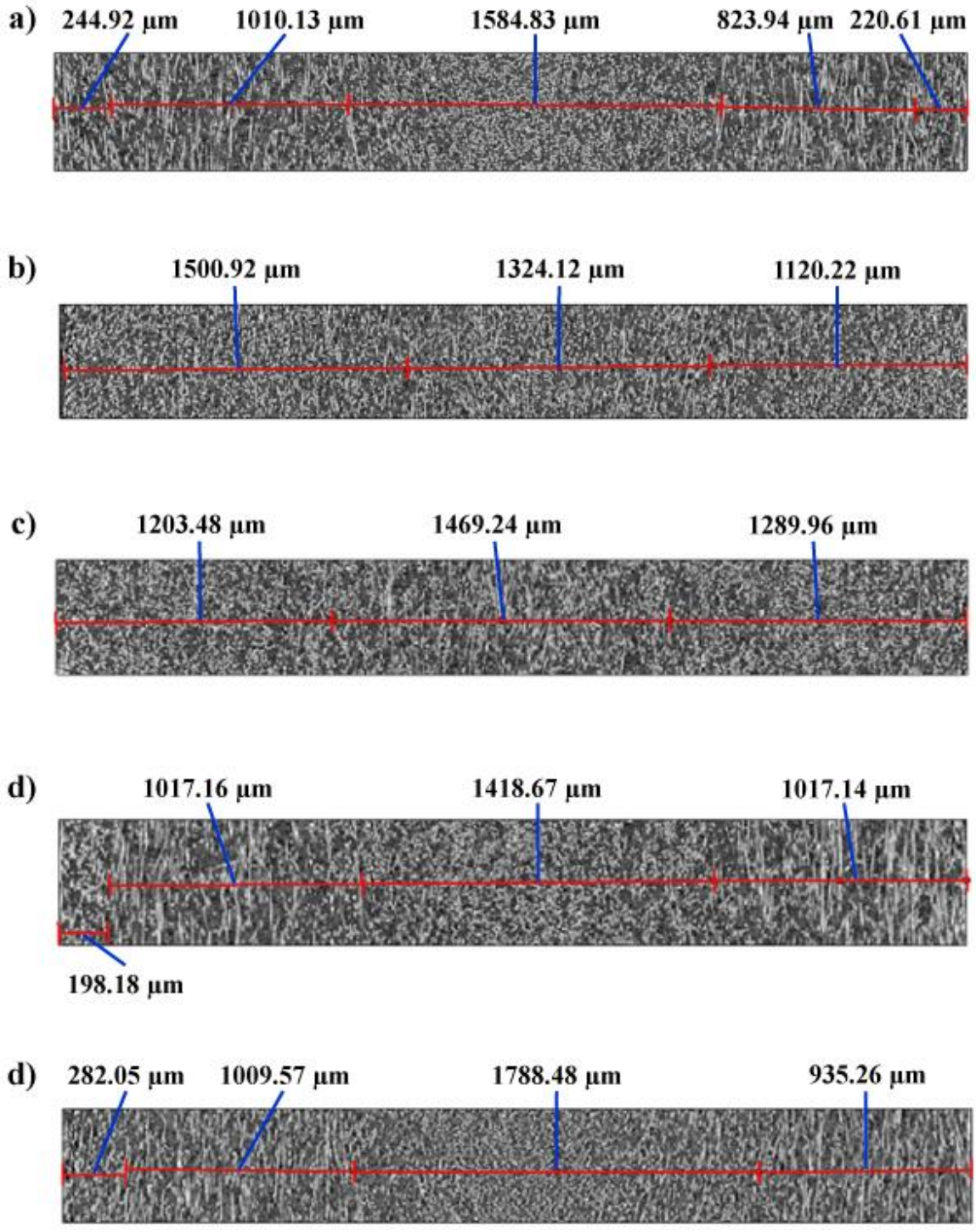

Figure 6-1 Fibre distribution through the thickness of a) 0° specimen at room temperature, 45° specimen at room temperature, c) 90° specimen at room temperature, d) 0° specimen at 50° C, e) 0° specimen at 100° C

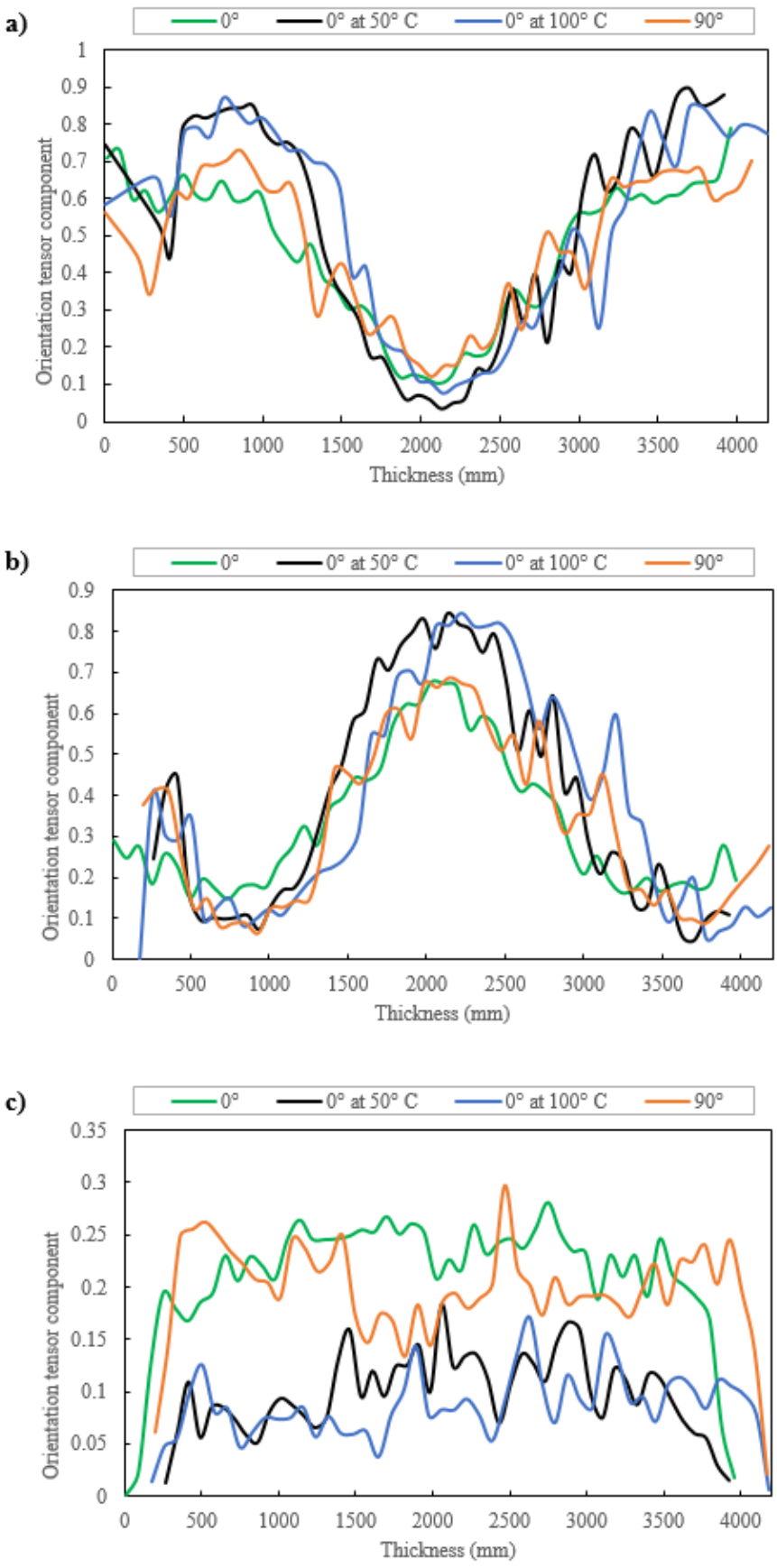

Figure 6-2 Measured orientation tensor a) a11 component, b) a22 component, c) a33 component

6.4 Digital volume correlation

In-situ tensile tests were carried out in the µCT at the Sheffield Tomography Centre at The University of Sheffield. The experiments were conducted at room temperature, 50 and 100° C. One specimen of each orientation was tested at room temperature, and two 0° specimens were tested at 50 and 100° C, one for each temperature. Figure 6-3 shows a schematic of the scanned region of the samples illustrating the location of the gauge length, the shell and core layers.

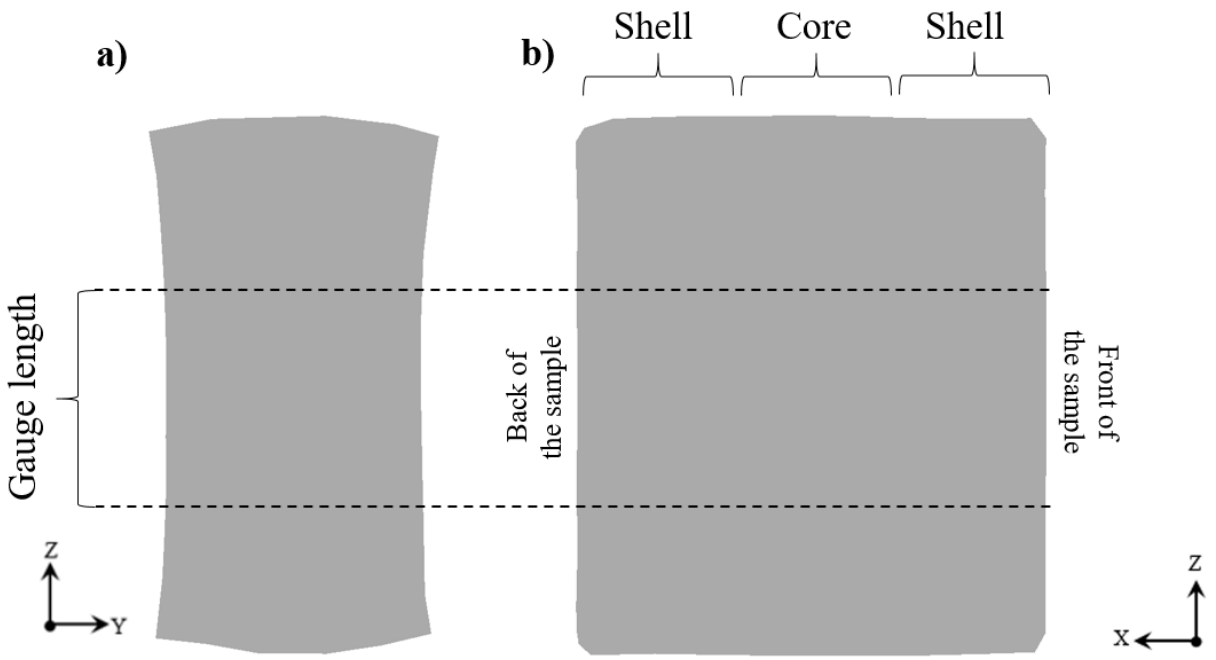

Figure 6-3 Schematic of the µCT sample views. a) front view, b) lateral view (thickness)

6.4.1 0° specimen at room temperature

Figure 6-4a-d shows the distribution of the strain component along the loading direction at the front face of the 0° specimen tested at room temperature. At 25% of the UTS, shown in Figure 6-4a, a strain localisation perpendicular to the load appeared. As the loading increased, the strain continued to intensify, but no other area on the surface developed strain concentrations, as seen in Figure 6-4b-d.

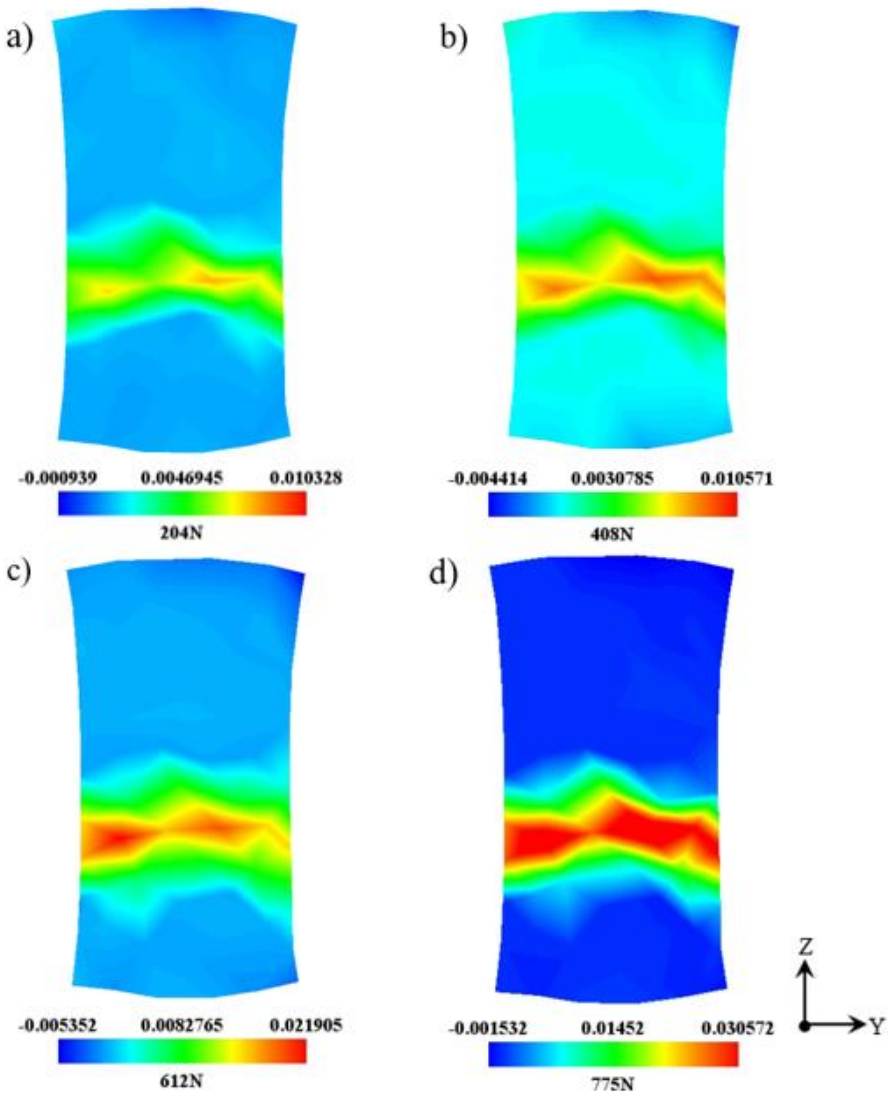

Figure 6-4 Tensile strain in the loading direction of a 0° specimen at room temperature at different stresses, a) 25% of UTS, b) 50% of UTS, c) 75% of UTS, d) 95% of UTS. Front view

Similar behaviour can be observed in Figure 6-5a-d, where a lateral view is presented. Strain concentration occurred at the beginning of the experiment and continued to develop, but no further strain localisation showed up. These strain concentrations seem to start from the front and the back of the specimen, growing up until they merge as the load increase.

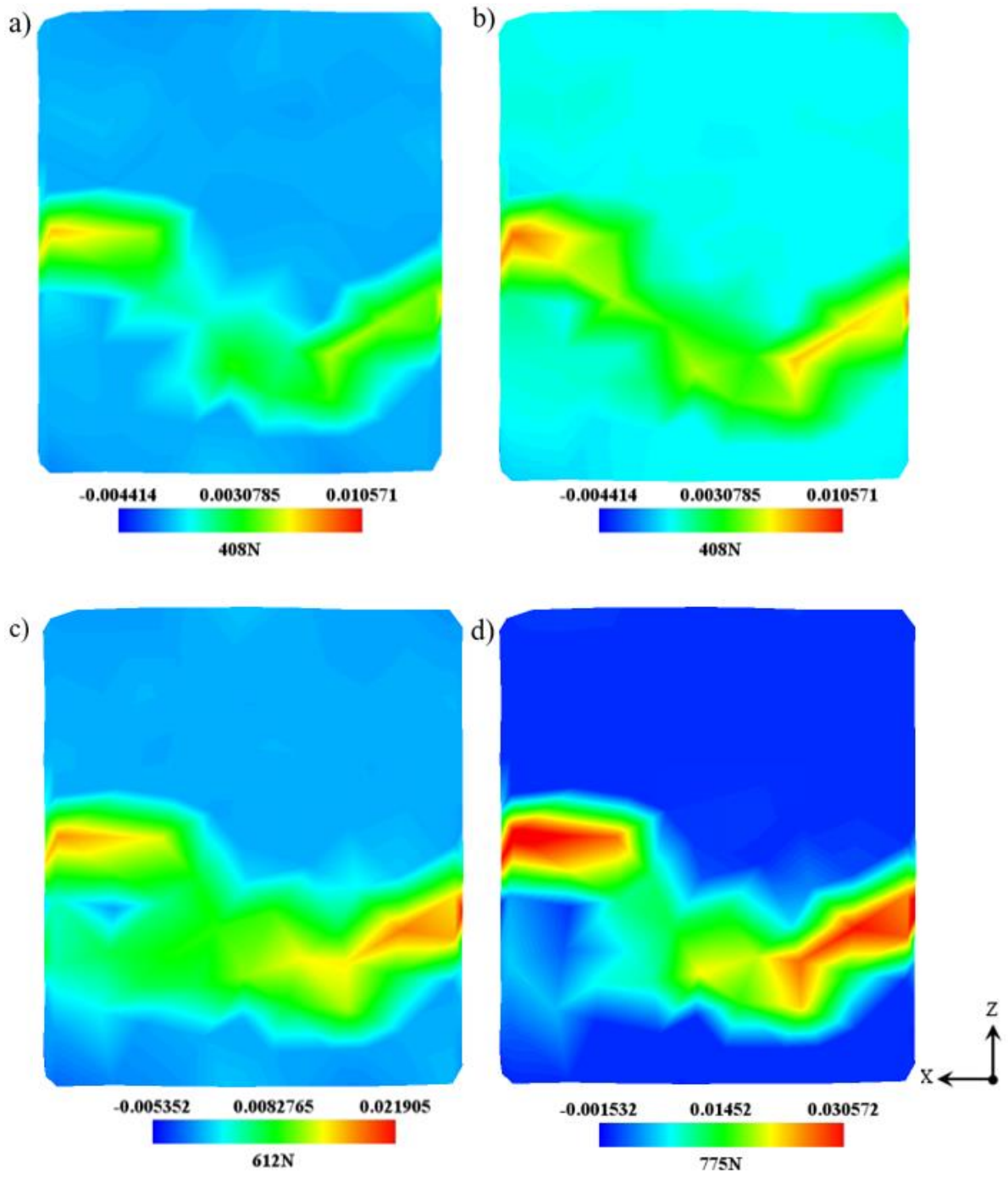

Figure 6-5 Tensile strain in the loading direction of a 0° specimen at room temperature at different stresses, a) 25% of UTS, b) 50% of UTS, c) 75% of UTS, d) 95% of UTS. Lateral view

In Figure 6-6a-d, it is illustrated a cut at the middle thickness in the plane YZ. A strain localisation occurred at an early loading stage, growing toward the lateral surfaces of the specimen. This strain localisation seems to be below the strain concentration at the front surface shown in Figure 6-4a-d but agrees with the position of the strain path shown in Figure 6-5a-d.

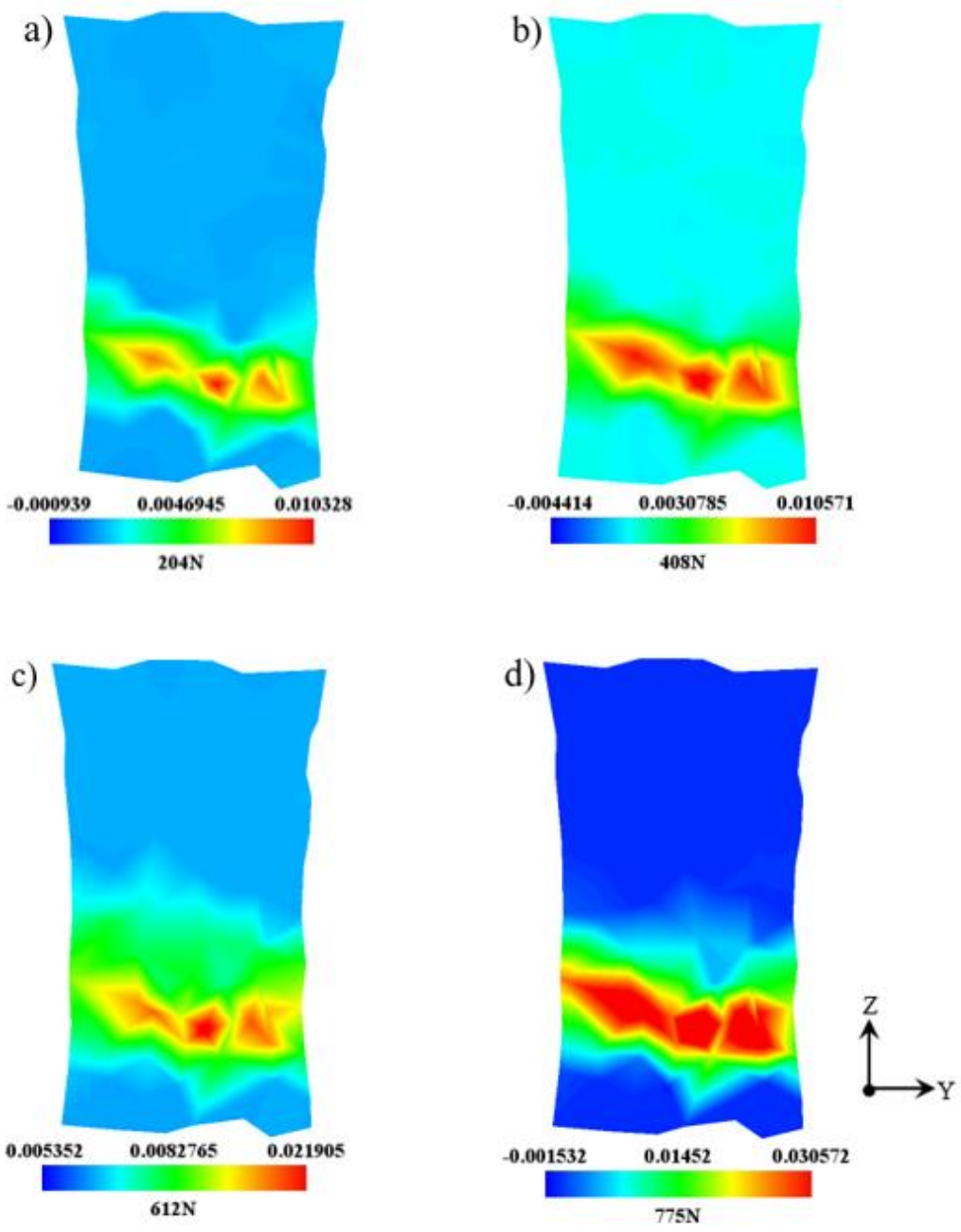

Figure 6-6 Tensile strain in the loading direction of a 0° specimen at room temperature at different stresses, a) 25% of UTS, b) 50% of UTS, c) 75% of UTS, d) 95% of UTS. Front view at mid thickness

Figure 6-7a-d shows a cut in the XZ plane of the deformed meshes at the centre of the specimen, revealing a strain localisation at the core and some strain concentrations coming from the front and back surface of the specimen. These strains at the surface merge with the strain concentration at the core. From Figure 6-7a-d, it is noticed that the highest increase of strain takes place between 50 and 75% of the UTS.

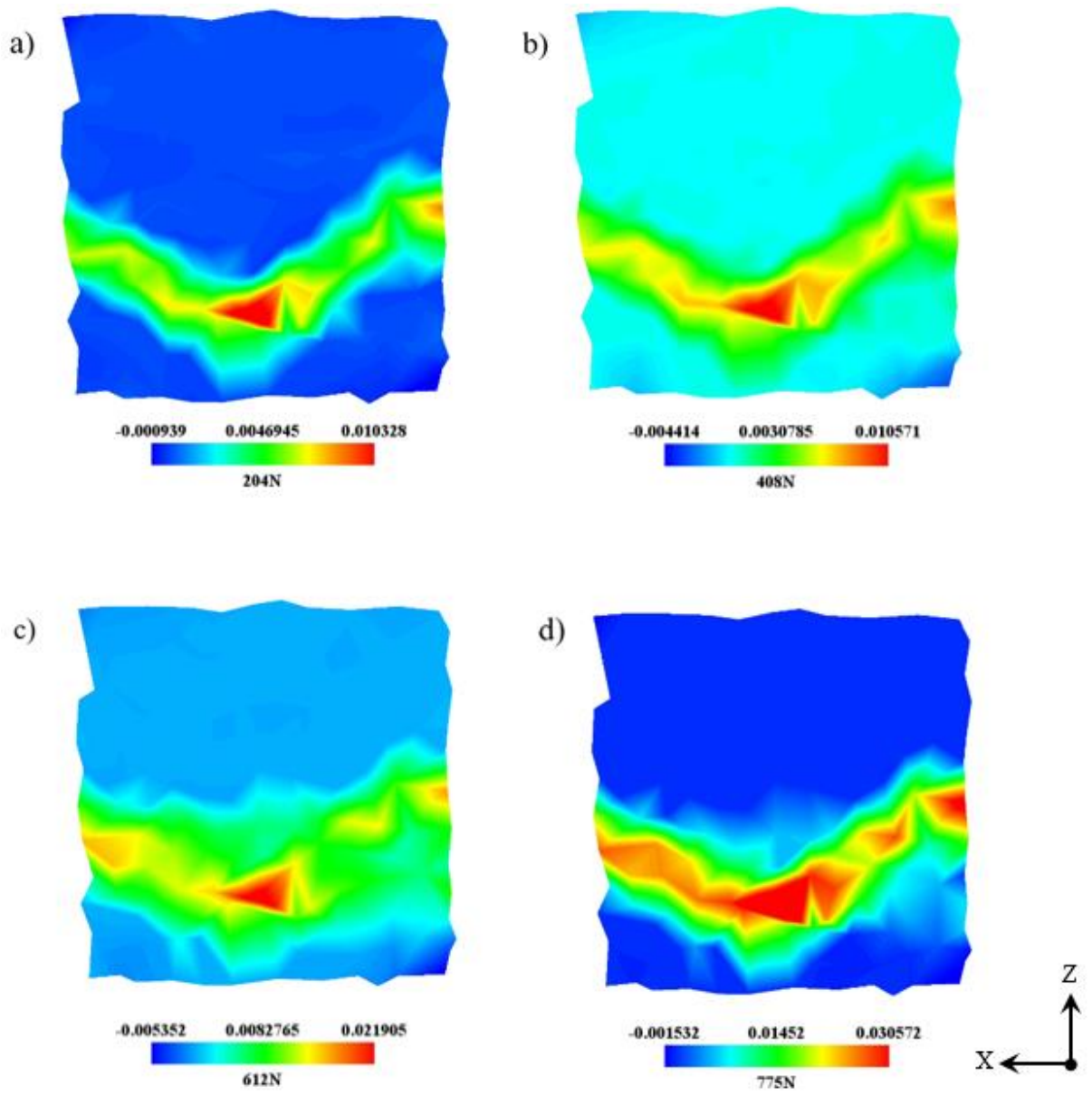

Figure 6-7 Tensile strain in the loading direction of a 0° specimen at room temperature at different stresses, a) 25% of UTS, b) 50% of UTS, c) 75% of UTS, d) 95% of UTS. Lateral view at mid thickness

The front and lateral views of the deformed mesh superimposed onto the microstructure of the specimen are illustrated in Figure 6-8a-b and Figure 6-9a-b. Figure 6-9b shows that the strain concentration occurs where there is a lower concentration of fibres and a significant separation between them. A similar pattern is observed at mid-thickness, shown in Figure 6-9a-b. Besides the low fibre concentration, the fibres are less oriented to the loading direction around the strain localisation.

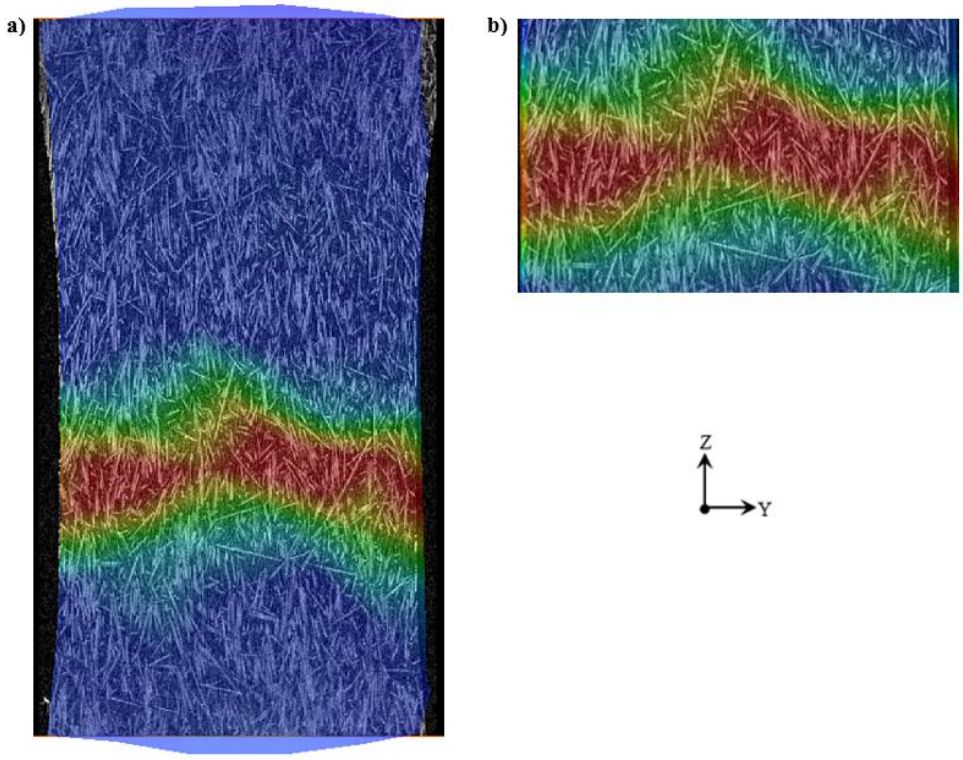

Figure 6-8 Superimposed deformed mesh on the microstructure of a 0° specimen. Front view. a) full gauge length of the specimen, b) zoom in to the region of strain localisation

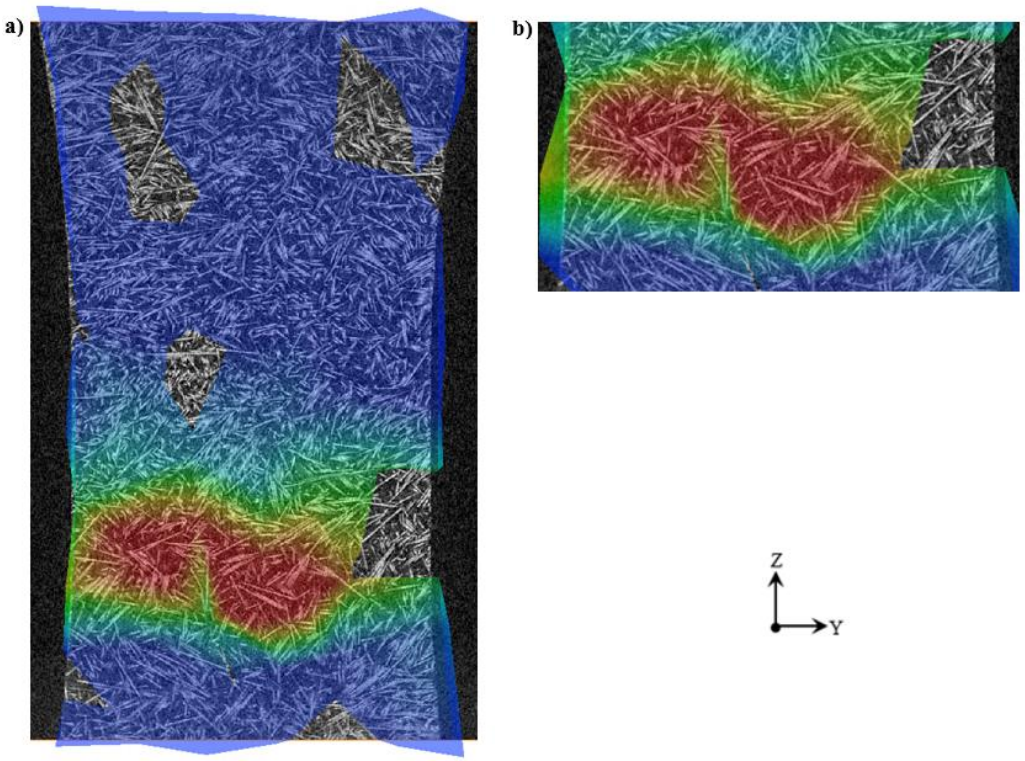

Figure 6-9 Superimposed deformed mesh on the microstructure of a 0° specimen. Front view at mid-thickness. a) full gauge length of the specimen, b) zoom in to the region of strain localisation

Analysing the lateral view of the deformed mesh at 75% of the UTS overlapped on the microstructure of the specimen, as depicted in Figure 6-10a-d, the strain concentration also appears to be located in a region where the fibres are more aligned to the direction of the load. Figure 6-10b shows that the strain at the surface is higher near the edge of the specimen, where a layer of fibres seems to be randomly oriented. At mid-width below the surface, the strain concentration is in the region of the core and at the surface, as illustrated in Figure 6-10d.

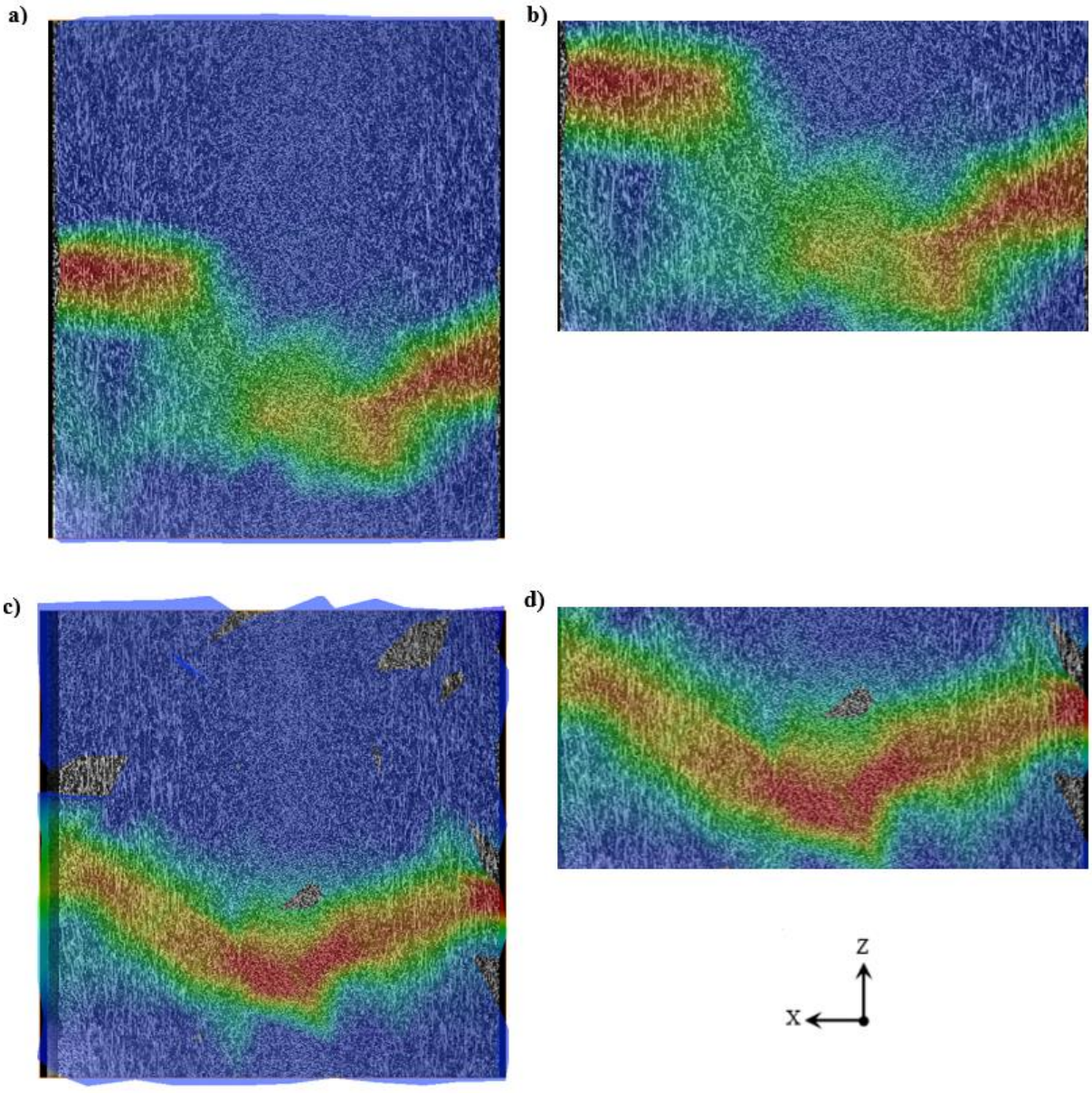

Figure 6-10 Superimposed deformed mesh on the microstructure of a 0° specimen. Lateral view. a) full gauge length of the specimen, b) zoom in to the region of strain localisation, c) Lateral view at mid-width, d) zoom in to the region of strain localisation at mid-width

Once the fractured specimen is overlapped on the deformed mesh at 75% of the UTS, one can observe that the strain localisation is close to the fracture path, as seen in Figure 6-11a-b.

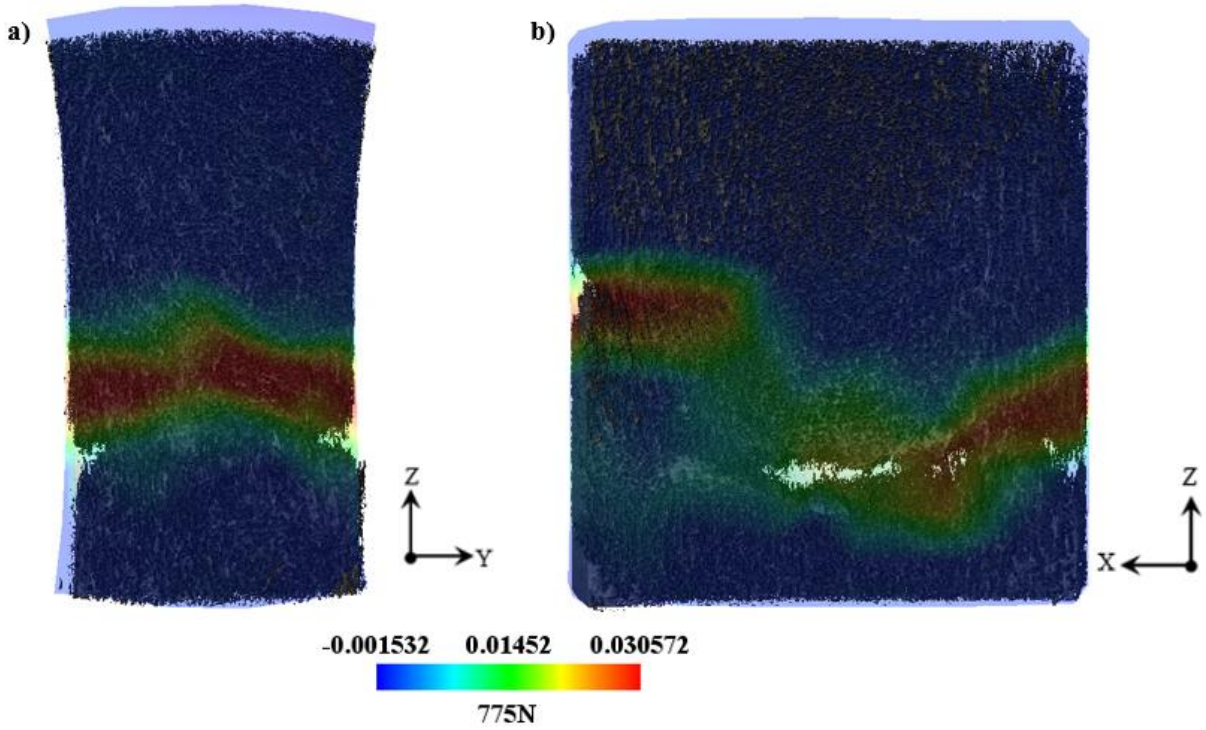

Figure 6-11 Deformed DVC mesh superimposed on the fractured 0° specimen. a) Front view, b) lateral view

6.4.2 45° specimen at room temperature

The 45° specimen failed when the load corresponding to 95% of the UTS was applied. Thus, only three loading conditions were used for the DVC analysis. The strain in the loading direction on the front surface of the specimen is shown in Figure 6-12a-c. A strain localisation occurred at 50% of the UTS close to the middle of the gauge length, as shown in Figure 6-12b. This strain concentration continued to grow until the specimen failed. One can see in Figure 6-12b-c that the strain localisation is at an angle. This could be due to the fibre orientation.

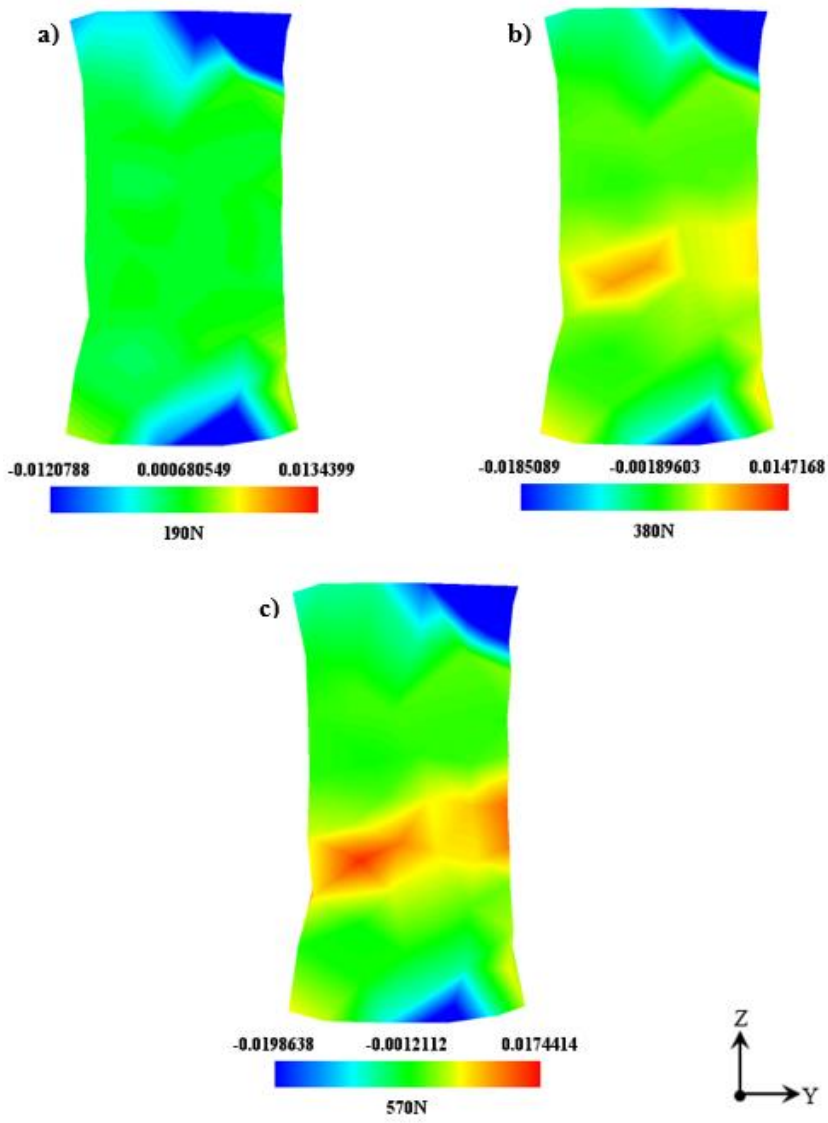

Figure 6-12 Tensile strain in the loading direction of a 45° specimen at room temperature at different stresses, a) 25% of UTS, b) 50% of UTS, c) 75% of UTS. Front view

A lateral view of the specimen is shown in Figure 6-13a-c. Figure 6-13a shows a strain concentration at the bottom close to the centre, starting from the back of the specimen. This strain merges with the front strain, as seen in Figure 6-13b and c. The strain value only increased by 9.5% from 25% of the UTS to 50% of the UTS. This value continued to grow by a further 18.9%, from 50% of the UTS to 75% of the UTS.

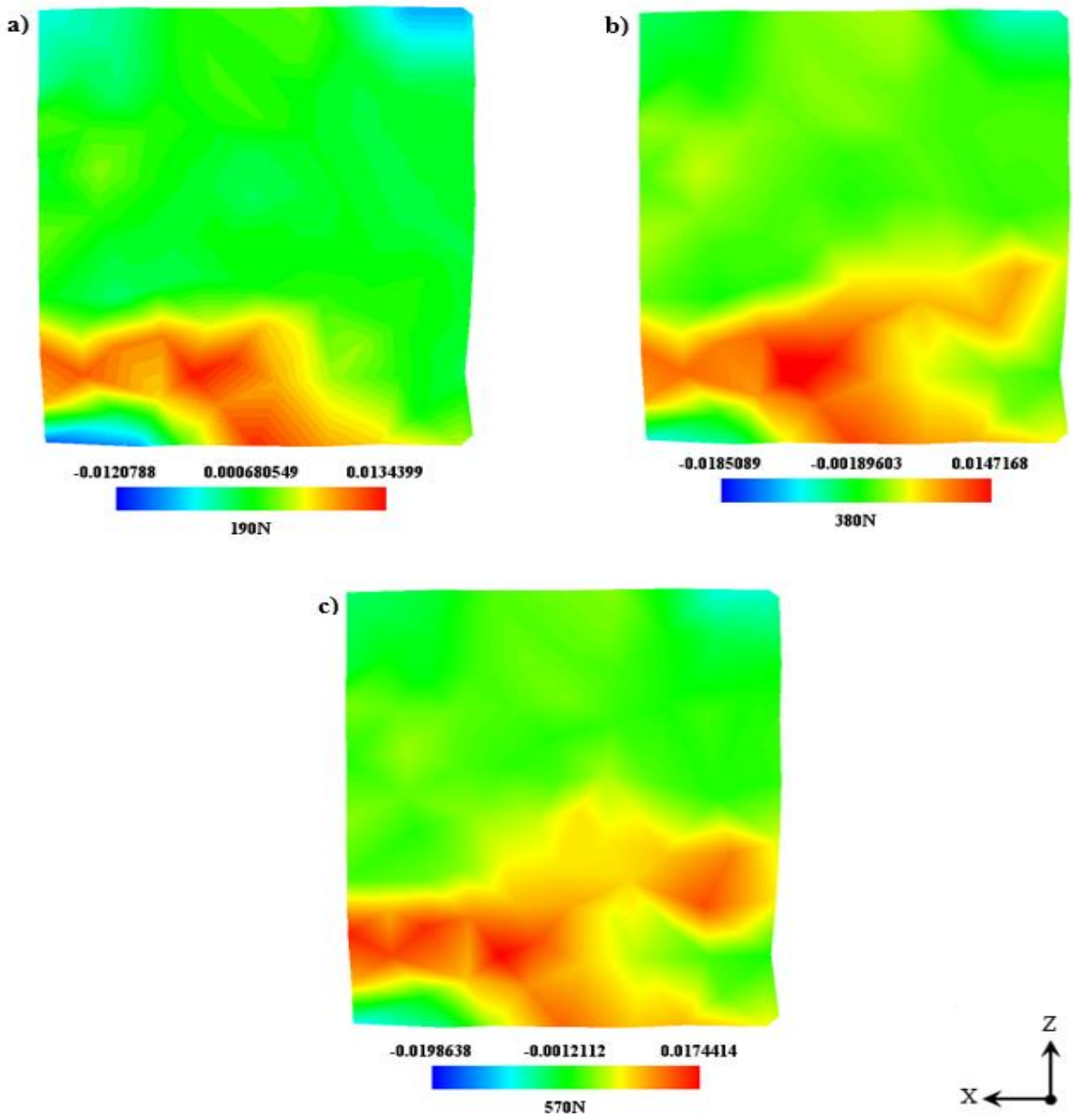

Figure 6-13 Tensile strain in the loading direction of a 45° specimen at room temperature at different stresses, a) 25% of UTS, b) 50% of UTS, c) 75% of UTS. Lateral view

Figure 6-14a-c depicts a front view of a cut at mid-thickness in the YZ plane, which shows a band of strain at the lower part of the specimen. This strain localisation is closer to the beginning of the specimen's radius, where the geometry change could cause a stress concentration.

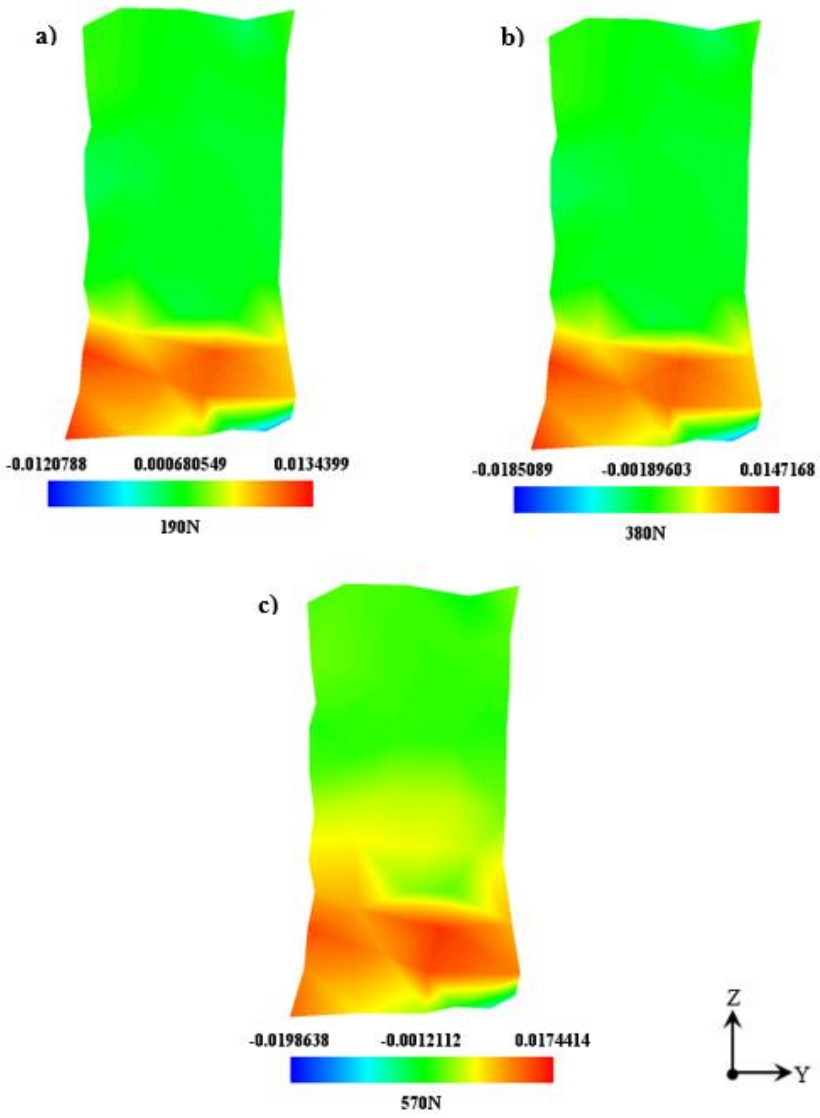

Figure 6-14 Tensile strain in the loading direction of a 45° specimen at room temperature at different stresses, a) 25% of UTS, b) 50% of UTS, c) 75% of UTS. Front view at mid thickness

A cut at the middle of the width in plane XZ is illustrated in Figure 6-15a-c. The strain localisation observed at the bottom close to the centre of the specimen seems to correspond to the centre of the strain concentration shown at the surface in the lateral view (see Figure 6-13a-c). The strain localisation increases from 0.0134399 to 0.0174414 and expands towards the front surface.

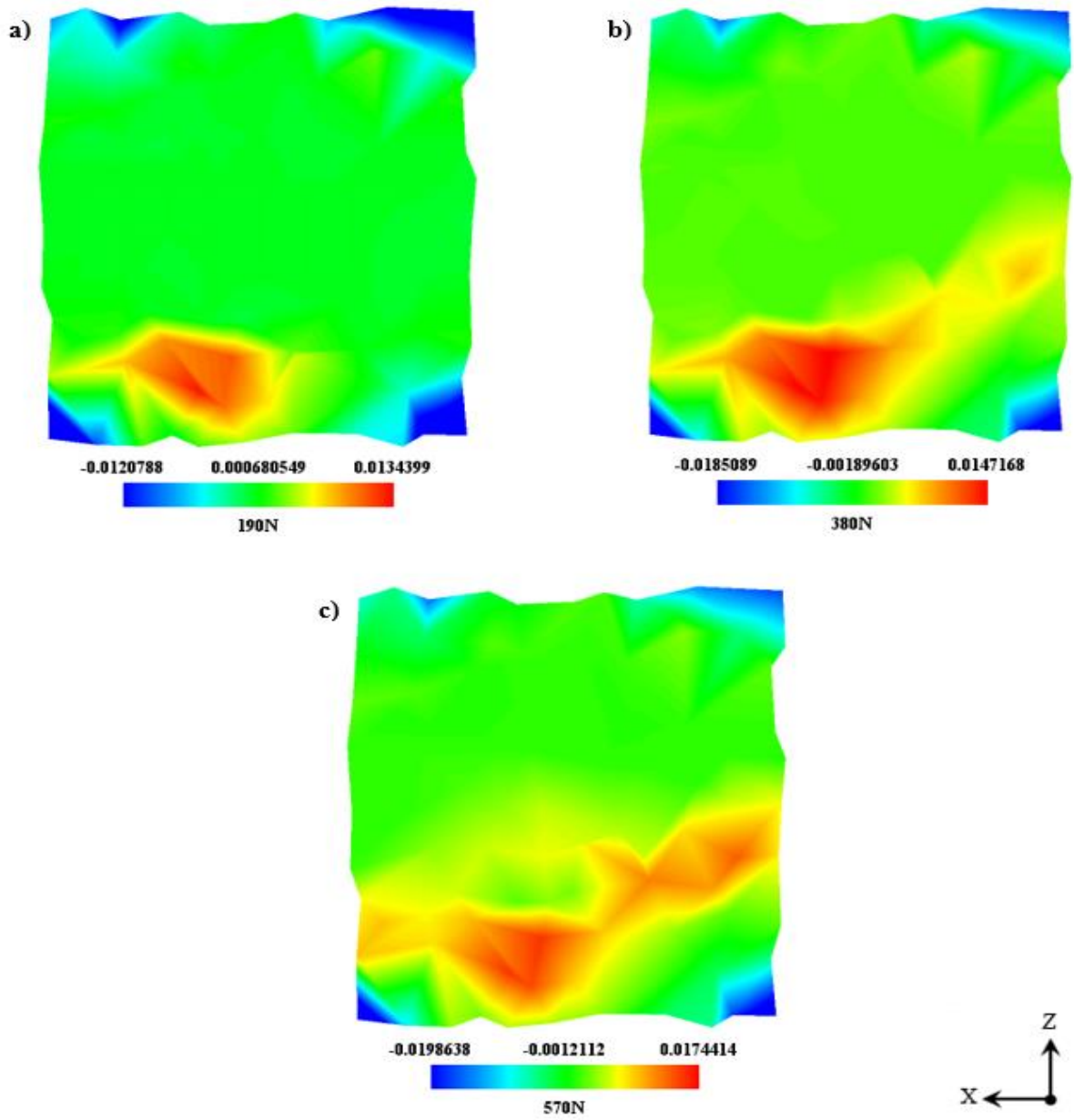

Figure 6-15 Tensile strain in the loading direction of a 45° specimen at room temperature at different stresses, a) 25% of UTS, b) 50% of UTS, c) 75% of UTS. Lateral view at mid width

Figure 6-16a-b and Figure 6-17a-b depicts the front and lateral view of the deformed mesh overlapped on the microstructure of the specimen. The zoom-in to the strain concentration in the front view, shown in Figure 6-16b, exposes that the strain localisation seems to occur where there is a lower concentration of fibres. On top of that, in Figure 6-17b, where the zoom-in to the strain concentration of the lateral view is illustrated, the strain appears to be in a region where the fibres are less oriented in the loading direction.

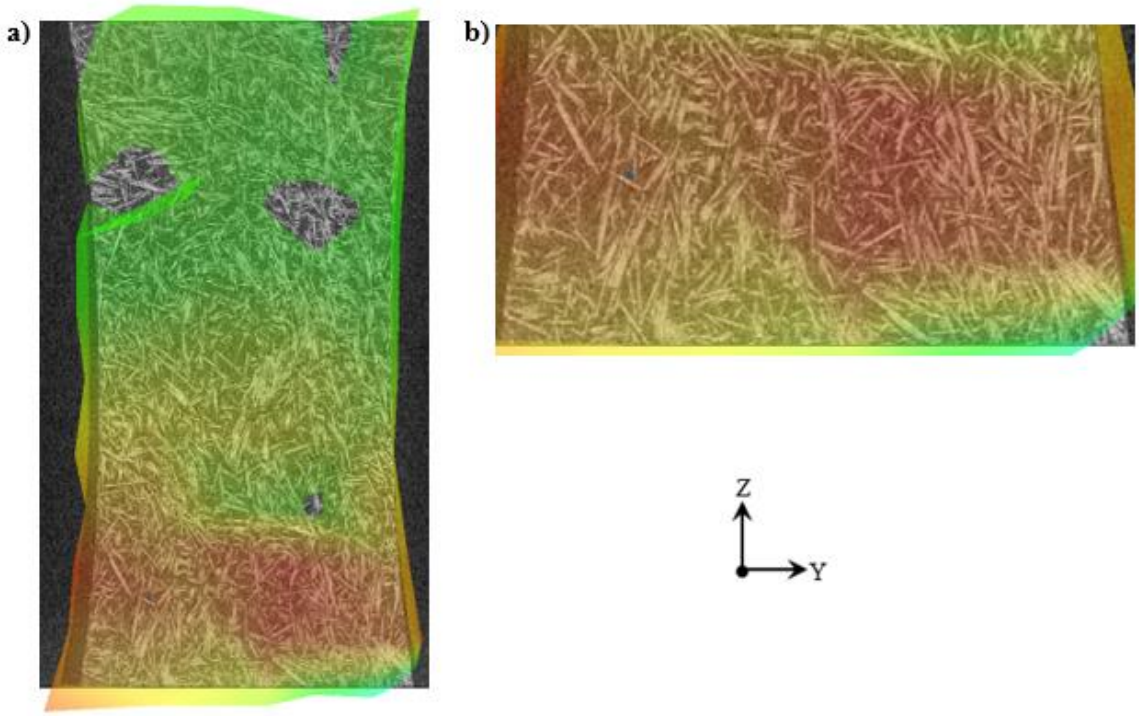

Figure 6-16 Superimposed deformed mesh on the microstructure of a 45° specimen. Front view. a) full gauge length of the specimen, b) zoom in to the region of strain localisation

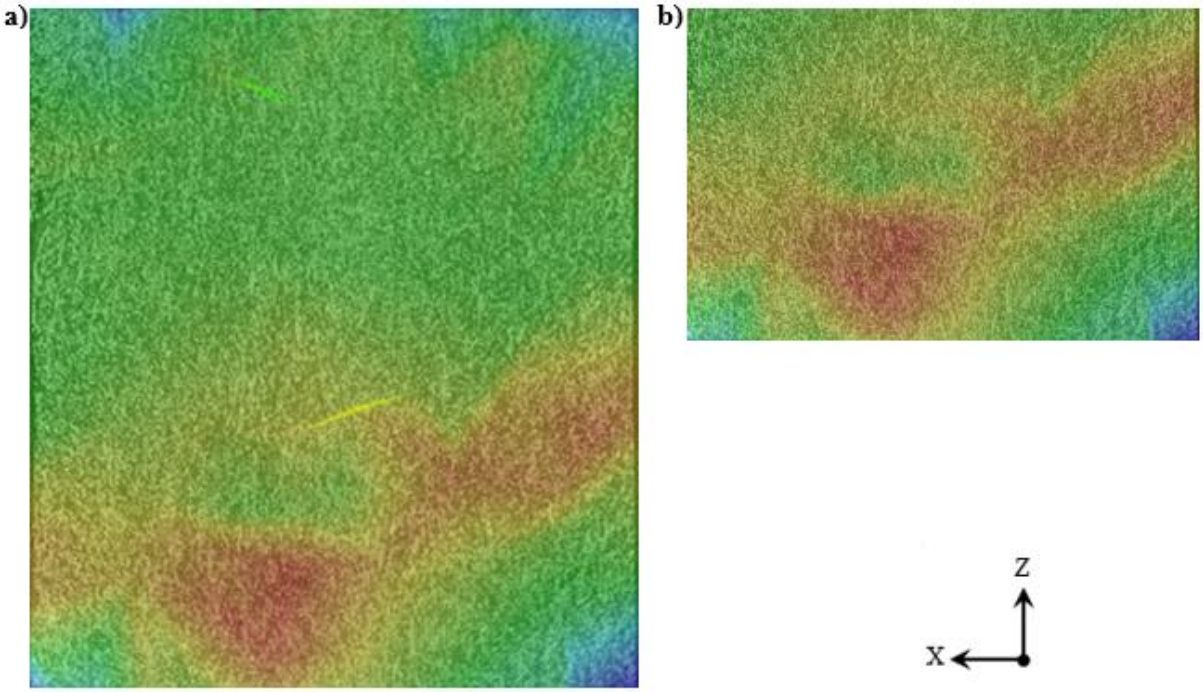

Figure 6-17 Superimposed deformed mesh on the microstructure of a 45° specimen. Lateral view. a) full gauge length of the specimen, b) zoom in to the region of strain localisation

The superimposed fracture specimen on the deformed mesh at the last loading stage, shown in Figure 6-18a-b, reveals that the strain localisation matches the fracture path on the specimen. Figure 6-18a shows that the angled strain corresponds to the angled fracture path.

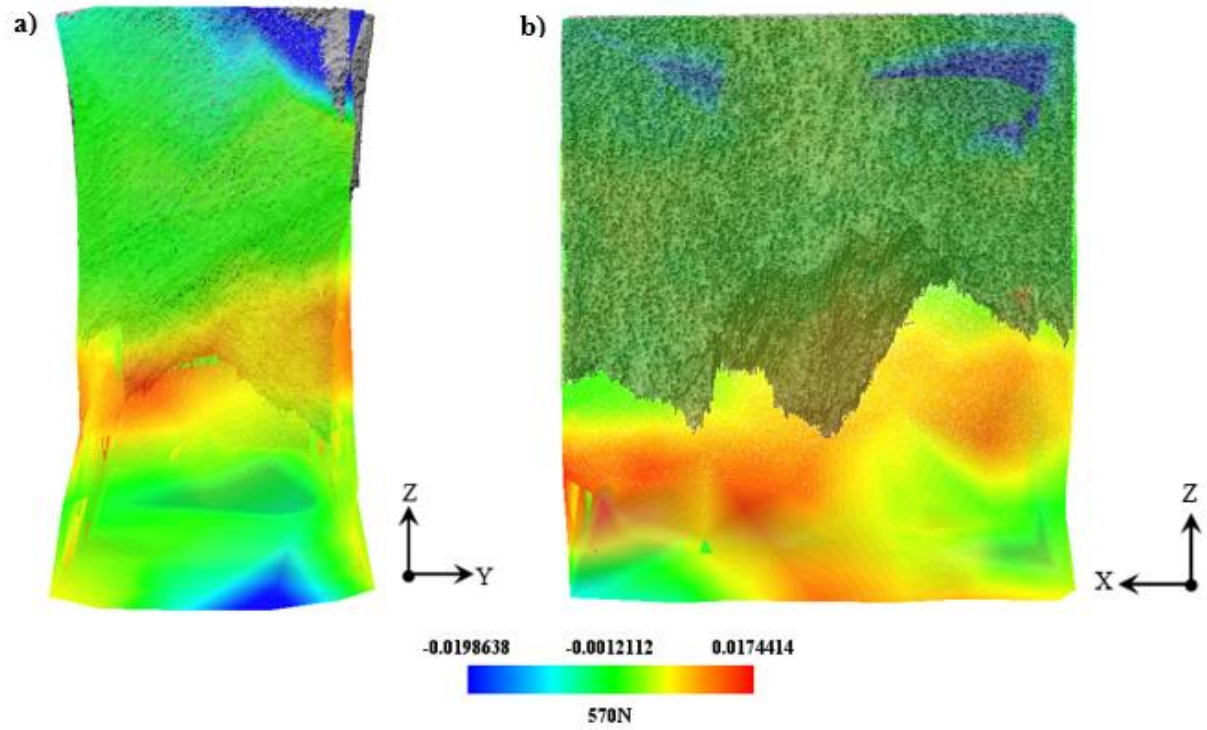

Figure 6-18 Deformed DVC mesh superimposed on the fractured 45° specimen. a) Front view, b) lateral view

Examination of the μCT images of the broken 45° specimen reveals a secondary crack starting from the edge near the fracture surface, as can be seen in Figure 6-19. One can observe that the crack followed the fibre-matrix interface of a long fibre and propagated through the fibre ends of shorter nearby fibres. Above the secondary crack, more damage can be noticed, mainly debonding of fibres at the tip and a few broken fibres oriented in the loading direction. Figure 6-20 shows similar damage: fibre end debonding that grows through the fibre-matrix interface and very few broken fibres.

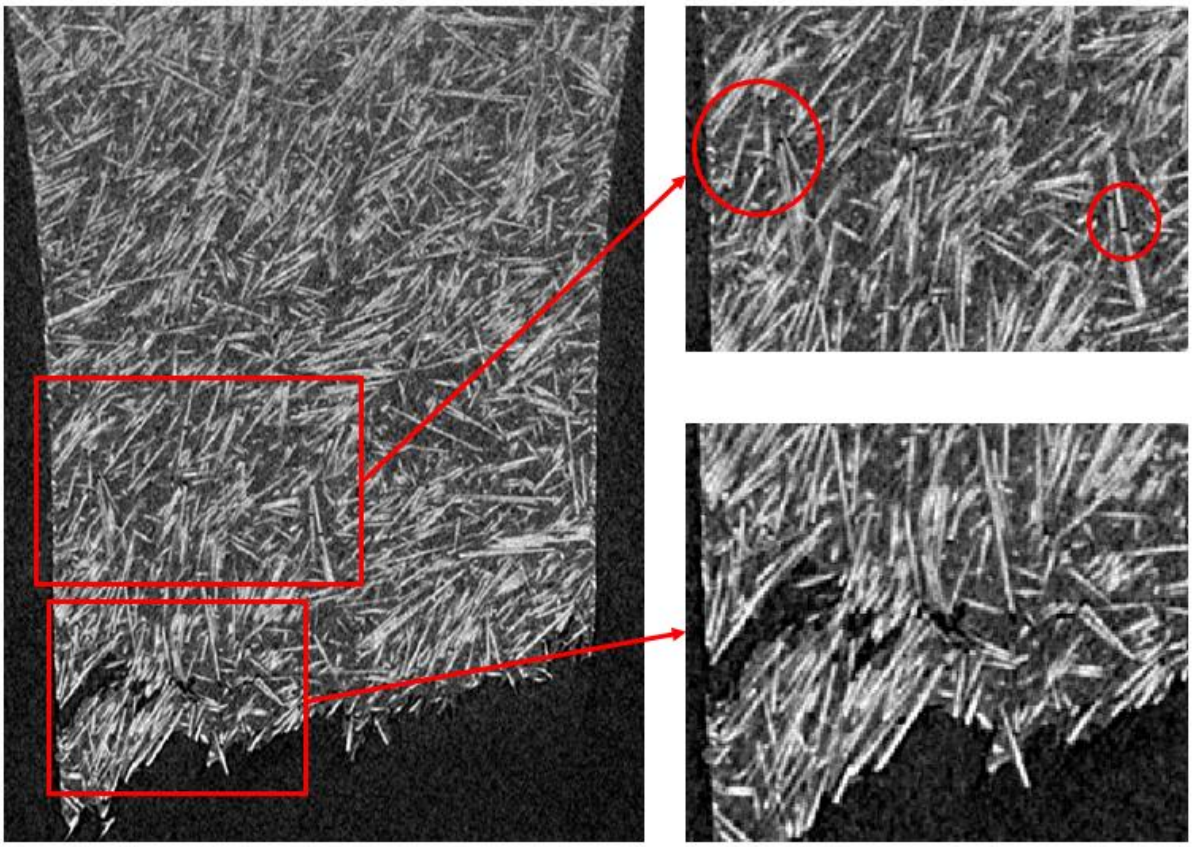

Figure 6-19 µCT image of the broken 45° specimen

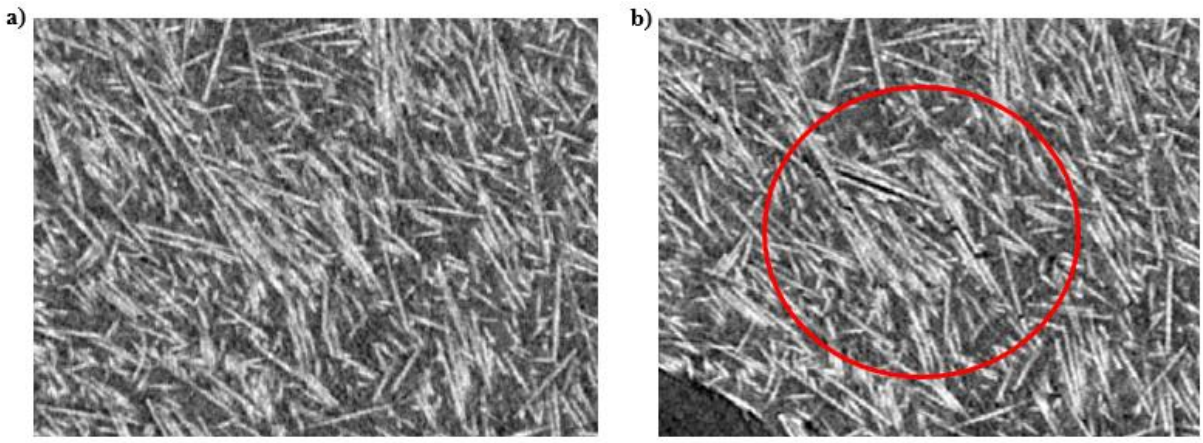

Figure 6-20 µCT image of the 45° specimen. a) before loading, b) after failure

6.4.3 90° specimen at room temperature

After conducting a DVC analysis on the gauge length of the 90° specimen tested at room temperature, the surface of the specimen exposed an angled strain concentration at 25% of the UTS, as seen in Figure 6-21a. At 50% of the UTS, shown in Figure 6-21b, more strain localisation appeared, and the strain became more distributed on the gauge length. At this stage, the strain increased by 12% compared to the strain at 25% of the UTS. Figure 6-21c illustrates the strain at 75% of the UTS, where the strain incremented a further 12.42%, and the strain distribution remained very similar. The specimen failed before reaching 95% of the UTS. Thus, no DVC analysis was carried out at that stress level.

A lateral view of the strain distribution over the surface of the specimen is depicted in Figure 6-22a-c. As can be seen in Figure 6-22a, the first load stage (25% of the UTS) generated a strain concentration mid-way between the edge and the core of the specimen, where the fibres are transversally aligned to the loading direction. Next, a second strain localisation appears at the other edge of the specimen at 50% of the UTS (see Figure 6-22b), which merged with the first strain concentration through lower strain areas. Finally, at 75% of the UTS, a more homogeneous strain distribution developed, and the value of the two strain concentration previously mentioned increased.

When inspecting a cut at the mid-thickness in the plane YZ, as illustrated in Figure 6-23a-c, two regions of higher strain are visible at the first load step (Figure 6-23a), one at the bottom and a second area starting from the right edge of the specimen. At this loading step, the strain seems lower than the strain on the surface (Figure 6-21a). Figure 6-23b presents the second load step when a band of strain concentration appears in the middle of the gauge length. This band of strain concentration looks like the propagation of the strain at the right side of the first load stage. At the final load step shown in Figure 6-23c, another strain localisation came into sight at the top right part of the gauge length. It is also noticeable that the strain is lower than at the surface of the specimen.

A cut at the mid-width in plane XY is shown in Figure 6-24a-c. Similar to what was found in the cut at mid-thickness, as seen in Figure 6-24a, the strain concentration that occurred at the first load step was lower than the strain at the surface. As the second load was applied, a strain path crossing the middle of the gauge length developed, having the highest value at the left edge of the specimen, as can be observed in Figure 6-24b. Figure 6-24c shows the third load stage. It is noticeable that the highest strain shifted towards the middle of the shell layer

where the fibres are transversal to the loading direction and that the strain was more homogeneous through the gauge length.

Figure 6-25a-b illustrates the microstructure at the surface of the specimen superimposed on the deformed mesh at the last load step, and Figure 6-26a-b shows the microstructure at mid-thickness overlapped on the deformed mesh at mid-thickness at the same load step. In Figure 6-25b, it is possible to observe that, similar to the other specimens, the strain localisation occurred in a region where the fibre density was low, and the fibres were poorly oriented towards the loading direction. This was also observed in Figure 6-26a-b, where it can be noticed that the strain that went across the width of the specimen followed the sides and the end of the fibres.

Doing a similar procedure on the lateral views, superimposing the microstructure on the deformed mesh at the maximum load step, reveals an analogous behaviour of the strain, concentrating on the location of weak fibre alignment in the loading direction, as can be seen in Figure 6-27a-d. The maximum strain value in Figure 6-27b appears to be located at the shell layer close to the core layer, where the fibres are aligned to the load direction. At mid-width, the highest strain is also located in a region near the core layer, see Figure 6-27d.

Figure 6-28a-b shows the deformed mesh at the last load step overlapped on the fractured specimen. Figure 6-28a depicts the front view, where it is noticeable that the strain is near the fracture path and is angled in the same orientation. Probably they do not match because the fracture occurred in the following step, where there is no DVC analysis. The lateral view is shown in Figure 6-28b and exposes that the strain concentration in the lateral view is nearby the fracture path and follows a similar trajectory.

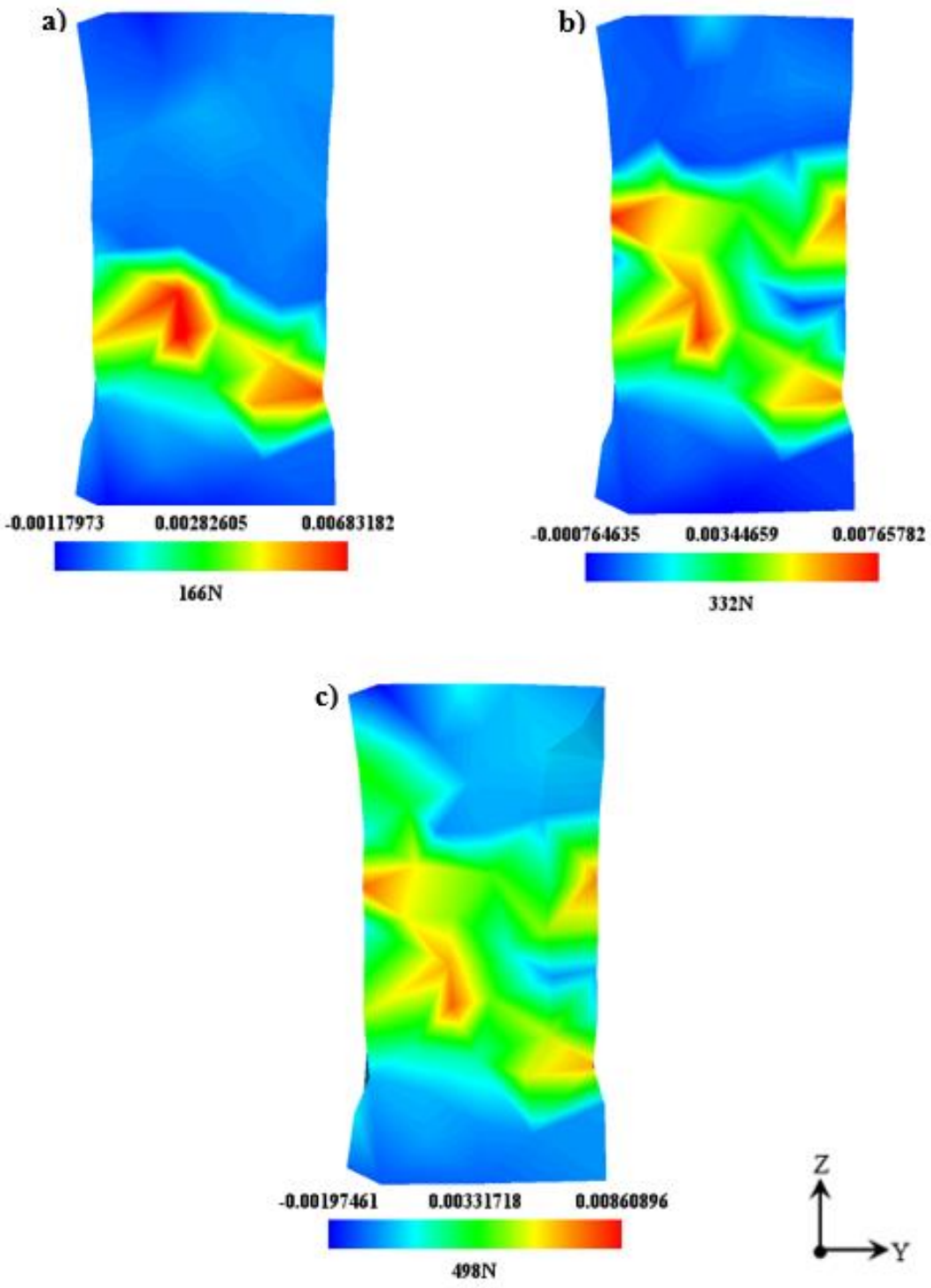

Figure 6-21 Tensile strain in the loading direction of a 90° specimen at room temperature at different stresses, a) 25% of UTS, b) 50% of UTS, c) 75% of UTS. Front view

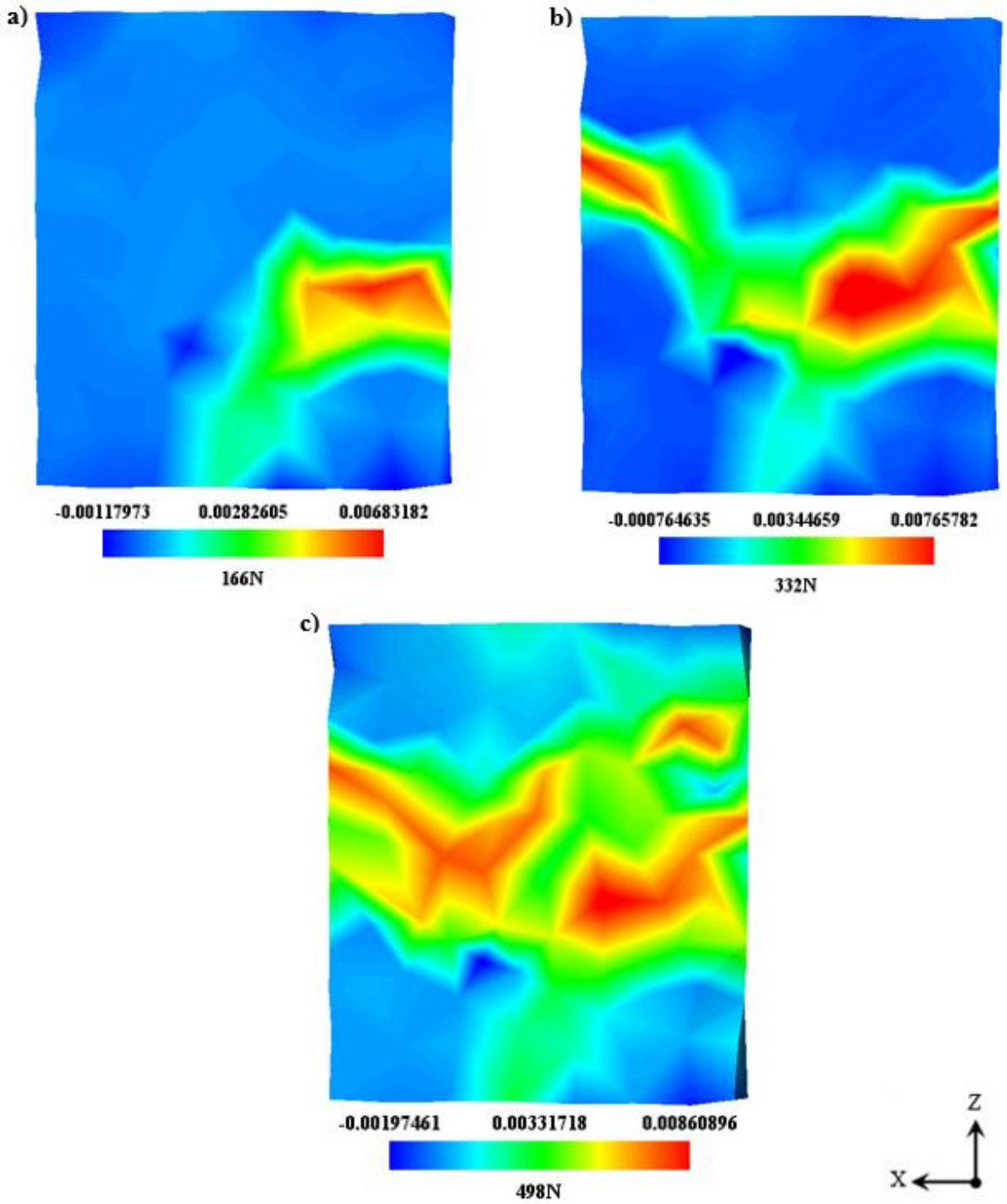

Figure 6-22 Tensile strain in the loading direction of a 90° specimen at room temperature at different stresses, a) 25% of UTS, b) 50% of UTS, c) 75% of UTS. Lateral view

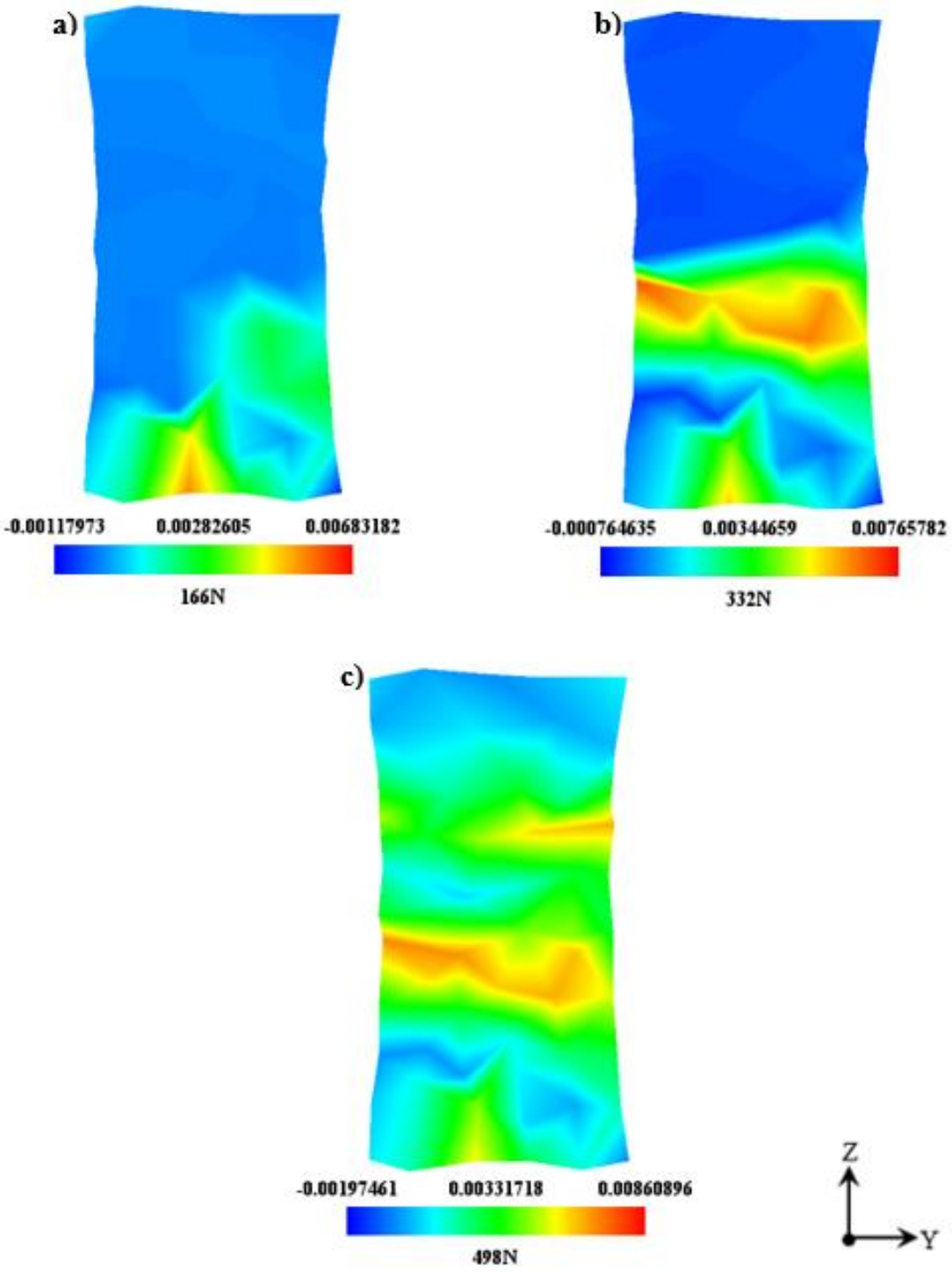

Figure 6-23 Tensile strain in the loading direction of a 90° specimen at room temperature at different stresses, a) 25% of UTS, b) 50% of UTS, c) 75% of UTS. Front view at mid-thickness

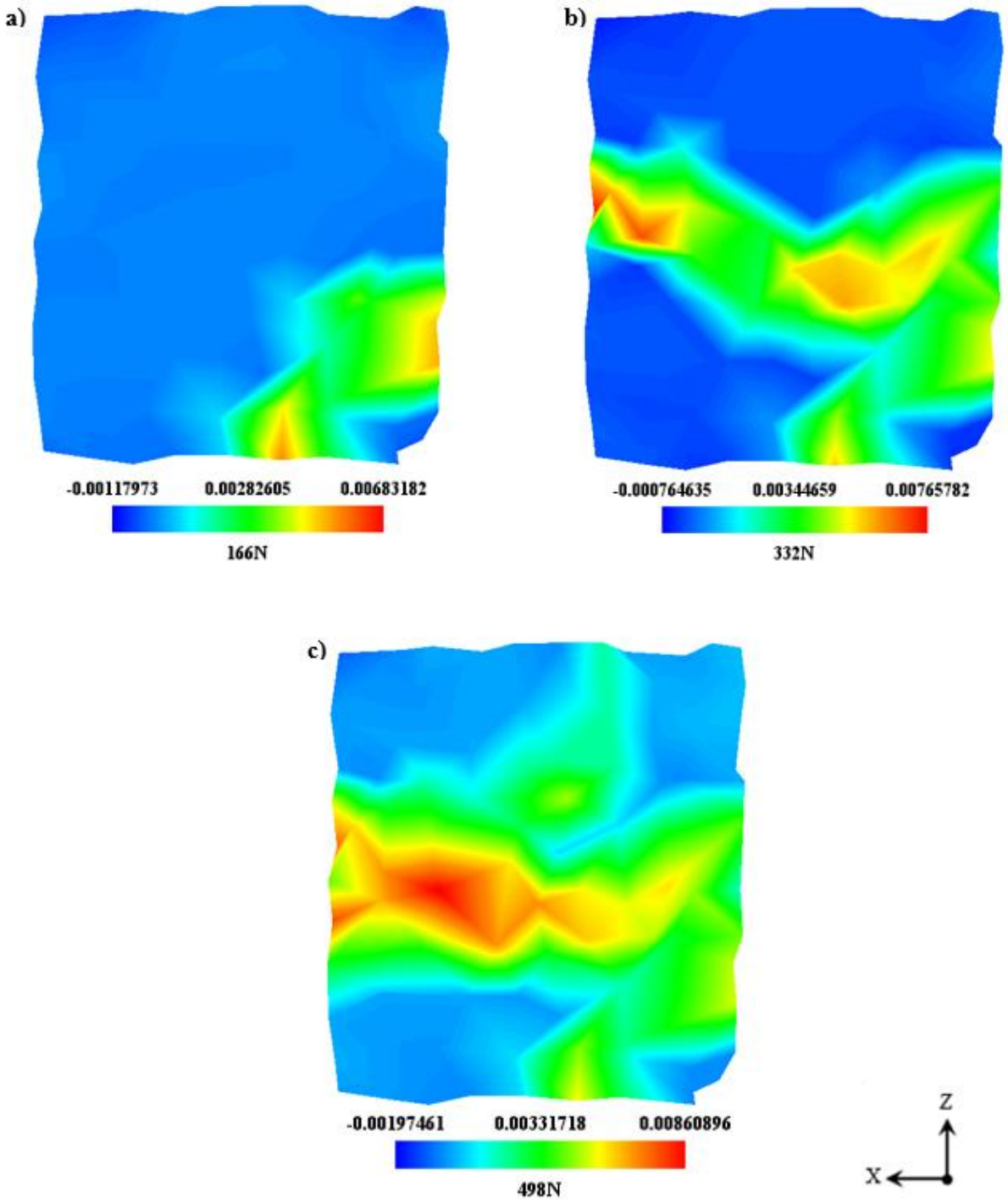

Figure 6-24 Tensile strain in the loading direction of a 90° specimen at room temperature at different stresses, a) 25% of UTS, b) 50% of UTS, c) 75% of UTS. Lateral view at mid-width

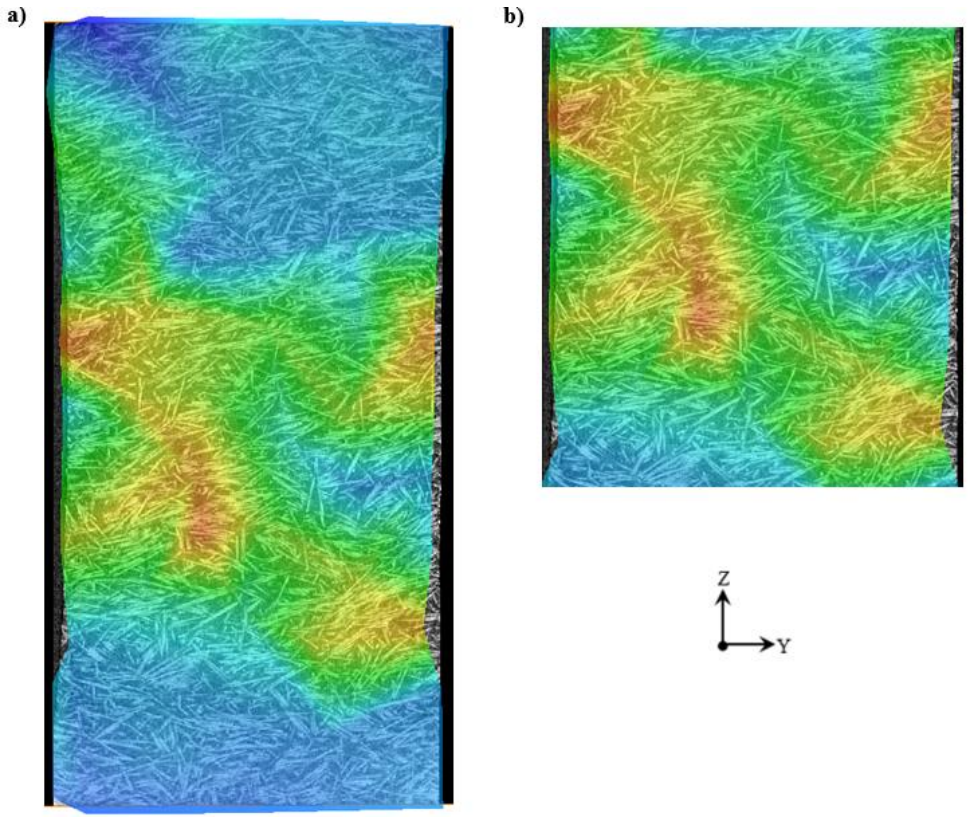

Figure 6-25 Superimposed deformed mesh on the microstructure of a 90° specimen. Front view. a) full gauge length of the specimen, b) zoom in to the region of strain localisation

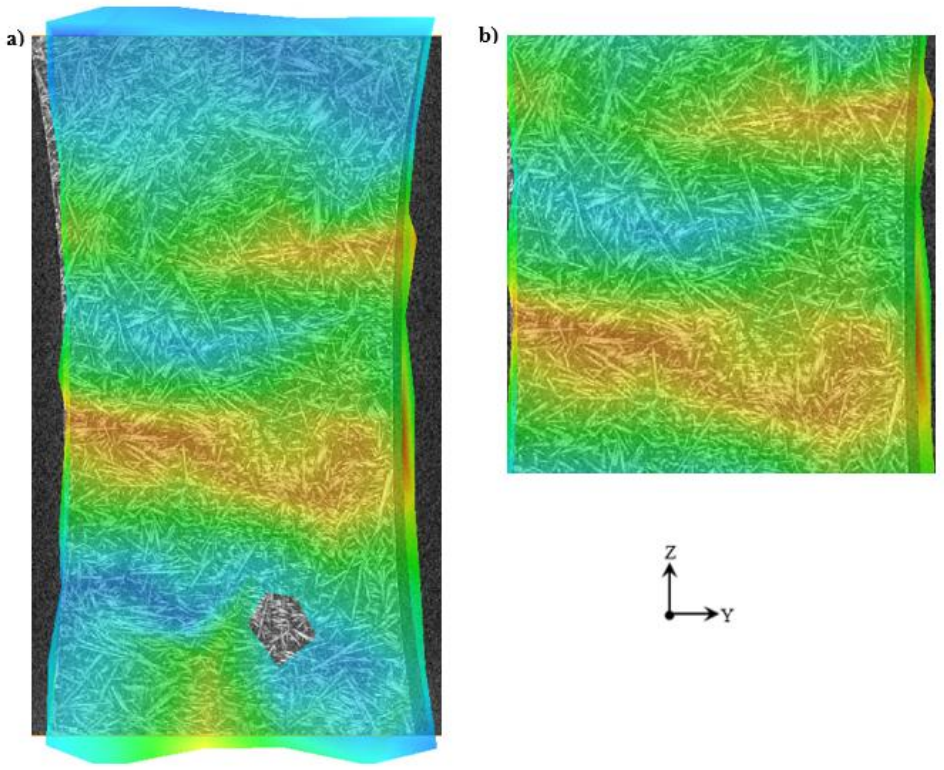

Figure 6-26 Superimposed deformed mesh on the microstructure of a 90° specimen. Front view at mid-thickness. a) full gauge length of the specimen, b) zoom in to the region of strain localisation

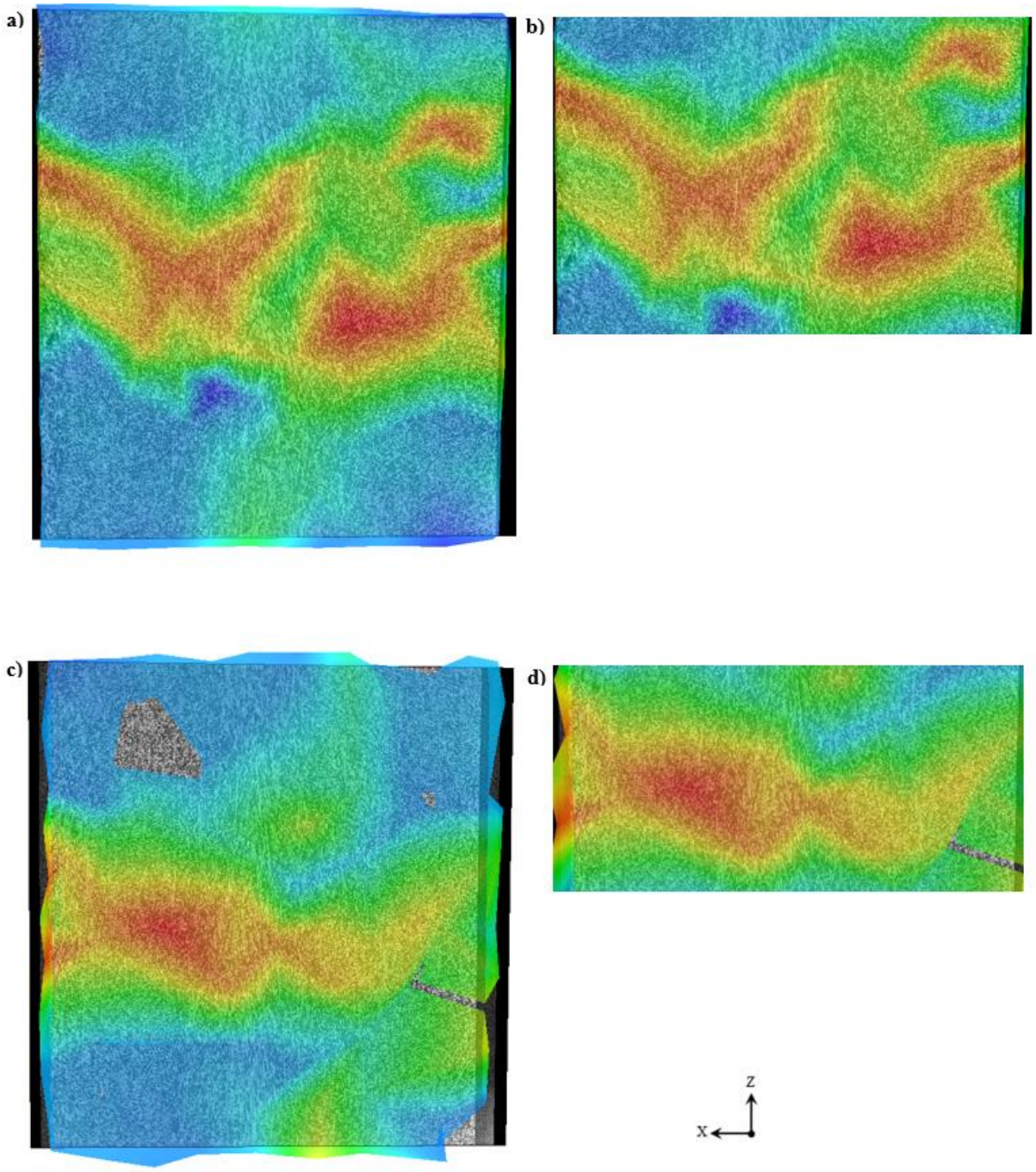

Figure 6-27 Superimposed deformed mesh on the microstructure of a 90° specimen. Lateral view. a) full gauge length of the specimen, b) zoom in to the region of strain localisation, c) Lateral view at mid-width, d) zoom in to the region of strain localisation at mid thickness

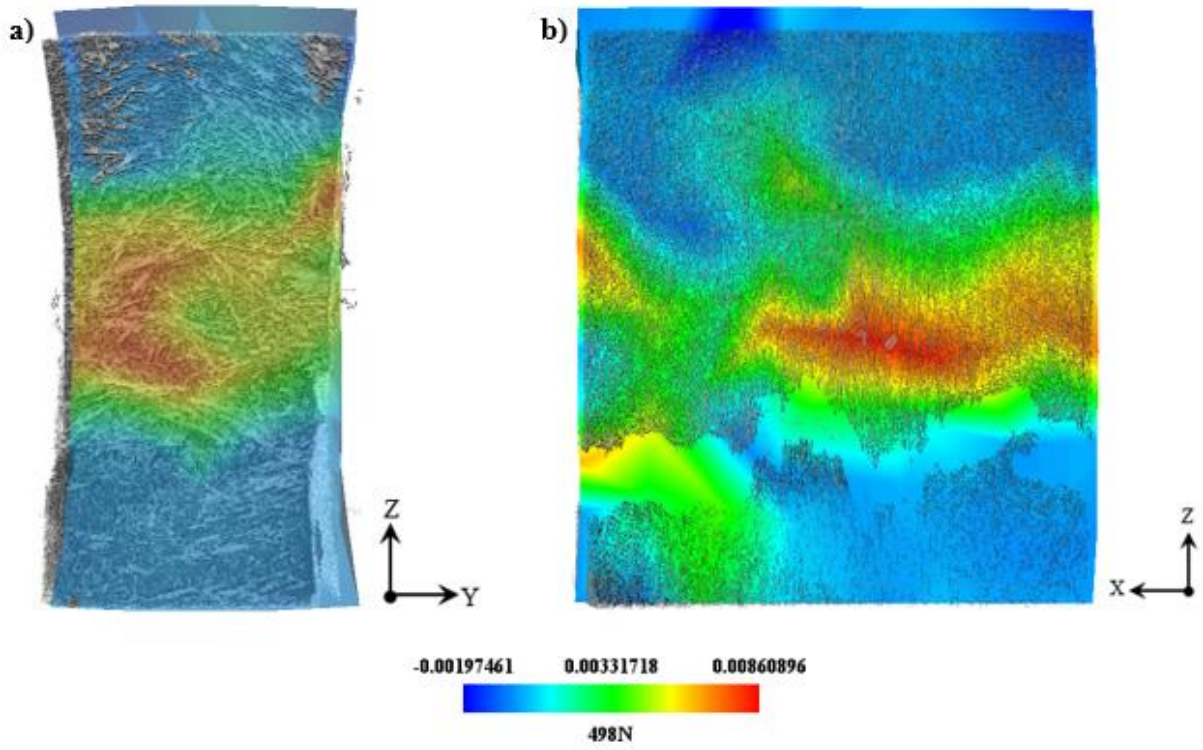

Figure 6-28 Deformed DVC mesh at 75% of the UTS superimposed on the fractured 90° specimen. a) Front view, b) lateral view

6.4.4 0° specimen at 50° C

An in-situ tensile test at 50° C was carried out inside the µCT using a 0° specimen. The details of the testing have been described in Chapter 3. The strain evolution on the front surface of the 0° sample tested at 50° C is shown in Figure 6-29a-d. During the first load step, Figure 6-29a, a strain concentration transversal to the force applied formed in the middle section of the gauge length of the sample, which continued to grow in value as the load was applied. In Figure 6-29b, the maximum value of the strain concentration increased by 147% compared to the first load stage. At 75% of the UTS, illustrated in Figure 6-29c, the strain localisation incremented 79% more than at 50% of the UTS (Figure 6-29b). Finally, at the last load stage, the strain concentration rose by 20% more than the previous load step, as can be seen in Figure 6-29c and Figure 6-29d.

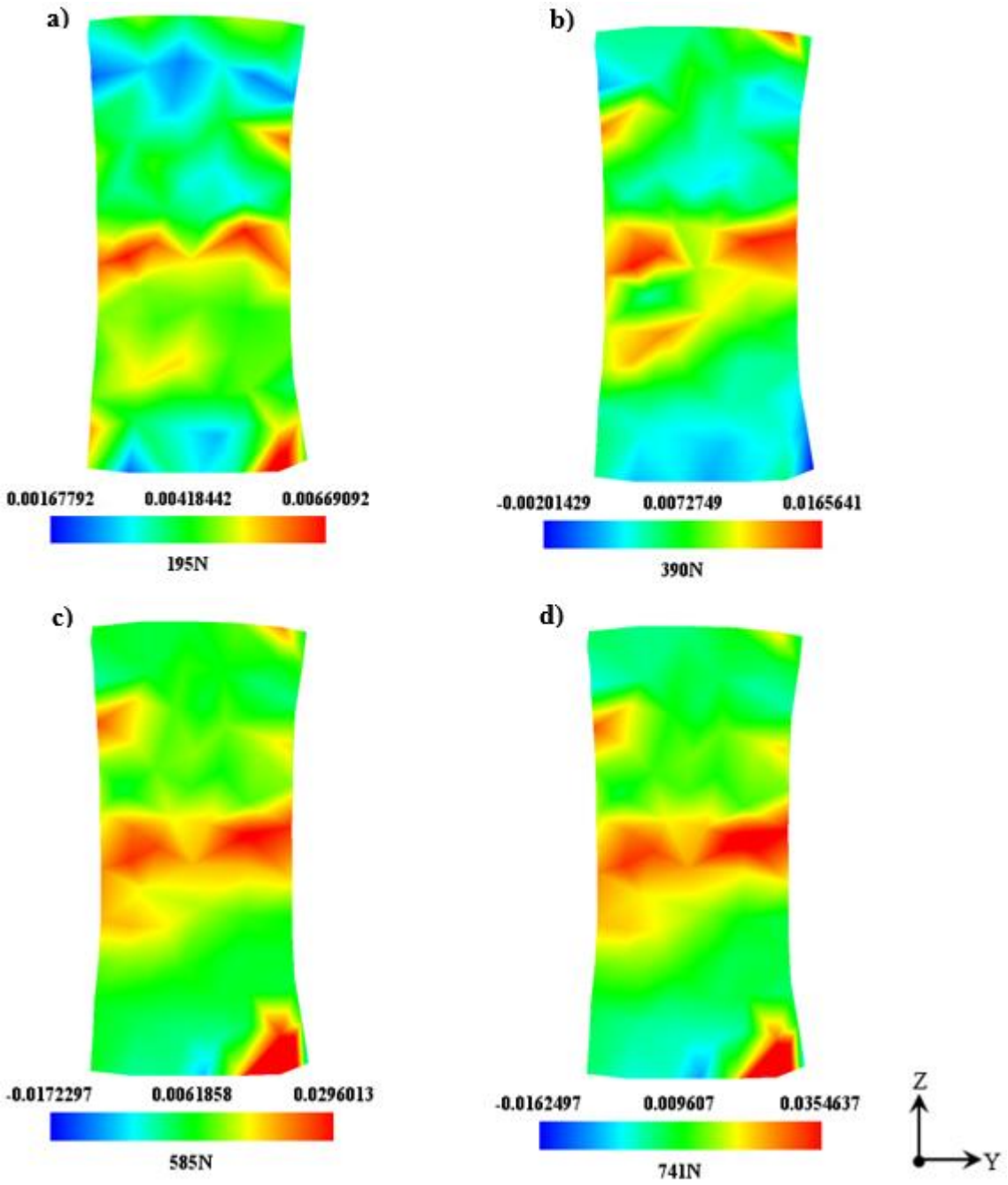

Figure 6-29 Tensile strain in the loading direction of a 0° specimen at 50°C at a) 25% of UTS, b) 50% of UTS, c) 75% of UTS, d) 95% of UTS. Front view

Figure 6-30a-d presents the development of the strain field on a lateral surface of the coupon. As can be seen in Figure 6-30a, a strain concentration starting from the right edge was formed and extended up to near the core region. At 50% of the UTS, shown in Figure 6-30b, two higher strain localisations were generated below the first strain concentration, and more strain evolved at the top left side of the sample. When the load reached 75% of the UTS, the strain at the edges of the specimen appeared to extend towards the centre of the coupon, as

illustrated in Figure 6-30c. Finally, at 95% of the UTS, shown in Figure 6-30d, the strain distribution seems to remain similar to the previous load step.

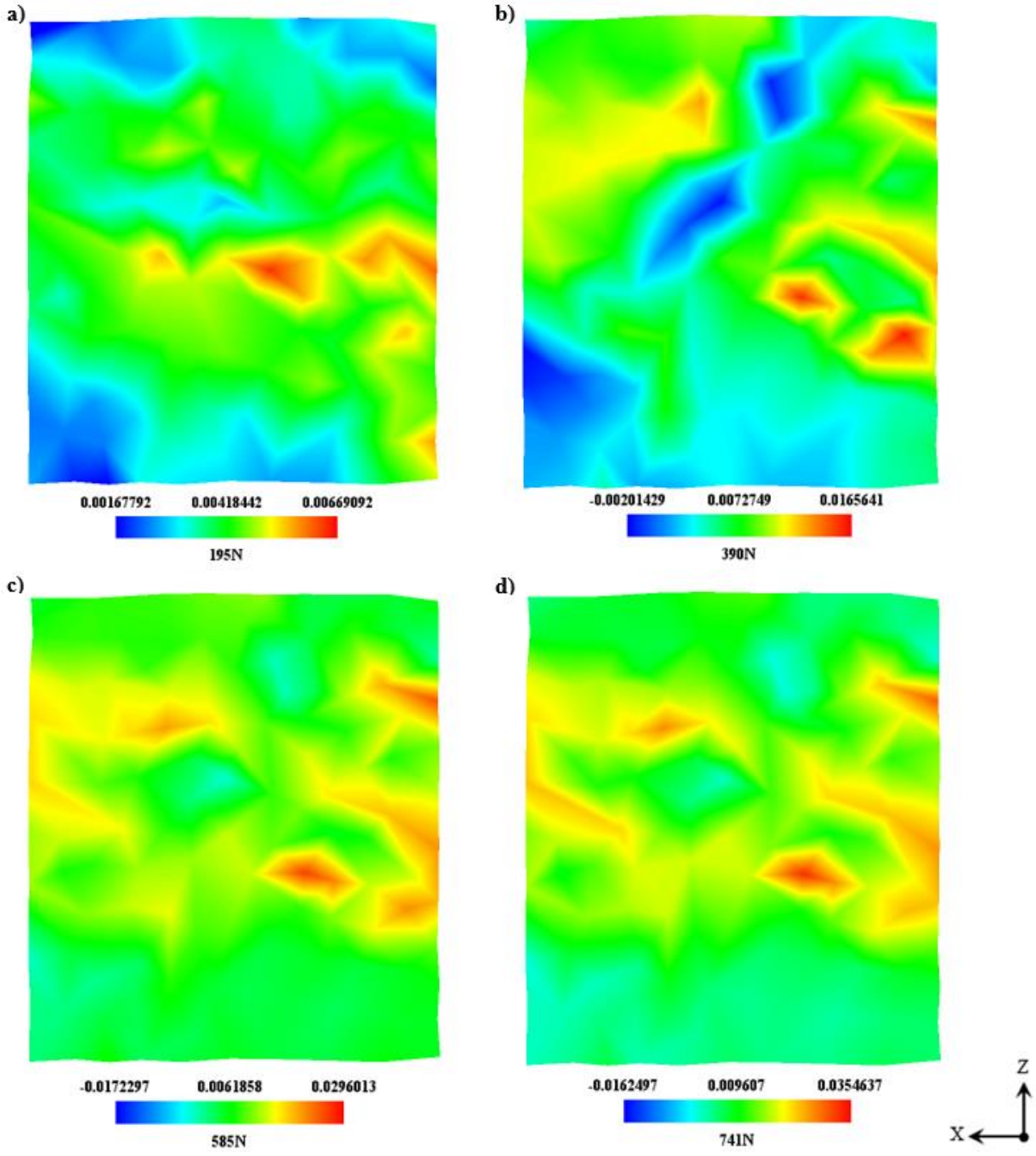

Figure 6-30 Tensile strain in the loading direction of a 0° specimen at 50°C at a) 25% of UTS, b) 50% of UTS, c) 75% of UTS, d) 95% of UTS. Lateral view

Figure 6-31a-d shows the strain evolution in the middle of the thickness. When the specimen was loaded at 25% of the UTS, a strain localisation occurred at the middle of the gauge length, as seen in Figure 6-31a. As the load reached 50% of the UTS, the strain concentrated in a region close to the edge of the specimen, as depicted in Figure 6-31b. At 75% of the UTS,

Figure 6-31c, the strain distribution seemed homogeneous in the gauge length, with the strain concentration now extended from one edge to another of the specimen. Figure 6-31shows the strain field at 95% of the UTS. At this loading stage, the strain seems to remain homogeneous with an increase in the value of the strain concentration only.

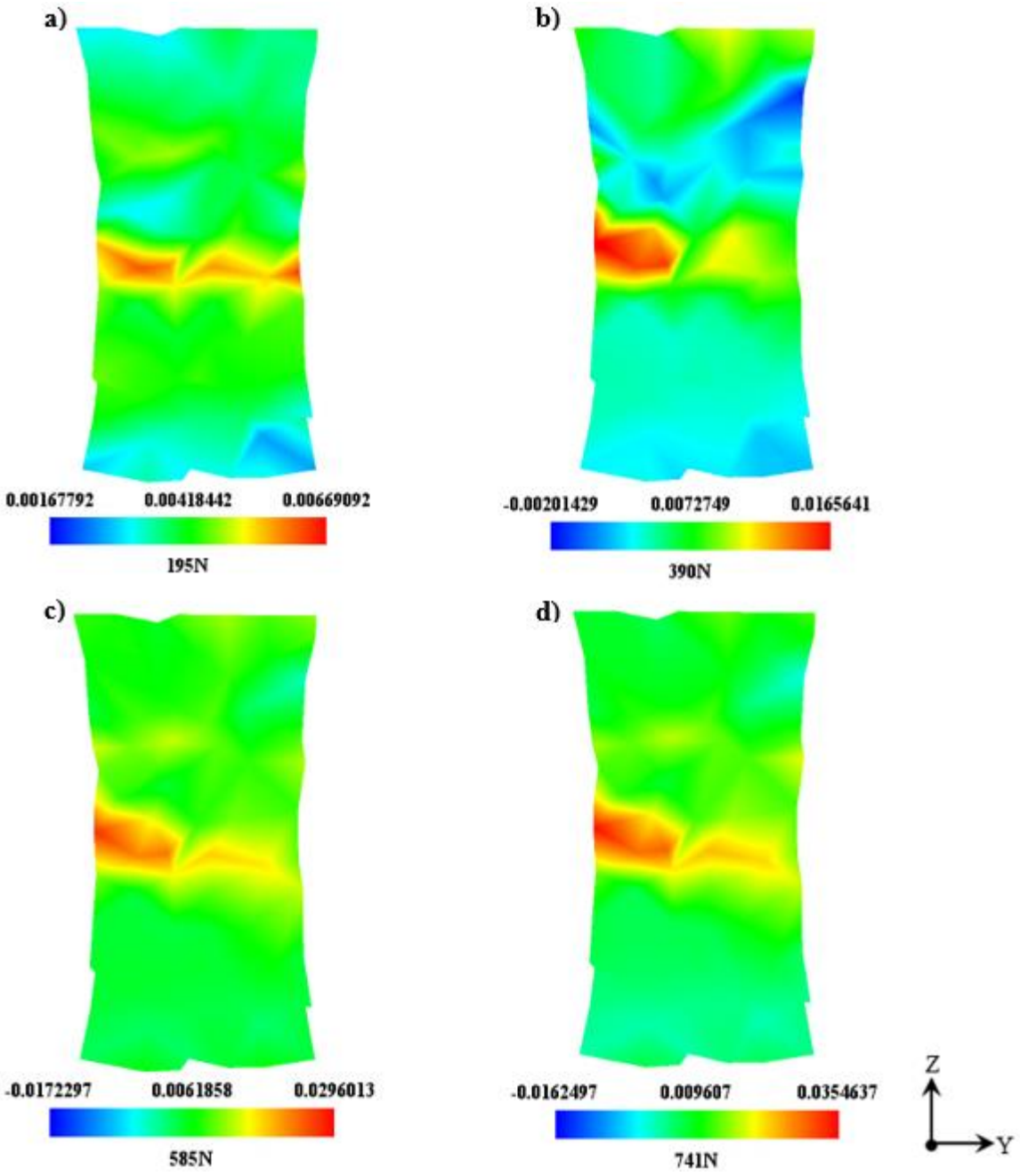

Figure 6-31 Tensile strain in the loading direction of a 0° specimen at 50°C at a) 25% of UTS, b) 50% of UTS, c) 75% of UTS, d) 95% of the UTS. Front view at mid-thickness

In Figure 6-32a, one can see that at mid-width at 25% of the UTS, a strain localisation starts at the front of the specimen and extends to the core region. At 50% of the UTS, shown in

Figure 6-32b, the initial strain concentration starts to merge with a strain localisation at the top. Figure 6-32c illustrates that the strain becomes homogeneous all over the gauge length and that the strain concentration increased its value at the front of the specimen. This strain increment occurred in the skin region, where the fibres are randomly oriented. Figure 6-32d shows the strain distribution at the final loading stage. This strain distribution is very similar to the previous stage, but the value of the highest strain incremented.

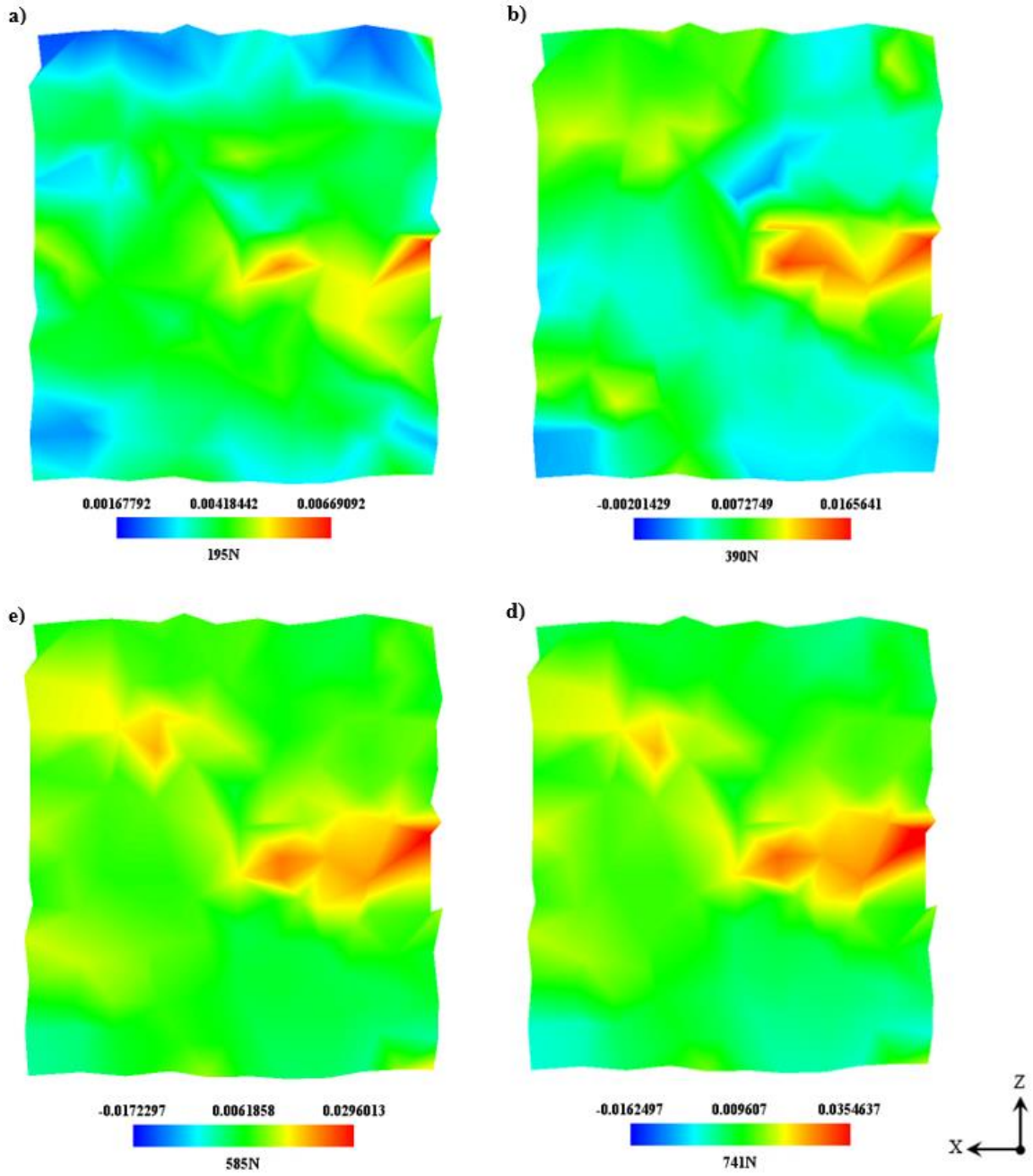

Figure 6-32 Tensile strain in the loading direction of a 0° specimen at 50°C at a) 25% of UTS, b) 50% of UTS, c) 75% of UTS, d) 95% of UTS. Lateral view at mid-width

Inspecting Figure 6-33a, where the specimen's microstructure is overlapped on the deformed mesh at the final load step, it is visible that, again, the strain concentration happened at a region of low fibre density. Figure 6-33b presents a cut at the mid-thickness of the sample, and the deformed mesh overlapped. It is possible to observe that at this point, the strain concentration occurred where most of the fibres are oriented perpendicular to the loading direction.

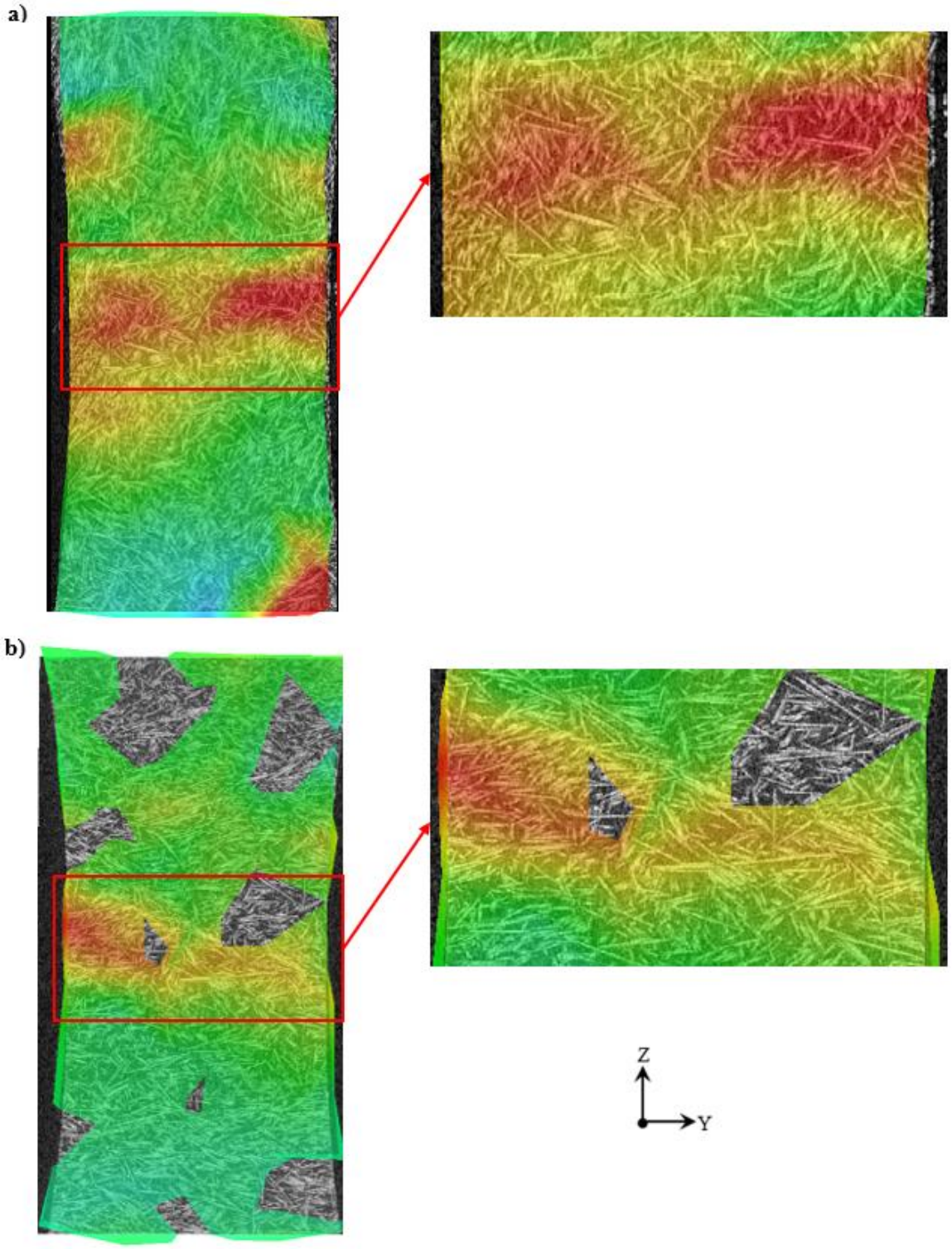

Figure 6-33 Superimposed deformed mesh on the microstructure of a 0° specimen at 50° C. Front view. a) front surface, b) cut at mid-thickness

Figure 6-34a shows the lateral surface of the deformed mesh superimposed on the microstructure. It is noticeable that the highest strain concentration is located in the core region near the shell layer, almost in the transition between those layers. Strain concentrations

at the skin layer are visible on both sides of the sample. In Figure 6-34b, one can see similar behaviour under the surface at the mid-width of the specimen.

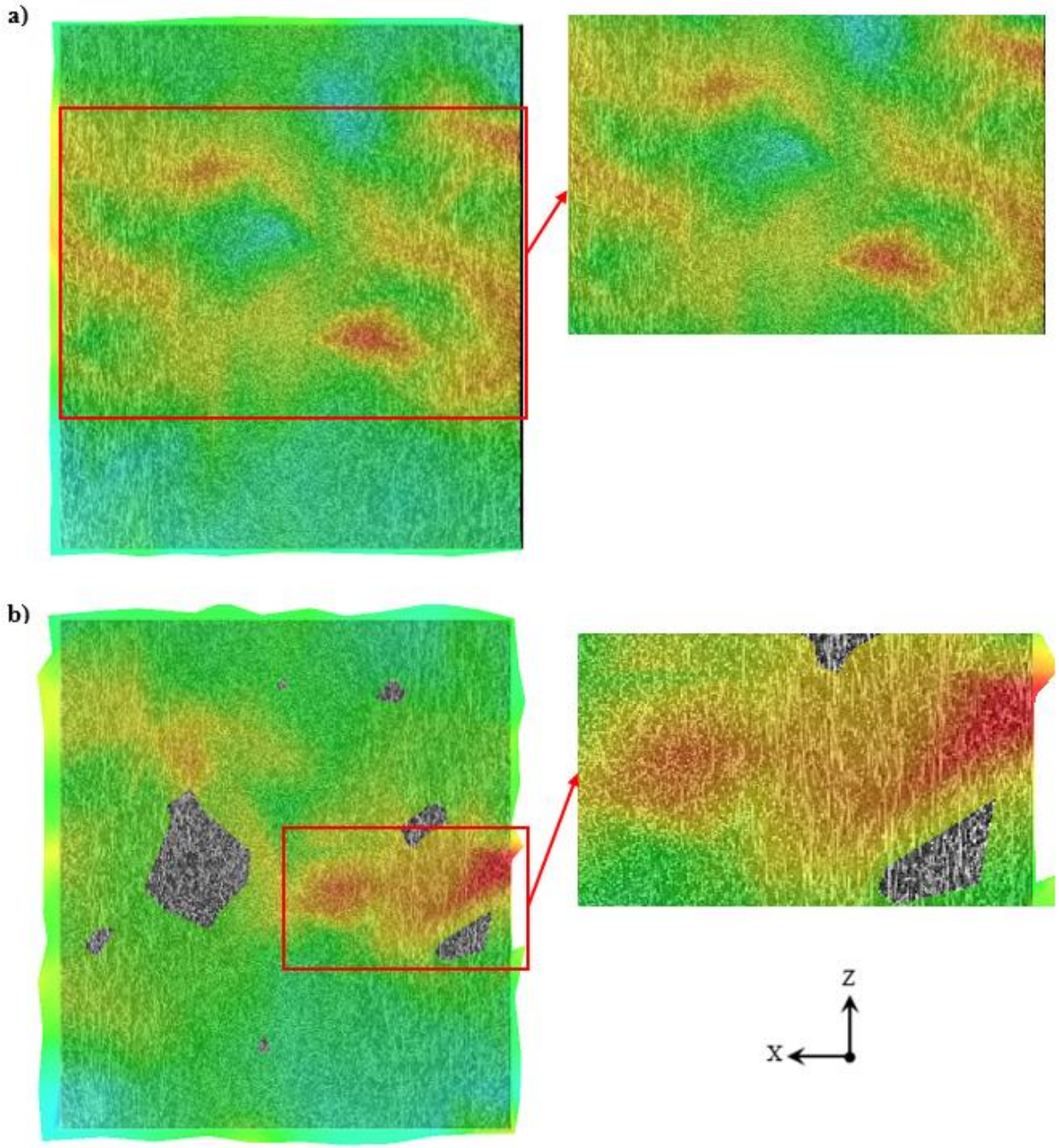

Figure 6-34 Superimposed deformed mesh on the microstructure of a 0° specimen at 50° C. Lateral view. a) surface, b) cut at mid-width

Careful examination of the μCT images revealed damage in the sample as shown in Figure 6-35. The damage mechanism detected were: fibre failure, matrix cracking, debonding at the fibre matrix interface and mainly debonding at the fibre ends.

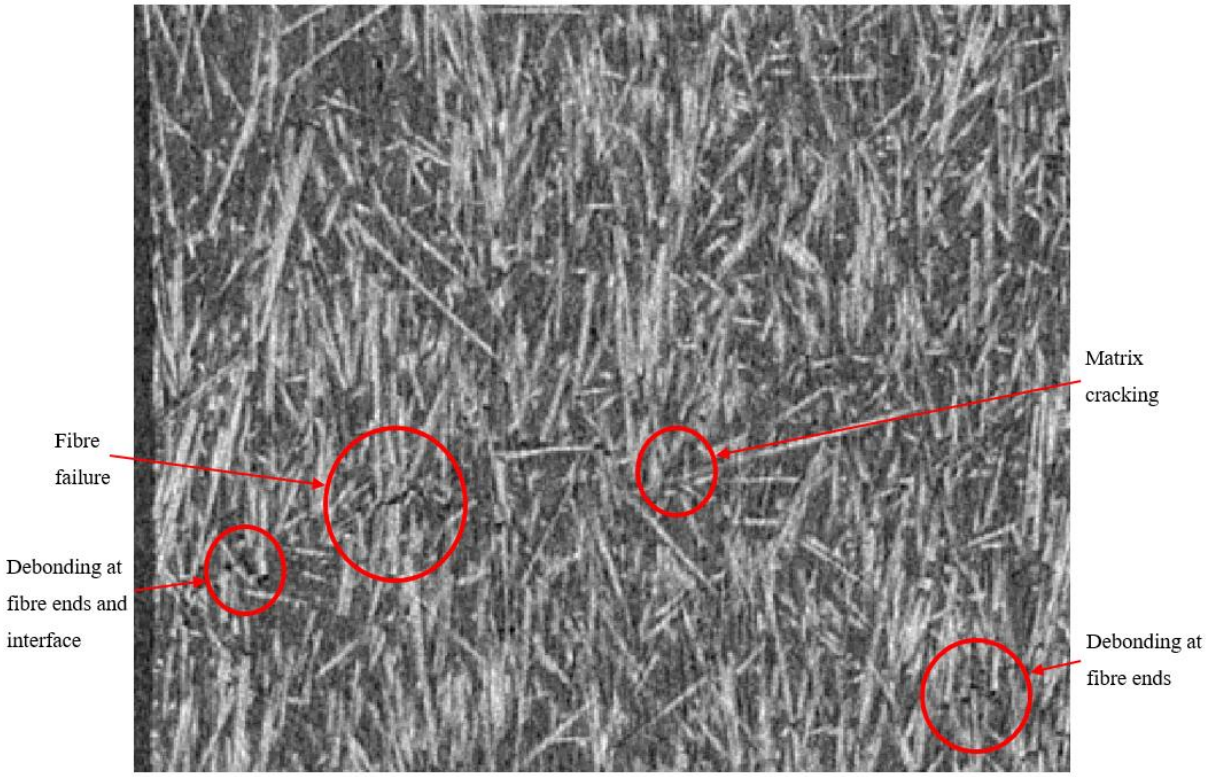

Figure 6-35 µCT image of 0° specimen at 50° C showing damage in the sample

6.4.5 0° specimen at 100° C

Figure 6-36a-d shows the strain distribution of a 0° coupon tested at 100° C inside the µCT. As seen in Figure 6-36a, when the sample was loaded at 25% of the UTS, strain concentrations formed close to the end of the gauge length. At 50% of the UTS, two evident strain localisations appeared near the specimen's shoulders, as illustrated in Figure 6-36b. In the next load step, Figure 6-36c, the bottom strain concentration decreased, but the top one remained. Figure 6-36d depicts the final load step, where the bottom strain concentration disappeared, and the top strain localisation increased by 45% from the previous load stage.

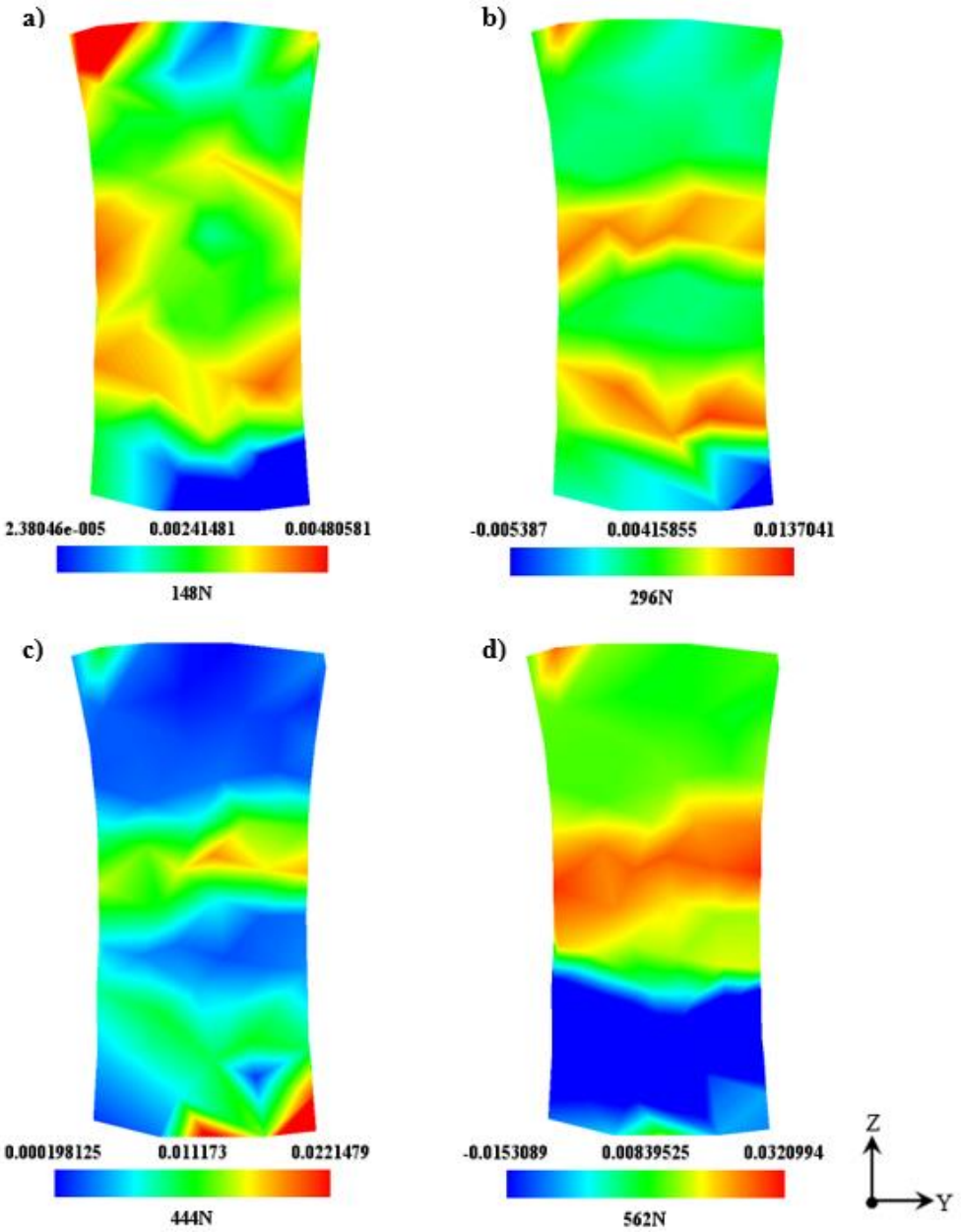

Figure 6-36 Tensile strain in the loading direction of a 0° specimen at 100° C at a) 25% of UTS, b) 50% of UTS, c) 75% of UTS, d) 95% of UTS. Front view

Figure 6-37a shows the lateral view at the first load step. It seems that the strain concentrations at the front surface go along the thickness of the sample. At 50% of the UTS, Figure 6-37b, the strain concentrates in three regions. The bottom strain is concentrated in the thickness's front and middle. In contrast, the concentration at the top is at a region shifted from the centre of the thickness. In the third load step, the strain at the top remained, whereas the bottom strain was reduced, as illustrated in Figure 6-37. Finally, at 95% of the UTS, the top strain concentration increased through the thickness, as seen in Figure 6-37d.

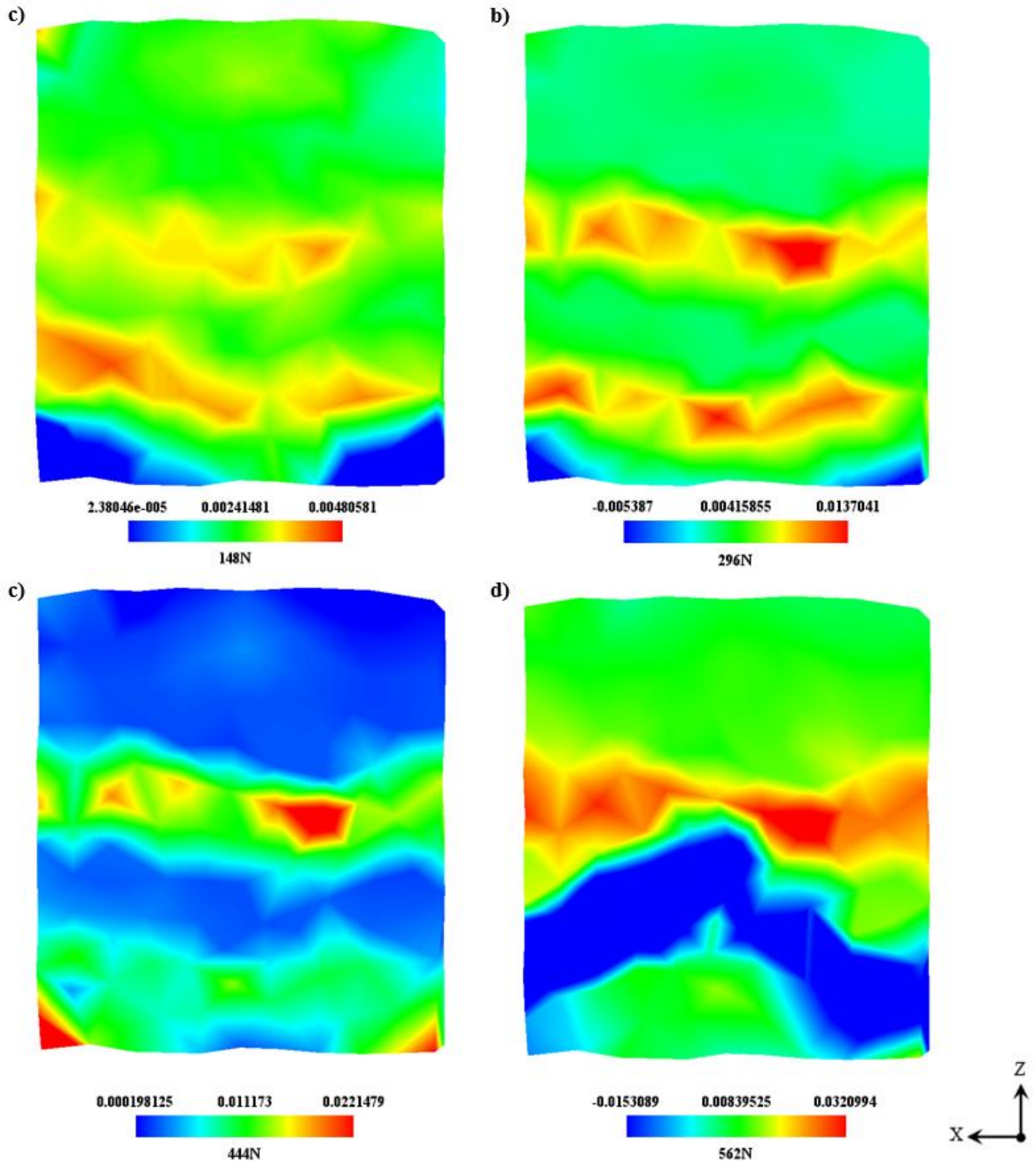

Figure 6-37 Tensile strain in the loading direction of a 0° specimen at 100° C at a) 25% of UTS, b) 50% of UTS, c) 75% of UTS, d) 95% of UTS. Lateral view

The strain evolution at a cut through the thickness is shown in Figure 6-38a-d. The strain development was similar to the one observed at the surface, shown in Figure 6-36a-d. The difference observed was that the strain concentration seemed near the specimen's edge.

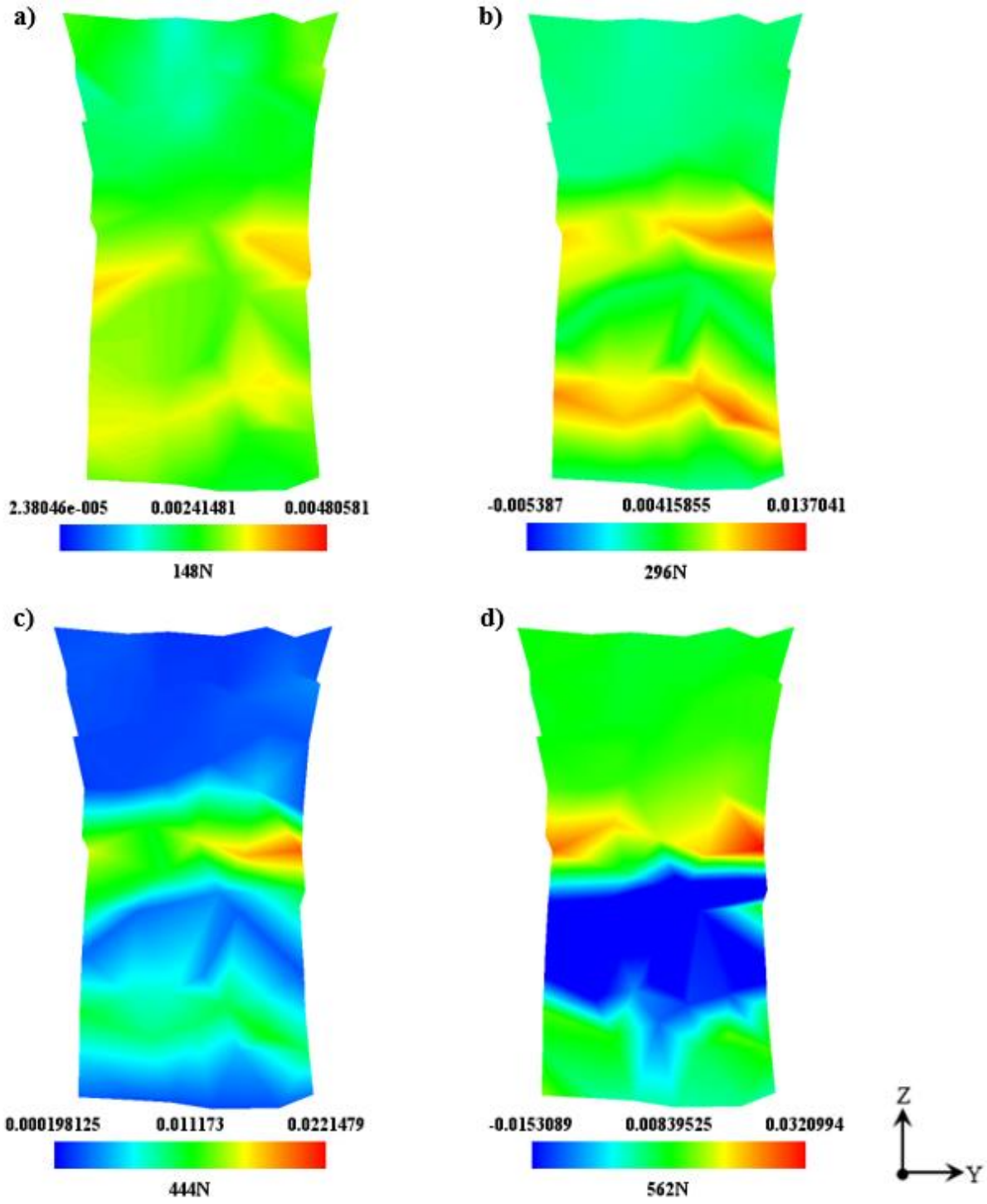

Figure 6-38 Tensile strain in the loading direction of a 0° specimen at 100° C at a) 25% of UTS, b) 50% of UTS, c) 75% of UTS, d) 95% of the UTS. Front view at mid-thickness

Figure 6-39a-d illustrates the strain development at a lateral cut at mid-width in the plane XZ. The strain evolution observed resembles the strain on the surface.

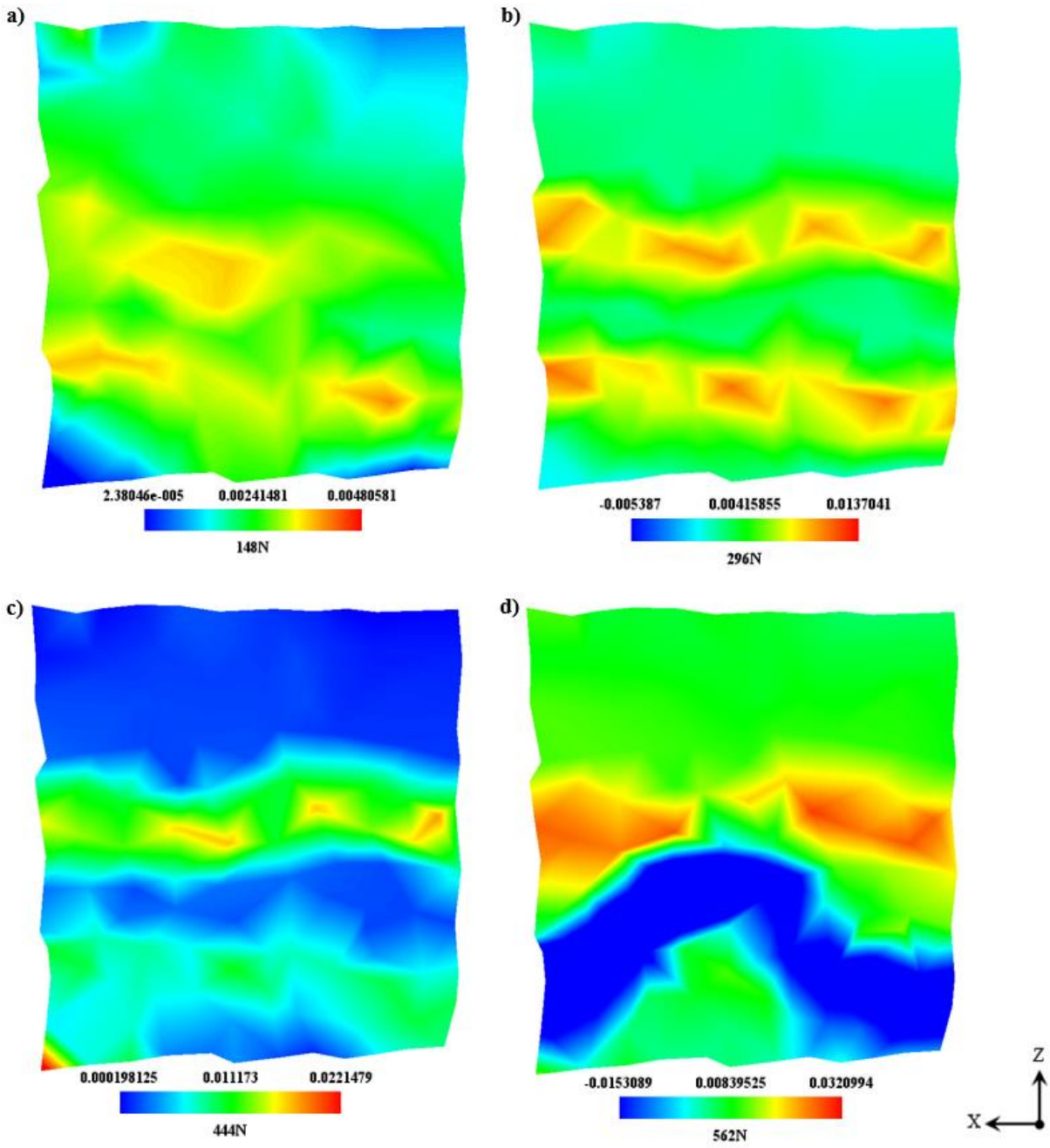

Figure 6-39 Tensile strain in the loading direction of a 0° specimen at 100° C at a) 25% of UTS, b) 50% of UTS, c) 75% of UTS, d) 95% of UTS. Lateral view at mid-width

Observing Figure 6-40a, it is noticeable that the strain seems to follow a path through the fibre ends. In contrast, at mid-thickness, shown in Figure 6-40b, the strain appears to localise at an area of low fibre density and poor alignment.

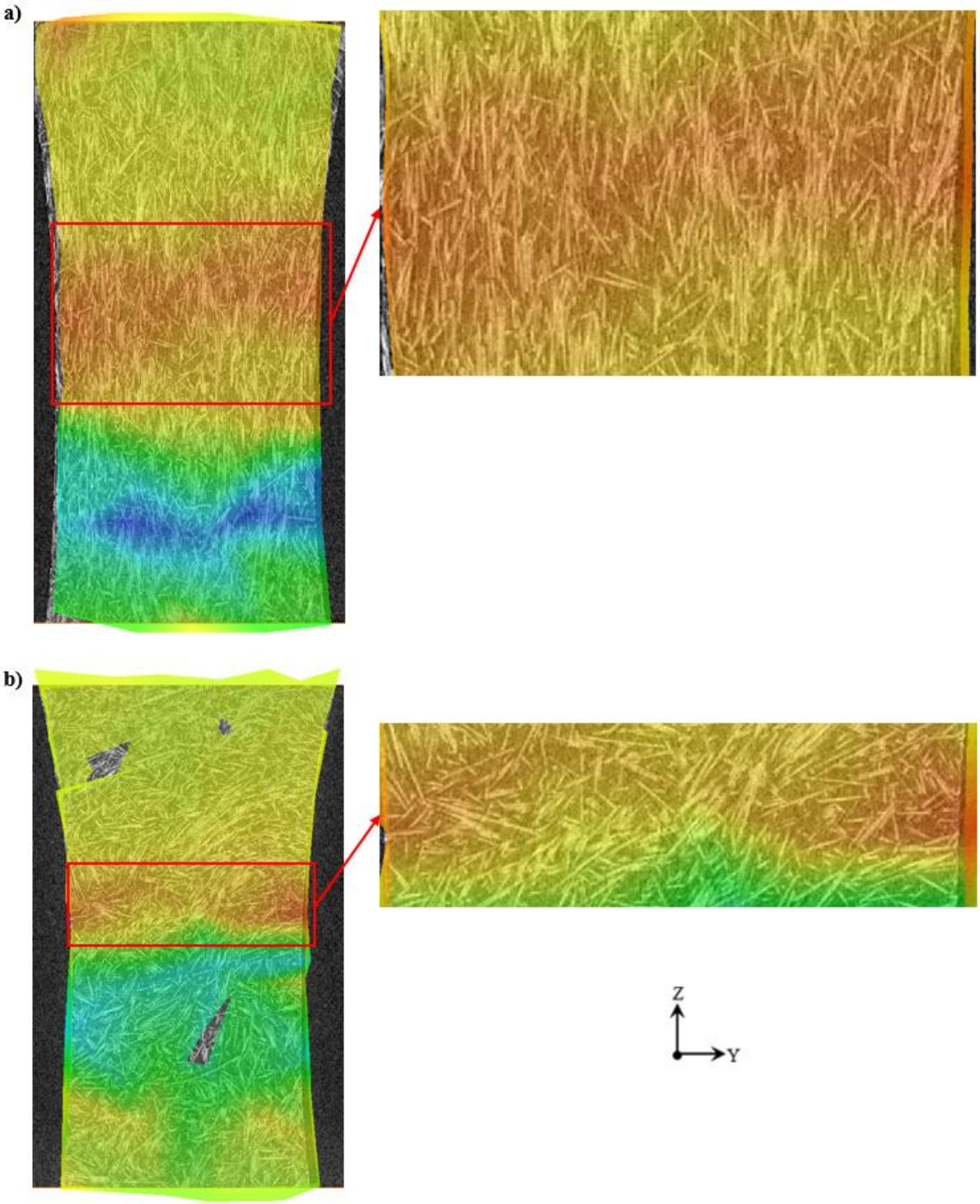

Figure 6-40 Superimposed deformed mesh on the microstructure of a 0° specimen at 100° C. Front view. a) front surface, b) cut at mid-thickness

A lateral view of the microstructure superimposed on the deformed mesh at the final load step is depicted in Figure 6-41a-b. Figure 6-41a reveals that the highest strain localisation appears at a region between the shell layer and the core, where the fibre orientation changes from 0° to 90°. Besides this, the strain localisation took place in regions with low fibre density. At mid-

width, Figure 6-41b, the strain at the shell layer (where the fibres are oriented at 0°) seems to follow a path where there are fibres at 90° mixed.

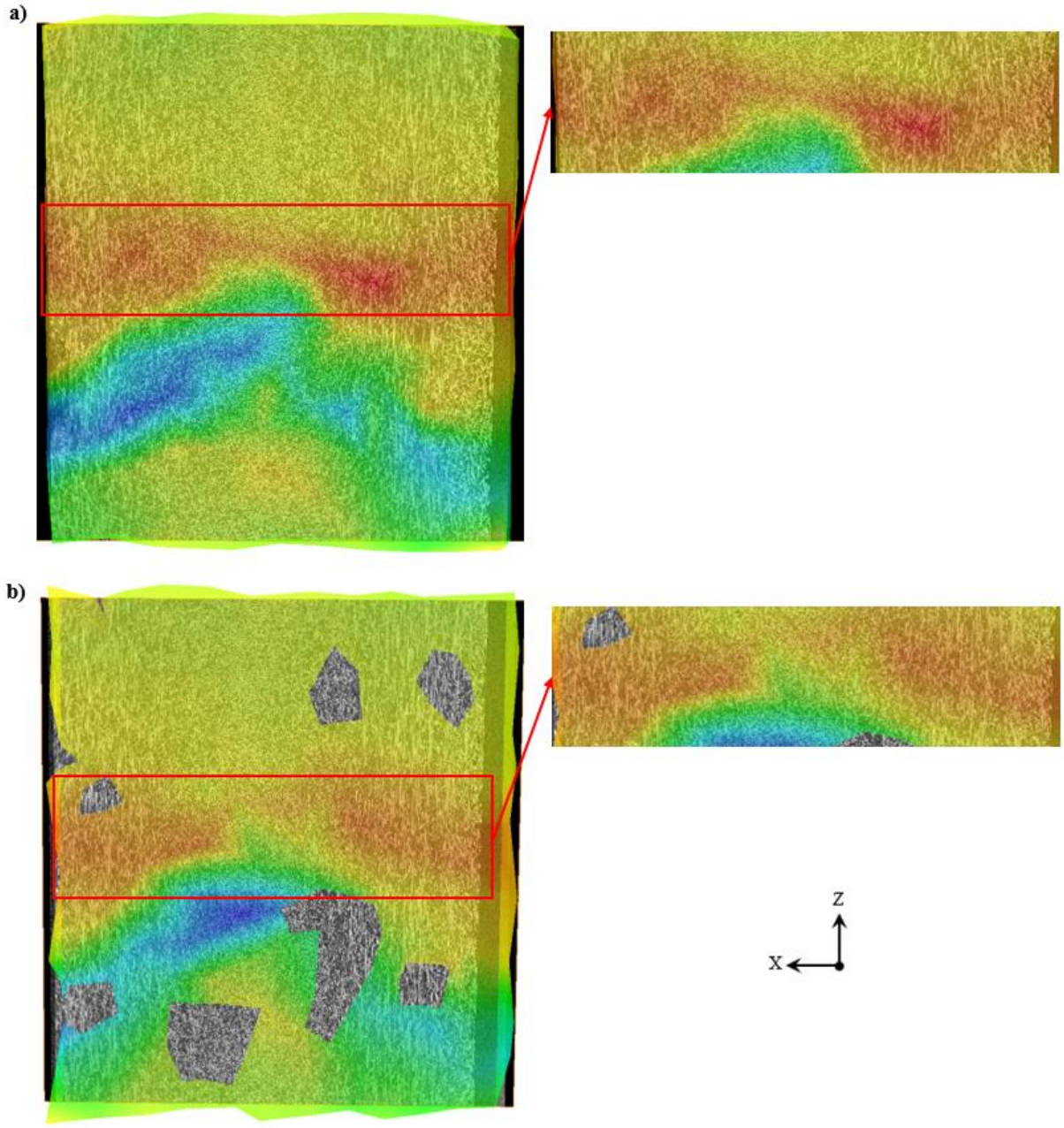

Figure 6-41 Superimposed deformed mesh on the microstructure of a 0° specimen at 100° C. Lateral view. a) surface, b) cut at mid-width

6.5 X-ray scanning of fatigued specimens after failure

Figure 6-42a shows the front view of the scanned fracture surface of a 0° specimen used in the fatigue testing at 50°C. It can be seen that the secondary crack started from the edge of the specimen. In Figure 6-42b, the lateral view of the sample is illustrated, along with an image of

a region with the most significant crack opening, typically the location of crack initiation. In this image, it seems that the secondary crack followed a path along the sides and tips of the fibres, with a limited number of broken fibres.

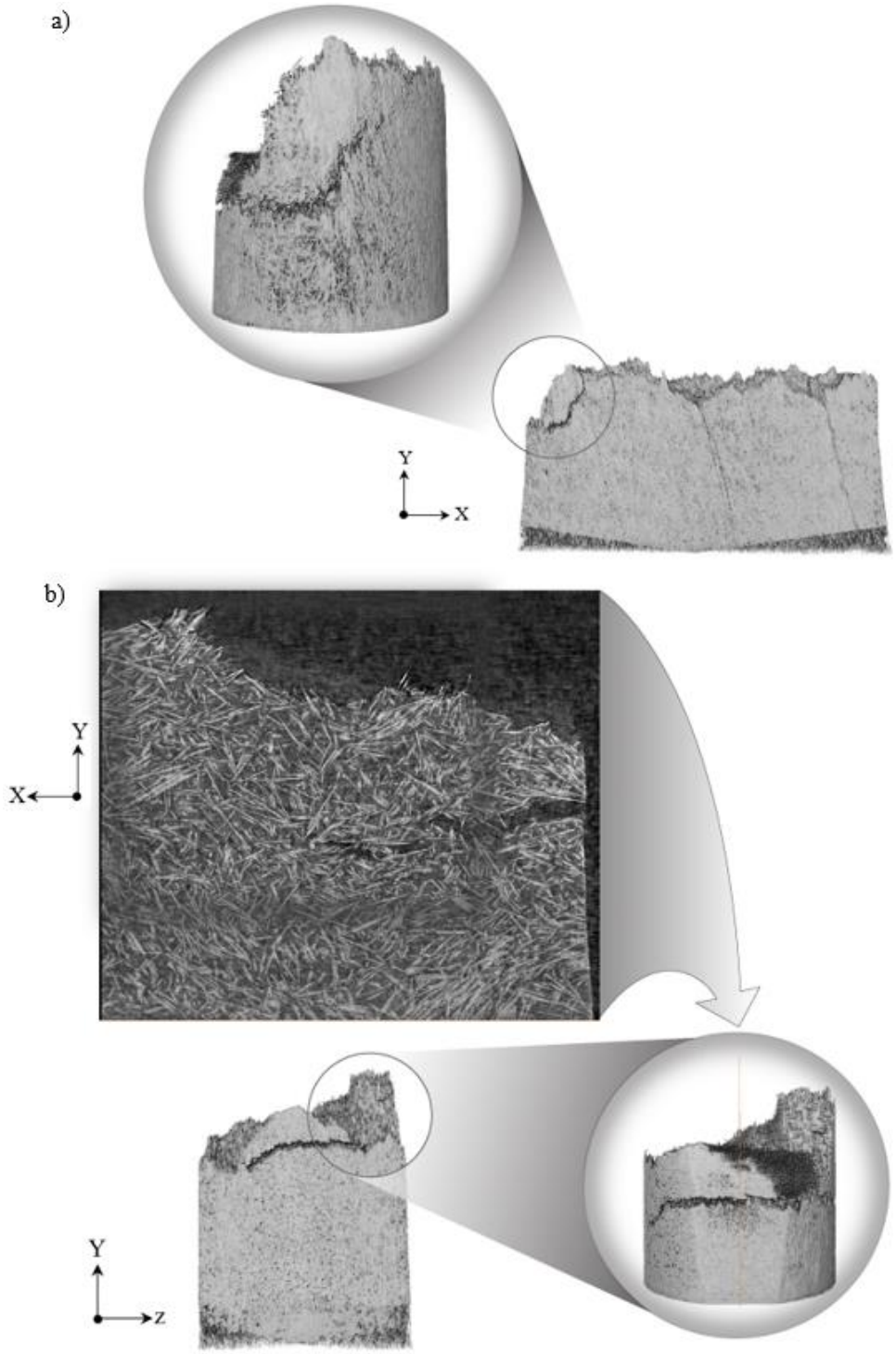

Figure 6-42 Scanned fracture surface of a fatigue 0° specimen tested at 50° C. a) front view, b) lateral view

Similar to what was shown in Figure 6-42a, the secondary crack detected in the 90° specimen tested at 50° C started from the sample edge, as seen in Figure 6-43a. Figure 6-43b illustrates an image below the surface of the secondary crack. In this image, a third crack was revealed under the surface. Unlike the secondary crack, this third crack does not start from the coupon edge. However, analogous to the other crack, it mainly propagated through the sides and tips of the fibres.

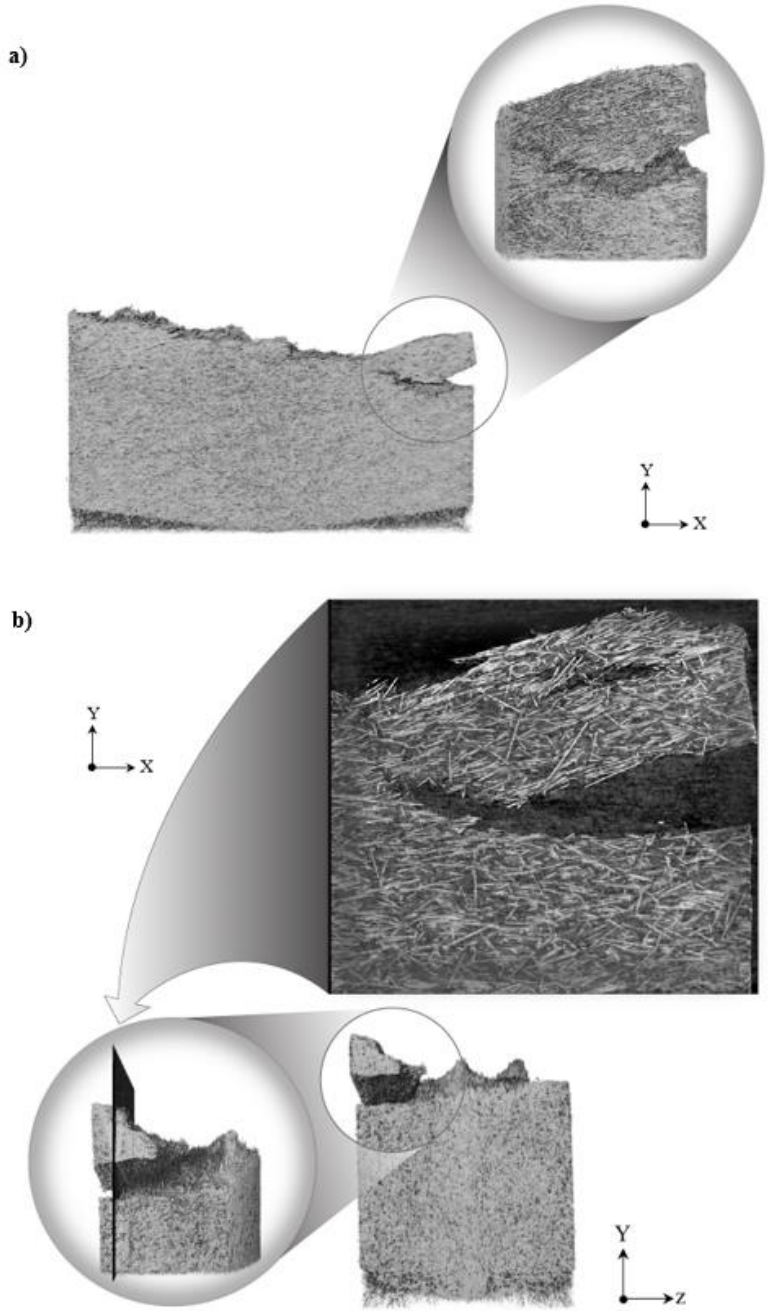

Figure 6-43 Scanned fracture surface of a fatigue 90° specimen tested at 50° C. a) front view, b) lateral view

Figure 6-44a depicts an image of the surface of a 90° specimen tested at 100° C, where a crack is very evident. Going below the surface, it is noticeable that the crack is located and follows a region of highly concentrated fibres oriented transversal to the load, as seen in Figure 6-44b. This crack continues to 229.2 μm below the surface, as shown in Figure 6-44c, where the concentration of poorly oriented fibres seems to be reduced.

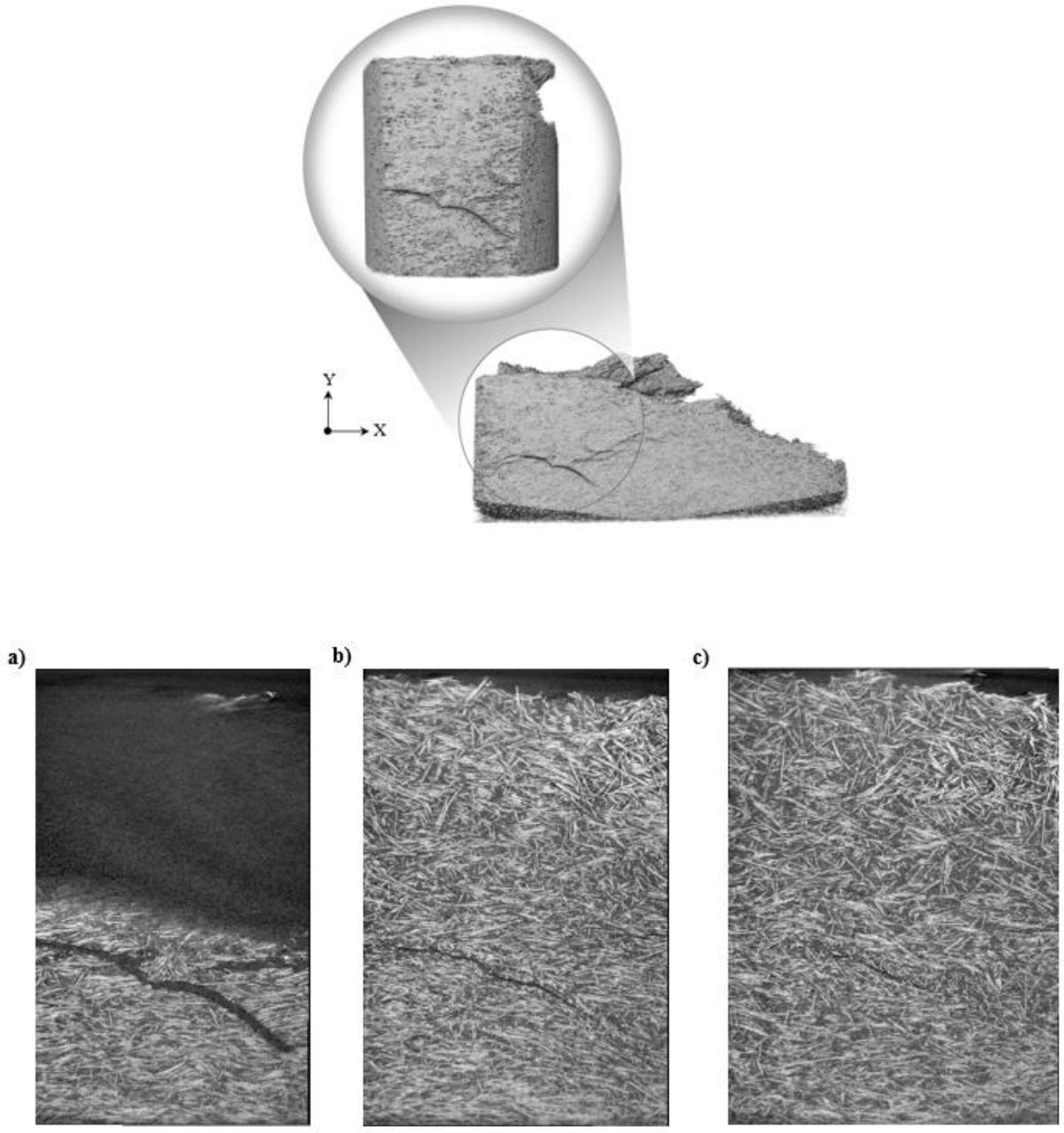

Figure 6-44 Scanned fracture surface of a fatigue 90° specimen tested at 100° C. a) surface, b) 114.6μm below the surface, c) 229.2μm below the surface

6.6 Fracture surfaces

As mentioned in section 3.9, SEM observations were carried out on tensile and fatigue specimens of the three orientations and temperatures to gather information on the failure mechanisms.

6.6.1 Tensile 0° specimens

Figure 6-45a-f, Figure 6-46a-d, and Figure 6-47a-d show the fracture surfaces of 0° coupons tested at room temperature, 50° C and 100° C, respectively. Three regions are distinguishable on the three samples: two shell layers where the fibres are oriented in the loading direction and one core layer where the fibres are transversal to the load. In the core region of the three samples, mostly a plane fracture surface is observed. Figure 6-45a,c, Figure 6-46b and Figure 6-47a,c are close-up views of areas in the core of the three specimens where this plane surface is observed. In contrast, a rough fracture surface is seen in the shell layers.

On one side of the specimens, matrix ductility was noticeable. Figure 6-45e is a zoom-in to the fibre tips of the sample tested at room temperature, where an extended matrix ductility is observed in the shell layer. This matrix deformation was also observed at 50° and 100° C, as shown in Figure 6-46a and Figure 6-47d, respectively. Figure 6-47b,d, Figure 6-46c and Figure 6-47b show that more matrix ductility was noticed in the core region.

On the other side of the samples, less matrix ductility was seen. Figure 6-47f illustrates a region of low matrix deformation, where the fibres are almost clean of matrix and some holes, probably of fibres pulled out, are present. Figure 6-46d illustrates the same in the coupon tested at 50° C, and Figure 6-47d-e show this for the specimen at 100° C. Besides this clean fracture surface, some chunks of material appear where there is a high density of fibres, giving the rough apparel of the overall fracture surface.

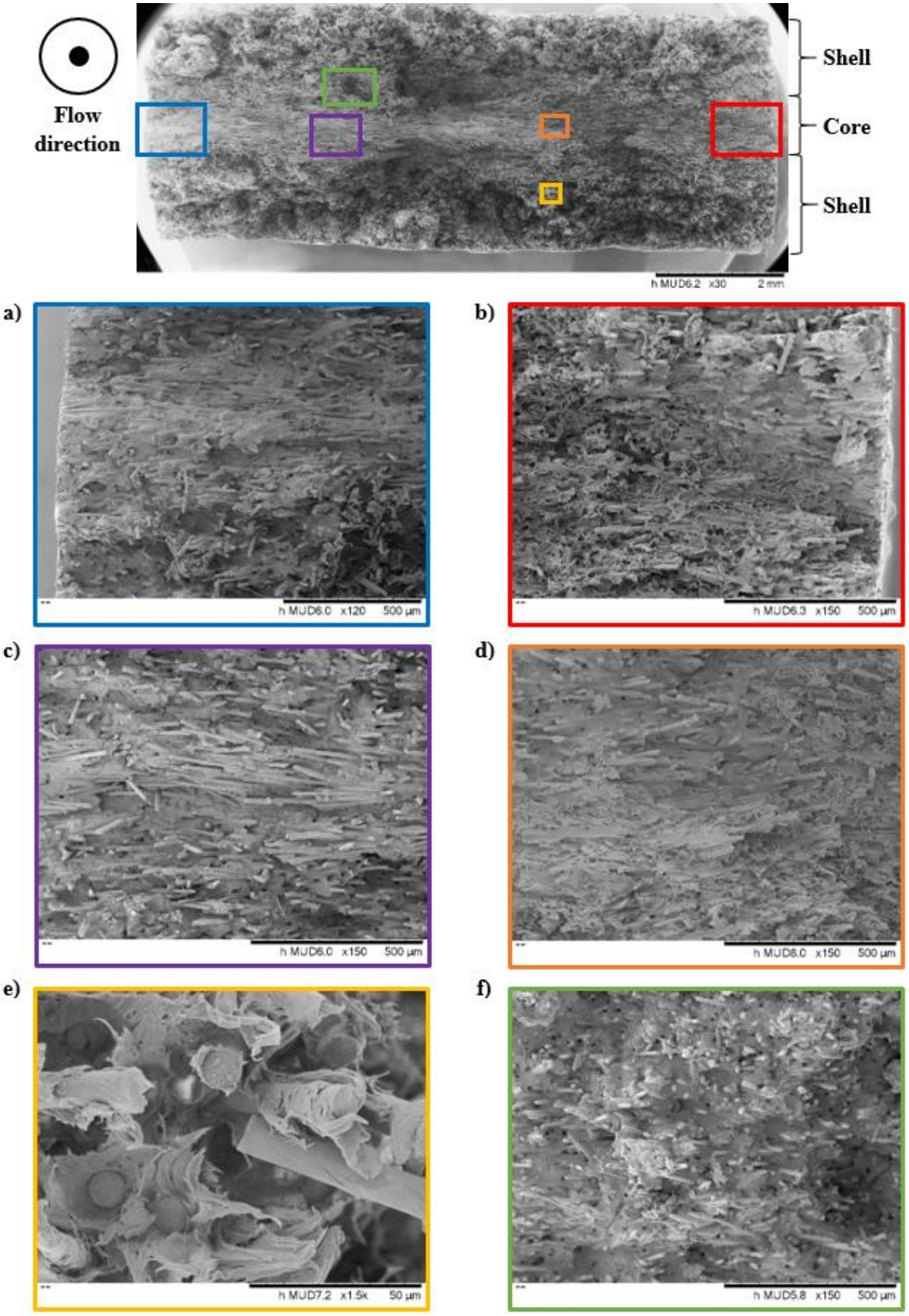

Figure 6-45 Fracture surface of a tensile 0° specimen at room temperature

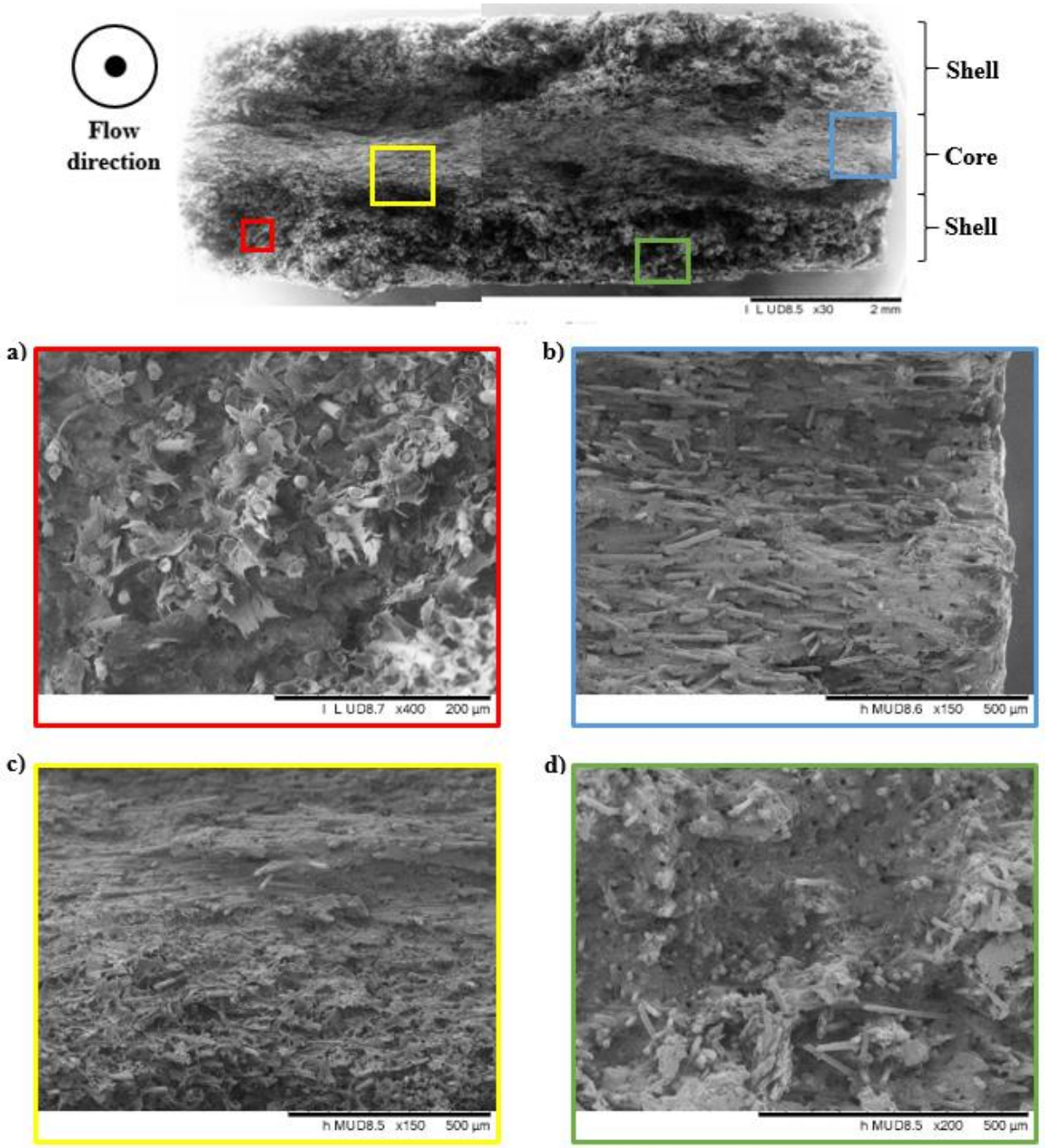

Figure 6-46 Fracture surface of a tensile 0° specimen at 50° C

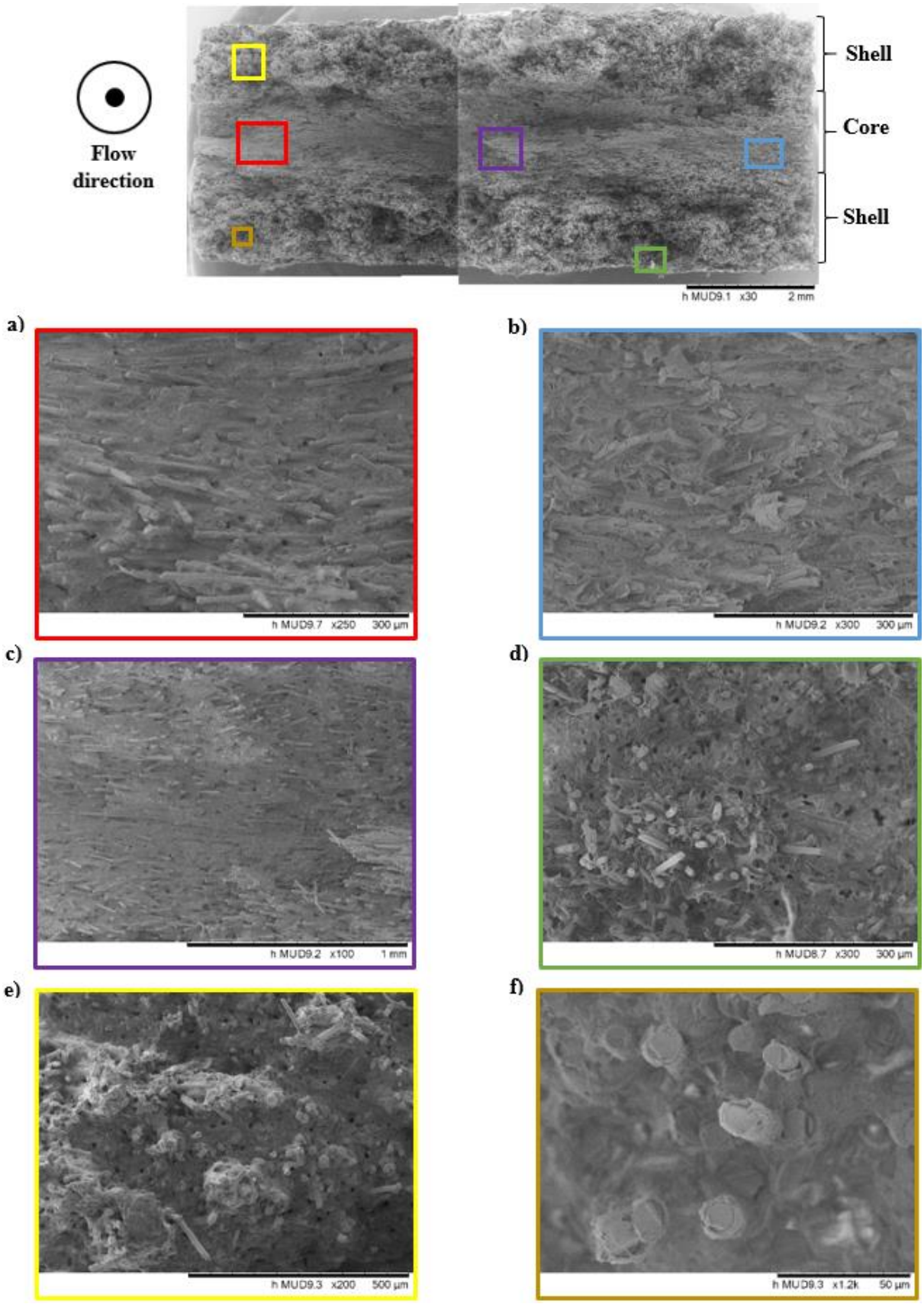

Figure 6-47 Fracture surface of a tensile 0° specimen at 100° C

6.6.2 Tensile 45° specimens

Figure 6-48a-d presents the fracture surface of a tensile 45° sample tested at room temperature. The fracture surface presents a zig-zag look caused by the fibre distribution and a step-like appearance. Similar to the 0° specimen, one region of the specimen exhibited more matrix ductility than the other. Figure 6-48shows evidence of fibre fracture, especially in the region where no matrix deformation appeared. Besides broken fibres, the fibres showed minimal matrix covering them, as illustrated in Figure 6-48a-b. On the other side of the coupon, the fibres seemed to be covered with leftover matrix, and a lot of matrix deformation was observed, see Figure 6-48c-d.

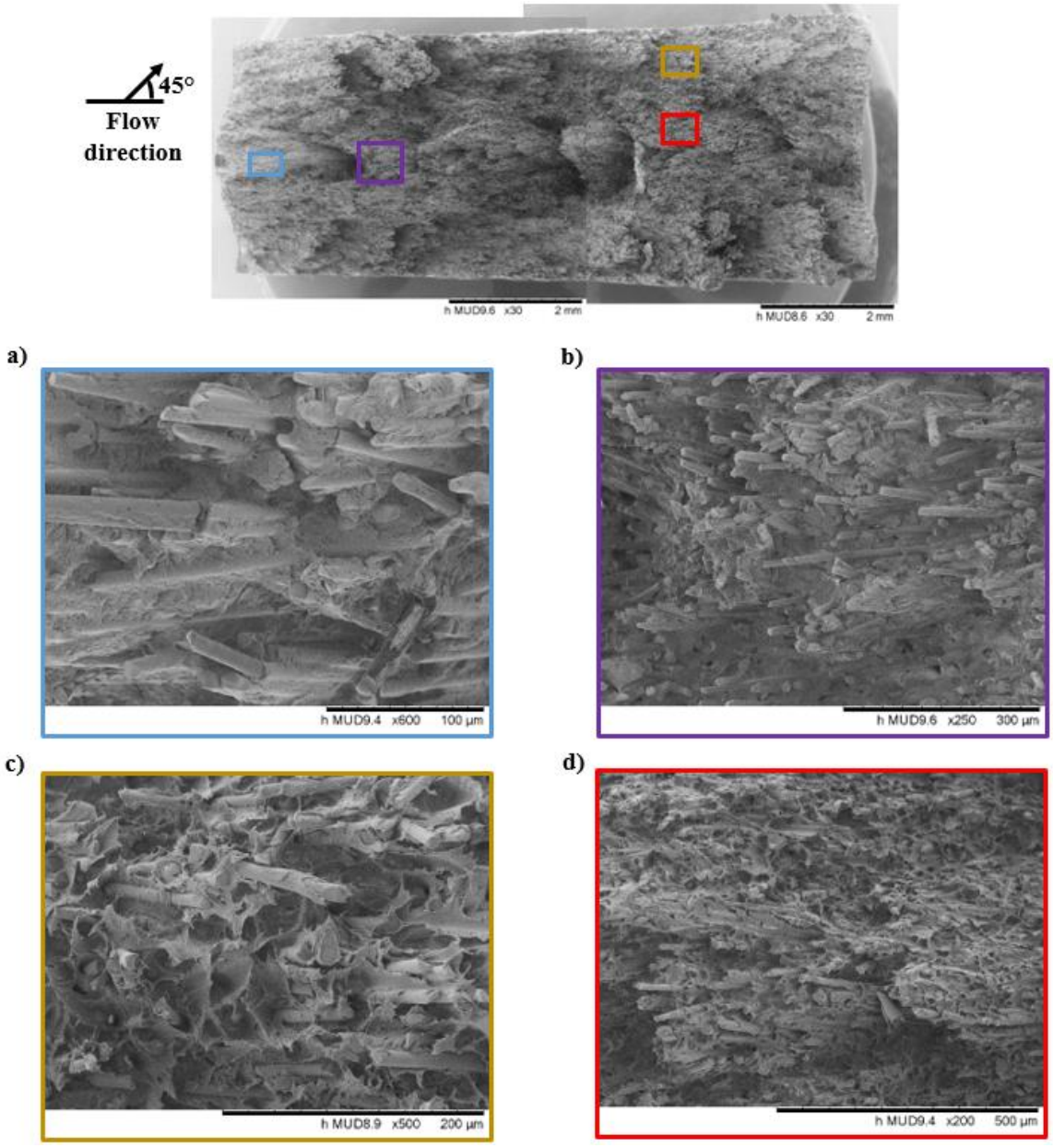

Figure 6-48 Fracture surface of a tensile 45° specimen at room temperature

The fracture surface of a tensile 45° specimen tested at 50° C is shown in Figure 6-49a-d. Analogous to the room temperature sample, the fracture surface exhibited a zig-zag and step-like appearance. However, unlike the room temperature specimen, the fracture surface presented a V shape, with the core layer more profound than the shell layers. Again, a zone with high matrix deformation and another with no matrix deformation were observed. Figure 6-49a,c are close-up views of regions with no matrix ductility and a clean surface. In contrast, Figure 6-49b,d illustrate the matrix deformation found on the other side of the specimen, with some matrix covering the fibres and matrix failure at the fibre tips, as shown in Figure 6-49d.

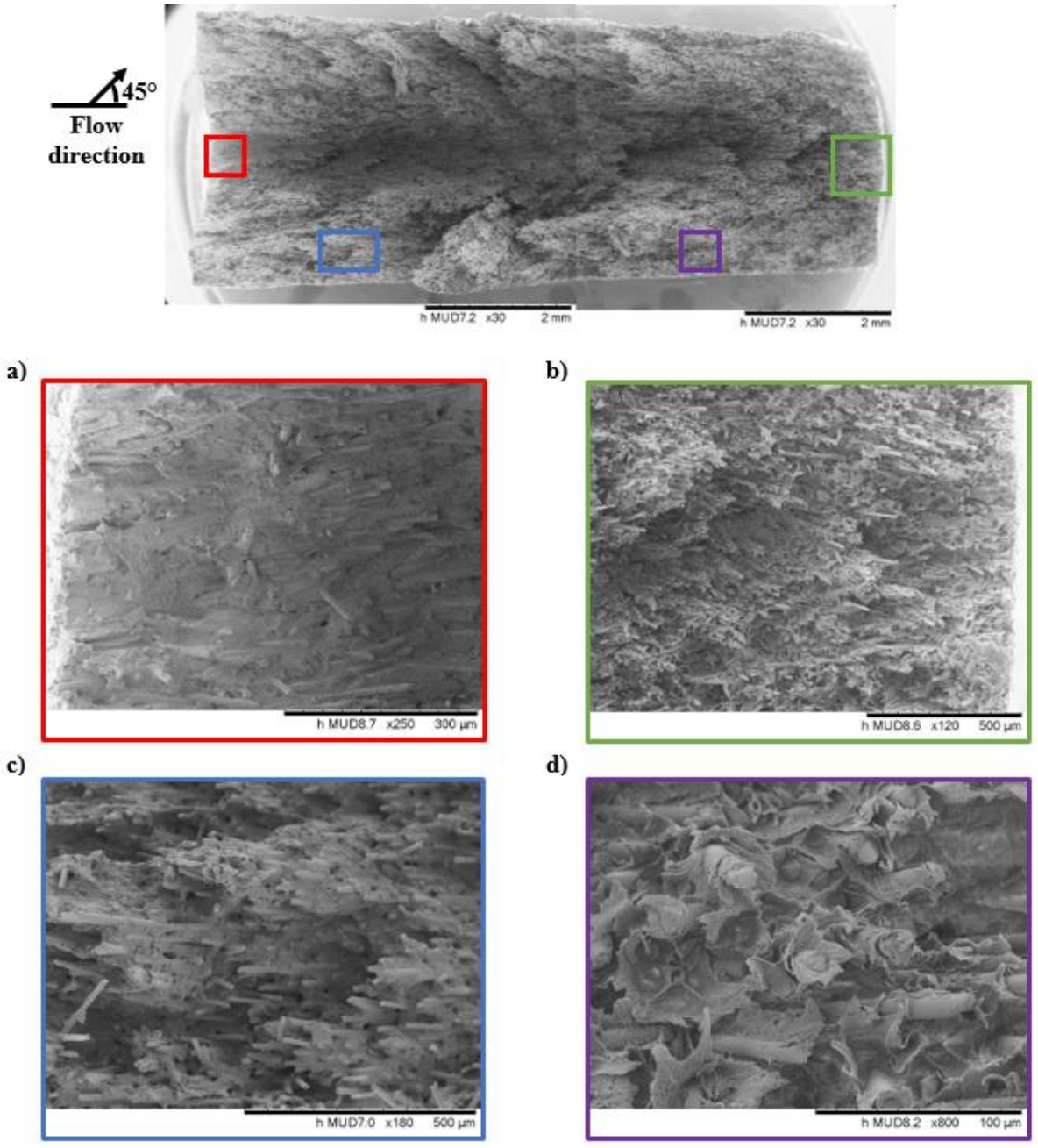

Figure 6-49 Fracture surface of a tensile 45° specimen at 50° C

Figure 6-50a-d presents the fracture surface of a tensile 45° sample tested at 100° C. A zig-zag, step-like and V shape fracture surface was also observed at this temperature. Figure 6-50a-b show this step-like look in more detail. In addition to this, no fractured fibres were noticed. Similar to the specimens tested at the previous temperatures, a region of high matrix deformation was identified, as shown in Figure 6-50c-d. Figure 6-50d is a close-up view at the fibre tips in a region of high matrix ductility, and it is noticeable that the matrix seemed to fail at the fibre tips leaving traces of matrix.

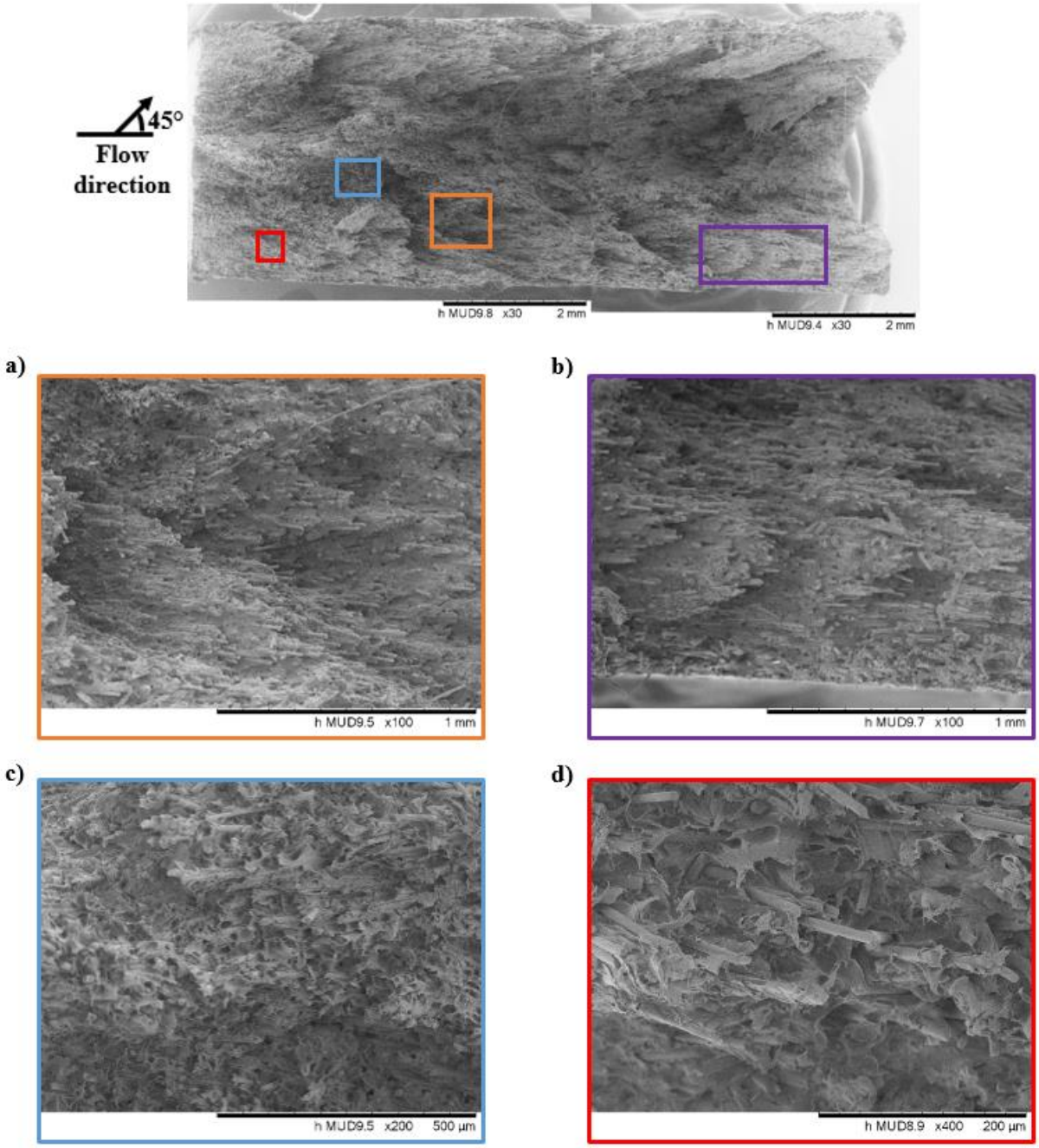

Figure 6-50 Fracture surface of a tensile 45° specimen at 100° C

6.6.3 Tensile 90° specimens

Figure 6-51a-d shows the fracture surface of a 90° specimen tested at room temperature. In contrast to the other coupons, no matrix ductility was observed in the 90° sample. Figure 6-51a illustrates a region where the fibres are transversally oriented to the load, and a flat fracture surface is seen. Also, some marks where fibres were debonded entirely from the matrix without deformation are noticed. Figure 6-51b reveals a flat fracture surface that goes through the fibre tips where the fibres are oriented in the loading direction. Some chunks of material are visible where a fibre concentration is located, as seen in Figure 6-51c. Finally, Figure 6-51d shows a fracture surface that follows the different fibre layers giving a step look.

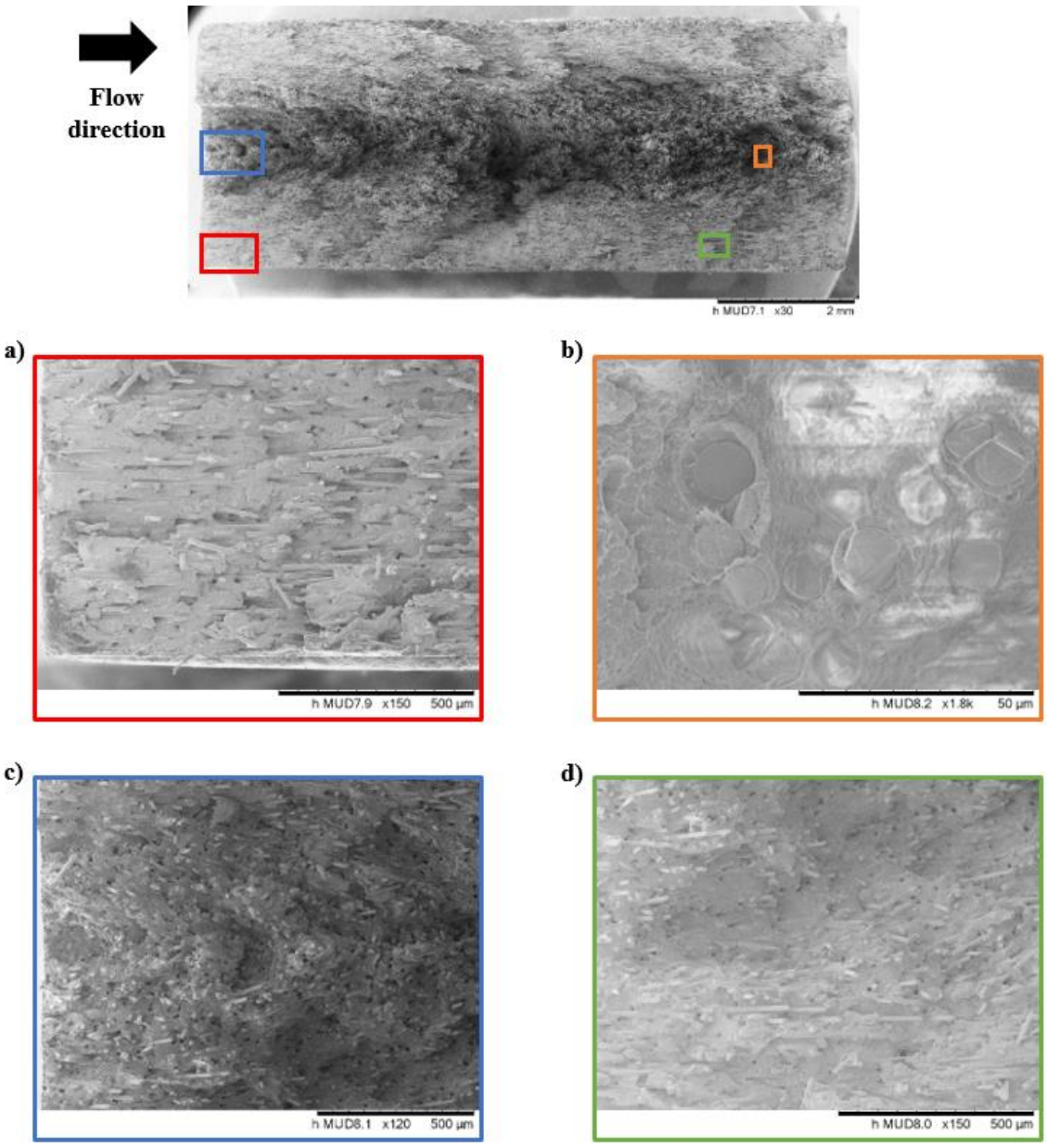

Figure 6-51 Fracture surface of a tensile 90° specimen at room temperature

The fracture surface of the 90° specimen tested at 50° C is shown in Figure 6-52a-d. Opposite to the room temperature sample, the specimen at this temperature showed a vast region of matrix deformation. Figure 6-52a is a zoom-in to the region where a hole was observed in the centre of the coupon. This area presented a mostly flat surface with minor matrix deformation and circular gaps where possible fibre pull-out occurred. In a region where fibres are transversal temperature. In the core area, where the fibres are oriented to the load, a few broken fibres are seen, as illustrated in Figure 6-52c. An extensive amount of fibre pull-out was observed in a smaller section where minimal matrix deformation is seen, as illustrated in Figure 6-52d. to the load, Figure 6-52b shows huge matrix ductility, contrary to what was observed at room

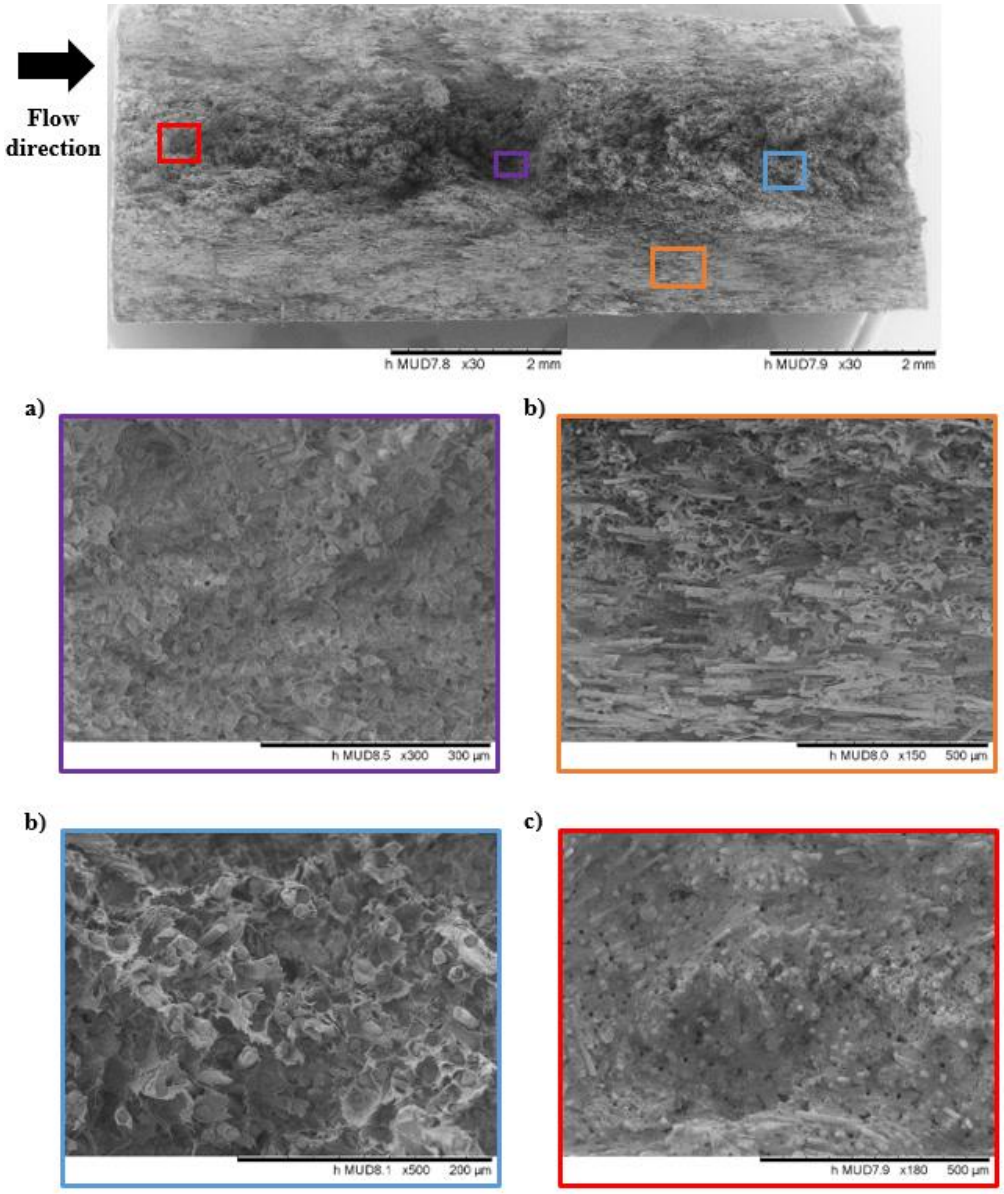

Figure 6-52 Fracture surface of a tensile 90° specimen at 50° C

At 100° C, the 90° specimen showed a vast area of matrix ductility, as shown in Figure 6-53a-d. Similar to the sample at 50° C, holes were observed in the core region. Figure 6-53a presents a close-up view of one of the holes, showing a flat surface at the centre surrounded by an area of deformed matrix. In the core region, Figure 6-53b, high matrix ductility is visible, with bundles of fibre where more material is localised. Analogous to the other temperatures, steps can be observed in the fracture surface, as seen in Figure 6-53c. Besides this, broken fibres were found in the core region, with matrix covering the fibres, see Figure 6-53d.

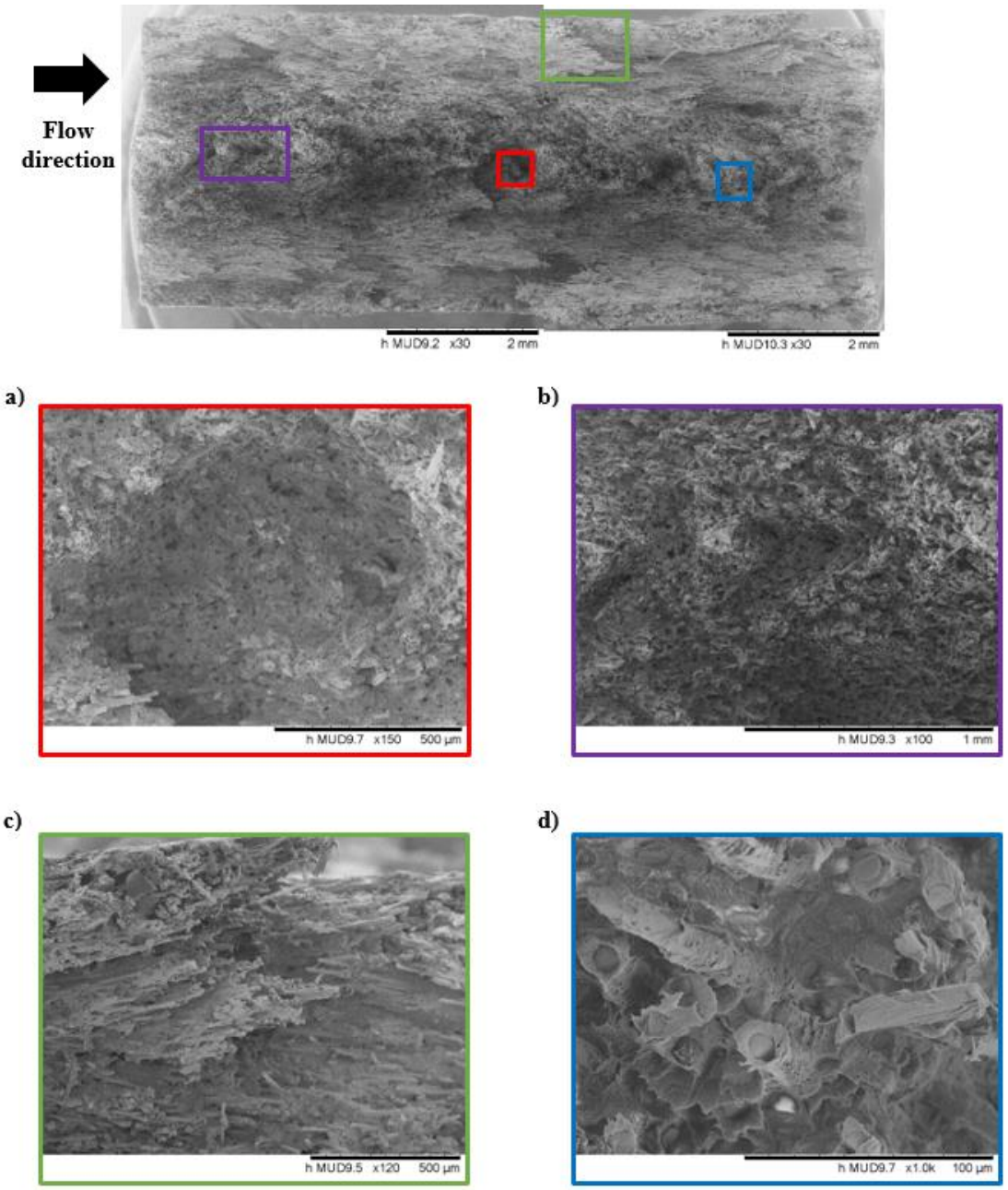

Figure 6-53 Fracture surface of a tensile 90° specimen at 100° C

6.6.4 Fatigue 0° specimens

The fracture surfaces of specimens fatigue tested were analysed as well. The shell-core-shell structure typical of injected moulded SFRP was observed in all samples. Figure 6-54a-b shows the fracture surface of a fatigue 0° specimen tested at room temperature. Very low matrix ductility was seen on the overall fracture surface. The fracture plane seemed flat in the core layer with no matrix deformation, as seen in Figure 6-54a. In the shell layers, the fracture surface was rougher, and evidence of fibre pull-outs was seen, represented by the considerable number of holes found, as illustrated in Figure 6-54b. In this region, the fibres appear clean, with no matrix covering them.

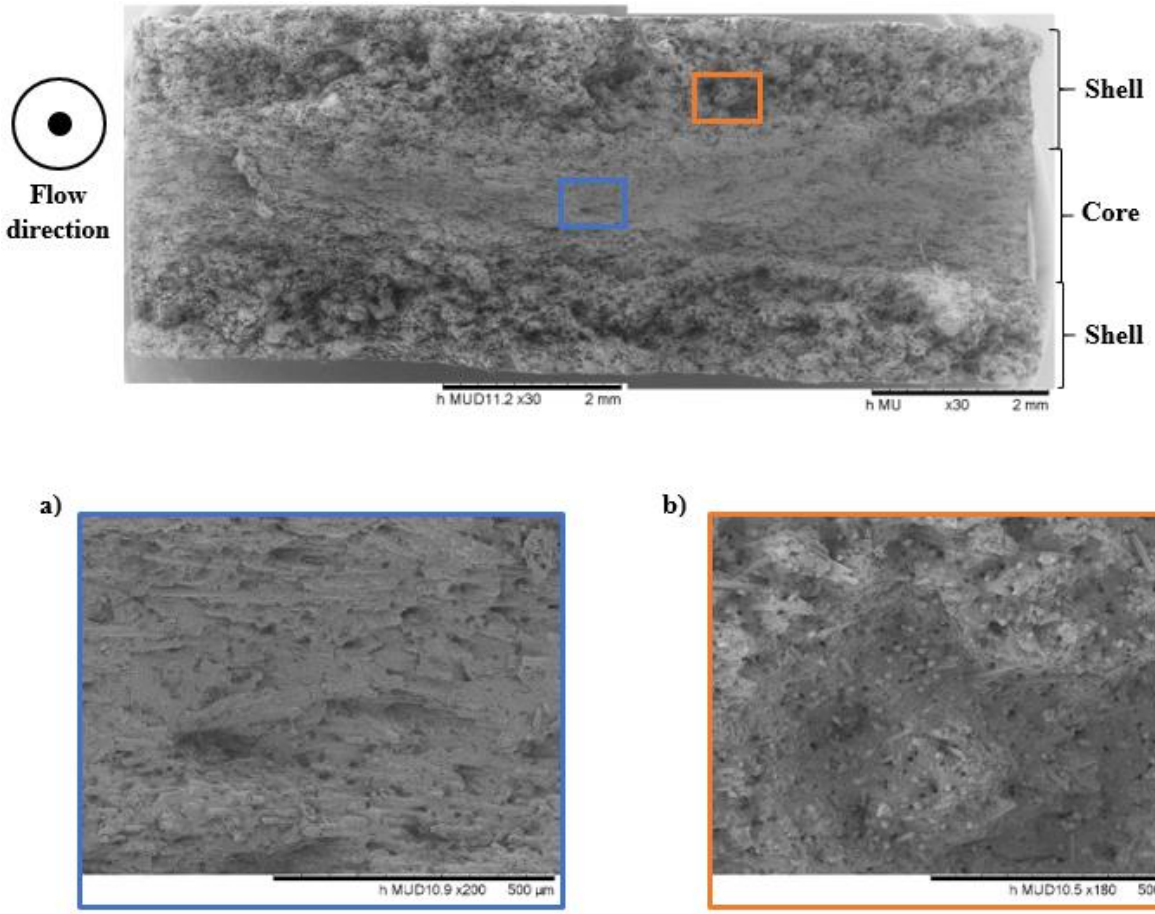

Figure 6-54 Fracture surface of a fatigue 0° specimen at room temperature

Figure 6-55a-c depicts the fracture surface of a 0° specimen tested at 50° C. At this temperature, more matrix deformation was observed over the entire fracture plane compared to the room temperature sample. Even at the core region, where at room temperature it was utterly flat, at this temperature, the matrix seemed to show some deformation, as illustrated in Figure 6-55a. Transition zones were noticed in areas such as the one shown in Figure 6-55.

On the left side, the matrix seems flat with minor deformation. On the other side, the matrix is significantly deformed, and some remanent matrix covers the fibres. Few broken fibres were detected, as shown in Figure 6-55, and they were mainly located in regions with low matrix ductility.

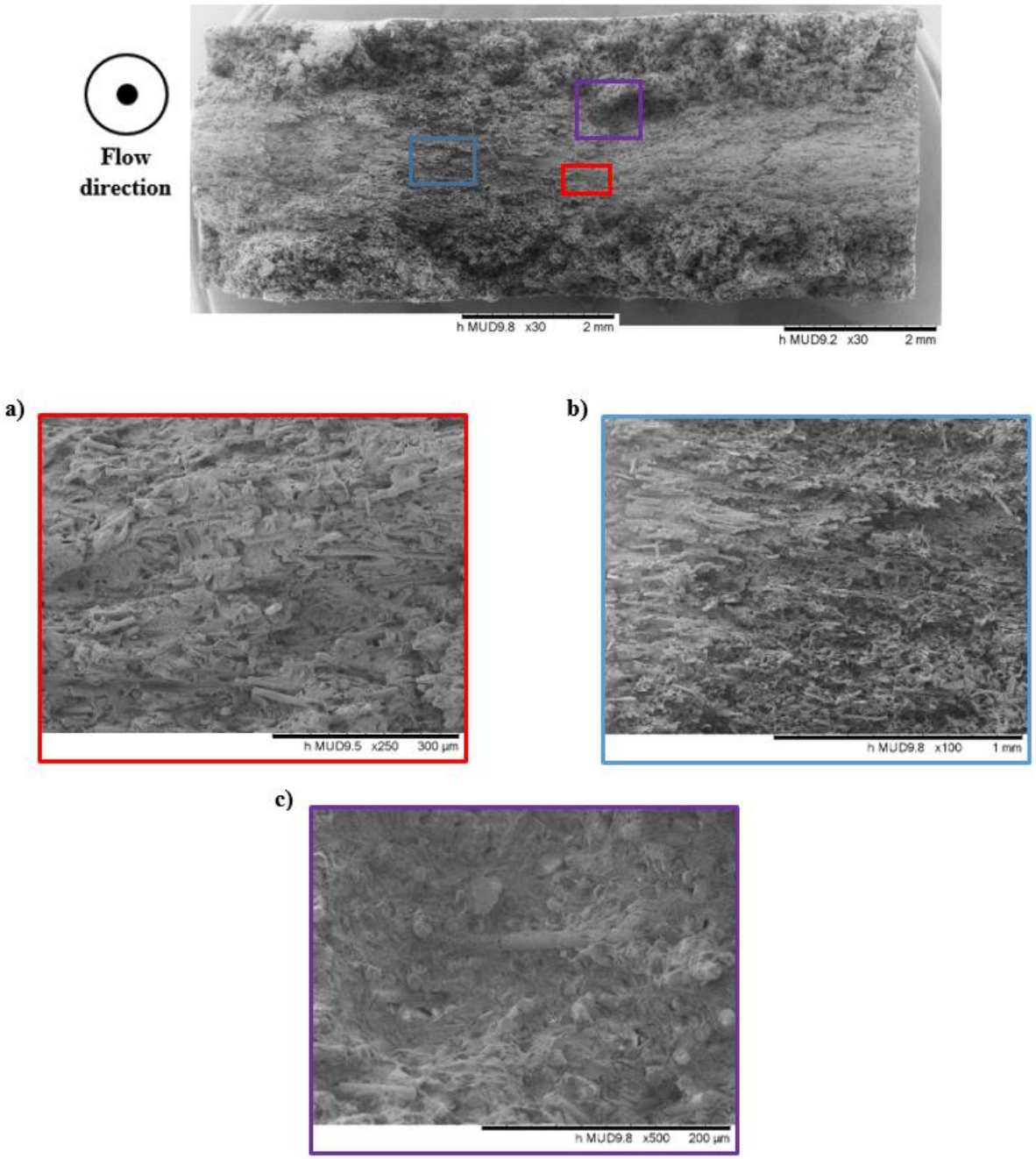

Figure 6-55 Fracture surface of a fatigue 0° specimen at 50° C

Figure 6-56a-c illustrates the fracture surface of a 0° specimen tested at 100° C. At this temperature, the fracture plane presented a vast area of deformed matrix. Figure 6-56a shows a region in the core layer with a lot of matrix deformation, and remanent matrix covers the

fibres. A similar aspect was found in zones of the shell layers, as seen in Figure 6-56b. A few transition areas were also detected, as depicted in Figure 6-56c, where one side seems to present matrix deformation and on the other, a smoother surface and fibres with no matrix covering them. Very few broken fibres were identified.

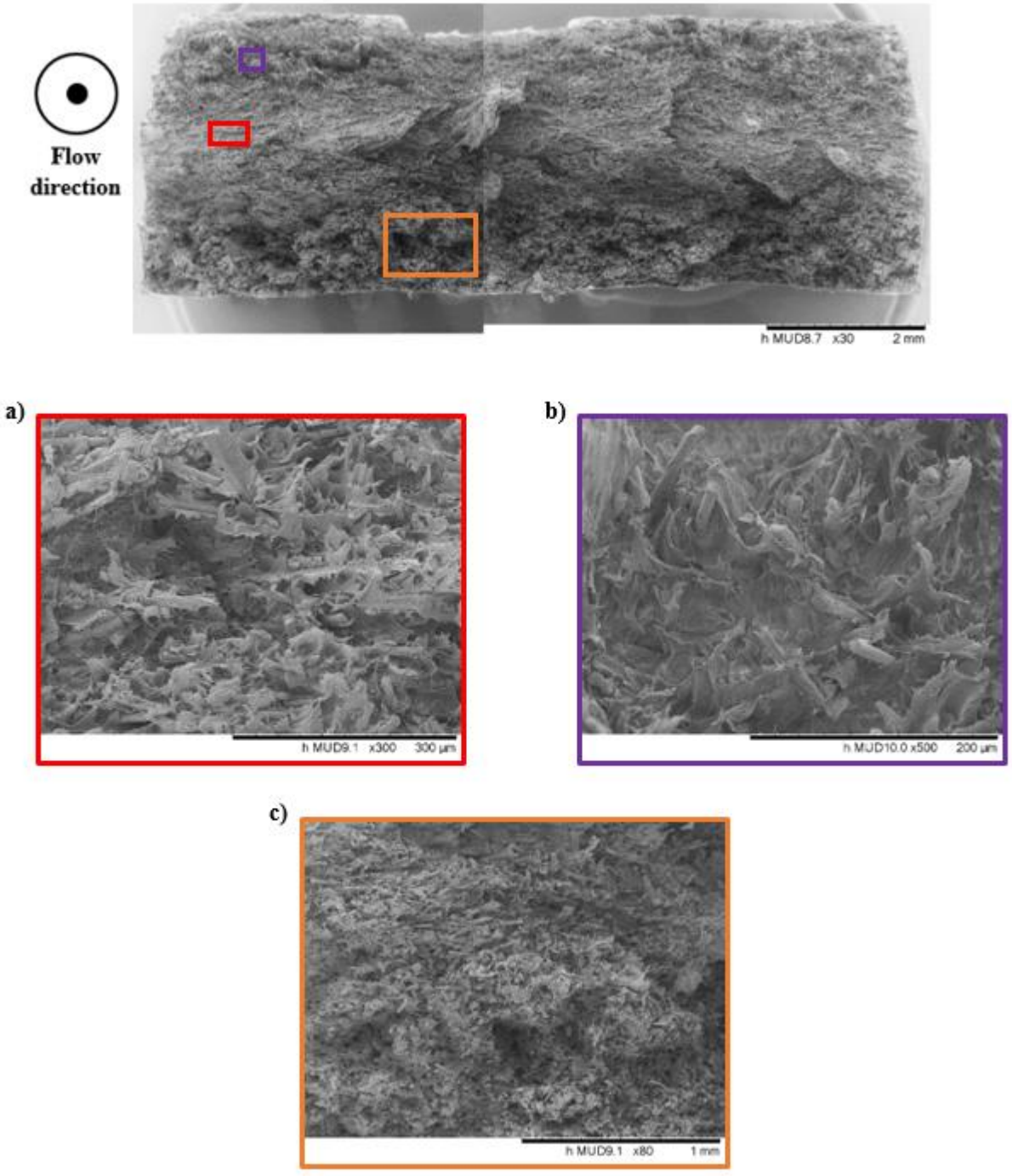

Figure 6-56 Fracture surface of a fatigue 0° specimen at 100° C

A secondary crack was noticed below the fracture surface. Figure 6-57a is a close-up view of the crack tip. A lot of matrix deformation can be observed ahead of the crack tip. In addition,

some voids have already formed mainly around the fibres. It can also be seen that a bundle of fibres stopped the crack propagation, as shown in Figure 6-57b, Besides that, it seems that the crack propagated across the matrix surrounding the fibres through the fibre-matrix interface of the fibres oriented transversal to the load direction.

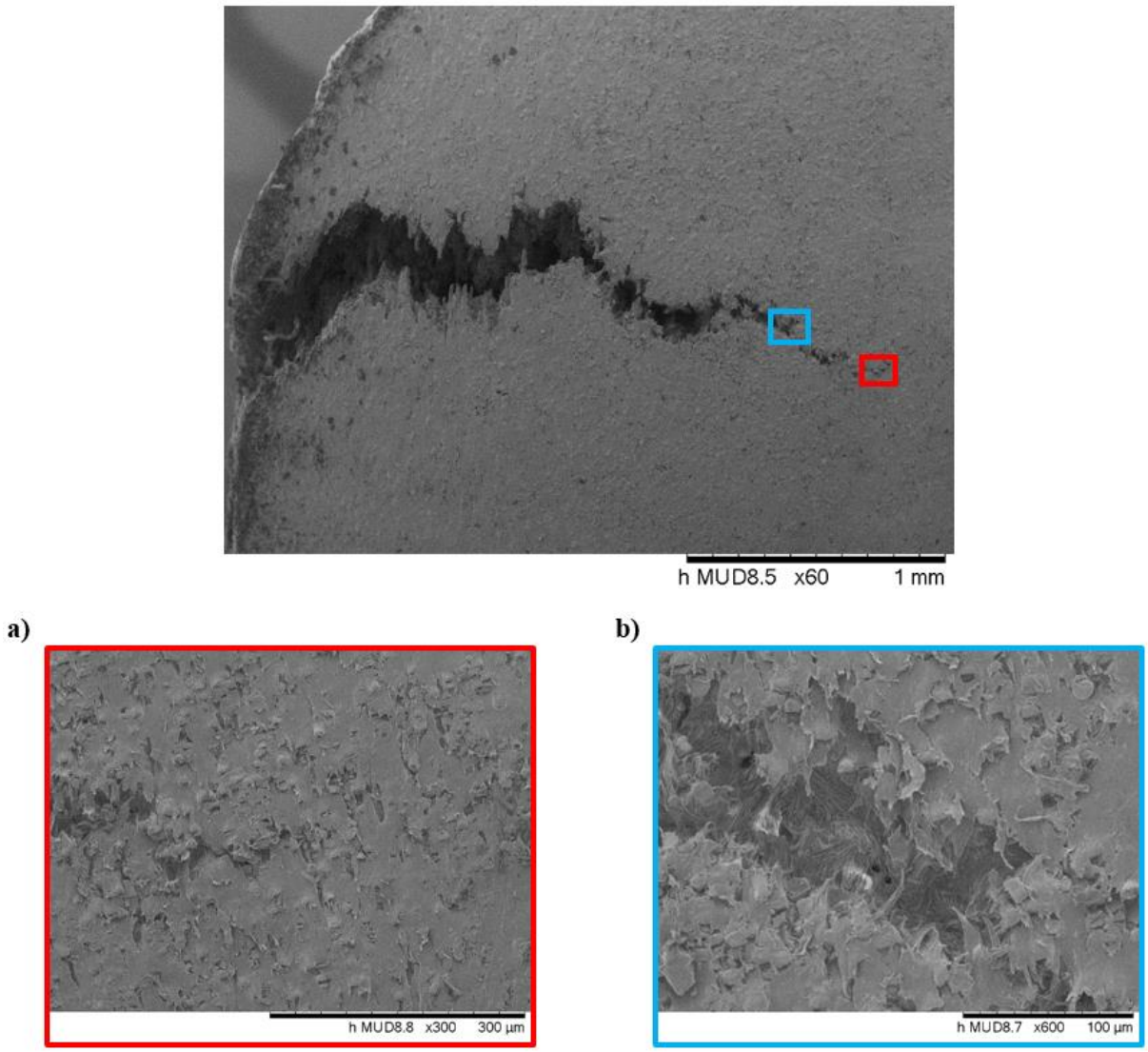

Figure 6-57 Secondary crack in a fatigue 0° specimen at 100° C

6.6.5 Fatigue 45° specimens

Figure 6-58a-c depicts the fracture surface of a 45° specimen used in the fatigue testing at room temperature. Similar to the 45° coupons used in the tensile testing, the fracture plane presents a zig-zag and step appearance, with an extensive area of deformed matrix. However, different from the tensile 45° sample at room temperature, this fatigue sample showed a V shape fracture surface even at room temperature. Figure 6-58a shows a zoom-in to a region with low matrix ductility, but clear evidence of fibre debonding is visible. Fibre debonding

was also observed in regions of high matrix ductility, as seen in Figure 6-58b, where besides this, fibre pull-out and matrix deformation at the fibre tips were noticed. As illustrated in Figure 6-58c, broken fibres were also observed.

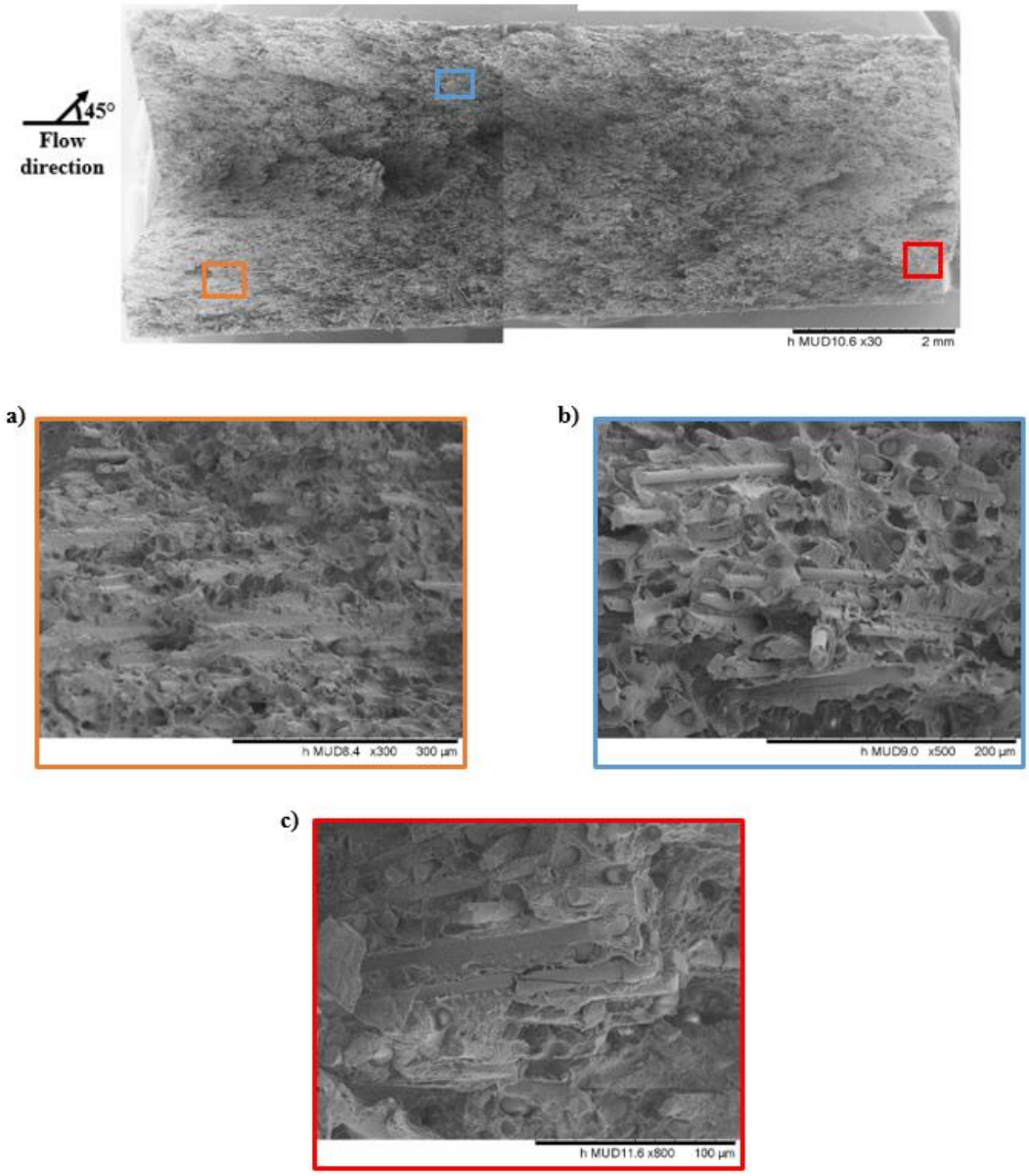

Figure 6-58 Fracture surface of a fatigue 45° specimen at room temperature

Figure 6-59a-b shows the fracture surface of a fatigue 45° sample tested at 50° C. Similar to the room temperature coupon, the fracture plane presented a significant area of deformed matrix. However, the step-like appearance was more notorious than at room temperature. Figure 6-59a is a close-up view of a region in the core, where some matrix deformation can be seen at the fibre tips, and indications of fibre debonding are also visible. As illustrated in

Figure 6-59b, some broken fibres were noticed with considerable matrix deformation at the fibre tips, and more evidence of debonding was found.

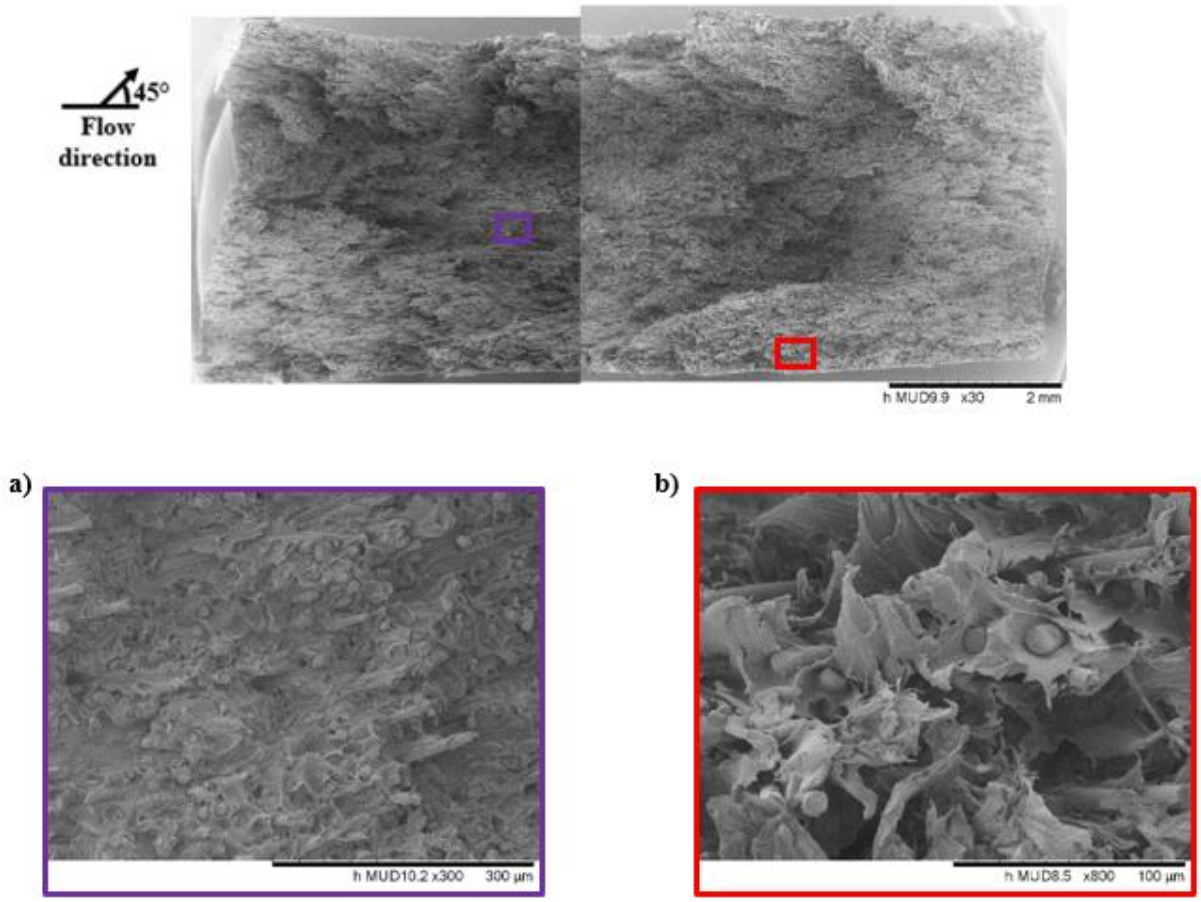

Figure 6-59 Fracture surface of a fatigue 45° specimen at 50° C

The fracture surface of a fatigue 45° specimen tested at 100° C is shown in Figure 6-60a-b. The overall appearance of the fracture plane is similar to the other fatigue 45° specimens tested at room temperature and 50° C, presenting a step-like form following the direction of the fibre orientation. Figure 6-60a is a close-up view of a region in the core where minor matrix deformation is observed. Again, the step look following the fibre orientation is evident. Most of the fracture surface showed matrix ductility, as illustrated in Figure 6-60b. Remanent matrix was seen covering the sides and tips of the fibres.

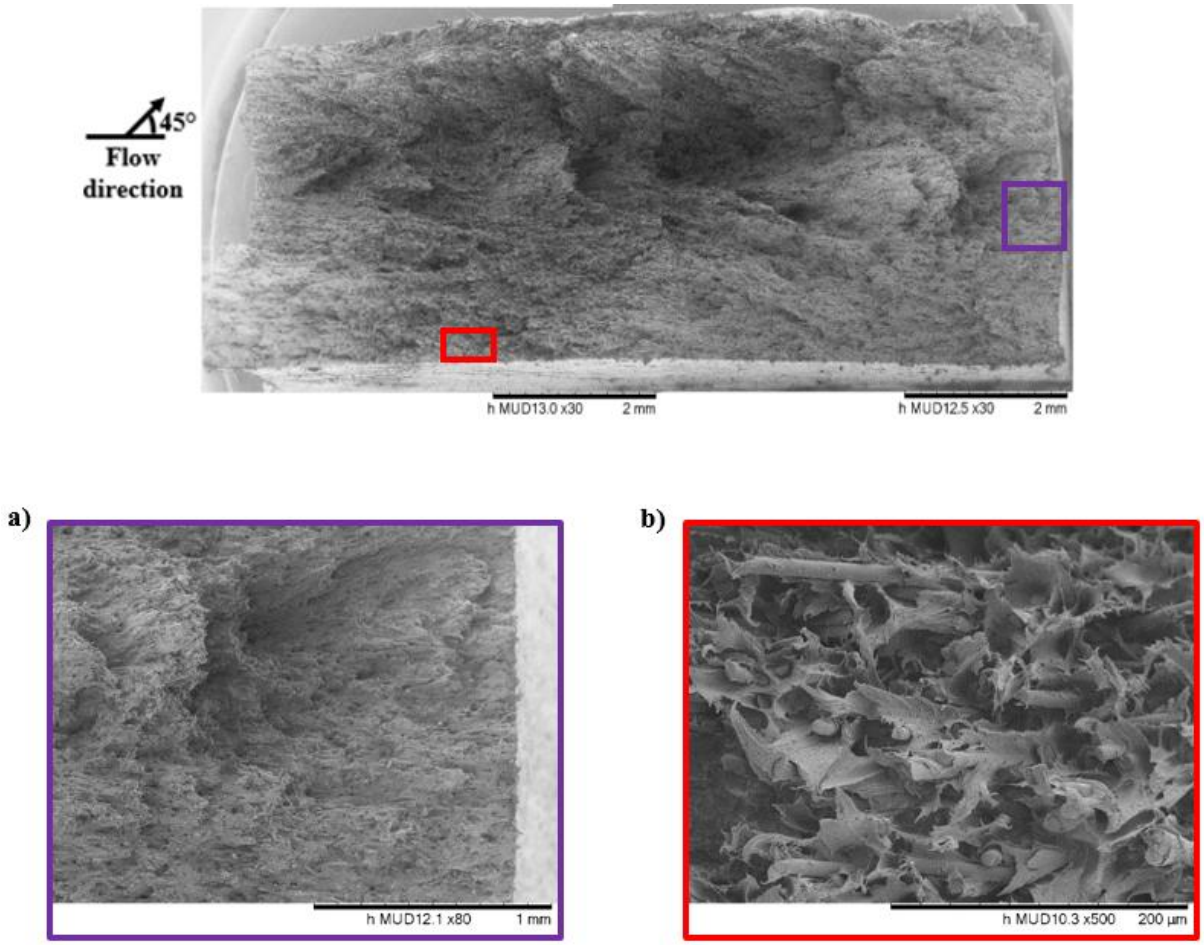

Figure 6-60 Fracture surface of a fatigue 45° specimen at 100° C

6.6.6 Fatigue 90° specimens

Figure 6-61a-b presents the fracture surface of a 90° specimen used in the fatigue testing at room temperature. Similar to previous samples, the division of the microstructure is evident, exhibiting a shell-core-shell structure. The shell layers, where the fibres were oriented transversal to the loading direction, show a mainly flat fracture plane. In comparison, the core layer, a region where the fibres were oriented to the load, presents a rough fracture surface. A few holes in the core region were noticed where the material seemed ripped off. Figure 6-61a shows a close-up view of one of those holes in the core. The matrix in this location exhibit low ductility, and several circular holes present evidence of fibre pull-out. In addition, there are chunks of material with a high concentration of fibres. Figure 6-61b depicts a zoom-in to an area in the shell layer where it is possible to observe minimal matrix deformation and a step appearance caused by the different layers of fibres.

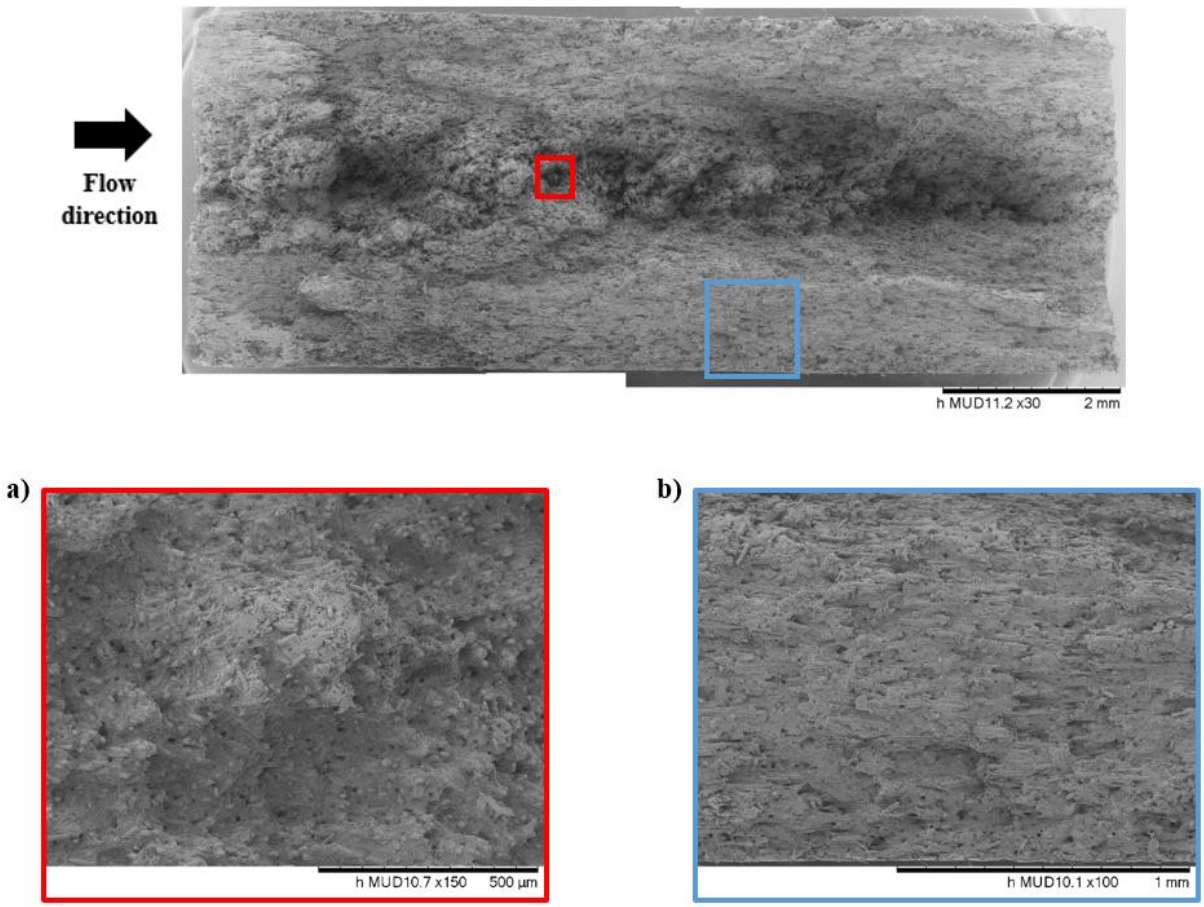

Figure 6-61 Fracture surface of a fatigue 90° specimen at room temperature

Figure 6-62a-e illustrates the fracture surface of a 90° specimen used in the fatigue testing conducted at 50° C. At this temperature, the sample presented a fracture surface with higher matrix deformation, and the step-like appearance is more evident than at room temperature. Figure 6-62a shows a zoom-in to a region in the shell layer where matrix deformation is observed. Transition zones were also noticed, such as the one shown in Figure 6-62b. On one side, the matrix seems more deformed than on the other side. Even in the core region, Figure 6-62c, the matrix appears to be deformed with deformed matrix at the fibre tips and evidence of fibre pull-out. As shown in Figure 6-62d, broken fibres were detected mainly in the core region with remanent matrix covering them. Figure 6-62e is a close-up view of a region where a crack was detected. It can be seen that the crack path follows the fibre-matrix interface, causing the fibre to debond from the matrix.

A secondary crack was noticed below the fracture surface, as illustrated in Figure 6-63. Analysing Figure 6-63, one can observe multiple more minor cracks surrounding the crack.

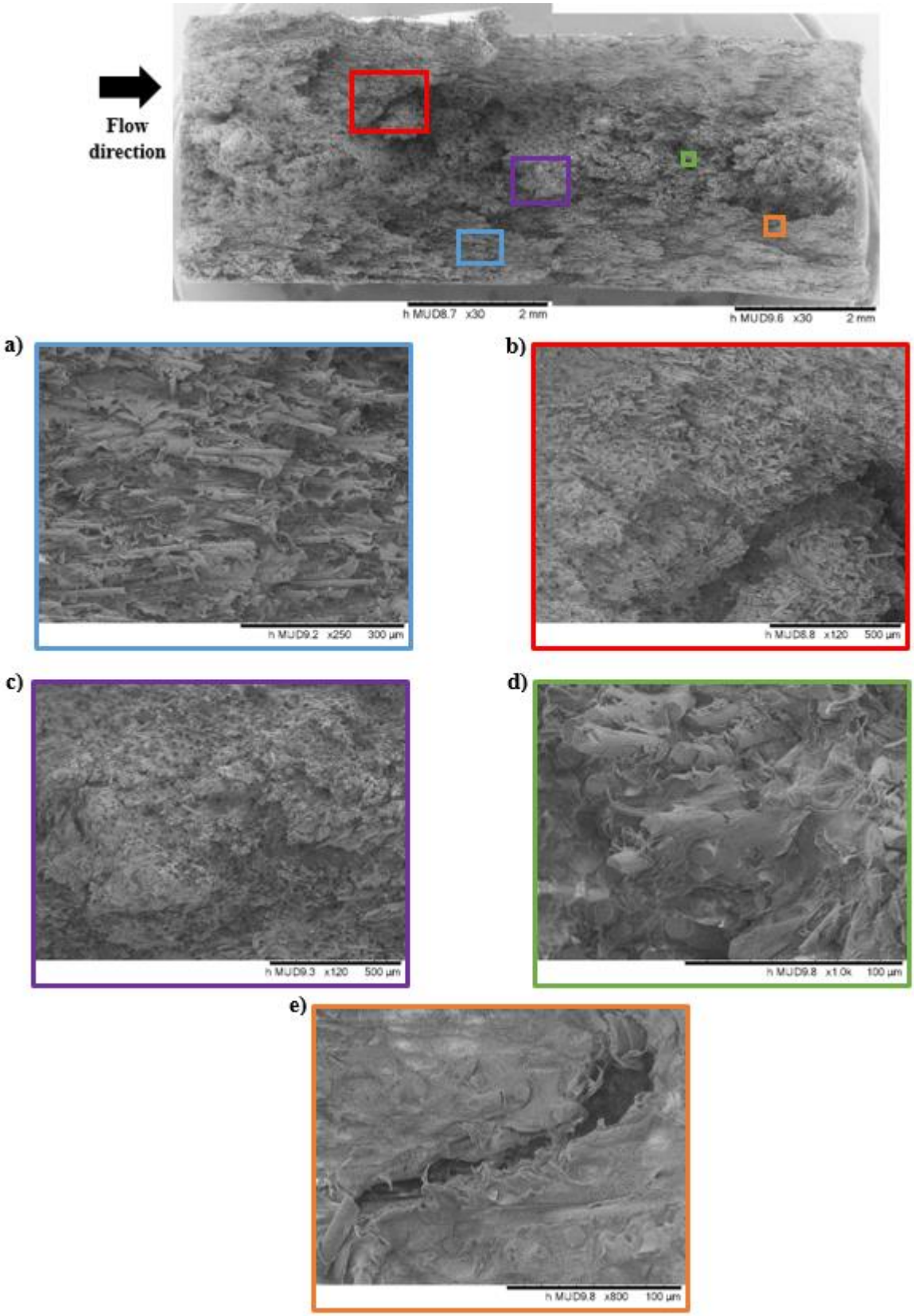

Figure 6-62 Fracture surface of a fatigue 90° specimen at 50° C

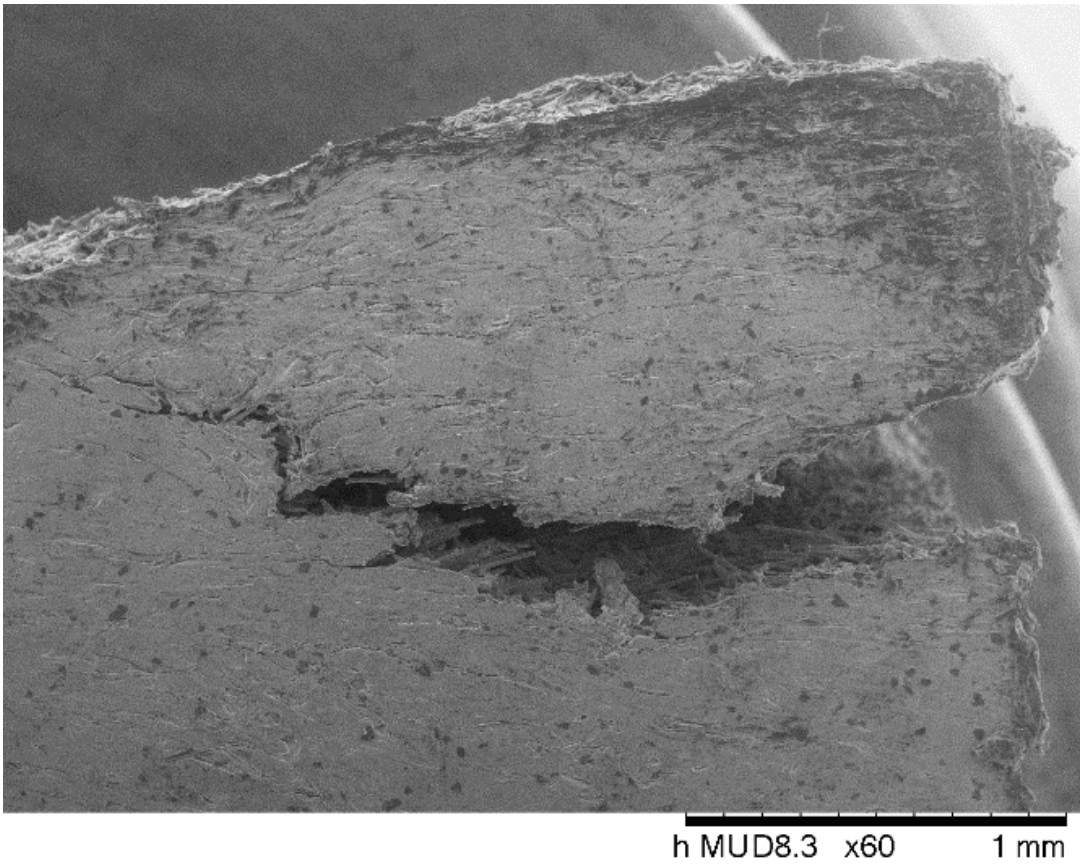

Figure 6-63 Secondary crack in a fatigue 90° specimen at 50° C

The fracture surface of one fatigue 90° sample tested at 100° C is shown in Figure 6-64a-b. The fracture surface presented high matrix ductility, as seen in the 50° C specimen. In the shell layers, some regions showed a flat fracture surface, and others exhibited matrix deformation, as seen in Figure 6-64a. In addition, holes in the core region of the sample were observed. Figure 6-64b shows a close-up view of one of them. The fracture surface presented a minor matrix deformation, with evidence of fibre pull-outs suggested by the circular holes in the matrix.

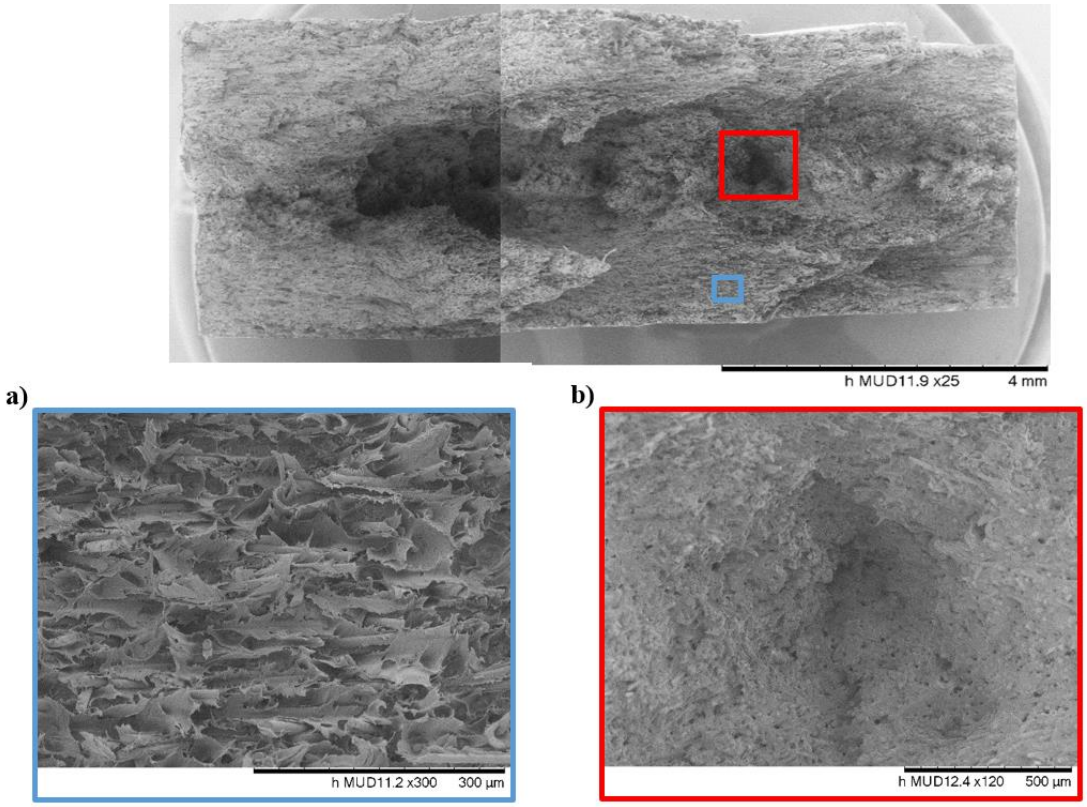

Figure 6-64 Fracture surface of a fatigue 90° specimen at 100° C

6.7 Conclusion

This chapter presented the results of the experimental program. Tensile tests at room temperature, 50° C and 100° C were conducted on specimens milled from plaques at 0°, 45° and 90° with respect to the injection flow. An evident effect of the temperature was observed, with the samples tested at 100° C exhibiting the lowest Young's modulus and UTS. The influence of the orientation of the coupon was also noticed, being the specimen cut at 0° samples the ones showing a higher Young's modulus and UTS. Digital image correlation was used during the tensile testing to measure the strain distribution on the surface of the specimens. It was also possible to capture the crack initiation in a few samples with the acquired images.

Fatigue tests were also carried out at the same temperatures using samples cut at the same orientation. Again, a clear effect of the temperature and orientation was observed. Similar to the tensile behaviour, the temperature had a detrimental influence on the fatigue lives of the specimens. The Basquin's coefficient and exponent were obtained for the three orientations and temperatures, as well as the measurement of hysteresis loops was performed.

Micro-computed tomography images were used to estimate the fibre orientation tensor and measure the length and diameter of the fibres. This fibre length was compared against the calculated fibre critical length, $l_c = 525.071$ μm, which was larger than the average fibre length (226 μm).

In-situ tensile tests were conducted at room temperature, 50° C and 100° C inside the micro-computed tomography, and digital volume correlation was performed using the obtained images. These types of experiments and analyses allowed to observe the strain evolution below the surface of the samples. In addition, the microstructure images were superimposed on the digital volume correlation results to obtain more information on the strain localisations. These tests and analyses are scarce in the literature and provide valuable information in the attempt to understand the initiation and propagation of cracks in SFRP.

Furthermore, fractured fatigue samples showing secondary cracks were scanned to investigate the damage mechanisms, and evidence of subsurface cracks was detected.

Finally, the fracture surfaces of tensile and fatigue specimens tested at the three temperatures were observed using SEM to study the damage mechanisms.

7 MODELLING RESULTS

7.1 Injection moulding simulation

The injection moulding simulation provides information on the material microstructure, such as the orientation tensor. The details of the boundary conditions and setup are described in Chapter 4.

Figure 7-1 shows the a11 component of the orientation tensor for the surface and cross-section of the plaque. This a11 component describes the degree of fibre alignment in the direction of the injection flow, ranging from 0 (no alignment) to 1 (perfect alignment). It can be noticed that the fibre alignment in the direction of the flow increases towards the plaque edges. While in the region where the centre of the gauge length was located, the fibre orientation is more random.

Inspecting the thickness view, it seems that the model was able to reproduce the skin-shell-core structure, showing a decrease in fibre alignment from the surface towards the centre of the plaque.

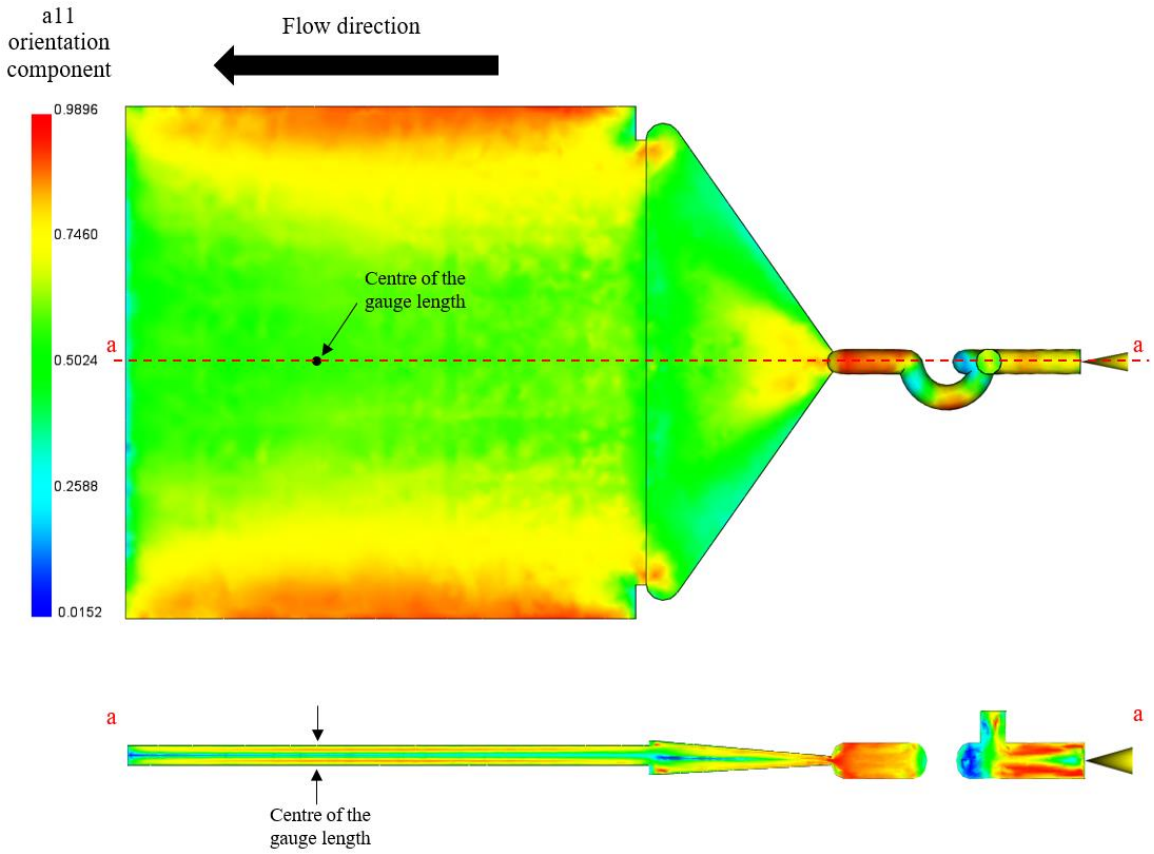

Figure 7-1 Moldflow a11 orientation component results. Surface and thickness views

The Moldflow Rotational Diffusion model used in the simulation of the injection moulding process was calibrated using the orientation tensors measured with the μCT. Figure 7-2a-c shows the comparison of the measured orientation tensor and the obtained from the simulation of the injection moulding process. This results are the best achieved by varying the parameters of the MRD model. It can be seen in Figure 7-2a that the model produced a thinner core layer than the one measured by the μCT and underestimated the misalignment in the a11 component in the core. However, it was able to estimate the maximum value correctly. Figure 7-2b shows the variation of the a22 component through the thickness, and it can be observed that the core is also thinner than the one measured. Regarding the a33 component, Figure 7-2c shows that the model underestimated the out-of-plane alignment.

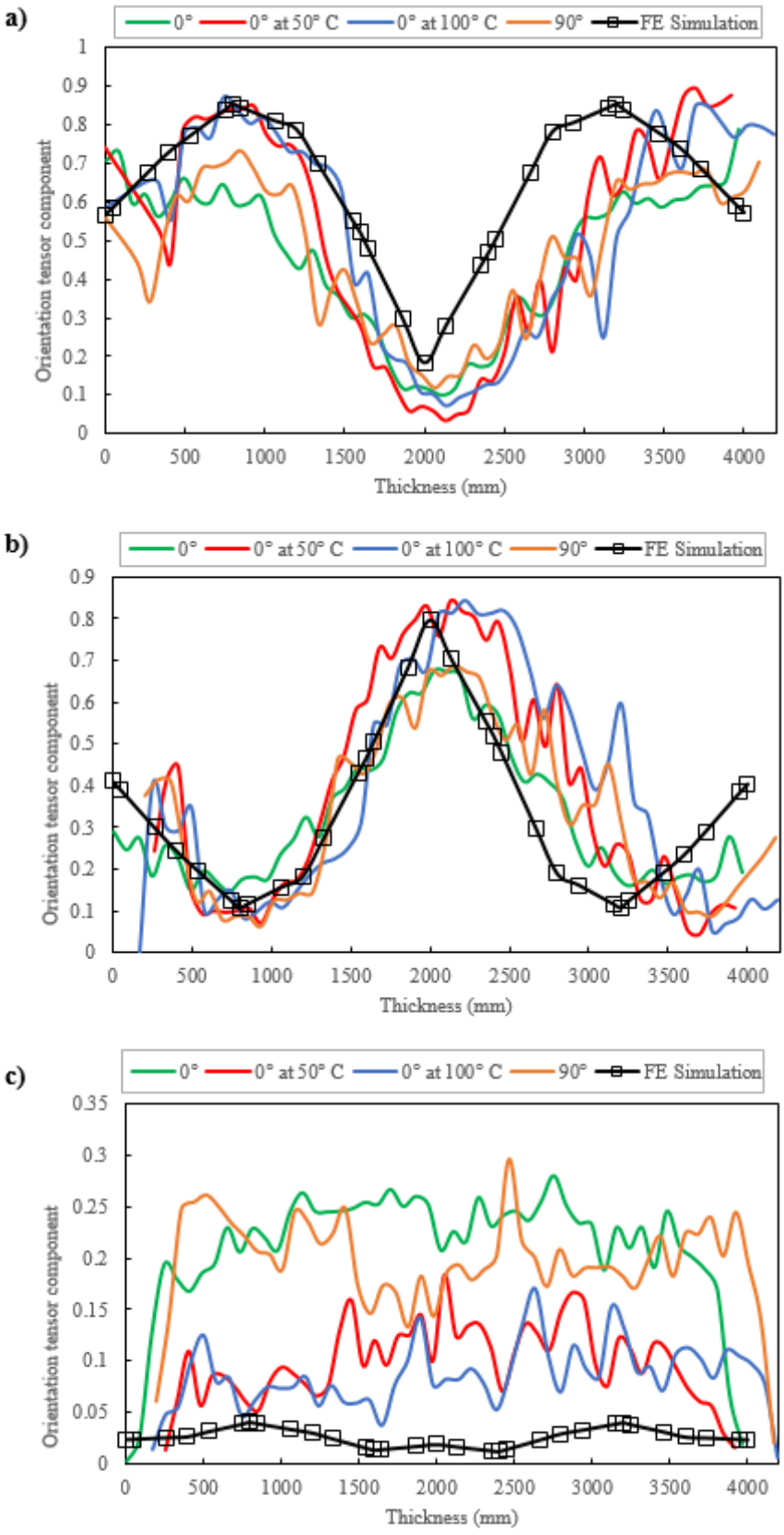

Figure 7-2 Measured orientation tensor compared to simulation results. a) a11 component, b) a22 component, c) a33 component

7.2 Stress analysis results

The most important result from the injection moulding simulation was the fibre orientation tensor, which was later transferred to the structural mesh and used to calculate the material properties of each element. Then a stress analysis was conducted on specimens oriented at 0°, 45° and 90° with respect to the injection moulding direction by applying the boundary conditions described in Chapter 4. These stress analyses were carried out using the Newton method in the iterative solver within Abaqus/Standard. The material model explained in section 4.3.3 was employed for these analyses. The element type used was C3D8R and as mentioned in section 4.3, a mesh independence study was conducted refining the mesh towards the gauge length of the coupon as illustrated in Figure 4-5. With the results of these analyses, stress-strain curves were plotted and compared to the experimental ones. As seen in Figure 7-4, Figure 7-11 and Figure 7-18, it was necessary to calibrate the material model to better represent the real material response. For the reader's convenience, a schematic of the different views used to analyse the stress and strain distribution is shown in Figure 7-3. In this schematic, the location of the gauge length, shell layer and core layer is illustrated.

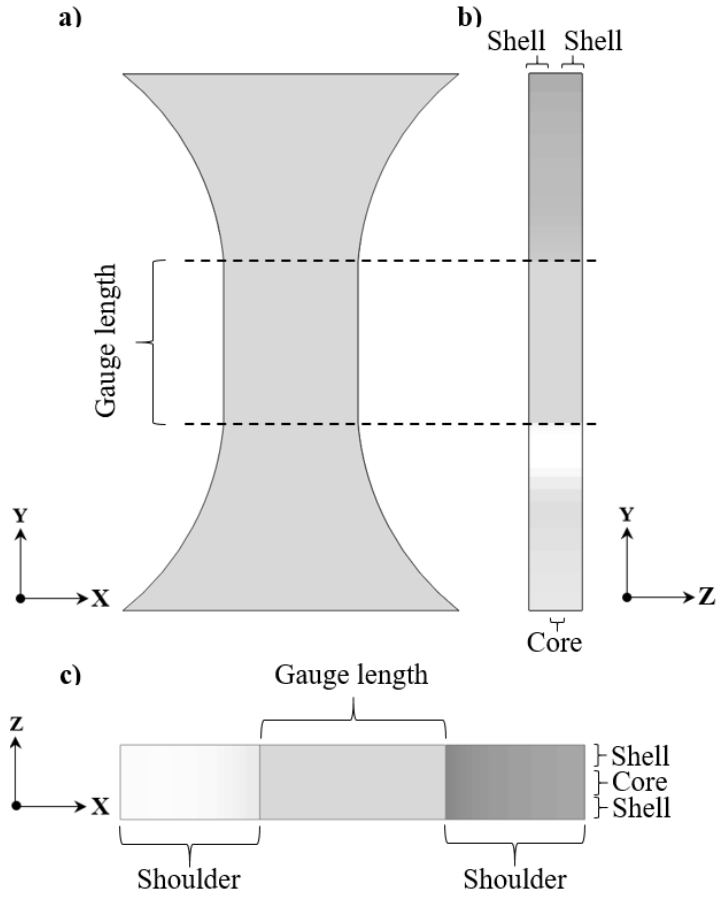

Figure 7-3 Schematic of the specimen's view. a) front view, b) lateral view (thickness), c) cross-section cut

7.2.1 Room temperature specimens

Figure 7-4 compares the experimental and simulated stress-strain curves of specimens tested at room temperature before and after performing a reverse engineering process. It can be observed that before adjusting the material model, the material response from the simulations seems stiffer than the actual behaviour. However, after reverse engineering, the simulations were in good agreement with the experimental data, showing a slightly higher UTS for all three orientations.

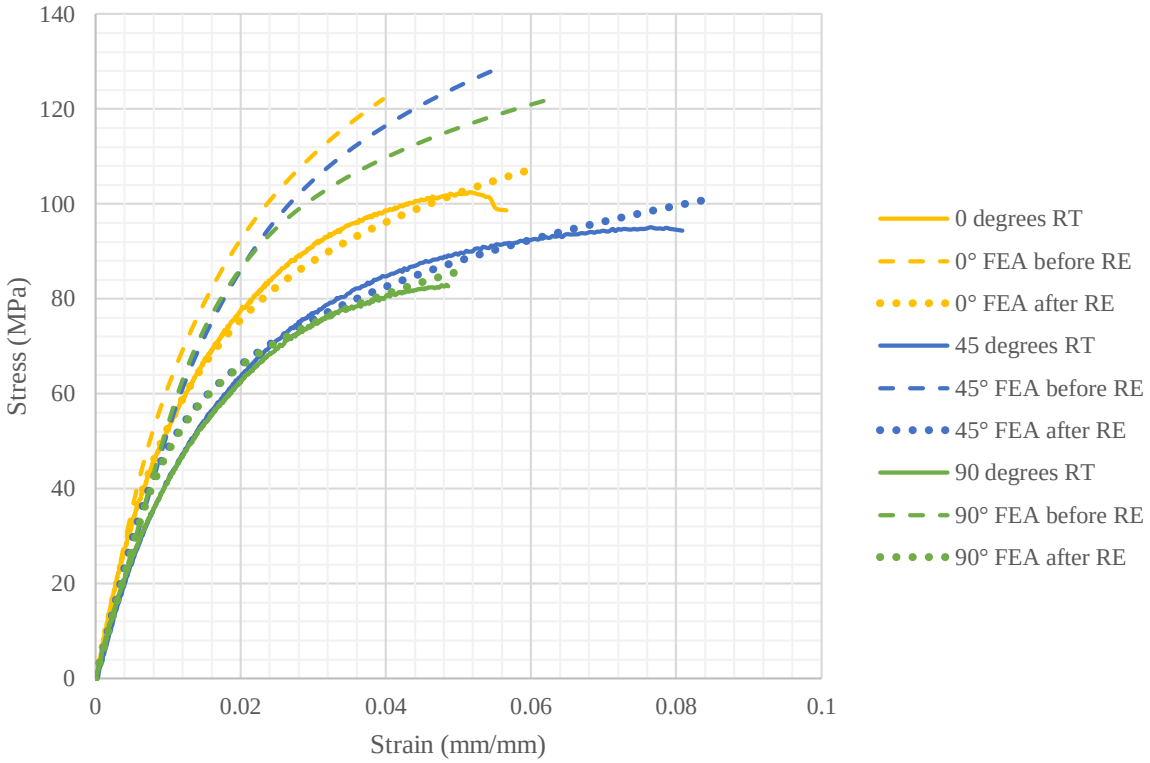

Figure 7-4 Comparison of experimental Stress-Strain and predicted curves before and after reverse engineering (RE) for specimens tested at room temperature

Table 7-1 shows the material properties before and after the reverse engineering process. It can be observed that the only modified parameters are the matrix and the Ramberg-Osgood parameters, leaving the fibre properties unmodified. This was because, as stated in 4.3.3, the matrix was responsible for the non-linear behaviour of the material.

Table 7-1 Material parameters at room temperature before and after reverse engineering (RE)

		Glass fibre		Matrix		Ramberg-Osgood model parameters	
Specimen orientation	Material model	Young's modulus (MPa)	Poisson's ratio	Young's modulus (MPa)	Poisson's ratio	σ_0 (MPa)	n
0°	Before RE	72000	0.2	2932.24	0.445312	185.401	13.6062
	After RE	72000	0.2	2932.24	0.445312	140.401	13.6062
45°	Before RE	72000	0.2	2932.24	0.445312	185.401	13.6062
	After RE	72000	0.2	2932.24	0.445312	67	14
90°	Before RE	72000	0.2	2932.24	0.445312	185.401	13.6062
	After RE	72000	0.2	2932.24	0.445312	130	13.6062

7.2.1.1 0° specimen

Figure 7-5a-f presents the evolution of stress and strain of a 0° specimen at different load levels at room temperature. At 10% of the UTS, stress concentrations at the gauge length ends are observed in the front and, especially, in the thickness view, where the maximum stress is located at the shell layers, as seen in Figure 7-5a. At the next load level, illustrated in Figure 7-5b, the stress at the thickness seems to no longer be located at the shell layer but concentrates in a region between the shell and the core layer. Regarding the front view, the stress appears more homogeneous, but some concentrations at the gauge length ends are still observable. Finally, in Figure 7-5c, the stress distribution at the end of the tensile tests is shown. It can be noticed that the stress on the front surface of the gauge length is entirely homogeneous and that the stress in the thickness is still concentrated in the region between the shell and core layer. It also appears that along the thickness, the stress seems to localise more on one of the layer transition regions. In terms of strain distribution, the front view exhibits similar behaviour as the stress, i.e., a homogeneous distribution on the gauge length with localisations at the ends that become less evident as the loading increases. However, along the thickness, the strain concentrates at the gauge length ends, covering the entire

thickness at the beginning of the loading, as seen in Figure 7-5d. This strain concentration seems to localise at the shell layers after the load goes above 50% of the UTS, as illustrated in Figure 7-5e-f, and remains concentrated in those regions.

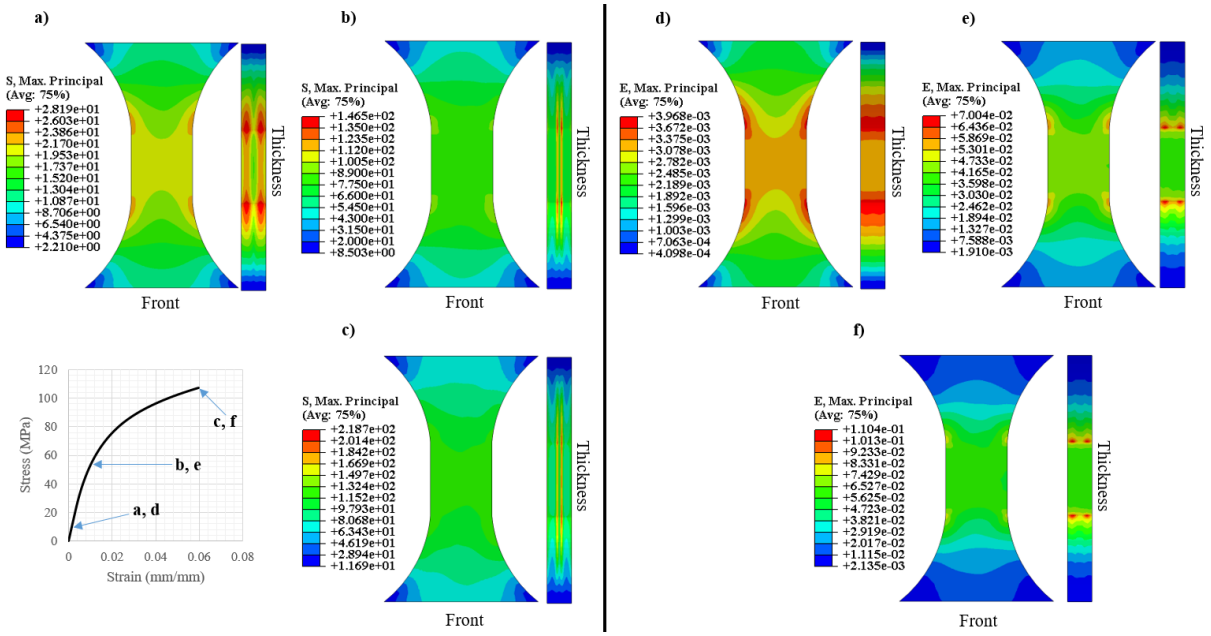

Figure 7-5 Evolution of the maximum principal stress and maximum principal strain distributions of a simulated tensile 0° specimen at room temperature

Figure 7-6a-b shows the stress and strain distribution through the thickness of a 0° specimen at the middle and end of the gauge length. As seen in Figure 7-6a, the stress concentration is near the surface and seems to be asymmetric at the middle and end of the gauge length, as seen in cuts a-a and b-b.

In terms of strain, cut c-c reveals strain localisations starting from the surface and consistent strain distribution inside the sample. In contrast to the stress, these strain concentrations seem symmetrical. On the other hand, the strain is homogeneous in the middle of the coupon, cut d-d, with a minor concentration at the very centre.

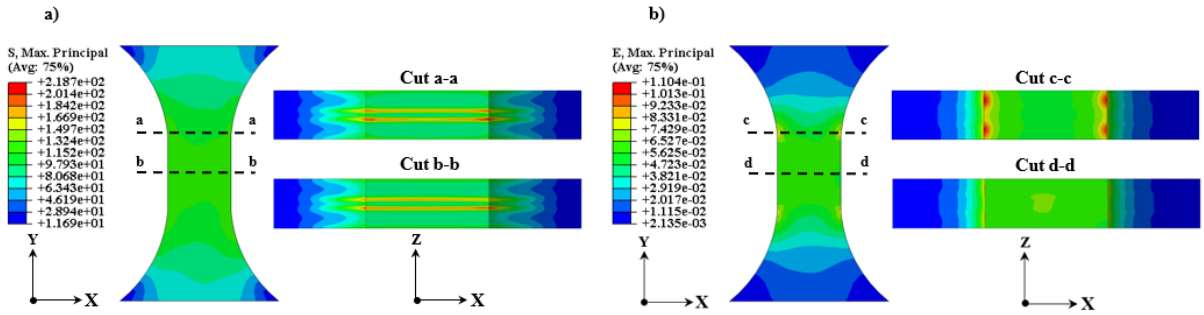

Figure 7-6 Cross section cuts at the middle and end of the gauge length of the 0° specimen at room temperature. a) stress distribution, b) strain distribution

7.2.1.2 45° specimen

The stress and strain distribution at 10%, 30% and 100% of the UTS are shown in Figure 7-7a-f. At 10% of the UTS, shown in Figure 7-7a,d, there are four noticeable stress and strain concentrations located at the ends of the gauge length. Observing the thickness at 10% of the UTS, see Figure 7-7a, a stress localisation at the bottom of the gauge length is present in the core layer and close to the surface. At the top of the gauge length, the stress concentration seems to be more distributed across the thickness. In terms of strain, the thickness view shows localisations at the gauge length ends that go across the entire thickness, and the bottom strain concentration is the one covering the most extensive area, as seen in Figure 7-7d. Figure 7-7b shows the stress distribution at 30% of the UTS. Three of the four stress concentrations at the gauge length ends are still present at this stress level, and the stress appears to be angled ~45°. However, in the thickness, the stress localised in a region between the shell and the core layers. Figure 7-7e illustrates the strain distribution at the same stress level. Similar to the stress, in the front view, the strain concentration is angled at ~45° and the highest strain localisation is at the top left corner of the gauge length end. Along the thickness, the strain concentrations at the gauge length ends remain present. However, the strain concentration at the top is the highest at this stress level. Finally, Figure 7-7c depicts the stress distribution at the end of the tensile test. A stress concentration starting at the top left corner of the gauge length oriented at ~45° is visible in the front view. In the thickness, the stress concentration at the top end of the gauge length becomes more predominant. At that stress level, the strain distribution on the surface remains oriented at ~45°, and only the top left strain localisation is visible, as seen in Figure 7-7f. Observing the thickness, only the strain concentration at the top of the gauge length remains.

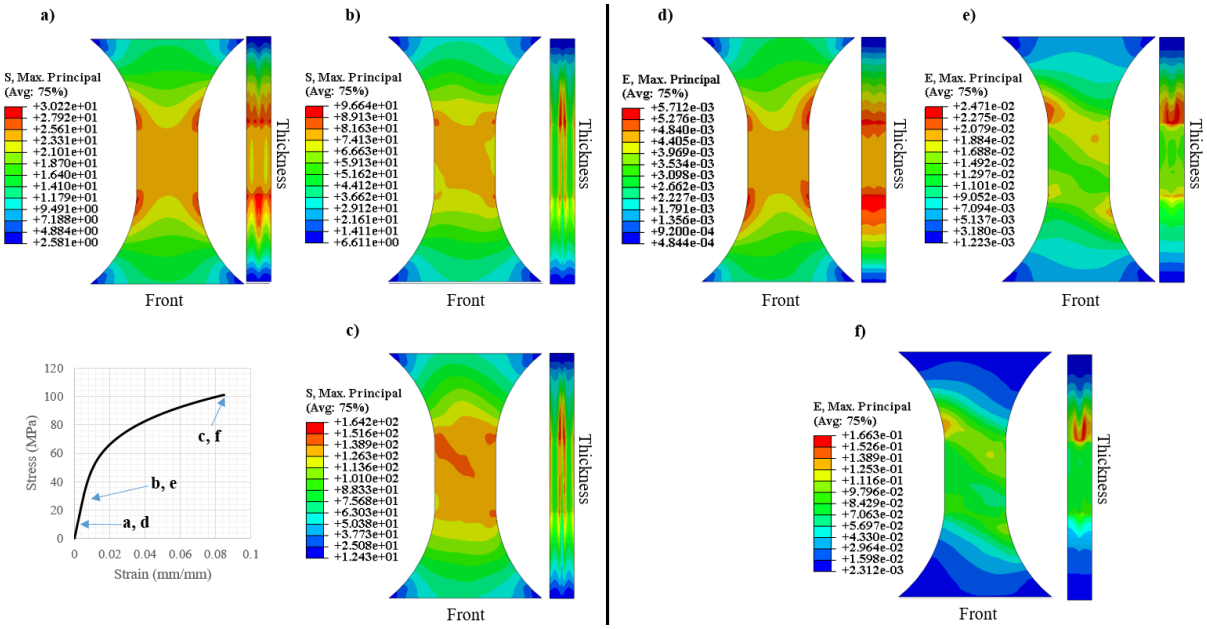

Figure 7-7 Evolution of the stress and strain distribution of a simulated tensile 45° specimen at room temperature

Figure 7-8a-b illustrates the stress and strain distribution through the thickness at the middle and end of the gauge length at the end of the tensile test. At the end of the gauge length, Figure 7-8a cut a-a, it is clear that the stress distribution is not entirely symmetrical. However, the stress distribution in the middle of the gauge length appears more symmetric, as seen in Figure 7-8a cut b-b.

The strain distribution seems skewed at ~45°, which is also visible through the thickness, as seen in Figure 7-8a-b. At the end of the gauge length, Figure 7-8b cut c-c, the highest strain concentration is located at the left side of the coupon, while in the middle, Figure 7-8b cut d-d, the strain concentration is at the right side of the coupon. At both locations, the strain concentrations are near the surface of the specimen.

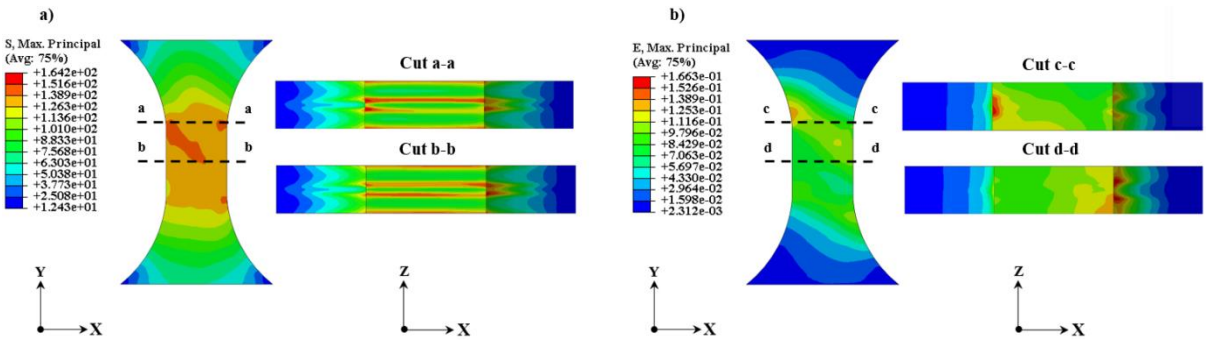

Figure 7-8 Cross section cuts at the middle and end of the gauge length of the 45° specimen at room temperature. a) stress distribution, b) strain distribution

7.2.1.3 90° specimen

Figure 7-9a-f shows the stress and strain evolution of a 90° specimen at different load levels during the tensile test simulation at room temperature. At 10% of the UTS, the stress on the front view seems homogeneous, as shown in Figure 7-9a, with a slightly higher stress concentration forming an "X" shape starting from the corners of the gauge length where small stress localisations are. Observing the lateral view, it is evident that the stress localises along the core layer, showing higher values at the gauge length ends. Figure 7-9b illustrates the stress distribution at 50% of the UTS. Here the "X" shape seems to be more marked, and the small stress concentrations at the corners increased their magnitude more than four times. At the thickness, the stress concentration appears to have moved from the core to the region between the core and shell layers. At the end of the test, Figure 7-9c, the stress mainly concentrates in the transition region. Regarding the strain distribution, as seen in Figure 7-9d-f, the strain on the front view localises predominantly in the four corners of the gauge length and develops an area of high strain in the middle at the last load level. In the thickness, the strain also remains concentrated at the end of the gauge length at all load levels.

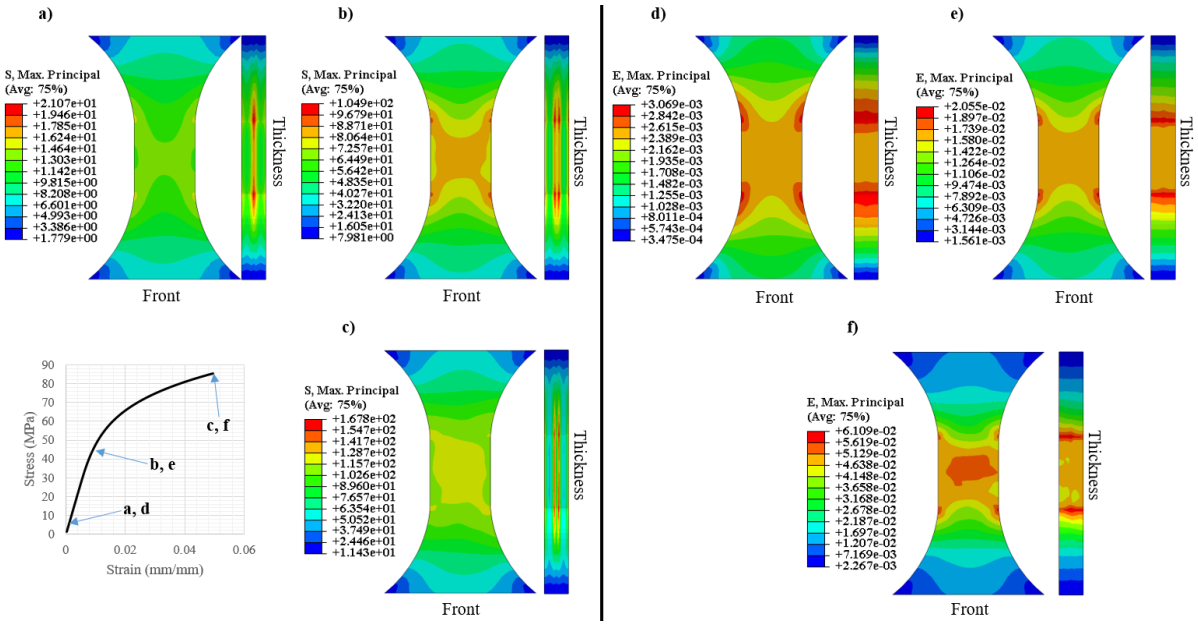

Figure 7-9 Evolution of the stress and strain distribution of a simulated tensile 90° specimen at room temperature

Figure 7-10a shows the through-thickness stress distribution at the middle and end of the gauge length at the end of the tensile test simulation. The stress is concentrated in the zone between the core and the shell layer at both locations. Figure 7-10b shows the strain

distribution at the same load. At the gauge length end, the strain concentration is at the lateral surfaces of the coupon, while in the middle, the strain seems to extend from the front surface.

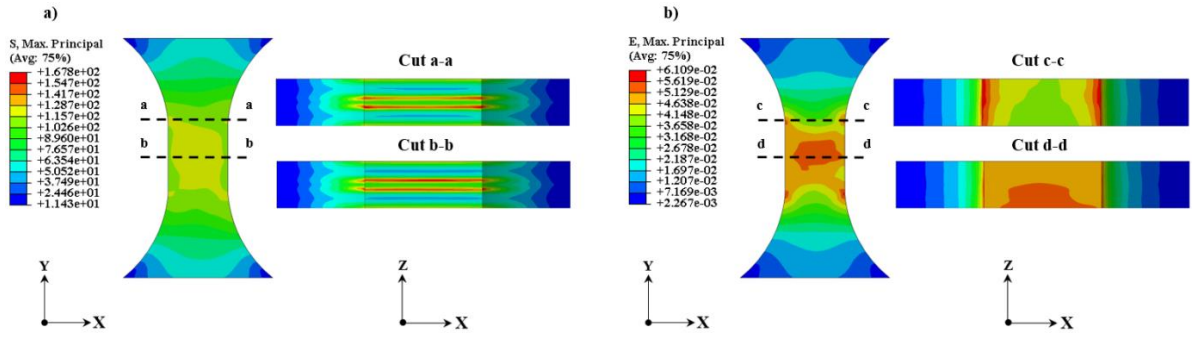

Figure 7-10 Cross-section cuts at the middle and end of the gauge length of the 90° specimen. a) stress distribution, b) strain distribution

7.2.2 50° C specimens

Similar to the room temperature curves, the simulated stress-strain curves presented a higher stiffness than the experimental curves, as seen in Figure 7-11. Good agreement between the experimental and simulated stress-strain curves was achieved after the reverse engineering process. The highest difference was observed in the 45° specimen, where the simulated stress-strain curve resulted in a UTS 4 MPa higher than the experimental and a stiffer behaviour.

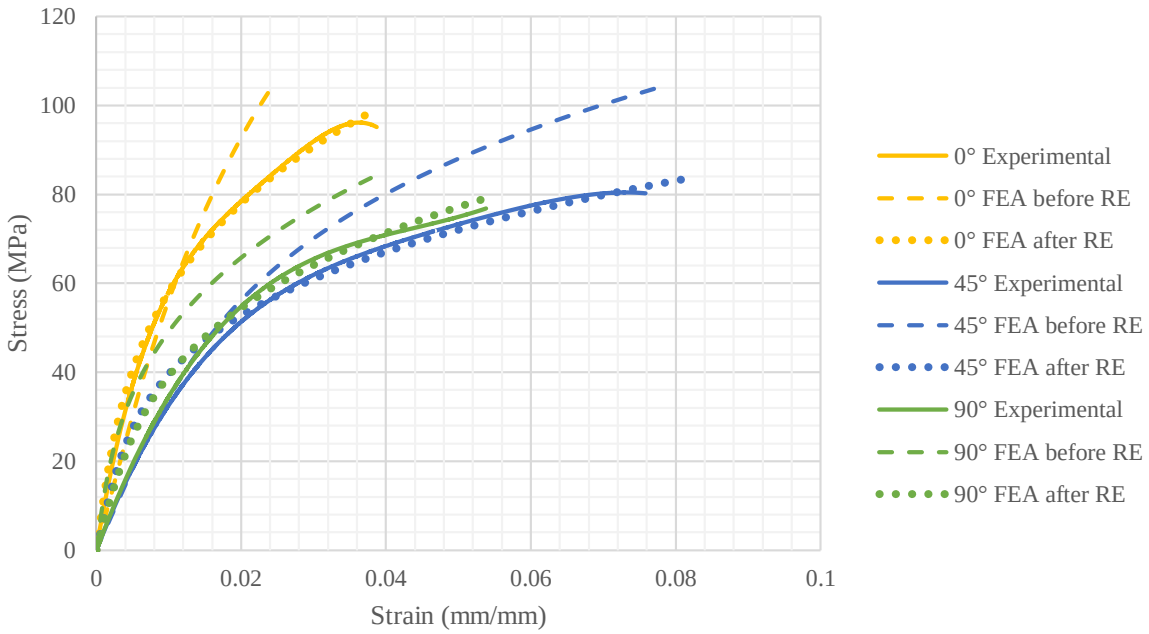

Figure 7-11 Comparison of experimental Stress-Strain and predicted curves before and after reverse engineering (RE) for specimens tested at 50° C

Table 7-2 presents the material properties before and after the reverse engineering procedure for the stress-strain curves of coupons at 50° C. In general, the model was able to reproduce the shape of the experimental curves.

Table 7-2 Material parameters at 50° C before and after reverse engineering (RE)

		Glass fibre		Matrix		Ramberg-Osgood model parameters	
Specimen orientation	Material model	Young's modulus (MPa)	Poisson's ratio	Young's modulus (MPa)	Poisson's ratio	σ_0 (MPa)	n
0°	Before RE	72000	0.2	5563.52	0.203441	23.1357	4.26809
	After RE	72000	0.2	1300	0.203441	29.1357	4.26809
45°	Before RE	72000	0.2	5563.52	0.203441	23.1357	4.26809
	After RE	72000	0.2	1300	0.203441	13	4.5
90°	Before RE	72000	0.2	5563.52	0.203441	23.1357	4.26809
	After RE	72000	0.2	1300	0.203441	23.1357	4.26809

7.2.2.1 0° specimen

Figure 7-12a-f illustrates the evolution of stress and strain of a 0° specimen during the tensile tests simulation at 50° C. At the beginning of the loading, Figure 7-12a, the stress was concentrated at the gauge length corners, as seen in the front view. In the thickness view, the highest stress was located in the shell layers. At 50% of the UTS, Figure 7-12b, the stress in the shell layers was transferred to the region between the core and the shell layers. The stress concentration remained in that location until the end of the tests, as seen in Figure 7-12c. The stress in other parts of the gauge length appeared to be mostly homogeneous. Figure 7-12d-f shows the strain distribution evolution during the test. It can be seen that the strain distribution continued to be similar during the test, showing a strain localisation at the corners of the gauge length and in the shell layers.

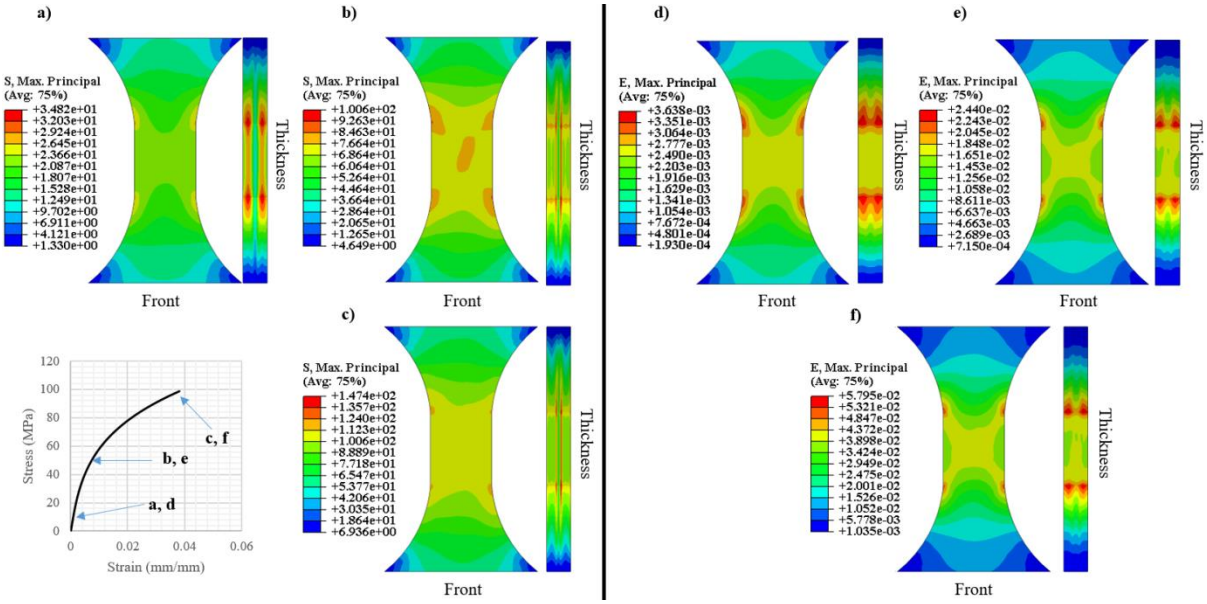

Figure 7-12 Evolution of the stress and strain distribution of a simulated tensile 0° specimen at 50° C

Figure 7-13a shows the through-thickness stress distribution at the middle and end of the gauge length at the end of the tensile test simulation. It is noticeable that the stress was located in the transition region between the core and the shell layers at both locations. In contrast, the strain depicted in Figure 7-13b was concentrated near the surface at the gauge length corners, while in the middle, a minor strain concentration is visible at the centre of the coupon.

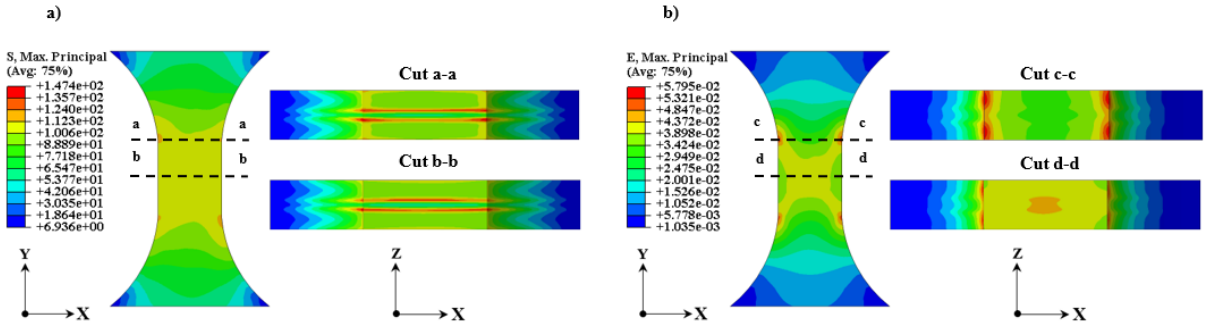

Figure 7-13 Cross-section cuts at the middle and end of the gauge length of the 0° specimen at 50° C. a) stress distribution, b) strain distribution

7.2.2.2 45° specimen

As seen in Figure 7-14a, the stress in the 45° specimen at the beginning of the simulated tensile test at 50° C was primarily located in the region between the core and shell layers along the thickness. In the front view, one can observe that the stress is concentrated at the four corners of the gauge length and seem to be angled at ~45°. Figure 7-14b shows that at

50% of the UTS, the stress on the coupon surface was homogeneous, with some localisations at the corners. Meanwhile, along the thickness, the stress was concentrated at the transition region between the shell and core layers. Also, it is noticeable that some high stress concentrations are close to the surface. At the end of the simulated tensile test, Figure 7-14c, the stress continued to be homogeneous on the sample's surface, but an angled stress localisation appeared. Along the thickness, the stress concentration remained in the same locations as at 50 % of the UTS. As seen in Figure 7-14d, at 10% of the UTS, the strain was concentrated in the corners of the gauge length, showing two main concentrations in opposite corners. Along the thickness, the strain showed an extensive localisation at the bottom end of the gauge length and two smaller concentrations at the top end. Lower strain magnitude regions connect both strain localisations along the transition area between the shell and core layers. Figure 7-14e illustrates the strain at 50% of the UTS, where it is observed that the strain on the surface is more homogeneous, and two angled higher strain concentrations were formed. Observing the thickness, one can notice that the strain becomes localised at the gauge length end in the transition region. A similar strain distribution is observed at the end of the simulated tensile test, as shown in Figure 7-14f.

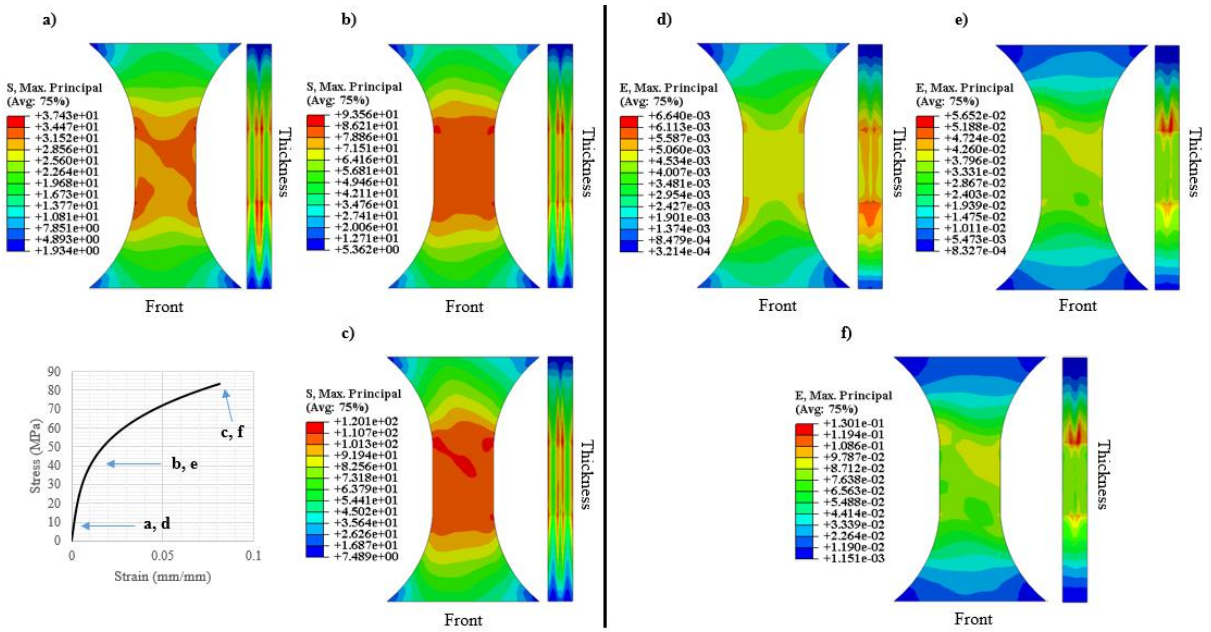

Figure 7-14 Evolution of the stress and strain distribution of a simulated tensile 45° specimen at 50° C

Two transversal cuts, one at the middle of the gauge length and one at the end, are depicted in Figure 7-15a-b. As illustrated in Figure 7-15a, the stress distribution seems quite similar at both locations, showing stress concentrations at the transition zone going across the thickness

and some localisation at the surface. The strain distribution is presented in Figure 7-15b. At the gauge length end, cut c-c, the strain appears to be concentrated near the surface of the sample. In the middle of the specimen, the strain shows some concentration on one side, where the angled strain is observed on the surface.

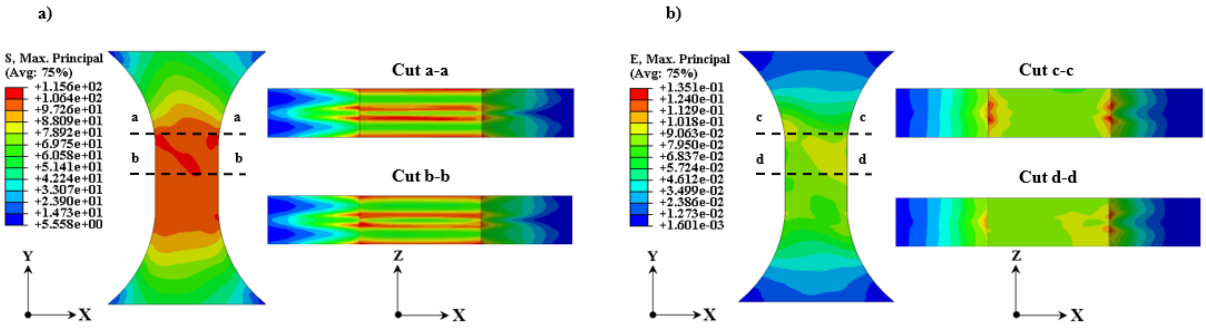

Figure 7-15 Cross section cuts at the middle and end of the gauge length of the 45° specimen at 50° C. a) stress distribution, b) strain distribution

7.2.2.3 90° specimen

The evolution of stress and strain distributions of the tensile test simulation of a 90° coupon is presented in Figure 7-16a-f. It can be observed that around 10% of the UTS, the strain seems uniform on the surface. Nevertheless, observing the thickness, one can see that the stress is concentrated in the core layer, as seen in Figure 7-16a. Around 50% of the UTS, Figure 7-16b, the stress tended to concentrate around the centre of the gauge length. Along the thickness, the stress localised in the region between the core and shell layers. Similar to the 90° specimen at room temperature, the stress continued to be localised in that thickness region until the end of the loading, as seen in Figure 7-16c. Nonetheless, the maximum stress was 12% lower than at room temperature.

On the other hand, the strain had a tendency to concentrate at the corners of the gauge length during the entire test, as seen in Figure 7-16d-f. However, some strain localisation appeared at the centre at around 50% of the UTS, as shown in Figure 7-16e. Along the thickness, the strain was concentrated around the gauge length ends during the entire test, with the highest strain located in the core region.

Figure 7-17a-b depicts two transversal cuts through the thickness of the specimen at the end of the test. The stress distribution at the middle and end of the gauge length is shown in Figure 7-17a. It is observed that the stress presents a similar distribution at both locations. Nonetheless, as seen in cut b-b, the stress in the middle is higher than at the gauge length end.

As seen in Figure 7-17b, the strain concentrates near the surface at the gauge length end covering the entire thickness with the highest values at the core region, while in the middle of the gauge length, the strain from the surface seems to go further into the thickness.

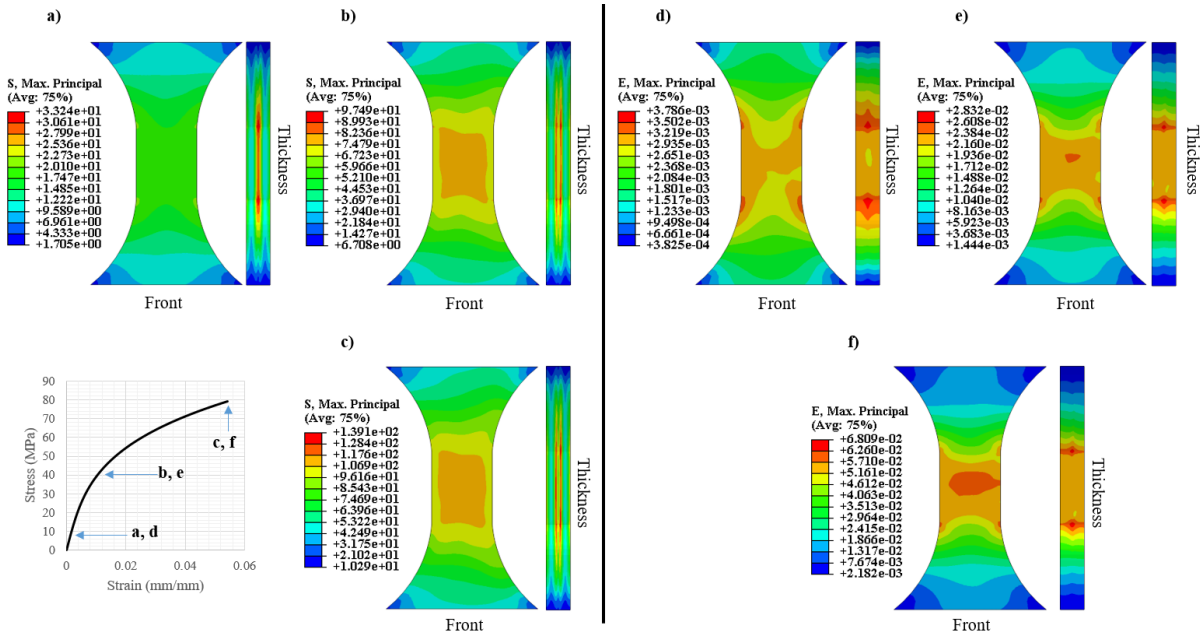

Figure 7-16 Evolution of the stress and strain distribution of a simulated tensile 90° specimen at 50° C

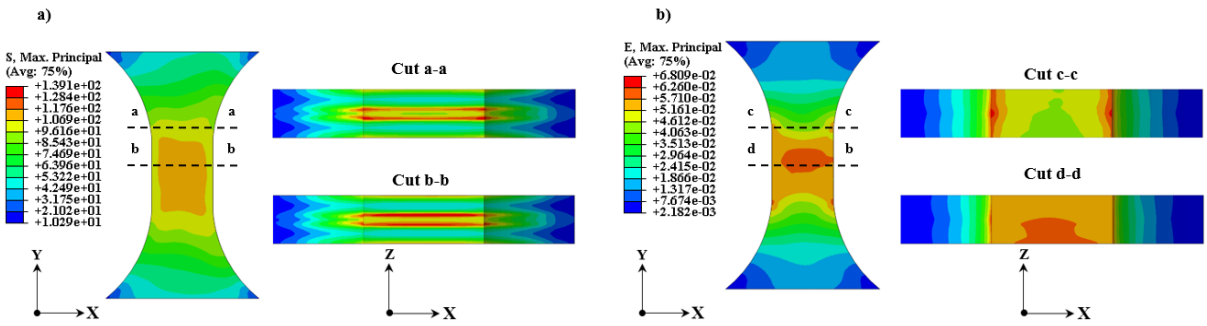

Figure 7-17 Cross-section cuts at the middle and end of the gauge length of the 90° specimen at 50° C. a) stress distribution, b) strain distribution

7.2.3 100° C specimens

The comparison of the experimental and simulated stress-strain curves at 100° C is shown in Figure 7-18. The behaviour of the simulated curves before the reverse engineering resembles the curves at the previous temperatures, showing a higher stiffness and UTS.

The simulated curve from the model of the 0° sample shows a reasonable agreement with the experimental curve using the reverse-engineered material model, especially at low stress levels, and shows a strain at break 9% larger. On the other hand, the 90° simulated coupon

exhibited a superior strain at break of 0.015 compared to the experimental curve and a UTS value 5 MPa higher. The curve obtained from the model of the 45° specimen also almost overlaps the experimental curve. However, it shows a smaller strain at break of 0.01 compared to the experimental one.

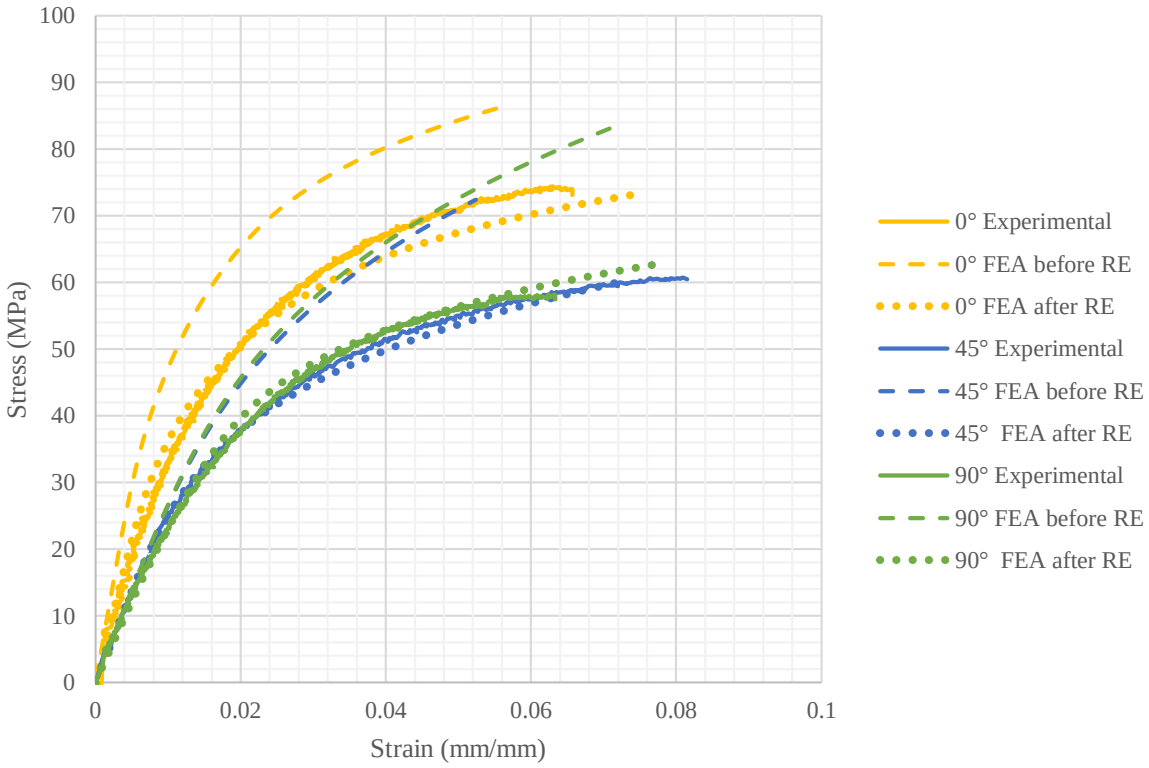

Figure 7-18 Comparison of experimental Stress-Strain and predicted curves before and after reverse engineering (RE) for specimens tested at 100° C

The material properties before and after the reverse engineering procedure are presented in Table 7-3.

Table 7-3 Material parameters at 100° C before and after reverse engineering (RE)

		Glass fibre		Matrix		Ramberg-Osgood model parameters	
Specimen orientation	Material model	Young's modulus (MPa)	Poisson's ratio	Young's modulus (MPa)	Poisson's ratio	σ_0 (MPa)	n
0°	Before RE	72000	0.2	1876.93	0.441744	83.9897	14.7513
	After RE	72000	0.2	700	0.203441	46.2714	13
45°	Before RE	72000	0.2	1876.93	0.441744	83.9897	14.7513
	After RE	72000	0.2	700	0.203441	20	7
90°	Before RE	72000	0.2	1876.93	0.441744	83.9897	14.7513
	After RE	72000	0.2	700	0.203441	35.2714	10

7.2.3.1 0° specimen

The evolution of stress and strain distribution of the tensile test simulation of a 0° coupon at 100° C is shown in Figure 7-19a-f. It can be seen in Figure 7-19a that at low load, the stress on the gauge length surface is uniform, but along the thickness, the stress concentrates in the shell layers, especially at the gauge length ends, where the stress is almost double than at the surface. At intermediate loads, Figure 7-19b, the stress concentrated at the gauge length ends, and these concentrations were connected in an "X" shape crossing the middle of the specimen. Along the thickness, the stress seemed to have moved towards the surface. Finally, at high loads, the stress on the surface seems to be homogenous, with some minor stress localisations near the gauge length ends, as seen in Figure 7-19c. Meanwhile, the stress concentrates at the region between the core and shell layer along the thickness.

Figure 7-19d-f shows the evolution of strain distribution during the simulated tensile test. It is noticeable that at low load, the strain concentrates at the gauge length ends at both the surface and along the thickness, and as the load increases, the stress magnitude intensifies at these locations. On the surface, it remains at the gauge length ends, but it concentrates in the shell layers along the thickness.

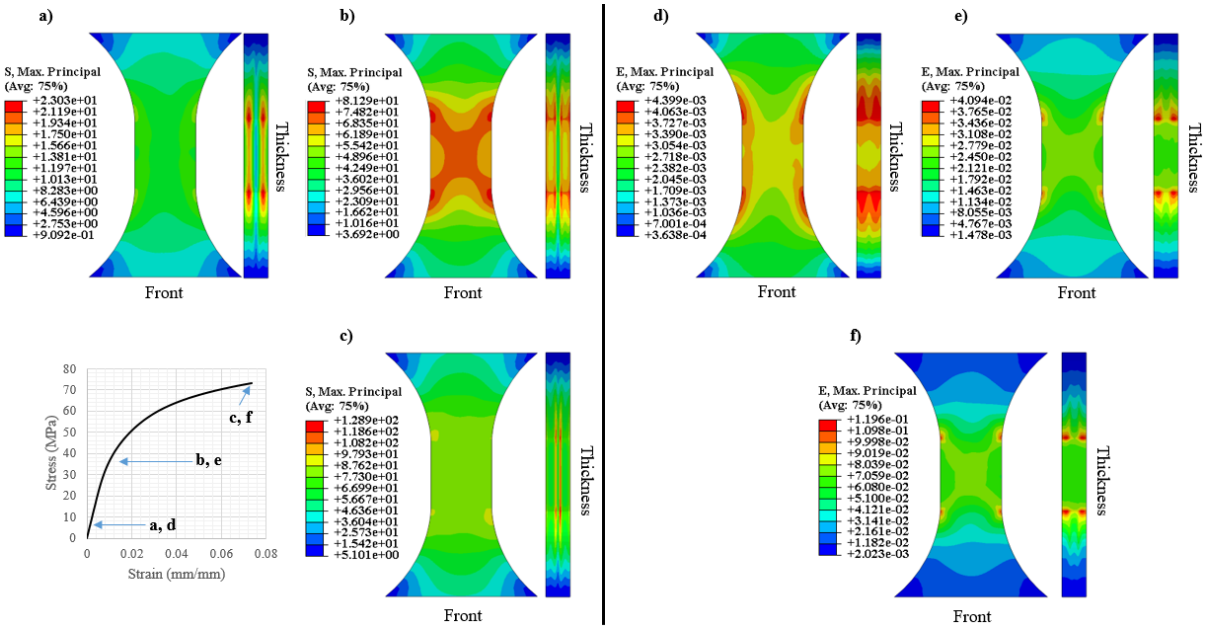

Figure 7-19 Evolution of the stress and strain distribution of a simulated tensile 0° specimen at 100° C

Figure 7-20a-b presents the through thickness stress and strain distribution at the middle and end of the gauge length of the 0° specimen at the end of the simulated tensile test. In Figure 7-20a it can be seen that the stress at the gauge length ends is localised in the transition region and goes all along the width of the specimen. It is also visible that the highest stress at this location is concentrated near the surface. In the middle of the sample, the stress is also concentrated all along the specimen's width in the region between the core and shell layers. Figure 7-20b depicts the strain distribution at the same locations. At the end of the gauge length, the strain appears to be concentrated in the shell layers and near the surface of the sample. In contrast, in the middle of the gauge length, the strain seems to increase towards the centre of the coupon.

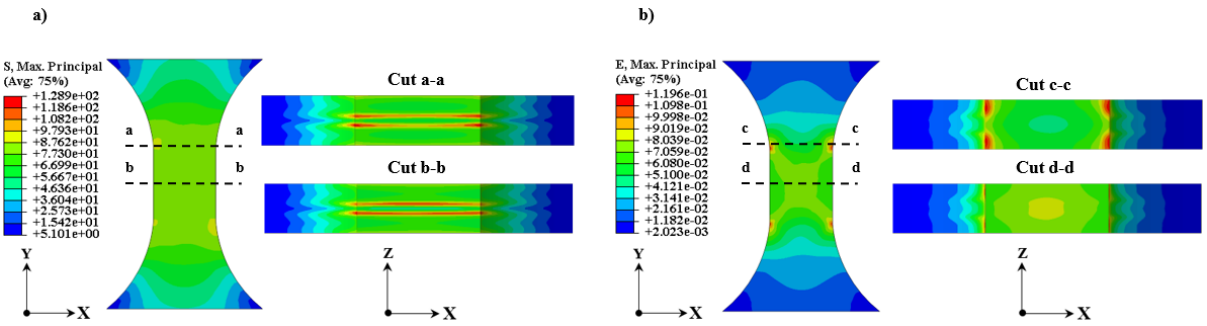

Figure 7-20 Cross-section cuts at the middle and end of the gauge length of the 0° specimen at 100° C. a) stress distribution, b) strain distribution

7.2.3.2 45° specimen

Figure 7-21a-f illustrates the stress and strain distribution for a 45° coupon under different load levels. Similar to the 45° specimens at previous temperatures, at a low load, the stress was uniform on the surface of the coupon with some concentrations at the gauge length corners, as seen in Figure 7-21a. At intermediate loads, Figure 7-21b, a stress concentration appeared at a ~45° angle in the centre of the gauge length. Finally, at the end of the test, the stress was homogenous on the sample's surface, as depicted in Figure 7-21c. Regarding the stress along the thickness, it presented an analogous behaviour to the previous 45° coupons: the stress is localised at the core layer at the bottom of the gauge length at low loads. Then, at intermediate loads, Figure 7-21b, it concentrates near the surface and the region between the core and shell layers, remaining like this until the end of the test, see figure Figure 7-21c.

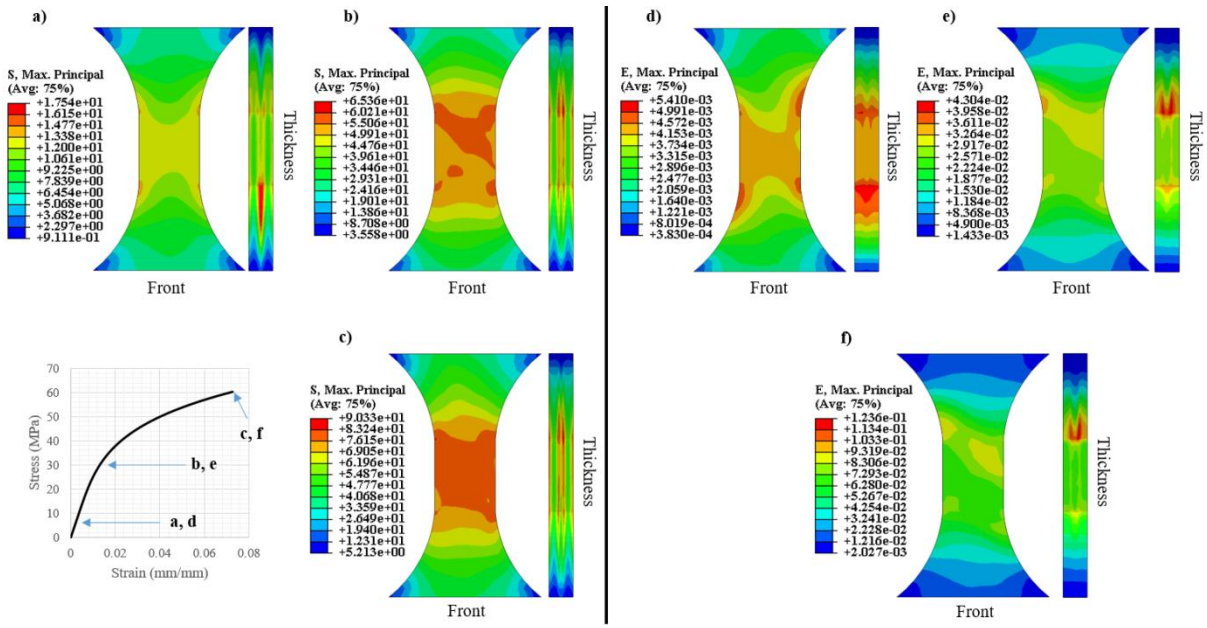

Figure 7-21 Evolution of the stress and strain distribution of a simulated tensile 45° specimen at 100° C

Figure 7-22a-b shows a transversal cut at the middle and end of the gauge length, exhibiting the stress and strain distribution through the thickness. At the gauge length end, some stress concentrations are located at the corners and the middle close to the surface. A lower stress concentration crosses the entire sample's width, following a path through the core layer, as seen in Figure 7-22a. This stress concentration crossing the width is also observable in the middle of the gauge length.

Figure 7-22b presents the strain distribution through the thickness at the same locations, end and middle of the gauge length. It is visible that at the gauge length end, the strain

concentration is close to the surface and extends towards the centre of the coupon. In contrast, strain seems uniform in the middle of the gauge length, with only a few small concentrations close to the surface.

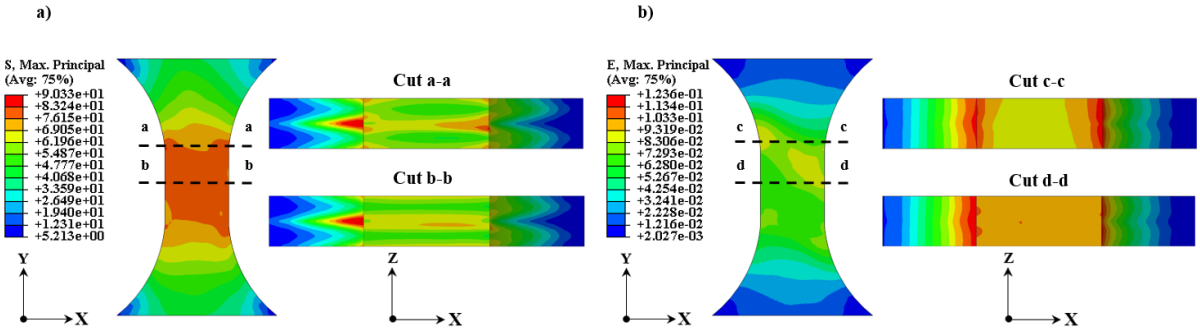

Figure 7-22 Cross section cuts at the middle and end of the gauge length of the 45° specimen at 100° C. a) stress distribution, b) strain distribution

7.2.3.3 90° specimen

Finally, Figure 7-23a-f presents the evolution of stress and strain of a 90° specimen at different loads during the simulation of the tensile test at 100° C. Similar to the 90° sample at 50° C, at low load, the stress is uniform on the surface and concentrates at the core layer, as seen in Figure 7-23a. Meanwhile, the strain concentrates at the ends of the gauge length, as illustrated in Figure 7-23d. Around 50% of the UTS, a stress concentration started to form in the centre of the gauge length, as seen in the front view of Figure 7-23b. The stress along the thickness is now localised between the core and the shell layers. At this load level, the strain at the gauge length ends along the thickness is higher than on the surface, see Figure 7-23e. By the end of the test, the stress remained concentrated between the core and shell layers, and a lower concentration at the surface centre can be observed in Figure 7-23c. The strain at this point is mainly concentrated at the centre of the gauge length, as illustrated in Figure 7-23f. Small strain concentrations on the core layer are visible in the thickness view.

Figure 7-24a-b depicts cuts through the thickness at the middle and end of the gauge length at the end of the simulated tensile test of the 90° specimen at 100°C. Figure 7-24a shows that the stress distribution is similar at the middle and end of the gauge length. This is because both locations present stress concentration between the core and shell layers along the width. Nevertheless, the cut in the middle reveals a higher stress magnitude than at the end of the gauge length. The strain distribution at those locations is shown in Figure 7-24b. Again, the strain at the gauge length end seems to be concentrated near the sample's lateral surfaces. The

opposite to this is observed in the middle, where the strain concentration extends from the specimen's front surface and covers almost the entire cross-section.

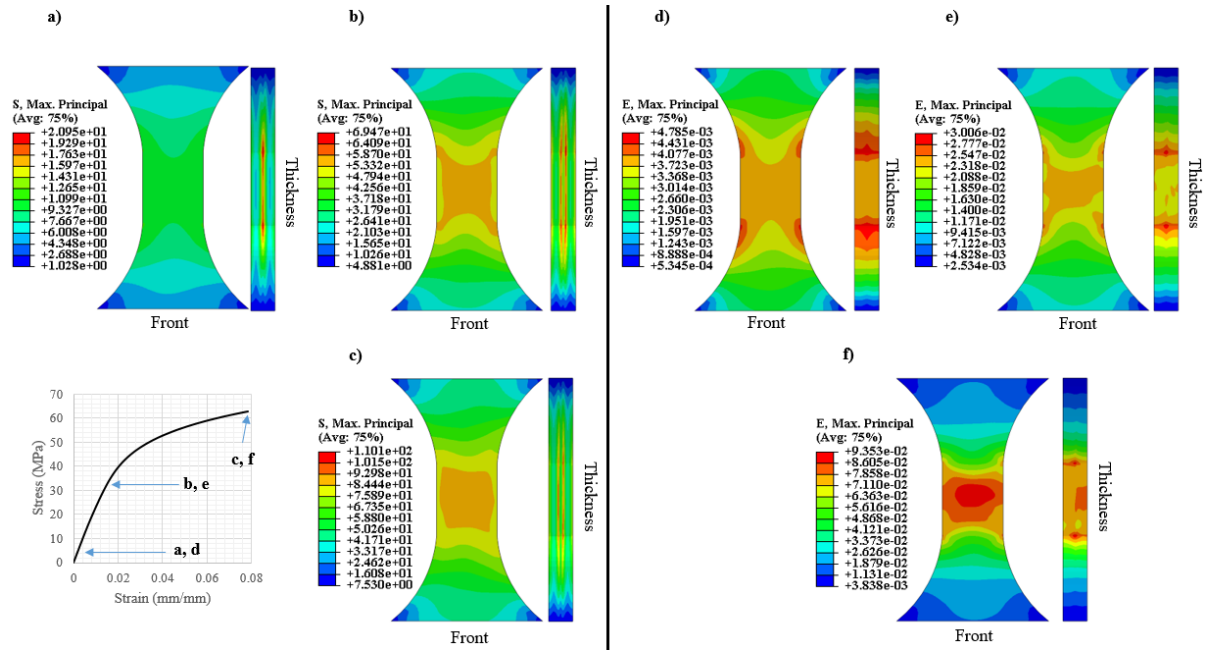

Figure 7-23 Evolution of the stress and strain distribution of a simulated tensile 90° specimen at 100° C

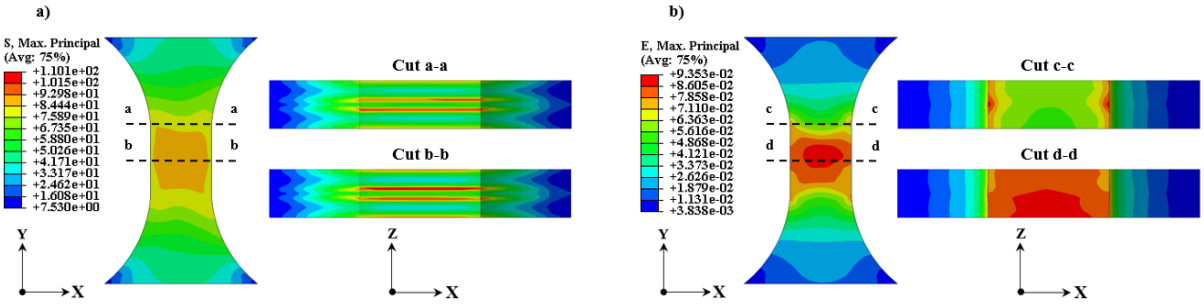

Figure 7-24 Cross section cuts at the middle and end of the gauge length of the 90° specimen at 100° C. a) stress distribution, b) strain distribution

7.3 Fatigue life predictions

In order to conduct the fatigue life predictions, stress analyses were carried out on specimens modelled at the three orientations. The loads utilised were selected according to the maximum stress of the experimental results. As decribed in section 4.4, with the results of these stress analyses and the orientation tensor, the fibre share was calculated. This fibre share was later used to compute the resultant interpolated S-N curve in order to estimate the fatigue life of the 45° coupons.

Figure 7-25 shows the results of the S-N fatigue modelling for the three coupon orientations and temperatures tested. In order to validate the fatigue life predictions, the results obtained following the process described in section 4.4 for the 45° specimens were compared against the experimental results. It can be observed that at all temperatures, the predicted S-N curves lay close to the experimental data. The predicted room temperature curve seems to overestimate the fatigue life. On the other hand, the predicted curve for the coupons at 50 and 100° C showed a particularly good agreement with the experimental results at intermediate and long fatigue lives.

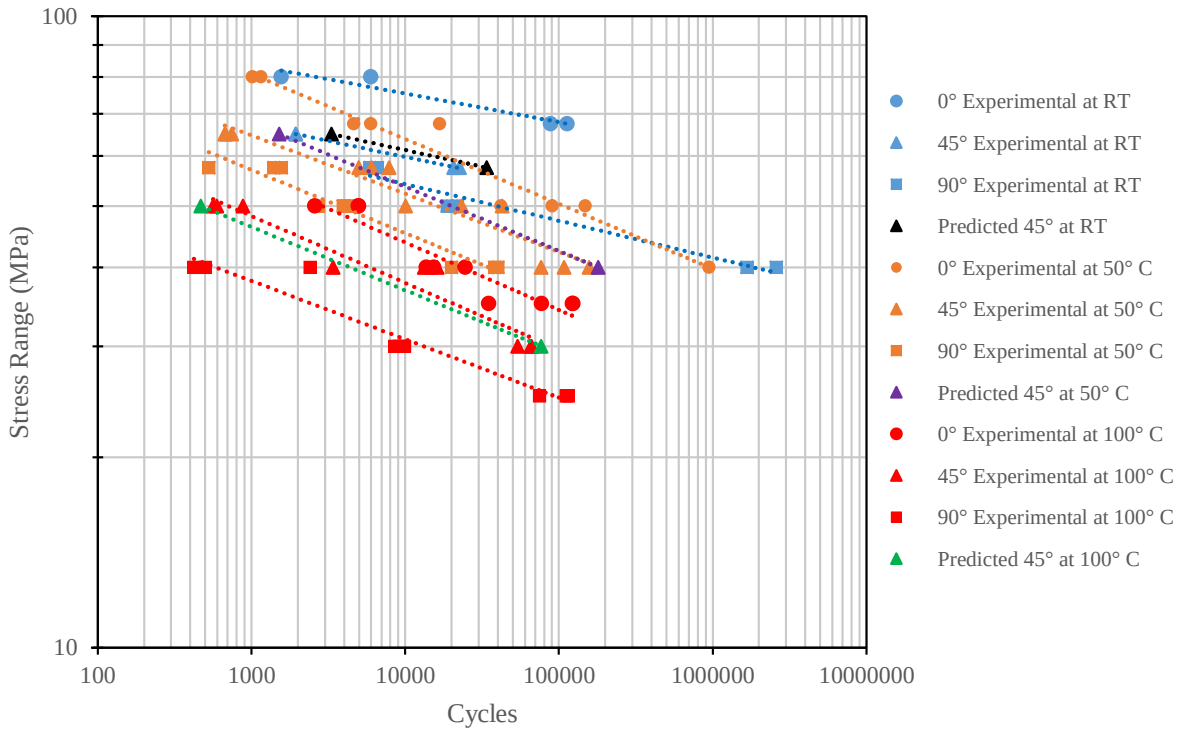

Figure 7-25 Results of S-N fatigue modelling

Basquin's equations for the predicted and experimental curves at the three temperatures are presented in Table 7-4.

Table 7-4 Basquin's equations for experimental data and model prediction at different temperatures

Temperature	Specimen orientation	Experimental data	Model prediction
Room temperature	0°	$\sigma = 114.33N^{-0.045}$	-
	45°	$\sigma = 95.542N^{-0.061}$	$\sigma = 99.763N^{-0.053}$
	90°	$\sigma = 92.642N^{-0.058}$	-
50°C	0°	$\sigma = 164.65N^{-0.103}$	-
	45°	$\sigma = 122.22N^{-0.092}$	$\sigma = 138.79N^{-0.105}$
	90°	$\sigma = 113.92N^{-0.1}$	-
100°C	0°	$\sigma = 117.22N^{-0.107}$	-
	45°	$\sigma = 100.15N^{-0.106}$	$\sigma = 92.629N^{-0.1}$
	90°	$\sigma = 72.086N^{-0.092}$	-

7.4 Conclusion

This chapter presents the results of the multi-stage modelling methodology and fatigue life predictions. The modelling methodology started with the manufacturing process simulation of the plaque from where the coupons were extracted. The model was adjusted using the results from the μCT and successfully reproduced the shell-core-shell structure typical of injected moulded components. Then the resultant orientation tensors of the injection moulding simulation were transferred from the nodes of the injection moulding mesh to the closest integration points of the specimen's mesh. This involved relocating and rotating the specimen's mesh to match the position of the specimen within the plaque using node coordinates and element connectivity information from Abaqus and Moldflow. Integration points were computed for each mesh, and the closest integration point between meshes was identified. The orientation tensor was then calculated from the nodes of the plaque's mesh to the closest integration points of each element of the specimen's mesh using the shape function of the tetrahedral element used in the injection moulding simulation.

Then tensile test simulations were conducted. These tensile test simulations showed that the material model overestimates the material's stiffness and strength at all temperatures, and a reverse engineering process was necessary to adjust the material properties.

Analysis of the stress and strain evolution at different load levels revealed concentrations at the end of the gauge length. At intermediate and high loads, all the samples presented stress

localisations in the transition region between the shell and core layers at all temperatures. Examination of the through thickness stress at the middle and end of the gauge length exposed that this stress concentration goes all across the specimen width.

In contrast, the strain concentration varied depending on the specimen orientation, not the temperature, except for the 90° sample. This orientation showed a strain concentration in the core layer that decreased in size as the temperature increased.

Finally, fatigue life predictions were presented for 45° specimens at the three temperatures tested, showing good agreement with the experimental results.

8 DISCUSSION

In this chapter, the previous experimental and modelling results are discussed in order to gain a better understanding of the behaviour and failure mechanism of SFRP at high temperatures under quasi-static and cyclic loads.

8.1 Fibre orientation distribution

The manufacturing process has a significant effect on the microstructure of the SFRP. For this study, the SFRP used was produced by injection moulding, which caused a shell-core-shell structure due to the fountain flow. The microstructure was analysed through µCT images at the centre of the sample gauge lengths. The results, presented in Figure 6-1a-e, show the microstructure at the centre of the samples, where the shell-core-shell structure is visible. However, the 0° specimens used for the in-situ tests at high temperatures exhibited an asymmetric fibre distribution, presenting an extra skin layer only on one side of the sample. These asymmetries caused by the manufacturing process, perhaps a difference in temperature between the mould walls, are likely to produce asymmetric stress and strain distributions that ultimately will affect the failure process of the sample.

The orientation tensor was estimated at the same location using the XFiber extension of the commercial software Avizo, later used to adjust the injection moulding simulation parameters. An accurate prediction of the fibre orientation distribution is crucial to predict the mechanical response correctly via finite element analyses. For this project, the Moldflow Rotational Diffusion model [101] was used to predict the fibre distribution, as it has been shown to produce the most accurate results [37, 102]. This model has four key parameters that modify the prediction of fibre orientation, and a parametrical study was conducted as part of the model calibration, achieving a good agreement with the maximum values in the shell layers. However, even though it is known that the D1, D2 and D3 parameters give the model more flexibility to match the experimental data [39], the model was unable to reproduce the µCT measured core accurately, as shown in Figure 7-2a-c. Compared to the experimental data, the width of the predicted core layer was underestimated, and the fibre alignment was overestimated. This is a recognised limitation of the currently available models and has been reported in several studies [22, 37, 39]. A possible improvement is the one proposed by Li and Luye [103], which suggests coupling the MRD model with a fibre-induced viscosity model.

8.1 Tensile behaviour and failure mechanisms

The evident effect of fibre orientation and temperature is visible in the results shown in Figure 5-1 and Figure 5-2a-c. This observed effect is in agreement with results found in the literature on other SFRP [22, 103, 104].

Results of the fibre distribution, see Figure 6-1a-e, show that the shell layers occupy more than half of the material thickness. Furthermore, these shell layers for the 0° specimens correspond to the load direction, resulting in more fibres aligned to the load. Thus, giving the coupons a better loading capacity, presenting higher Young's modulus and UTS at all temperatures. In contrast, the 90° samples have the inverse fibre distribution with shell layers transversal to the load direction, which resulted in lower Young's modulus and UTS.

On the other hand, the results of the 45° specimens showed a similar Young's modulus and UTS than the 90° samples but higher strain at break. In addition, at 45°, few fibres are aligned to the load, indicating a significant role of the matrix in bearing the load. This could explain the similarity of Young's modulus and UTS between the 45 and 90° specimens. However, the 90° samples have fibres oriented in the loading direction at the core, which could restrict the coupon deformation, thus showing less strain at failure.

Regarding the temperature effect, at room temperature and 50° C, the 0° coupons presented similar Young's modulus and UTS suggesting that the temperature only affected the matrix but not the fibres, which were the ones bearing the load. On the other hand, at 100° C, a decrease in Young's modulus and UTS is observed. This suggests that the effect on the matrix is more severe beyond the glass transition temperature (between 65 and 70°C for this material [44]), possibly facilitating the debonding of the fibres causing fibre pull-outs.

The 45 and 90° specimens continued to exhibit similar behaviour at 50 and 100° C. Presenting a marked decrease of Young's modulus and UTS at 100° C. Furthering supporting the assessment that after the transition temperature, the failure mechanisms are different and that the matrix has an important role. Nevertheless, the 45° samples showed a more considerable ductility as the temperature increased.

The experimental stress-strain curve presented in Figure 5-1 was used to adjust the material model for the stress simulations. Various approaches have been used in the literature to calculate the material parameters. For instance, Mortazavian and Fatemi [47] utilised the Halpin-Tsai model. Other studies, such as the one conducted by Vervoort [71], limited the

loads to levels low enough to consider a linear behaviour. Nevertheless, the obtained experimental stress-strain curves in this project showed a non-linear material response. Thus, a Ramberg-Osgood material mode was used for this investigation, which is a non-linear material model. To adjust this model, the matrix Young's modulus and Ramber-Osgood parameters were modified to achieve a good agreement with the experimental results. As explained in section 4.3.3, this material model considers that the matrix is responsible for the non-linear behaviour of the material. In this study, it was found that the Young's modulus of the matrix mainly affects the slope of the linear part of the simulated stress-strain curve. On the other hand, the σ_0 parameter was seen to influence the point where the stress-strain curves begin to become non-linear. While the parameter n, describes the curvature of the non-linear part, the higher the value, the more pronounced the curvature and the more strain at failure. An example of this is shown in Figure 8-1.

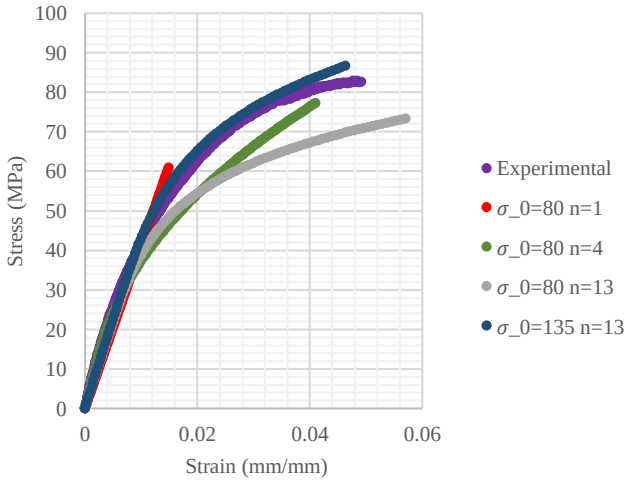

Figure 8-1 Effect of the Ramberg-Osgood parameters on the simulated stress-strain curve of a 90° specimen at room temperature

As depicted in section 7.2 the simulated stress-strain curves agreed with the experimental curves after modifying the material parameters. However, before amending the parameters, all the curves overestimated the stiffness and UTS of the coupons. The reason for this could be that the Ramber-Osgood model utilised does not consider any manufacturing defects that may affect the mechanical response of the material, such as poor bonding of the fibres or voids.

8.1.1 Strain field distributions

Digital image correlation was employed to study the strain distribution on the surface of the coupons during the tensile tests at room and high temperatures. The room temperature results showed a similar distribution to what has been found in the literature [47], as seen in Figure 8-2a-c. Figure 8-2a shows the comparison of 0° specimens where in both cases a crack starting from the edge of the coupon was observed. In addition, the effect of the fibre orientation on the strain distribution is visible in the 45° samples, as illustrated in Figure 8-2b, where an angled strain distribution is noticeable.

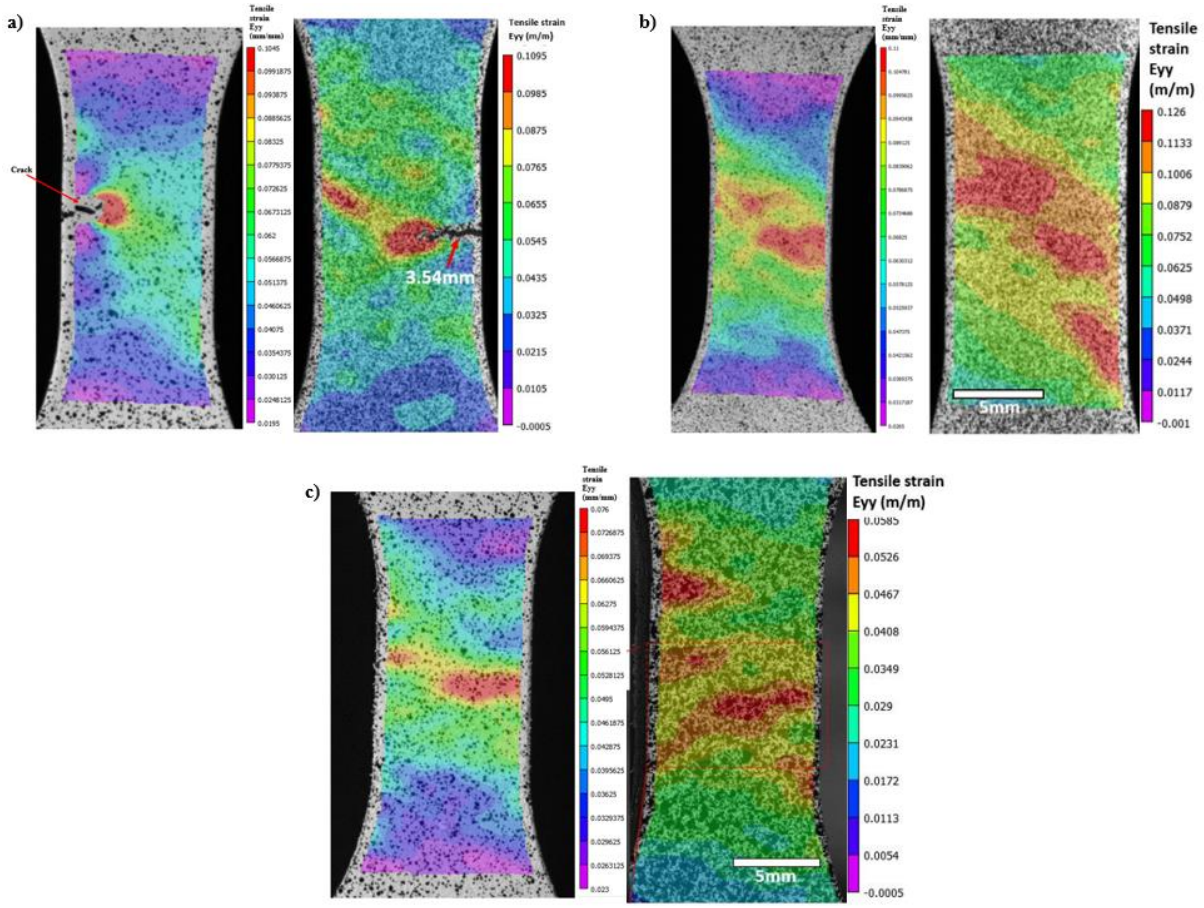

Figure 8-2 Comparison of DIC results at room temperature of the current study (left images) against results in the literature *[105]* **(right images). a) 0° specimen, b) 45° specimen, c) 90° specimen**

Figure 8-3a-c compares the strain distribution on the thickness between the FEA results and the DIC at 50°C. It is clear that the strain concentrations occur near the gauge length ends at the three orientations. It is also evident that the strain distribution is not homogeneous in the experimental results. In comparison, the modelling results show a more uniform strain distribution. This could be due to manufacturing imperfections or fibres more or less aligned

to the load in those locations that the present model could not capture. For instance, in Figure 8-3b, a crack can be observed close to the surface that modified the strain distribution, which the current model could not consider. Nevertheless, the models were able to reproduce the strain distributions and values with reasonable accuracy, except for the 0° specimen, which showed a maximum strain value 20% lower than the experimental.

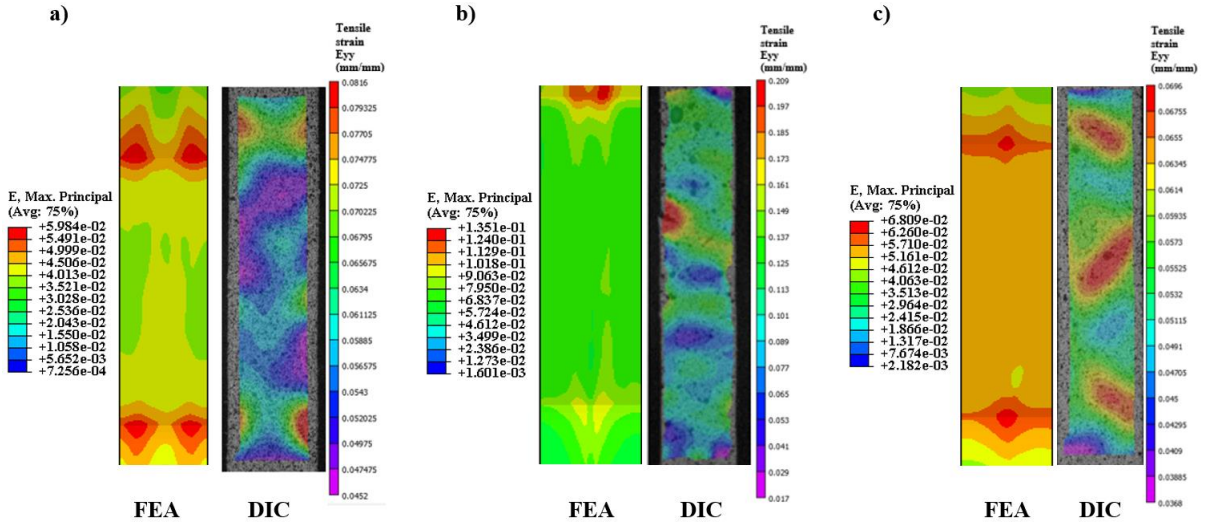

Figure 8-3 Thickness comparison between FEA and DIC for validation. a) 0° specimen, b) 45° specimen, c) 90° specimen. All samples were loaded in tension at 50° C

A comparison of the strain distribution on the front face between the FEA results and the experimental results at 100° C is shown in Figure 8-4a-c. The modelling results exhibit a good agreement with the experimental data in terms of distribution and values. Regarding the 0° specimen, Figure 8-4a showed strain concentration at the gauge length corners in the FEA results. The experimental results presented three cracks near the region of the bottom corners. One of these cracks seems to start from the sample edge, while the other two are in the middle of the width. Probably these two cracks initiated below the surface and propagated to the surface as the load increased. Figure 8-4b illustrates the strain distribution on the 45° coupons, where the effect of the fibre orientation is evident, producing an angled distribution in the experimental and simulated coupon. Finally, Figure 8-4c presents the comparison of the strain distribution in the 90° specimen, showing close maximum strain values, and a clear concentration in the middle of the gauge length in both the experimental and simulated coupon.

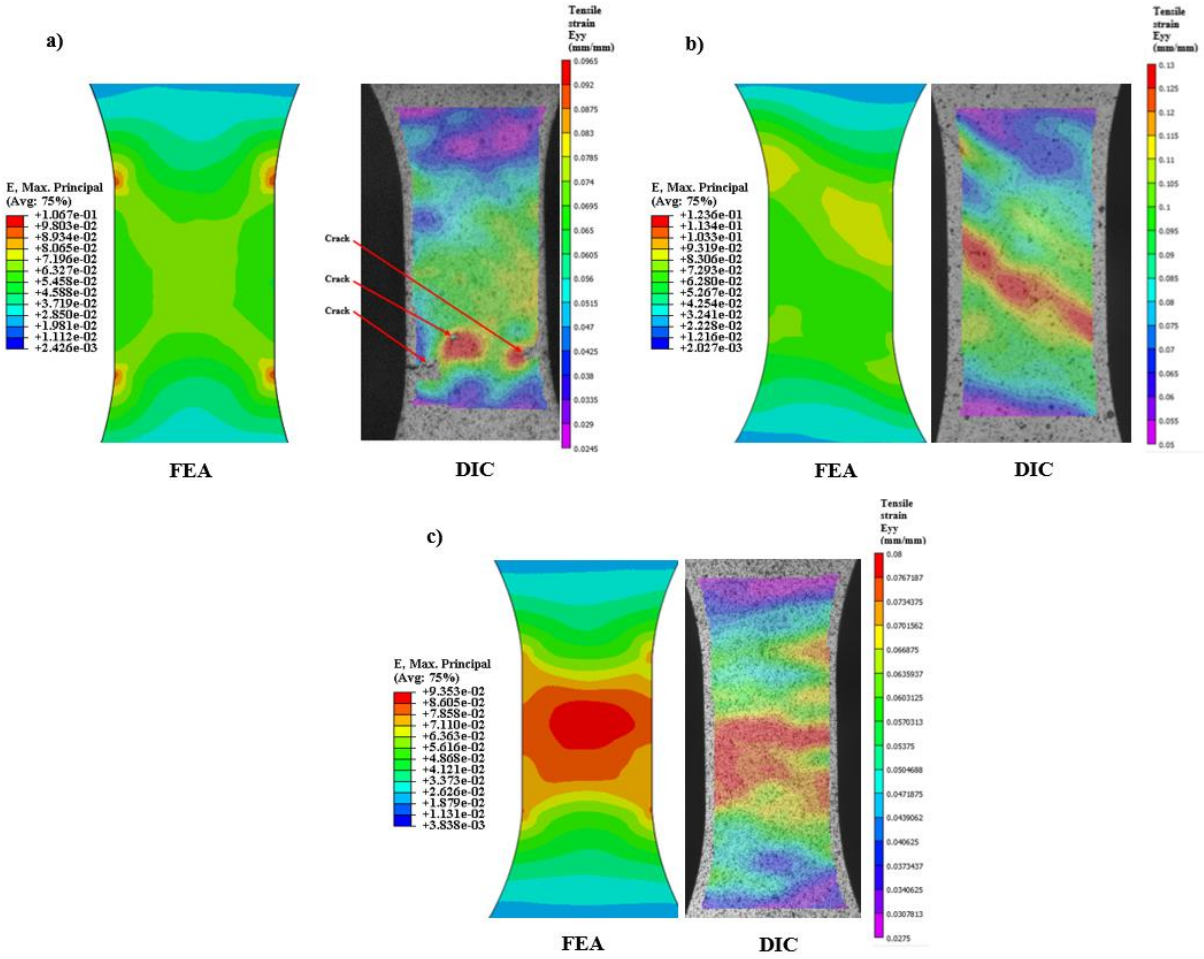

Figure 8-4 Comparison between FEA and DIC for validation. a) 0° specimen, b) 45° specimen, c) 90° specimen. All samples were loaded in tension at 100° C. Front view

The previous comparison gives the confidence to assume that if the DIC strain measurements are similar to the FEA strain, the FEA calculated stress and inner strain are representative of the actual stress and strain in the sample.

The calculated stress distributions shown in section 7.2 reveal that all the specimens, despite the orientation and temperature, presented stress concentrations in a region between the shell layers and the core. This could be due to the complex stress state in that region caused by the fibre orientation change between the layers.

8.1.2 Micro-tensile tests

Strain localisations near that transition region were also observed in the tensile test inside the μCT, as can be seen in the highlighted red circles in Figure 8-5a-d. This strain concentration was seen in all the samples except the 0° coupon tested at room temperature, which showed two strain localisations starting from the edge, Figure 8-6a, and a strain concentration in the

core layer below the surface at mid-width, illustrated in Figure 8-6b. This strain localisation at the core corresponds to a region where the fibres are perpendicular to the load direction, allowing the matrix to deform without any fibres to prevent it. Similar behaviour is observed in the 90° sample shown in Figure 8-5b. In this coupon, most of the strain concentration is covering the shell layers, which is where the fibres are less aligned to the load direction in this sample orientation.

Comparing the 0° specimen at room temperature with the samples tested at 50° and 100° C, it is noticeable that, at high temperatures, the strain distribution is not as localised as at room temperature. This is particularly visible in the coupon tested at 100° C, which presented the most homogeneous strain distribution.

Analysing all the images presented in section 6.4, it seems that the strain concentrations localise in regions where the fibre concentration is low. Besides this, once the strain concentration took place, its location did not change, it only expanded. This, gives a good estimation of the failure initiation, as the strain concentration path is very close to the fracture path of the samples, as seen in Figure 6-11, Figure 6-18 and Figure 6-28. Similar results were reported by Crupi et al. [41] using 2D DIC.

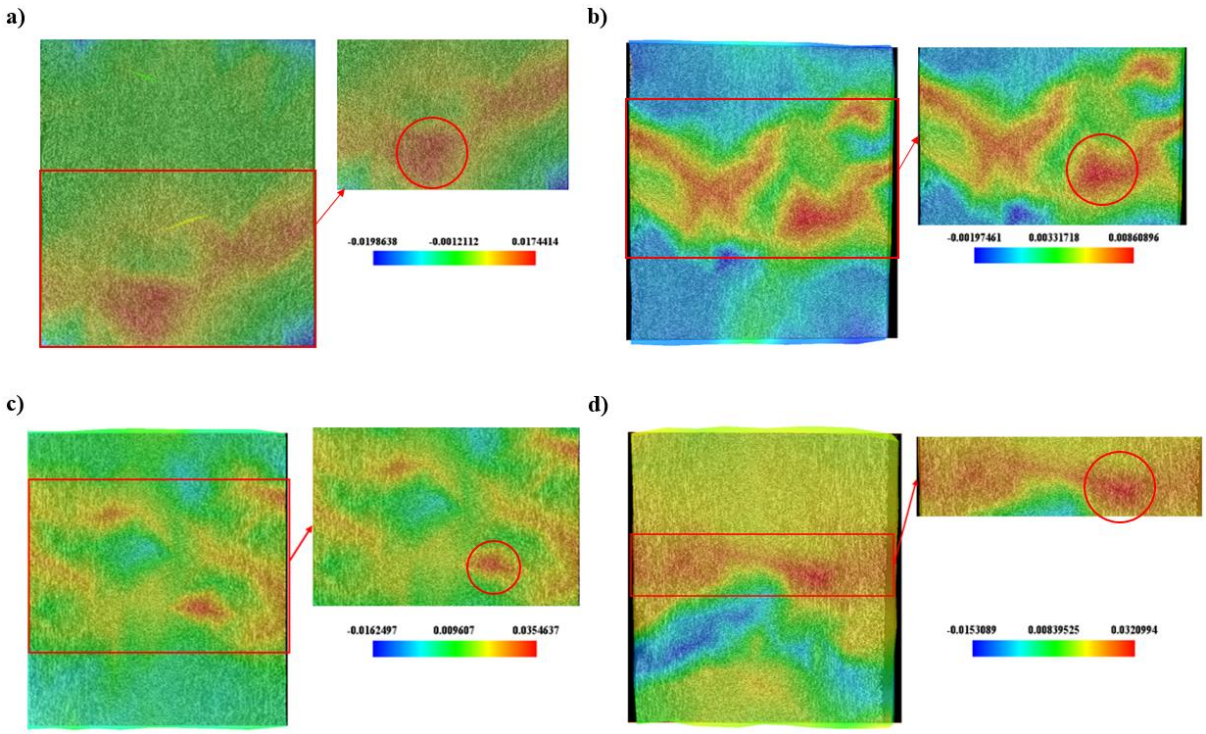

Figure 8-5 Comparison of DVC results at the end of the tensile test. a) 45° specimen, b) 90° specimen, c) 0° specimen at 50° C, d) 0° specimen at 100° C

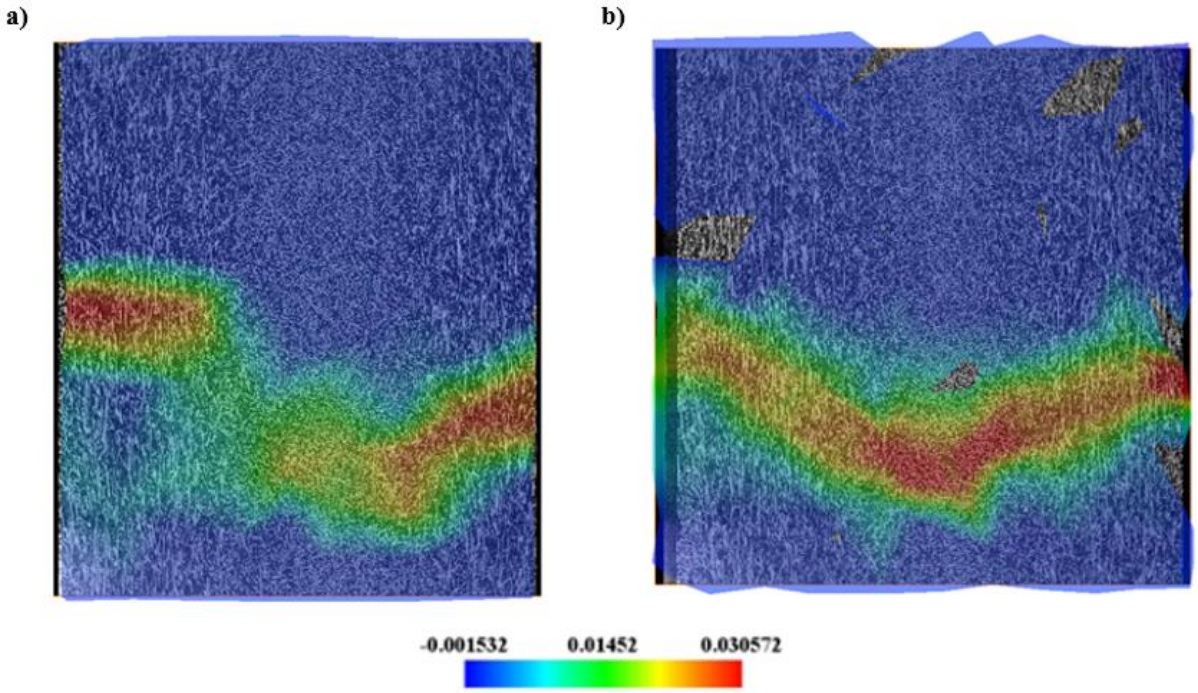

Figure 8-6 DVC results at the end of the tensile test for 0° specimen. a) lateral view at the surface, b) lateral view at mid-width

During the in situ tensile tests, damage mechanisms were detected as shown in Figure 6-19, Figure 6-20 and Figure 6-35. Below in Figure 8-7a-b is a comparison of the damage observed during the in situ tests against the damage reported in the literature [41]. One of the principal damage mechanisms seen was debonding of the matrix from the fibre tips. This damage mechanism can be caused by poor fibre matrix adhesion [40, 49] and the fibre geometry which turns the corners of the fibre ends into stress concentrations. The propagation of this fibre end debonding along the fibre sides can be one of the reasons for another damage mechanism detected, the debonding at the fibre matrix interface [49, 52]. Another possible reason for the fibre matrix interface debonding could be the short distance between fibres causing the stress fields around the fibres to interact [51, 52]. In addition to these damage mechanisms, fibre failure was observed. This mechanism appears to occur in fibres that are highly aligned to the load direction and seems to be a stress-driven phenomenon [49]. Finite element simulations using the real fibre orientations can be used to estimate the stress on the fibres to determine if they are beyond the UTS of the glass fibres. Fibre failure creates new fibre ends that can lead to the development of debonding at the fibre ends and interface, generating more damage to the material. Figure 6-35shows a fourth damage mechanism, matrix cracking, which was developed in the bulk of the material and propagated transversally to the load direction.

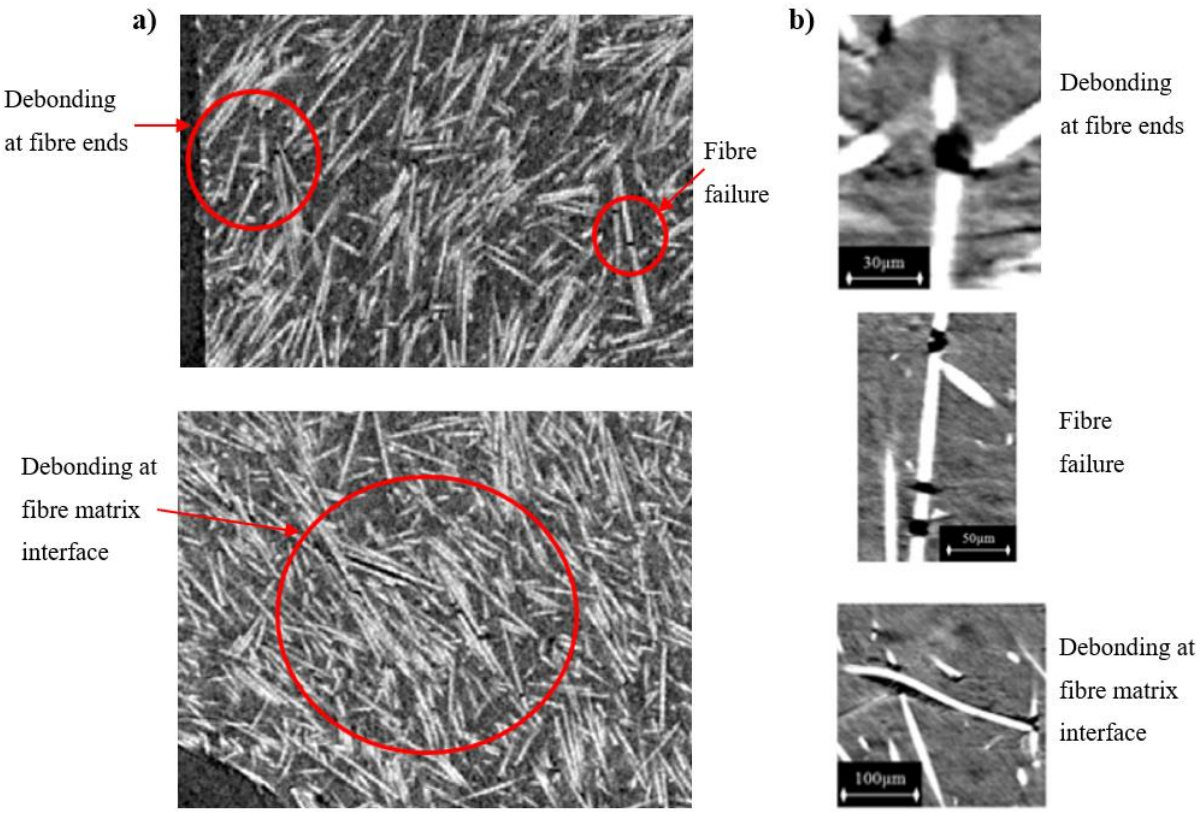

Figure 8-7 Comparison of damage during in situ tensile tests. a) damage found in this study, b) damage reported in the literature [53]

8.1.3 Crack initiation and propagation under tensile load

Based on all the information gathered during this study, a chronology of the failure process is proposed for the SFRP at room and high temperatures.

For the 0° specimens at room and high temperatures, the strain first starts to accumulate near the edge of the specimen in the shell layers, as seen in Figure 8-8, and debonding at the fibre ends occurs. In these locations, the fibres are aligned to the load direction favouring this damage mechanism. Figure 8-9a-c illustrates the stress results of the finite element analysis of the 0° specimens at the three temperatures tested, and stress concentrations in the shell layers are also noticeable. Later these debonding at the fibre ends might have propagated along the sides of the fibres inducing the fibres to be pulled out from the matrix. As the fibres are pulled out, the capability of the material to bear the load is reduced and the material begins to exhibit non-linear behaviour [53], as observed in the stress-strain curves shown in Figure 5-1. Since the stress is redistributed to the matrix due to the pulled-out fibres, the matrix fails and connects the interfacial failure of the fibre pull-outs. This bridging of the fibre pull-outs forms the initial macro crack.

This is supported by SEM observations of the shell layer, depicted in Figure 8-10a-c, which show high matrix ductility around the fibres. This suggests that the crack might have started there and slowly propagated, giving time to the matrix to accommodate leading to matrix stretching.

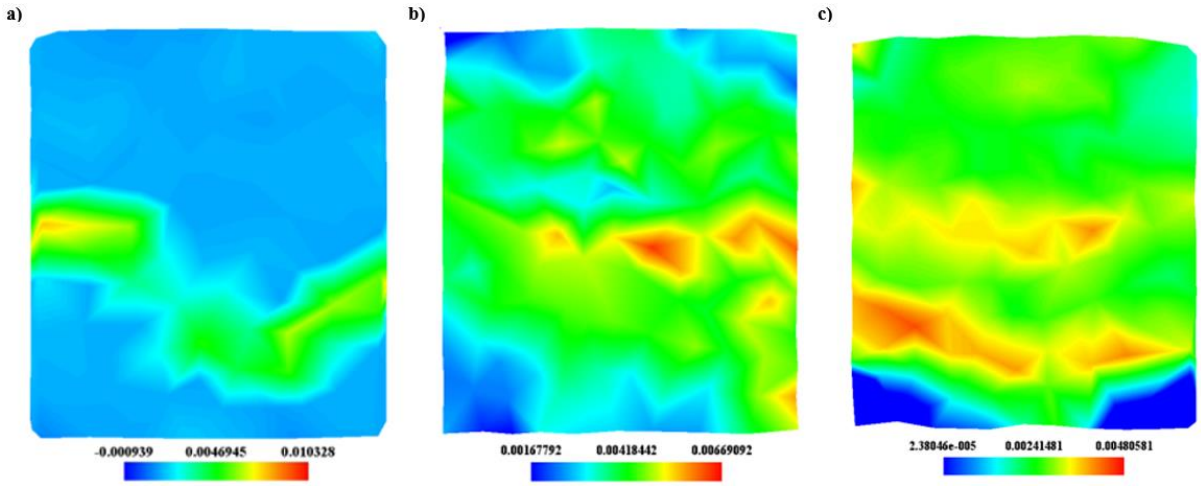

Figure 8-8 Lateral view of the DVC results for 0° specimens at a) room temperature, b) 50° C, c) 100° C

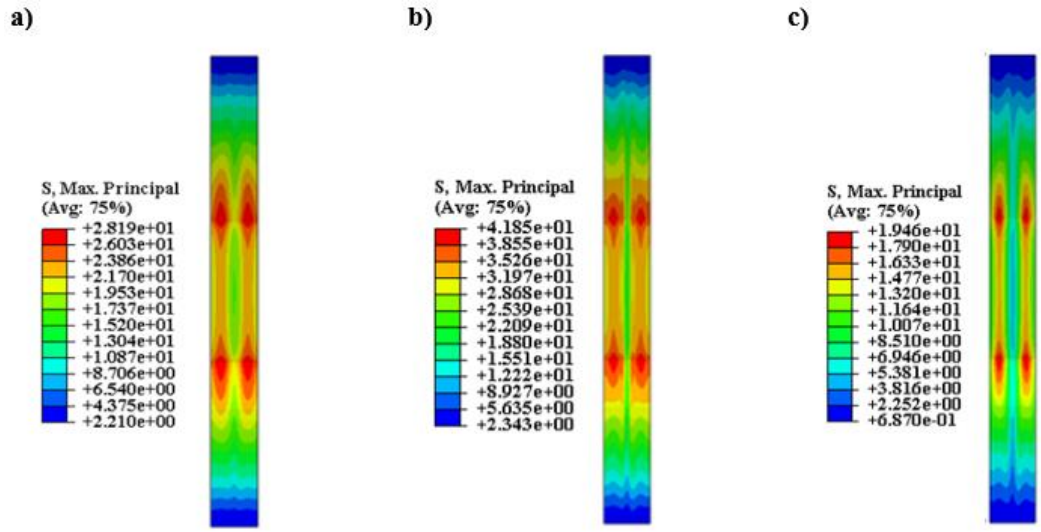

Figure 8-9 Stress in the thickness of 0° specimens at a) room temperature, b) 50° C, c) 100° C

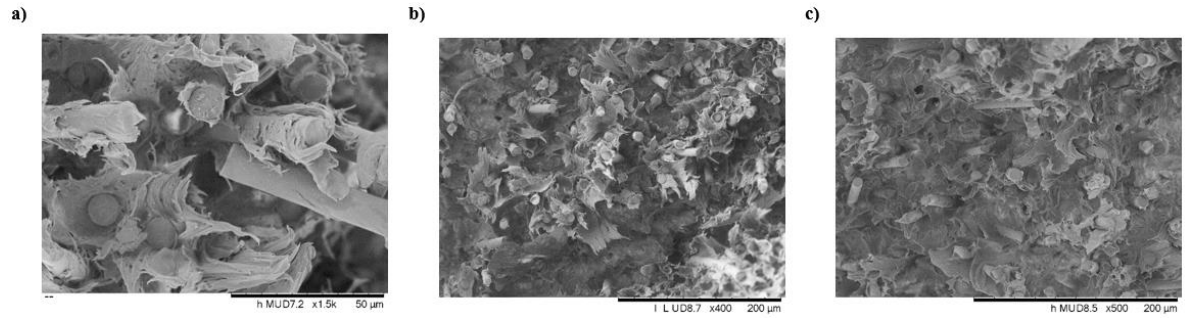

Figure 8-10 SEM images of the shell layer of 0° specimens at a) room temperature, b) 50° C, c) 100° C

Once the crack has initiated, it slowly propagates towards the centre of the sample following the path with less fibre concentration, as suggested by the DVC results shown in sections 6.4, where it is clear that the highest strain path follows the regions with the lowest fibre concentration.

After the crack has reached the transition region between the shell layers and the core, the propagation accelerates leading to the final failure of the sample. The transition region is an area of high concentration of stress, as revealed by the finite element results shown in Figure 8-11a-c. A reason for this could be that in the core layer, the fibres are oriented transversally to the load, allowing the matrix to deform more, while in the shell layers, the fibres oriented to the load restrict the matrix deformation. Therefore, generating high shear stress.

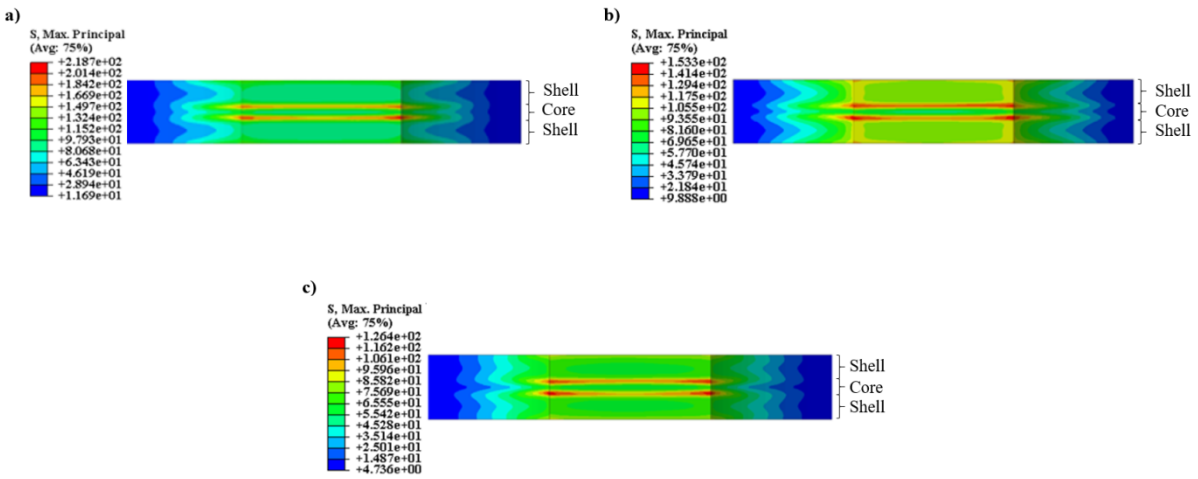

Figure 8-11 Cross-section view of the gauge length of 0° specimens at a) room temperature, b) 50° C, c) 100° C

The rapid crack propagation causes the material to fail in a brittle form, leaving a flat fracture surface in the core where the crack propagated mainly through the fibre-matrix interface. In

the other shell layer on the other side, the fibres are pulled-out with minor matrix deformation or break.

These two types of failure modes, ductile and brittle, are illustrated in Figure 8-12a-c and have also been reported in the literature on SFRP [49, 52].

Figure 8-13 presents a schematic of the proposed failure process described previously.

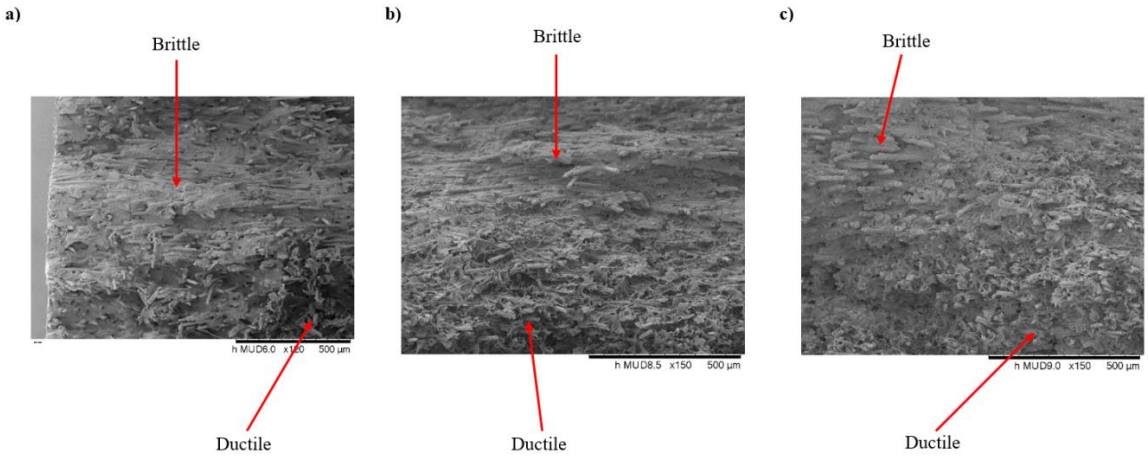

Figure 8-12 Transition area between ductile and brittle failures in 0° specimens under tension at a) room temperature, b) 50° C, c) 100° C

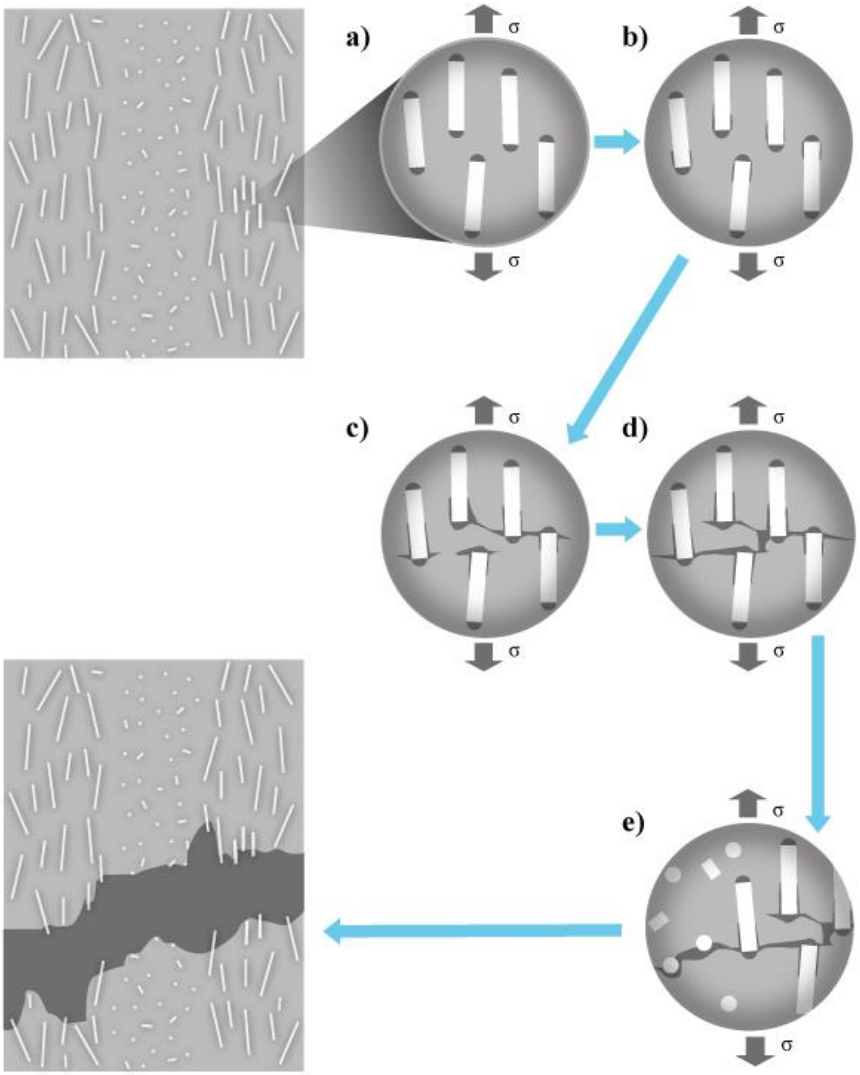

Figure 8-13 Chronology of tensile failure 0° specimen. a) debonding at fibre ends, b) propagation of debonding to the fibre-matrix interface, c) propagation of debonding, d) initial crack, e) rapid propagation

A similar failure process takes place in the 90° specimens. In the shell layer, where the fibres are transversal to the load direction, the stress accumulates in the fibre end corners and debonding of the fibre-matrix interface occurs. The stress in the matrix continues to grow and the debonded interfaces are joined by matrix cracking. This gives origin to the initial crack. Evidence of this could be the strain evolution reported in Figure 5-41 and Figure 5-43, which shows the strain concentrating and propagating from the shell layers towards the centre in the surface and below the surface of the sample.

An effect of temperature at this coupon orientation is noticed. At room temperature, the fracture surface in the shell layers is flat, as seen in Figure 8-14a. In contrast, at high

temperatures, the fracture surface shows matrix ductility, as illustrated in Figure 8-14b-c, but the described process of crack initiation is likely to occur in the same way.

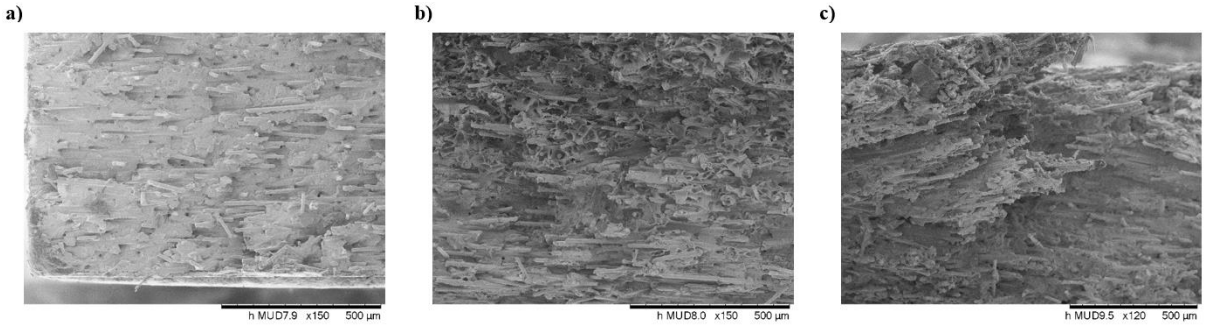

Figure 8-14 SEM images of the shell layer of 90° specimens at a) room temperature, b) 50° C, c) 100° C

After the crack initiation, it propagates to the centre of the specimen, reaching a critical size after passing the layer transition zone, leading to the final failure. Similar to the crack initiation, the temperature has an effect on the final failure. At room temperature, the final failure occurs in a brittle way, with fibre pull-outs as primary damage mechanisms, as can be seen in Figure 8-15a, where no matrix deformation is observed and several holes from the fibres pulled-out are present. At 50° C, minor matrix ductility is noticeable in the core region, see Figure 8-15b. Finally, at 100° C, shown in Figure 8-15c, the matrix deformation is clearly evident. This suggests that the matrix softening due to the temperature allows the matrix to be drawn more before the debonding of the fibre. The higher strain at break with temperature increase seen in Figure 5-2 could be explained by this.

Figure 8-16a-c shows a schematic of the proposed failure process described previously.

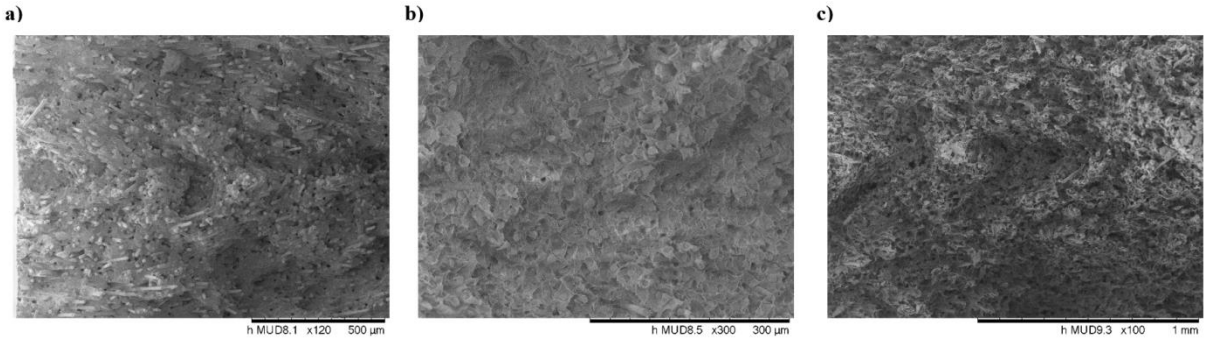

Figure 8-15 SEM images of the core layer of 90° specimens at a) room temperature, b) 50° C, c) 100° C

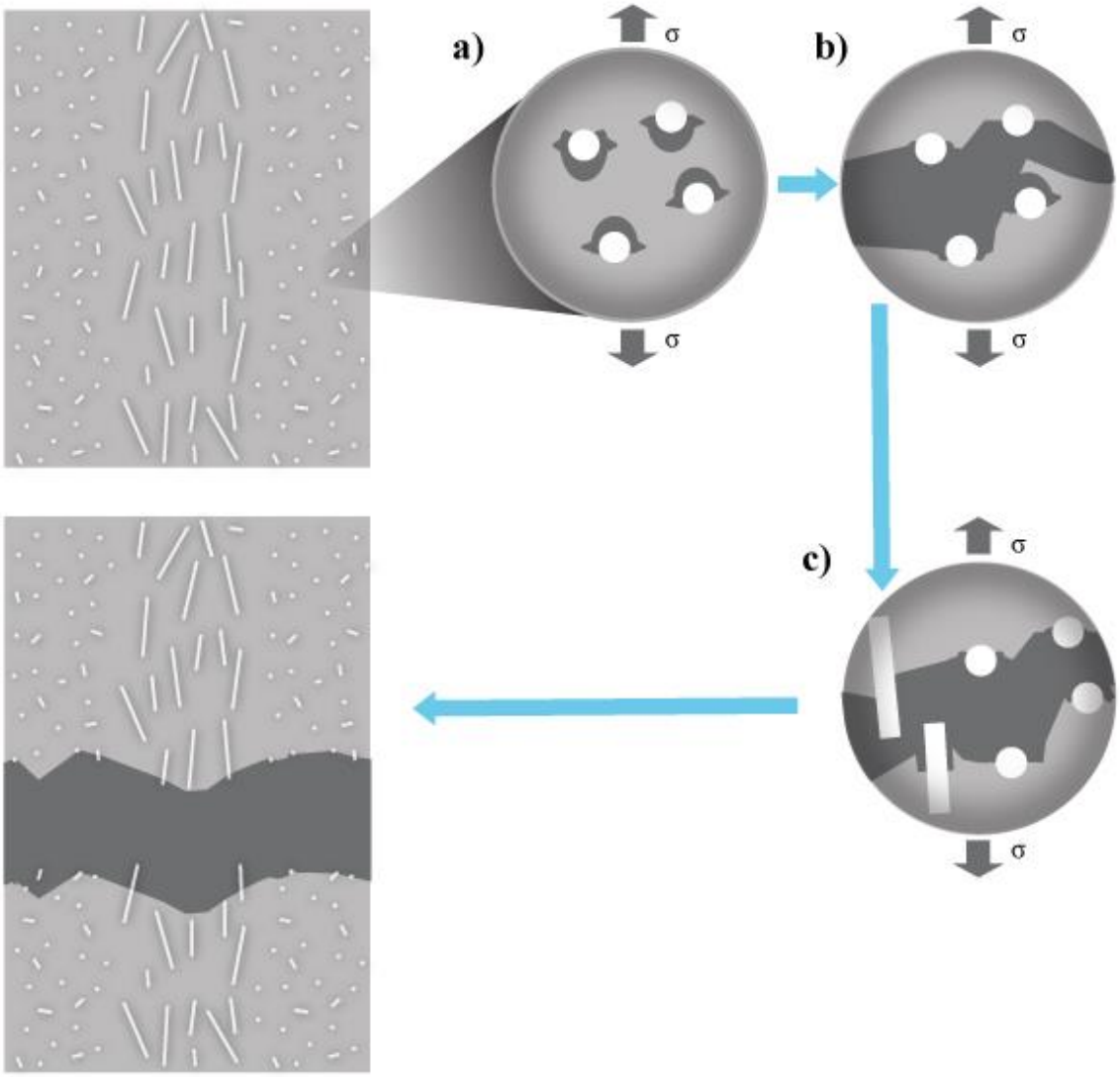

Figure 8-16 Chronology of tensile failure 90° specimen. a) debonding at fibre- matrix interface b) propagation of debonding to the adjacent fibre-matrix interface and initial crack, e) rapid propagation through pulled-out fibres

Lastly, in the 45° samples, accordingly to what is observed in the strain evolution shown in Figure 6-13 and Figure 6-15, it seems that the strain concentrates in the layer transition region and on the surface of the samples, making it difficult to determine a location for the crack initiation. Observing the SEM images presented in section 6.6 of the 45° specimens, one can observe that there is matrix ductility at one of the shell layers and the core. This matrix ductility was observed only on one side of the sample. From this can be inferred that the damage may occur at the same time near the sample surface, in the shell layer, and near the core. In addition, the image of the secondary crack, presented in Figure 6-19, reveals that the

crack initiated from the edge of the specimen. The most probable scenario is that debonding happened in fibre ends close to the surface, followed by debonding in the fibre sides, coalescing with debonded fibre ends as the crack moves towards the centre, where a similar situation of debonding at fibre ends and the interface is taking place.

Once the crack has reached a critical size, rapid propagation occurs causing a brittle failure. This idea is supported by the little matrix deformation observed in the SEM images of section 6.6 and the fibres without matrix debris.

The SEM observations used to draw this scenario were similar at the three temperatures, suggesting that this sequence of events happen at the three temperatures in a similar manner.

8.1 Fatigue behaviour and damage mechanisms

Analogous to the tensile results, the effect of fibre orientation and temperature on the fatigue life is visible as illustrated in Figure 5-12. This influence has been reported in the literature of SFRP [41, 47, 106-108]. Coupons with more fibres aligned to the load, in this case, the 0° specimens, showed a higher fatigue life compared to any other orientation. In terms of temperature, the samples tested at room temperature presented the longest fatigue lives and the specimens tested at 100° C exhibited the shortest.

Strain measurements were taken in the middle of the specimens with an extensometer. In Figure 5-13 and Figure 5-14, the stiffness decrease is plotted. It is observed that the graphs for the 0° specimens remain constant up to the end of the fatigue life where they suddenly drop. In contrast, the 45° and 90° coupons showed a decrease in stiffness at the beginning of the fatigue life, especially at high load levels, and then they presented a constant slope up to the sample failure. This behaviour has been observed previously by Lizama-Camara [109] and De Monte et al. [73]. A possible reason for this could be that in the 0° specimens the damage mechanisms happening at the beginning are primarily fibre end debonding, while in the other specimen orientations, the less favourable fibre orientations propitiate more severe damage mechanisms such as debonding at the fibre-matrix interface.

Hysteresis loops were plotted, as shown in Figure 5-17 and Figure 5-18. Similar to previous studies conducted at room and high temperatures [41, 109], a displacement of the hysteresis loops in the strain axis is visible. This can be explained by the effect of the mean load causing creep. Hysteresis loops represent the energy dissipation during the cyclic loading and give an

idea of the overall material behaviour. However, they are not suitable to identify local damage mechanisms.

The fatigue modelling methodology followed in this work, starting from the simulation of the manufacturing process, then the stress analysis and concluding with the fatigue life predictions led to good fatigue life estimates. Unlike similar studies [41, 109, 110], where only room temperature predictions were carried out, in this thesis, fatigue life estimations at high temperatures were performed, with validation of the intermediate stages using state-of-the-art experimental techniques such as µCT measurements and digital image correlation. In contrast to what has been done in previous investigations [41, 74, 111], the results presented in Figure 7-25 demonstrated that it is not necessary to perform a reverse engineering process to obtain S-N curves of the fully aligned and transversal coupons and avoids the need to manufacture special plaques with fixed fibre orientation. Thus, reducing time and costs.

This fatigue life prediction method has proved to yield very reasonable estimations. However, the linear nature of the method limits its applicability to fatigue data linearly distributed between 0° and 90° specimens. This condition has been proven to be true in previous studies [41] for R=0. Nevertheless, for R≠0 this condition is not always met [105] and more work needs to be done to develop a different method.

8.1.1 Crack initiation and propagation under fatigue loads

Similar to the tensile loads, a timeline of damage mechanisms leading to failure is proposed for fatigue loads at room and high temperatures.

Different damage mechanisms were detected by the X-ray scanning of fatigue specimens after failure and SEM observations presented in sections 5.3.5 and 5.4, such as fibre failure, debonding at fibre ends and fibre-matrix interface.

In the SEM observations, the 0° samples at room temperature showed a flat fracture surface in the core layer with some matrix deformation and minor matrix ductility in the shell layers. On the other hand, the specimens at high temperatures presented matrix deformation over the entire fracture surface, especially the coupons tested at 100° C.

Even though Figure 5-61 shows a secondary crack starting from the edge of the specimen, it also reveals that the crack initiated from the fibre end of a fibre transversally oriented to the load direction. This may indicate that for fatigue loads, the damage begins in the core layer with the fibres oriented in a less favourable direction. Supporting evidence could be the

matrix ductility observed in the core, as presented in Figure 8-17 for the three temperatures, indicating a slow crack propagation. Similar results have been reported in the literature [41]

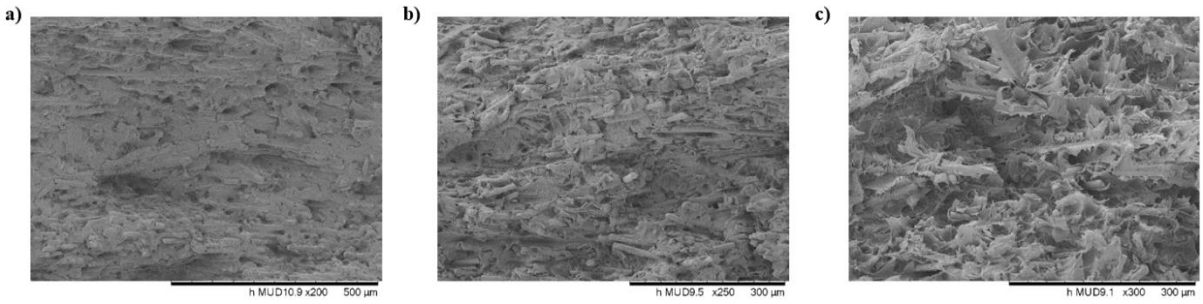

Figure 8-17 SEM images of the core layer of fatigue 0° specimens at a) room temperature, b) 50° C, c) 100° C

The fibre ends acted as stress concentrations, favouring the initiation of debonding that later propagates to the sides of the fibres. The fibres oriented at 90° to the load direction favour the propagation of debonding between the fibres producing a flat surface. Figure 6-46b shows a transition region that suggests that the crack started near the centre of the sample and propagated from there towards the shell layers and specimen edges, as illustrated in Figure 8-18.

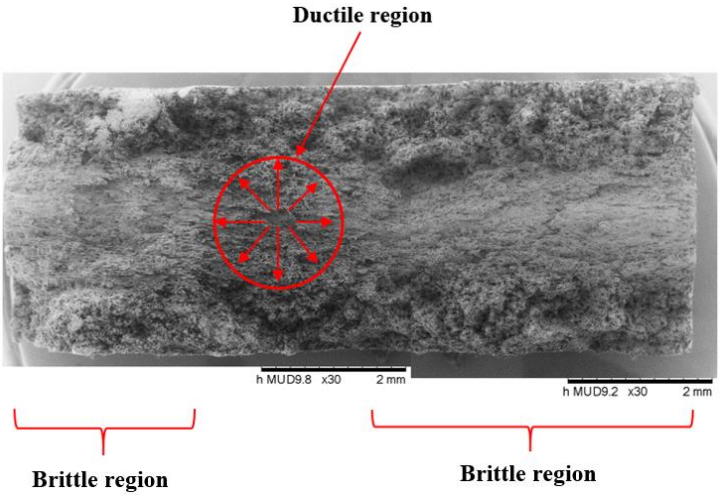

Figure 8-18 Propagation of damage. Ductile and brittle fracture regions

Figure 6-57 depicts the crack path and crack tip of a fatigued 0° specimen tested at 100° C, where voids are noticed due to the high matrix deformation. These voids could have coalesced and been the crack propagation mechanisms at high temperatures. While at room temperature, the joining of debonded fibre ends and interfaces is the most likely propagation mechanism. Once the damage propagation has reached a critical size, fast propagation takes

place leaving a brittle fracture surface on the room temperature coupons but matrix ductility continues in the high temperature specimens. When the crack reaches the shell layers, the fracture surface becomes more tortuous due to the fibres oriented transversally to the crack path inducing crack deviation.

For the 90° specimens, the crack initiation is likely to occur in the shell layers, where the corners of the fibres oriented transversal to the load direction acted as stress concentrations and propitiated the debonding that later propagated to the fibre sides. This is similar to what takes place in the core layer of the 0° specimens.

Figure 5-82 shows an image of a secondary crack in a 90° specimen fatigue tested at 50° C. In the image, micro-cracks are observed around and in front of the crack. These micro-cracks are perpendicular to the load direction and could have been formed by matrix failure. This indicates that the propagation of the crack for the coupons tested at high temperatures could be due to the joining of these micro-cracks ahead of the crack tip. In contrast, at room temperature, the propagation takes place through the debonded fibre-matrix interfaces, from the interface of one fibre to another [41].

The final failure of the samples occurred due to the rapid propagation of the crack after reaching a critical size. This produces a brittle fracture in the room temperature samples, while in the high temperature specimens a ductile fracture surface is observed because of matrix softening due to the temperature.

Finally, in the 45° specimens the fibres in the core and shell layers are oriented at 45° with respect to the load. This orientation creates high shear stress which causes the fibre-matrix debonding. The initiation and propagation of the crack are related to the joining of the debonded fibre-matrix interfaces from one fibre to another. This gives the fracture surface the zig-zag appearance shown in the SEM images of section 6.6.5.

9 CONCLUSION

The main objective of this thesis was to generate new knowledge of the damage mechanisms in short fibre-reinforced polymers at elevated temperatures under tensile and fatigue loads.

In order to achieve this, an extensive experimental program was carried out using state-of-the-art techniques such as digital image correlation at elevated temperatures, in situ mechanical testing in an X-ray micro-computed tomography microscope at high temperatures and digital volume correlation.

The experimental characterisation showed that the PA66GF50 presents a highly anisotropic mechanical response due to the fibre orientation distribution and high sensitivity to the temperature, reducing the Young's modulus by around 2000 MPa and approximately 20 MPa for the UTS in all orientations at 100° C. The fatigue strength was also severely affected by the temperature, decreasing the fatigue life up to 60 times between the room temperature and 50° C and 50 times between 50 and 100° C for the 90° specimens tested at low stress levels.

Furthermore, the analyses of the X-ray micro-computed tomography and SEM images revealed four main damage mechanisms at room and high temperatures and under both types of loads. These damage mechanisms were: fibre failure, matrix cracking, debonding at the fibre-matrix interface and debonding at the fibre ends.

In combination with the experimental testing, a new multi-scale modelling approach was developed to aid the understanding of the damage mechanisms and failure process. This approach comprised a multi-stage modelling methodology that started with the manufacturing process simulation to account for the fibre orientation distribution caused by the injection moulding process. Finite element analyses were then carried out to investigate the heterogeneous stress and strain distributions in the specimens and ended with the fatigue life predictions. Each of these stages was validated using experimental results to assess the accuracy of the results. Even though the approach used for the fatigue life predictions produced reasonably accurate results, it is limited to load ratios of R=0 and constant amplitude loads. As a result, a new approach must be developed that considers the compressive part in load ratios of R=-1 and the effects of variable loads.

Based on the experimental results, modelling results and SEM images, damage chronologies were proposed for tensile and fatigue loads at both room and high temperatures. In these chronologies, the local fibre orientations play a key role in the initiation and development of

damage. In addition to this, differences between crack initiation locations for tensile and fatigue loads were observed. Finally, an effect of the temperature on the crack propagation seems to occur under fatigue loads.

The proposed damage chronologies can be summarised as follows:

Tensile load	Fatigue load
i. In the shell layers, debonding at the fibre ends in the 0° samples occurs and along the fibre-matrix interface in the 90° specimens. In the 45° coupons, debonding at the fibre-matrix interface and fibre ends near the surface of the sample takes place.	i. In the 0° specimens, debonding at the fibre-matrix interface occurs in the core layer. This process takes place in the shell layer in the 45° and 90° samples.
ii. In the 0° specimens, the debonding propagates to the sides of the fibres. In the 45° and the 90° samples, the debonding propagates to the adjacent fibre-matrix interfaces and the initial crack occurs.	ii. The debonding of the fibre-matrix interfaces propagates from one fibre to another for the three coupon orientations causing the initial crack.
iii. The debonding propagates to the contiguous fibres in the 0° samples and the initial crack appears. In the 45° and 90° specimens, after the crack reaches a critical size, rapid propagation takes place leading to the final failure.	iii. At high temperatures, voids are formed in the 0° samples and micro-cracks are developed in the 90° specimens. These voids and micro-cracks are used in combination with debonded fibre ends and fibre-matrix interfaces to propagate the initial crack, while in the 45° coupons, the propagation happens through the debonded fibre-matrix interfaces. At room temperature, the crack propagation slowly occurs through the debonded fibre-matrix interfaces and fibre ends for the three specimen orientations.
iv. Finally, in the 0° specimens the crack propagates rapidly through the fibre ends and fibre-matrix interfaces causing the final failure.	iv. Finally, after the crack extends to a critical size, rapid propagation takes place leading to the final failure.

Although these chronologies seem reasonable, the fatigue chronology was based on constant amplitude tests and scanning of failed samples. To confirm the proposed sequence of events and expand the knowledge of the damage mechanisms of SFRP, interrupted fatigue tests need to be conducted to observe the evolution of damage at different numbers of cycles. Besides that, fatigue tests using variable amplitude loads should be carried out to observe their influence on the damage mechanisms.

As mentioned before, moisture has an important impact on the mechanical response of SFRP. This study was restricted to moisture content in the range of 1-1.4% and more research is needed to understand the effect of humidity on the damage mechanisms.

Nevertheless, the results presented in this thesis can form the basis for future research to increase the understanding of the damage mechanisms of SFRP.

9.1 Future work

In order to enhance, complement and extend the knowledge of the behaviour and damage mechanisms of SFRP, the following directions are suggested:

- In this work, the damage mechanisms and behaviour at elevated temperatures were studied. However, it is known that low temperatures also have an effect on SFRP. Thus, more research needs to be conducted at low temperatures to have a broader knowledge of the temperature effect on the damage mechanisms and increase the usability of these composites for more applications.

- Additional testing at different stress ratios, especially at R=-1, is needed to understand the effect of the compressive load on the fatigue damage mechanisms.

- Tests using variable loads are required to study the effect of load sequence on the damage mechanisms of SFRP.

- Further confirmation of the proposed damage chronologies using experimental techniques such as in situ tensile tests at high temperatures inside X-ray micro-computed tomography using samples of different orientations and in situ tensile tests in SEM. In addition, detailed X-ray micro-computed tomography scans at different

numbers of cycles and stress levels using thin fatigued samples to achieve a better resolution are required to corroborate the suggested damage timeline.

- Multi-axial testing is essential to comprehend the effect of combined stress on the damage mechanisms and understand the mechanical response of SFRP under complex stress scenarios.

- A material model needs to be developed that includes the damage mechanisms observed in this investigation and any further findings that may have an influence on the behaviour of SFRP. This will allow for conducting more accurate finite element analysis and benefit the design of components made of composites, which is the ultimate goal for several industries such as the automotive industry.

The focus of this thesis has been the short glass-fibre reinforced thermoplastics. However, the experimental framework could be used for materials with other types of reinforcements such as particles, flakes and whiskers. Besides this, the experimental techniques herein used could be further developed and refined for use in future research on SFRP and other materials.

In addition to that, the findings of this research could be used to design and manufacture more durable, safe and reliable SFRP components that can withstand high temperatures. This could have applications in industries such as aerospace, automotive, energy and medical devices.

APPENDIX

The structure of the Python scripts used in this work is detailed here.

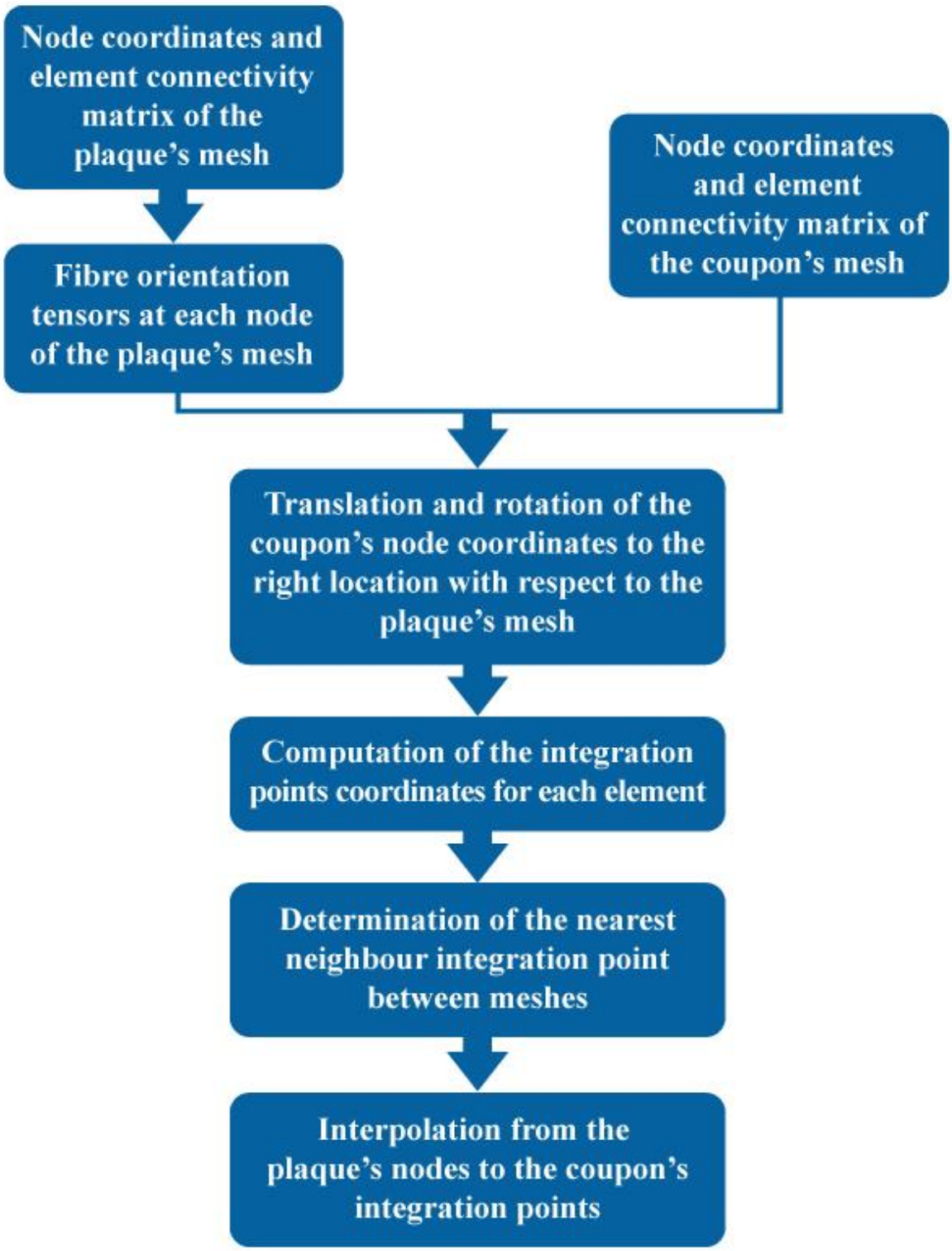

Figure A-1 Schematic of the Python workflow for the mappig of the rientation tensors

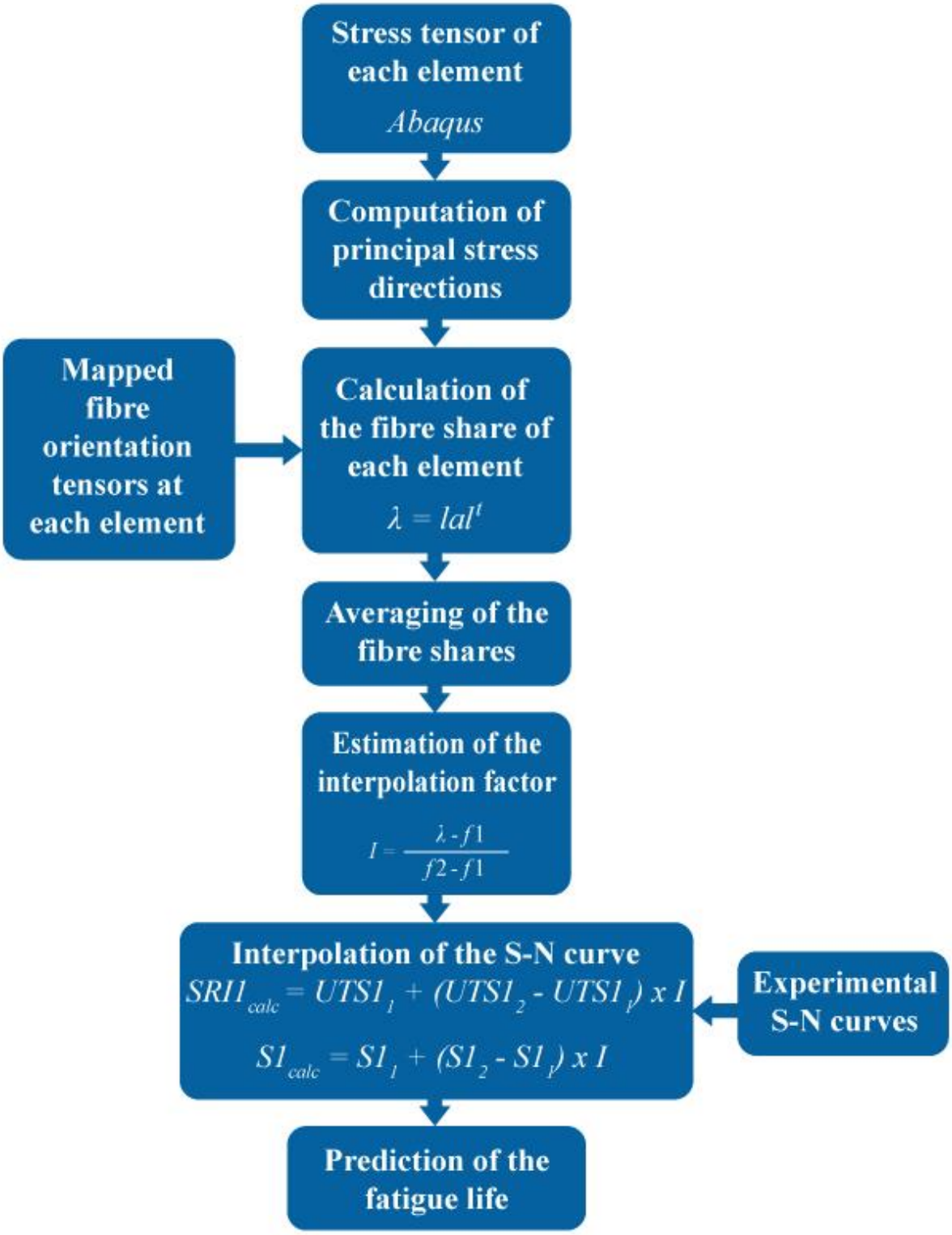

Figure A-2 Workflow of the Python script for fatigue life estimation

REFERENCES

[1] *Regulation (EU) No 333/2014 of the European Parliament and of the Council of 11 March 2014 amending Regulation (EC) No 443/2009 to define the modalities for reaching the 2020 target to reduce CO2 emissions from new passenger cars*, 2014.

[2] E. Belmonte, "Multi-scale modeling of the fatigue behavior for short fiber reinforced thermoplastics," PhD, Dipartimento di tecnica e gestione dei sistemi industriali, Univertita Degli Studi Di Padova.

[3] K. Chawla, K., *Composite Materials Science and Engineering*, Third ed. Springer, 2012.

[4] F. Dillenberger, *On the anisotropic plastic behaviour of short fibre reinforced thermoplastics and its description by phenomenological material modelling*. Germany: Springer Vieweg, 2019.

[5] P. K. Mallick, *Fiber-reinforced composites: Materials, Manufacturing and Design*, Third ed. CRC Press, 2007.

[6] M. Biron, *Thermoplastics and thermoplastic composites*. Oxford, UK: Elsevier, 2013.

[7] Y. S. Yu and B. Lauke, *Science and Engineering of Short Fibre Reinforced Polymer Composites*. CRC Press, 2009.

[8] N. G. McCrum, C. P. Buckley, and C. B. Bucknall, *Principles of Polymer Engineering*, Second ed. Oxford University Press, 2011.

[9] S. Fu and B. Lauke, "Effects of fiber length and fiber orientation distribution on the tensile strength of short fiber reinforced polymers," *Composites Science and Technology*, vol. 56, pp. 1179-1190, 1996.

[10] M. Aykol, N. A. Isitman, E. Firlar, and C. Kaynak, "Strength of short fiber reinforced polymers: Effect of fiber length distribution," *Polymer Composites,* vol. 29, no. 6, pp. 644-648, 2008, doi: 10.1002/pc.20480.

[11] Y. T. Zhu, W. R. Blumenthal, and T. C. Lowe, "Determination of Non Symmetric 3D Fiber Orientation Distribution and Average Fiber Length in Short Fiber Composites," *Journal of Composite Materials,* vol. 31, no. 13, pp. 1287-1301, 1997.

[12] L. M. Vas, F. Ronkay, and T. Czigány, "Active fiber length distribution and its application to determine the critical fiber length," *Polymer Testing,* vol. 28, no. 7, pp. 752-759, 2009, doi: 10.1016/j.polymertesting.2009.06.006.

[13] D. A. Norman and R. E. Robertson, "The effect of fiber orientation on the toughening of short fiber-reinforced," *Journal of Applied Polymer Science,* vol. 90, pp. 2740-2751, 2003.

[14] B. Agarwal, D., L. Broutman, J., and K. Chandrashekhara, *Analysis and performance of fiber composites*, Third ed. Wiley, 2006.

[15] A. Kelly and W. R. Tyson, "Tensile properties of fibre-reinforced metals: copper/tungsten and copper/molybdenum," *Journal of the mechanics and physics of solids,* vol. 13, no. 6, pp. 329-350, 1965, doi: doi:10.1016/0022-5096(65)90035-9.

[16] G. Ozkoc, G. Bayram, and E. Bayramli, "Effects of polyamide 6 incorporation to the short glass fiber reinforced ABS composites: an interfacial approach," *Polymer,* vol. 45, pp. 8957-8966, 2004.

[17] J. R. Vinson and R. L. Sierakowski, *The Behavior Of Structures Composed Of Composite Materials* Second ed. (Solid mechanics and its applications). Kluwer Academic Publishers, 2004.

[18] S. K. De and J. R. White, *Short Fibre-Polymer Composites*. Cambridge, England: Woodhead publishing limited, 1996.

[19] R. Zheng, R. I. Tanner, and X.-J. Fan, *Injection Molding Integration of Theory and Modeling Methods*. Springer-Verlag Berlin Heidelberg, 2011.

[20] M. F. Arif, N. Saintier, F. Meraghni, J. Fitoussi, Y. Chemisky, and G. Robert, "Multiscale fatigue damage characterization in short glass fiber reinforced polyamide-66," *Composites Part B: Engineering*, vol. 61, pp. 55-65, 2014, doi: 10.1016/j.compositesb.2014.01.019.

[21] J. M. Park and S. J. Park, "Modeling and Simulation of Fiber Orientation in Injection Molding of Polymer Composites," *Mathematical Problems in Engineering*, vol. 2011, pp. 1-14, 2011, doi: 10.1155/2011/105637.

[22] Y. A. Lizama-Camara, C. Pinna, Z. Lu, and M. Blagdon, "Effect of the injection moulding fibre orientation distribution on the fatigue life of short glass fibre reinforced plastics for automotive applications," in *2nd CIRP Conference on Composite Material Parts Manufacturing (CIRP-CCMPM 2019)*, 2019: Elsevier, pp. 255-260.

[23] M. Vincent, T. Giroud, A. Clarke, and C. Eberhardt, "Description and modeling of fiber orientation in injection molding of fiber reinforced thermoplastics," *Polymer*, vol. 46, no. 17, pp. 6719-6725, 2005, doi: 10.1016/j.polymer.2005.05.026.

[24] S. G. Advani and C. L. Tucker, "The Use of Tensors to Describe and Predict Fiber Orientation in Short Fiber Composites," *Journal of Rheology*, vol. 31, no. 8, pp. 751-784, 1987, doi: 10.1122/1.549945.

[25] Autodesk. "Theoretical basis for fiber orientation prediction." https://help.autodesk.com/view/MFIA/2019/ENU/?guid=GUID-50FF496F-0E3E-43CE-B30B-4B12CC24F7DE (accessed May 28th, 2022).

[26] J. S. Cintra and C. L. Tucker, "Orthotropic closure approximations for flow-induced fiber orientation," *Journal of Rheology,* vol. 39, no. 6, pp. 1095-1122, 1995, doi: 10.1122/1.550630.

[27] S. Montgomery-Smith, D. Jack, and D. E. Smith, "The Fast Exact Closure for Jeffery's equation with diffusion," *Journal of Non-Newtonian Fluid Mechanics,* vol. 166, no. 7-8, pp. 343-353, 2011, doi: 10.1016/j.jnnfm.2010.12.010.

[28] F. Folgar and C. L. Tucker III, "Orientation Behavior of Fibers in Concentrated Suspensions," *Journal of Reinforced Plastics and Composites,* vol. 3, pp. 98-119, 1984.

[29] G. B. Jeffery, "The motion of ellipsoidal particles immersed in a viscous fluid," *Proceedings of the Royal Society of London,* vol. 102, no. 715, pp. 161-179, 1922.

[30] R. Zurawik, J. Volke, J. C. Zarges, and H. P. Heim, "Comparison of Real and Simulated Fiber Orientations in Injection Molded Short Glass Fiber Reinforced Polyamide by X-ray Microtomography," *Polymers (Basel),* vol. 14, no. 1, Dec 22 2021, doi: 10.3390/polym14010029.

[31] M. Sepehr, G. Ausias, and P. J. Carreau, "Rheological properties of short fiber filled polypropylene in transient shear flow," *Journal of Non-Newtonian Fluid Mechanics,* vol. 123, no. 1, pp. 19-32, 2004, doi: 10.1016/j.jnnfm.2004.06.005.

[32] J. Wang, J. F. O'Gara, and C. L. Tucker, "An objective model for slow orientation kinetics in concentrated fiber suspensions: Theory and rheological evidence," *Journal of Rheology,* vol. 52, no. 5, pp. 1179-1200, 2008, doi: 10.1122/1.2946437.

[33] J. Wang and X. Jin, "Comparison of recent fiber orientation models in Autodesk Moldflow Insight simulations with measured fiber orientation data," in *Polymer Processing Society 26th Annual Meeting*, Banff, Canada, 2010.

[34] J. H. Phelps and C. L. Tucker, "An anisotropic rotary diffusion model for fiber orientation in short- and long-fiber thermoplastics," *Journal of Non-Newtonian Fluid Mechanics,* vol. 156, no. 3, pp. 165-176, 2009, doi: 10.1016/j.jnnfm.2008.08.002.

[35] H.-C. Tseng, R.-Y. Chang, and C.-H. Hsu, "Phenomenological improvements to predictive models of fiber orientation in concentrated suspensions," *Journal of Rheology,* vol. 57, no. 6, pp. 1597-1631, 2013, doi: 10.1122/1.4821038.

[36] H.-C. Tseng, R.-Y. Chang, and C.-H. Hsu, "The use of principal spatial tensor to predict anisotropic fiber orientation in concentrated fiber suspensions," *Journal of Rheology,* vol. 62, no. 1, pp. 313-320, 2018, doi: 10.1122/1.4998520.

[37] A. Bakharev, H. Yu, S. Ray, R. Speight, and J. Wang, "Using new anisotropic rotational diffusion model to improve prediction of short fibers in thermoplastic injection molding," *Society of Plastics Engineers: Lubbock, TX, USA*, 2018.

[38] Autodesk. "Moldflow Rotational Diffusion (MRD) Model." https://knowledge.autodesk.com/support/moldflow-insight/learn-explore/caas/CloudHelp/cloudhelp/2019/ENU/MoldflowInsight-Analyses/files/GUID-54ED8884-6EB2-44B9-98F4-9E6817CBF6F5-htm.html (accessed 3rd of June, 2022).

[39] A. J. Favaloro and C. L. Tucker, "Analysis of anisotropic rotary diffusion models for fiber orientation," *Composites Part A: Applied Science and Manufacturing,* vol. 126, 2019, doi: 10.1016/j.compositesa.2019.105605.

[40] V. Crupi, E. Guglielmino, G. Risitano, and F. Tavilla, "Experimental analyses of SFRP material under static and fatigue loading by means of thermographic and DIC techniques," *Composites Part B: Engineering,* vol. 77, pp. 268-277, 2015, doi: 10.1016/j.compositesb.2015.03.052.

[41] Y. Lizama-Camara, A, "Numerical and experimental fatigue analysis of short glass fibre reinforced polymers," PhD, Mechanical Engineering, The University of Sheffield, Sheffield, UK, 2020.

[42] B. Mouhmid, A. Imad, N. Benseddiq, S. Benmedakhène, and A. Maazouz, "A study of the mechanical behaviour of a glass fibre reinforced polyamide 6,6: Experimental investigation," *Polymer Testing,* vol. 25, no. 4, pp. 544-552, 2006, doi: 10.1016/j.polymertesting.2006.03.008.

[43] S. Barre and M. L. Benzeggagh, "On the use of acoustic emission to investigate damage mechanisms in glass fibre reinforced polypropylene," *Composite Science and Technology,* vol. 52, pp. 369-376, 1994.

[44] A. Bernasconi, P. Davoli, A. Basile, and A. Filippi, "Effect of fibre orientation on the fatigue behaviour of a short glass fibre reinforced polyamide-6," *International Journal of Fatigue,* vol. 29, no. 2, pp. 199-208, 2007, doi: 10.1016/j.ijfatigue.2006.04.001.

[45] M. Miwa and N. Horiba, "Effects of fibre length on tensile strength of carbon/glass fibre hybrid composites," *Journal of Materials Science,* vol. 29, pp. 973-977, 1994.

[46] S. A. Hitchen, S. Ogin, L., and P. A. Smith, "Effect of fibre length on fatigue of short carbon fibre/epoxy composite," *Composites,* vol. 26, no. 4, pp. 303-308, 1995.

[47] S. Mortazavian and A. Fatemi, "Effects of fiber orientation and anisotropy on tensile strength and elastic modulus of short fiber reinforced polymer composites," *Composites Part B: Engineering,* vol. 72, pp. 116-129, 2015, doi: 10.1016/j.compositesb.2014.11.041.

[48] M. Schoßig, C. Bierögel, W. Grellmann, and T. Mecklenburg, "Mechanical behavior of glass-fiber reinforced thermoplastic materials under high strain rates," *Polymer Testing,* vol. 27, no. 7, pp. 893-900, 2008, doi: 10.1016/j.polymertesting.2008.07.006.

[49] H. Rolland, N. Saintier, P. Wilson, J. Merzeau, and G. Robert, "In situ X-ray tomography investigation on damage mechanisms in short glass fibre reinforced thermoplastics: Effects of fibre orientation and relative humidity," *Composites Part B: Engineering*, vol. 109, pp. 170-186, 2017, doi: 10.1016/j.compositesb.2016.10.043.

[50] A. P. Vassilopoulos and T. Keller, *Fatigue of Fiber-reinforced Composites*. Springer, 2011.

[51] M. F. Arif, F. Meraghni, Y. Chemisky, N. Despringre, and G. Robert, "In situ damage mechanisms investigation of PA66/GF30 composite: Effect of relative humidity," *Composites Part B: Engineering*, vol. 58, pp. 487-495, 2014, doi: 10.1016/j.compositesb.2013.11.001.

[52] N. Sato, T. Kurauchi, S. Sato, and O. Kamigaito, "Microfailure behaviour of randomly dispersed short fibre reinforced thermoplastic composites obtained by direct SEM observation," *Journal of Materials Science*, vol. 26, pp. 3891-3898, 1991.

[53] H. Rolland, N. Saintier, and G. Robert, "Damage mechanisms in short glass fibre reinforced thermoplastic during in situ microtomography tensile tests," *Composites Part B: Engineering*, vol. 90, pp. 365-377, 2016, doi: 10.1016/j.compositesb.2015.12.021.

[54] J. Schijve, *Fatigue of Structures and Materials*. Springer, 2009.

[55] A. P. Vassilopoulos, *Fatigue Life Prediction of Composites and Composite Structures*. Woodhead Publishing Limited, 2010.

[56] J. J. Horst and J. L. Spoormaker, "Mechanisms of Fatigue in Short Glass Fiber Reinforced Polyamide 6," *Polymer Engineering and Science*, vol. 36, no. 22, pp. 2718-2726, 1996.

[57] A. zago and G. S. Springer, "Constant Amplitude Fatigue of Short Glass and Carbon Fiber Reinforced Thermoplastics," *Journal of Reinforced Plastics and Composites,* vol. 20, no. 07, pp. 564-595, 2001.

[58] F. Cosmi and A. Bernasconi, "Fatigue behaviour of short fibre reinforced polyamide morphological and numerical analysis of fibre orientation effects," presented at the Problematiche di Frattura nei Materiali per l'Ingegneria, Forni di Sopra, 2010.

[59] S. Mortazavian and A. Fatemi, "Fatigue behavior and modeling of short fiber reinforced polymer composites including anisotropy and temperature effects," *International Journal of Fatigue,* no. 77, pp. 12-27, 2015.

[60] N. Jia and V. A. Kagan, "Effects of Time and Temperature on the Tension-Tension Fatigue Behavior of Short Fiber Reinforced Polyamides," *Polymer Composites,* vol. 19, no. 4, pp. 404-414, 1998.

[61] K. Handa, A. Kato, and I. Narisawa, "Fatigue Characteristics of a Glass-Fiber-Reinforced Polyamide," *Journal of Applied Polymer Science,* vol. 72, pp. 1783-1793, 1999.

[62] M. De Monte, E. Moosbrugger, and M. Quaresimin, "Influence of temperature and thickness on the off-axis behaviour of short glass fibre reinforced polyamide 6.6 - cyclic loading," *Composites: Part A,* no. 41, pp. 1368-1379, 2010.

[63] W. L. Bradley and T. S. Grant, "The effect of the moisture absorption on the interfacial strength of polymeric matrix composites," *Journal of Materials Science,* no. 30, pp. 5537-5542, 1995.

[64] S. Barbouchi, V. Bellenger, A. Tcharkhtchi, P. Castaing, and T. Jollivet, "Effect of water on the fatigue behaviour of a pa66/glass fibers composite material," *Journal of Materials Science,* vol. 42, no. 6, pp. 2181-2188, 2007.

[65] C. P. Hoppel, "The effects of tension-tension fatigue on the mechanical behavior of short fiber reinforced thermoplastics," 1992, p. 509.

[66] H. Rolland, N. Saintier, I. Raphael, N. Lenoir, A. King, and G. Robert, "Fatigue damage mechanisms of short fiber reinforced PA66 as observed by in-situ synchrotron X-ray microtomography," *Composites Part B: Engineering*, vol. 143, pp. 217-229, 2018, doi: 10.1016/j.compositesb.2017.12.051.

[67] K. Noda, A. Takahara, and T. Kajiyama, "Fatigue failure mechanisms of short glass-fiber reinforced nylon 66 based on nonlinear dynamic viscoelastic measurement," *Polymer*, no. 42, pp. 5803-5811, 2001.

[68] Y. A. Lizama Camara, C. Pinna, Z. Lu, and M. Blagdon, "Multistage modelling and experimental validation of the fatigue life of a short fibre reinforced polymer (SFRP) composite," in *ICFC 7 - the 7th International Conference on Fatigue of Composites*, Vicenza, 2018.

[69] C. m. Sonsino and E. Moosbrugger, "Fatigue design of highly loaded short-glass-fibre reinforced polyamide parts in engine compartments," *International Journal of Fatigue*, vol. 30, pp. 1279-1288, 2008.

[70] P. Wilson and P. Heyes, "Fatigue of short fibre reinforced polymers: from material process to fatigue life of industrial components," in *12th International Fatigue Congress (FATIGUE 2018)*, 2018, vol. 165: MATEC Web of Conferences.

[71] *Product information Ultramid®A3WG10 CR bk564 PA66 GF50*, Ludwigshafen, Germany, 2021.

[72] B. Klimkeit *et al.*, "Multiaxial fatigue life assessment for reinforced polymers," *International Journal of Fatigue*, no. 33, pp. 766-780, 2011.

[73] S. Mortazavian and A. Fatemi, "Fatigue behavior and modeling of short fiber reinforced polymer composites including anisotropy and temperature effects,"

International Journal of Fatigue, vol. 77, pp. 12-27, 2015, doi: 10.1016/j.ijfatigue.2015.02.020.

[74] P. Wilson and P. Heyes, "Fatigue of short fibre reinforced polymers: from material process to fatigue life of industrial components," *MATEC Web of Conferences*, vol. 165, 2018, doi: 10.1051/matecconf/201816508003.

[75] "D618-13 Standard Practice for Conditioning Plastics for Testing," ed: ASTM, 2013.

[76] "D5229/D5229M-14 Standar Test Method for Moisture Absorption Properties and Equilibrium Conditioning of Polymer Matrix Composite Materials," ed: ASTM International, 2014.

[77] *D3039/D3039M-17 Standard Test Method for Tensile Properties of Polymer Matrix Composite Materials*, A. International, 2017.

[78] C. Solutions. "Vic 2D v6 Reference Manual." www.CorrelatedSolutions.com.

http://www.correlatedsolutions.com/supportcontent/Vic-2D-v6-Testing-

Guide.pdf (accessed 1st of August, 2022).

[79] W. LePage. "A practical guide to DIC." https://digitalimagecorrelation.org/ (accessed 1st of August, 2022).

[80] *E1012-19 Standard Practice for Verification of Testing Frame and Specimen Alignment Under Tensile and Compressive Axial Force Application*, A. International, 2019.

[81] *Moldflow Insight 2019*. (2019).

[82] *Abaqus 2017*. (2017).

[83] *Helius PFA 2019*. (2019).

[84] Autodesk, "Validation Brief: Structural Analysis of Fiber-Reinforced Plastics utilizing Advanced Material Exchange," 2015.

[85] T. Mori and K. Tanaka, "Average Stress in Matrix and Average Elastic Energy of Materials with Misfitting Inclusions," *Acta Metallurgica,* vol. 21, 1973.

[86] Y. Benveniste, "A new approach to the application of Mori-Tanaka's theory in composite materials," *Mechanics of Materials,* vol. 6, 1987.

[87] J. D. Eshelby, "The Determination of the Elastic Field of an Ellipsoidal Inclusion and Related Problems," *Proceedings of the Royal Society of London,* 1957.

[88] B. A. Nghiep Nguyen, S. K. Bapanapalli, V. Kunc, J. H. Phelps, and C. L. Tucker, "Prediction of the Elastic-Plastic Stress/Strain Response for Injection-Molded Long-Fiber Thermoplastics," *Journal of Composite Materials,* vol. 43, no. 3, pp. 217-246, 2008, doi: 10.1177/0021998308099219.

[89] B. A. Nghiep Nguyen and V. Kunc, "An Elastic-plastic Damage Model for Long-fiber Thermoplastics," *International Journal of Damage Mechanics,* vol. 19, no. 6, pp. 691-725, 2009, doi: 10.1177/1056789509338319.

[90] W. Ramberg and W. R. Osgood, "Description of Stress-Strain curves by three parameters," Washington, NACA Technical Note 1943.

[91] Autodesk. "Autodesk Helius PFA 2019 Theory Manual The plasticity Model." https://help.autodesk.com/view/ACMPAN/2019/ENU/?guid=GUID-F156C59C-37BE-437C-AD98-CD40B72BB89C (accessed 30th of June, 2022).

[92] Autodesk. "Autodesk Helius PFA 2019 Theory Manual Elastic and Plastic Coefficients." https://help.autodesk.com/view/ACMPAN/2019/ENU/?guid=GUID-846F14C4-3DEC-4686-88F5-EF3C91E865DF (accessed 07/07/2022, 2022).

[93] A. Primetzhofer, G. Stadler, G. Pinter, and F. Grün, "Lifetime assessment of anisotropic materials by the example short fibre reinforced plastic," *International Journal of Fatigue,* vol. 120, pp. 294-302, 2019, doi: 10.1016/j.ijfatigue.2018.06.013.

[94] A. Primetzhofer, G. Stadler, G. Pinter, and F. Grün, "Model Calibration and Data Set Determination Considering the Local Micro-Structure for Short Fiber Reinforced Polymers," *Journal of Composites Science*, vol. 5, no. 2, 2021, doi: 10.3390/jcs5020040.

[95] A. S. G. G. F. P. G. Primetzhofer, "Data set determination for lifetime assessment of short fibre reinforced polymers," *Journal of Plastics Technology*, vol. 15, 2019.

[96] A. Wilmes and K. Hornberger, "Influence of Fiber Orientation and Multiaxiality on the Fatigue Strength of Unnotched Specimens – Lifetime Estimation," *Procedia Engineering*, vol. 133, pp. 148-160, 2015, doi: 10.1016/j.proeng.2015.12.642.

[97] *nCode DesignLife Theory Guide*.

[98] "nCode DesignLife 13.1," ed.

[99] *FEMFAT 5.4*.

[100] Michael A. Sutton, Jean-Jose Orteu, and H. W. Schreier, *Image correlation for shape, motion and deformation measurements: basic concepts, theory and applications*, New York, N.Y.: Springer, 2009.

[101] F. W. J. Van Hattum and C. A. Bernardo, "A Model to Predict The Strength of Short Fiber Composites," *Polymer Composites*, vol. 20, no. 4, pp. 524-533, 1999.

[102] C. mbH. "CAMPUS - a material information system for the plastics industry, "Ultramid A3W Campus Datasheet"." https://www.campusplastics.com/campus/en/datasheet/Ultramid%C2%AE+A3W/BASF/20/738dcdf8/SI?pos=31 (accessed 07th of September, 2022).

[103] T. Li and J. F. Luye, "Flow-Fiber Coupled Viscosity in Injection Molding Simulations of Short Fiber Reinforced Thermoplastics," *Intern. Polymer Processing*, pp. 158-171, 2019.

[104] D. Gsellmann, M. Jerabek, and D. Salaberger, "Comparison of predicted and measured fiber orientations in injection molded parts."

[105] S. Vervoort, "Fatigue analysis of fibre-reinforced polymers," presented at the European Congress on Computational Methods in Applied Sciences and Engineering (ECCOMAS 2012), Vienna, Austria, 2012.

[106] N. Jia and V. A. Kagan, "Effects of Time and Temperature on the Tension Tension Fatigue Behavior of Short Fiber Reinforced Polyamides," *Polymer Composites,* vol. 19, no. 4, pp. 408-414, 1998.

[107] K. Handa, A. Kato, and I. Narisawa, "Fatigue Characteristics of a Glass Fiber Reinforced Polyamide," *Journal of Applied Polymer Science,* vol. 72, pp. 1783-1793, 1999.

[108] K. Noda, A. Takahara, and T. Kajiyama, "Fatigue failure mechanisms of short galss fiber reinforced nylon 66 based on nonlinear dynamic viscoelastic measurement," *Polymer,* vol. 42, pp. 5803-5811, 2001.

[109] M. De Monte, E. Moosbrugger, and M. Quaresimin, "Influence of temperature and thickness on the off-axis behaviour of short glass fibre reinforced polyamide 6.6 – cyclic loading," *Composites Part A: Applied Science and Manufacturing,* vol. 41, no. 10, pp. 1368-1379, 2010, doi: 10.1016/j.compositesa.2010.02.004.

[110] J. Lindhult and M. Ljungberg, "Fatigue Analysis of Anisotropic Short Fibre Reinforced Polymers by Use of Digimat and nCode DesignLife," Master, Department of Applied Mechanics, Chalmers University of Technology, Gothenburg, Sweden, 2015.

[111] P. Heyes, "Multiaxial Assessment method for fatigue calculations in composite components."